CH_4 Decomposition Kinetics on Supported Co and Ni Catalysts

by

YI ZHANG

B.Sc., Dalian University of Technology, 1993

M.Sc., Beijing University of Chemical Technology, 1999

A THESIS SUBMITTED IN PARTIAL FULFILMENT OF

THE REQUIREMENTS FOR THE DEGREE OF

DOCTOR OF PHILOSOPHY

in

THE FACULTY OF GRADUATE STUDIES

(DEPARTMENT OF CHEMICAL AND BIOLOGICAL ENGINEERING)

We accept this thesis as conforming

to the required standard

THE UNIVERSITY OF BRITISH COLUMBIA

February, 2004

Abstract

Methane activation is important in a number of reactions that aim to convert natural gas to more valuable products using supported metal catalysts. As a potential alternative to steam reforming and partial oxidation, catalytic decomposition of CH_4 may provide H_2 without CO contamination for use with PEM fuel cells. However, the mechanism of carbon deposition and catalyst deactivation during CH_4 decomposition is complex and not fully understood.

The present work is aimed at clarifying some aspects of catalyst deactivation during the decomposition of CH_4 at moderate temperatures on low loading Co and Ni catalysts. The experimental observations presented in the present work suggest that catalyst deactivation was a consequence of the competition between the rate of encapsulating carbon formation and the rate of carbon diffusion. Stable activity or catalyst deactivation during CH_4 decomposition was observed, depending on which of these two rates was greater. The experimental observations also show that the gas phase composition K_M, and catalyst properties such as metal particle size and metal-support interaction have a critical effect on catalyst deactivation: catalyst deactivation was reduced with increasing K_M and with increasing metal particle size; catalyst deactivation was increased by a strong metal-support interaction.

A general kinetic model of CH_4 decomposition on supported metal catalysts has been developed based on experimental observations and the deactivation mechanism described above. The initial rate increase was described by including the rate of carbon nucleation at the tailing face of the metal particle using two methods: Cluster nucleation (Kinetic Model I) and Boltzmann nucleation (Kinetic Model II). The fit of literature data to Kinetic Model I and Kinetic Model II confirmed the presence of carbon nucleation at the tailing face. The observed CH_4 decomposition activity profiles on supported Co catalysts with either stable activity or

declining activity were well described by the kinetic model. The site density profile along the metal particle was obtained and the effect of metal particle size on the CH_4 decomposition activity has been quantified by fitting the observed CH_4 decomposition activity profiles to the developed kinetic model.

Keywords: CH_4 decomposition; hydrogen production; filamentous carbon; deactivation; metal particle size; catalyst metal loading; coke formation threshold; carbon nucleation; kinetics.

Table of Contents

List of Tables

List of Figures

Nomenclature

$*$	Active site of catalyst metal surface;
$[CH_xS]$	Site density of active site occupied by adsorbed carbon species on the catalyst surface, where $x = 0 \sim 3$;
$[C_PS]$	Site density of active site occupied by encapsulated site occupied by encapsulating carbon;
$[HS]$	Site density of active site occupied by adsorbed hydrogen atom on the catalyst surface;
$[Sv], [S]$	Site density of available active site on the leading face;
$[Sv_0]$	Site density of the total active site on the leading face;
a	Activity factor;
a_c	Activity of carbon $a_C = K_e P_{CH_4} / P_{H_2}^2$;
a_{Ni}	Surface area of Nickel;
C	Amount of carbon deposited by the time;
C_{b1}	Carbon atom in the bulk phase of the metal crystal at site $ss1$;
C_{b2}	Carbon atom at site $ss2$ segregating out of the metal particle;
$c_{C(Ni,f)}$	Concentration of carbon dissolved in nickel at the front of the particle (gas side);
$c_{C(Ni,r)}$	Concentration of carbon dissolved in nickel at the rear of the particle (support side);
$c_{C(Ni,sat)}$	Saturation concentration of carbon in nickel;
CH_x	Carbon species, $x = 0 \sim 3$;
CH_xS, CH_x*	Adsorbed carbon species on the catalyst surface, $x = 0 \sim 3$;
CH_xS_1	Chemisorbed species on the metal active site S_1, $x = 0 \sim 3$;
CH_xS_2	Chemisorbed species on the support S_2, $x = 0 \sim 3$;
$C_{\max}$	Maximum amount of carbon deposited by the time;
$C_{Ni,f}$	Carbon dissolved in nickel at the front of the particle (gas side);
$C_{Ni,r}$	Carbon dissolved in nickel at the rear of the particle (support side);
C_p	Encapsulating carbon on the leading face of metal particle;
c_p	Heat capacity;

C_PS	Active site occupied by encapsulating carbon;
CS	Adsorbed single carbon atom on the active site;
C_w	Carbon atom at a site in the final carbon phase, most likely to be a carbon filament (whisker);
D	Diameter of reactor;
d	Reaction order with respect to the activity factor;
d_a	Average diffusion path length, $d_a = (2/3)d_p$;
$d[C_pS]$	Changing rate of site density of active site occupied by the encapsulating carbon;
D_1	Surface diffusivity of carbon at the interface of metal and support;
d_p	Average metal particle diameter;
d'_p	Average catalyst particle size;
D_s	Diffusivity of carbon in the metal particle;
$D_{s,Ni}$	Diffusivity of carbon in nickel;
dS_v	Changing rate of site density of active site of catalysts;
dx	Finite distance of the finite layer of metal slab;
E	Activation energy of reaction;
E_D	Activation energy of carbon diffusion through metal;
G	Mass velocity;
h_s	Heat transfer coefficient between catalyst exterior surface and bulk fluid;
HS , $H*$	Chemisorbed H species;
i	Size of critical cluster, 10;
$(i+1)N_r$	Carbon nucleation rate on the tailing face of the metal particle;
K	Symbol used for equilibrium coefficients;
k	Empirical rate constant for the carbon deposition reaction;
k_1	Defined as $k_1 = k'_1 P_{CH_4}$;
k'_1	Rate constant for reaction $CH_4 + 2S_1 \xrightarrow{k'_1} CH_3S_1 + HS_1$;
k_2	Defined as $k_2 = k'_2 \theta_{S_2}$;
k'_2	Rate constant for reaction $CH_3S_1 + S_2 \xrightarrow{k'_2} CH_3S_2 + S_1$;
k_3	Rate constant for reaction $2HS_1 \xrightarrow{k_3} H_2 + 2S_1$;

k_4	Rate constant for reaction $CH_3S_1 \xrightarrow{k_4} CH_xS_1 + \frac{3-x}{2}H_2$;
k_5	Rate constant for reaction $CH_3S_2 \xrightarrow{k_5} CH_xS_2 + \frac{3-x}{2}H_2$;
k_b	Effective thermal conductivity of catalyst bed, assuming 26.5 W/mK;
K_c	Equilibrium constant for reaction $C_{Ni,f} + * \Leftrightarrow C*$;
K_{CH}	Equilibrium constant for reaction $CH* + * \Leftrightarrow C* + H*$;
K_{CH_2}	Equilibrium constant for reaction $CH_2* + * \Leftrightarrow CH* + H*$;
k_{CH_3}	Forwarding reaction rate constant for $CH_3S + 3S \Leftrightarrow CS + 3HS$;
K_{CH_3}	Equilibrium constant for reaction $CH_3S + 3S \Leftrightarrow CS + 3HS$;
k_{CH_4}	Forwarding reaction rate constant for $CH_4 + 2* \Leftrightarrow CH_3* + H*$;
K_{CH_4}	Equilibrium constant for reaction $CH_4 + 2* \Leftrightarrow CH_3* + H*$;
K_{CH_4}'	Equilibrium constant for reaction $CH_4 + * \Leftrightarrow CH_4*$;
K_{const}	Constant in the Scherrer equation, 0.89;
k_d	Rate constant for the deactivation;
K_e	Equilibrium constant for reaction $CH_4 = C(graphite) + 2H_2$;
k_{encap}	Rate constant for encapsulating carbon formation;
k_f	Rate constant for the forwarding reaction of CH_4 dissociation $CH_4 + 2S \rightarrow CH_3S + HS$;
k_g	Combined rate constant for the gasification $k_g = k_r \frac{1}{K_{CH_3} K_H^2}$;
$K_{graphite}$	Equilibrium constant for the reaction with graphite carbon formation;
k_{growth}	Rate constant for the carbon growth step;
K_H	Equilibrium constant for reaction $2HS \xleftarrow{K_H} 2S + H_2$;
K_M	Defined as $P_{H_2}^2 / P_{CH_4}$;
$k_M^{-\prime}$	Defined as $k_M^{-\prime} = k_M^- \cdot K_H^{1/2}$;
K_M^*	Experimentally determined threshold constant for the CH_4 cracking;
k_M^+, k_M^-	Rate coefficients of the forward and the reverse reaction of the rate-determining step $CH_4* + * \Leftrightarrow CH_3* + H*$;

K_M^f	Filamentous carbon formation threshold;
k_{nucl}	Rate constant for the carbon nucleation step;
$K_{observed}$	Observed equilibrium constant for the reaction with filamentous carbon formation;
k_p	Thermal conductivity of catalyst particle, assuming 1.7×10^{-2} W/mK;
k_r	Reverse reaction constant $CH_4 + 2S \Leftrightarrow CH_3S + HS$;
K_r	Defined as $K_r = K_3K_4K_5$;
K_r'	Defined as $K_r' = K_r / K_H^{3/2} = K_3K_4K_5 / K_H^{3/2}$;
K_r''	Defined as term $K_r'' = K_r' / (K_c \cdot c_{C(Ni,sat)})$;
K_w	Equilibrium constant for reaction $C_{Ni,r} \Leftrightarrow C_W$;
L	Catalyst bed length;
L_M	Length of diffusion path of carbon in the metal;
L_R	Reactor length;
M	Molecular weight of graphitic carbon;
mc_0	Total number of moles of surface metal sites;
n	Reaction order;
$n_1(t)$	Site density of single carbon atom on the tailing face of metal slab;
$n_c(t,x)$	Site density of single carbon atom in the metal particle;
n_{CH_4}	Cumulative CH_4 consumption as a function of time-on-stream;
n_{CT}	Site density of carbon in the carbon tubes on the tailing face, for Kinetic Model I;
$n_i(t)$	Site density of critical cluster on the tailing face;
$n_j(t)$	Site density of small clusters containing j atoms;
n_M	Mass flux of carbon in the diffusion direction;
$n_p(t)$	Site density of encapsulating carbon on the leading face of metal slab;
N_{Pe}	Peclet number (Dimensionless);
$N_{Pe_{min}}$	Minimum Peclet number (Dimensionless);
Nr	Defined as $Nr = \frac{dn_x}{dt} = D_1 n_1 n_x$;
N_{Re_p}	Reynolds number based on particle diameter (Dimensionless);

$n_s(t)$	Site density of single carbon atom on the leading face;
$n_x(t)$	Site density of stable carbon cluster on the tailing face of metal slab;
P_{CH_4} , P_{H_2}	Partial pressure of CH_4 and H_2 in the gas phase;
P_{CO}	Partial pressure of CO;
P_{CO_2}	Partial pressure of CO_2;
R	Gas constant;
r	Measured methane decomposition rate;
r^*	Maximum rate of carbon deposition;
R'	Rate of reaction per unit mass of catalyst;
r_C	Carbon deposition rate;
r_d	Carbon diffusion rate leaving the leading face of the metal particle;
$\dot{r}_d$	Average carbon diffusion rate through the metal particle;
r_d'	Impinging carbon diffusion rate on the tailing face of the metal particle;
r_e	Encapsulating carbon formation rate;
$(r_f - r_g)$	Net rate of carbon formation;
r_f	Carbon deposition rate;
$r_{f,n}$	Net rate of carbon formation;
r_g	Carbon gasification rate;
r_{growth}	Carbon growth rate on the tailing face of the metal particle;
r_M	Radius of metal particle size;
$r_{\max}$	Maximum rate of carbon deposition rate;
r_{nucl}	Carbon nucleation rate on the tailing face of the metal particle;
r_P	Radius of catalyst particle;
$r_{r,n}$	Net rate of carbon removal;
r_t	Radius of rector;
R_V	Rate of reaction per unit volume of catalyst;
S , S_1	Metal Active site;
S_2	Support site;
$ss1$	A subsurface site just below the surface on which the surface reactions take place;

$ss2$	A subsurface site just below the interface between the nickel particle and the support;
S_v	Available active site on the leading face;
SV	Space velocity;
S_{v0}	Total active site on the leading face of catalyst;
T	Temperature;
t	Time-on-stream;
t^*	Time at which the rate of carbon deposition reaches its maximum value;
T_b	Temperature of bulk fluid;
T_s	Temperature of catalyst surface;
T_w	Temperature of reactor wall;
u	Superficial velocity;
V	Volume of reactor;
w	Instrumental peak broadening, $w = 0.004$ radians;
W	Full width at half maximum of the diffraction peak (FWHM);
x	Length in the carbon diffusion direction of metal slab;
X	Conversion of the reaction;
$xstable$	Defined as $xstable = \sigma_i D_i \int_0^{} n_1(t)dt$;
z	Direction of carbon diffusion in the metal;
β	Defined as $\beta = \sqrt{W^2 - w^2}$;
γ	Surface tension of carbon fibres;
ΔG_c	Free energy deviation between the reaction for filamentous carbon formation and graphite carbon formation;
$\Delta G^0_{graphite}$	Free energy observed for the reaction with graphite carbon formation;
$\Delta G^0_{observed}$	Free energy observed for the reaction with filamentous carbon formation;
ΔH	Heat of reaction;
ΔH^0_{298}	Standard heat of reaction at 298 K;
θ	Diffraction angle in the X-ray diffraction measurement, radians;
θ^*, θ_{S_1}	Surface coverage of the available surface active site;
$\theta_{CH_xS_1}$	Fractional surface coverage by species CH_xS_1, where $x = 0 \sim 3$;

θ_{CH_x}	Active site occupied by the species indicated by the subscription, where $x = 0 \sim 3$;
$\theta_{CH_xS_2}$	Fractional surface coverage by species CH_xS_2, where $x = 0 \sim 3$;
θ_{HS_1}	Fractional surface coverage by species HS;
Θ	Orientation angle between the graphite basal planes and the tube axis;
λ	Wavelength of radiation Cu Kα, 1.54 Å;
μ	Gibbs free energy for the graphite with radius r;
μ^*	Contribution of free energy from structural defects compared to graphite;
μ_0	Gibbs free energy for the graphite without curvature;
μ_g	Viscosity of the fluid, gas phase;
ρ	Density of gas phase;
ρ_c	Density of graphitic carbon;
ρ_M	Density of the metal;
ρ_p	Density of catalyst particle;
σ_i and σ_x	Capture number that describes the diffusion flows of single atoms to critical cluster or stable clusters;
$\sigma_x D_1 n_1 n_x$	Single carbon nucleation rate due to the growth of stable cluster;
Φ	Metal dispersion defined as the metal atoms on the surface relative to the reduced metal;
ω	Mass fraction of carbon in the metal;
ω_g	Mass fraction of carbon in the metal at the interface between the gas phase and metal phase;
ω_L	Mass fraction of carbon in the metal in the metal at the interface of metal and support;

Acronyms:

B.E.	Binding energy;
CAEM	Controlled atmosphere electron microscopy;
CFC	Catalytic filamentous carbon;
CN	Carbon nanofibres;
CVD	Chemical vapour deposition;
FID	Flame ionization detector;
FT	Fischer-Tropsch;
FWHM	Full width at half maximum of the diffraction peak;
GC	Gas chromatograph;
MFC	Mass flow controller;
MS	Mass spectroscopy;
MSI	Metal-support interaction;
PEM	Proton exchange membrane;
PV	Pore volume;
RDS	Rate determining step;
SA	Surface area;
SV	Space velocity;
TCD	Thermal conductivity detector;
TEM	Transmission electron microscopy;
TOF	Turnover frequency;
TPR	Temperature programmed reduction;
XPS	X-ray photoelectron spectroscopy;
XRD	X-ray diffraction;

Preface

Methane activation is important in a number of reactions that aim to convert natural gas to more valuable products using supported metal catalysts. These reactions include CH_4 steam reforming and dry reforming for synthesis gas production, and CH_4 homologation for higher hydrocarbon synthesis. As a potential alternative to steam reforming and partial oxidation, catalytic decomposition of CH_4 may provide H_2 without CO contamination for use with PEM fuel cells. However, the mechanism of carbon deposition and catalyst deactivation during CH_4 decomposition is complex and not fully understood.

The present work is aimed at clarifying some aspects of the catalyst deactivation during the decomposition of CH_4 at moderate temperatures on low loading Co and Ni catalysts. Effects of gas composition and supported metal catalyst properties, such as metal particle size and metal-support interaction, in particular, were examined. Furthermore, based on the experimental observations, a kinetic model was developed to describe the deactivation and steady growth of filamentous carbon after an initial rate increase that is ascribed to carbon nucleation. The organization of the present thesis is briefly outlined in the following section.

The present thesis includes 7 Chapters, References and Appendices. In Chapter 1, the interest in the application of CH_4 decomposition, the motivation and the objectives of the present study are presented. The detailed literature review of previous contributions and existing questions are discussed in Chapter 2. Then, the experimental set-up, catalyst characterization and activity measurement methods are presented in Chapter 3, including an explanation of how measured activity profiles were analyzed and presented in the present work. In Chapter 4, the deactivation mechanism is discussed based on the experimental observations of effect of gas phase compositions. Furthermore, the coking threshold and filamentous carbon formation

threshold, related the onset of carbon formation and the filamentous carbon formation, respectively, are presented. In Chapter 5, the effect of metal properties, such as the metal type and metal-support interaction, on the deactivation are presented. The correlation of the coking threshold and the difference between two thresholds with the metal particle size is also discussed. In Chapter 6, a kinetic model that includes carbon nucleation and encapsulating carbon formation is developed to describe the catalyst deactivation or steady growth of carbon filaments after the initial rate increase. In Chapter 7, the conclusions of the present study are summarized. Recommendations for future work are also presented. The important calculations and experimental details are shown in Appendix A to confirm that the operation conditions in the present study are in the differential reactor mode. The GC operating conditions, Calibration of GC and mass flow controller, XPS Spectra and XRD diffraction profiles of catalysts and the script file of kinetic model in Matlab are also provided in Appendices.

I wish to express appreciation to my supervisor, Dr. Kevin J. Smith, for the guidance and many valuable comments made throughout my study. I wish to thank my research committee members: Dr. X. Tony Bi, Dr. Keith A.R. Mitchell, and Dr. Paul A. Watkinson and colleagues for their help. I also wish to thank Dr. Xiaonial Li for the TPR measurement. I gratefully acknowledge Dr. K.C. Wong for XPS measurements and Dr. ChangChun Yu for helpful discussions of the XPS results. Finally, I wish to acknowledge the support of my husband, Weiguo Ma, who has shown a great deal of patience during my Ph. D studies.

Chapter 1 Introduction

1.1 CH_4 Decomposition

Hydrogen, being a clean source of energy, is predicted to be the fuel of the future. Currently, the production of hydrogen from hydrocarbons, particularly CH_4, has attracted a lot of attention for fuel cell applications. Among the fossil fuels, CH_4 has the highest H/C ratio and thus is the most obvious source for hydrogen. Steam reforming of CH_4 represents the current technology for hydrogen production. Other common methods of hydrogen production include auto-thermal reforming and partial oxidation. However, all these processes involve the formation of a large amount of CO_2 as a by-product and this is of concern since CO_2 is a major greenhouse gas. CO_2-free hydrogen production via CH_4 decomposition has been suggested as a possible route to circumvent CO_2 formation during H_2 production. Since only hydrogen and carbon are formed in the decomposition process, separation of hydrogen is not an issue. The other main advantage of this approach is the simplicity of the CH_4 decomposition process as compared to conventional H_2 production methods. For example, the high- and low- temperature water-gas shift reactions and CO_2 removal step (involved in the conventional methods) are completely eliminated (Choudhary et al., 2003a).

Furthermore, as a potential alternative to steam reforming and partial oxidation, non-oxidative cracking or decomposition of CH_4 may provide hydrogen without carbon monoxide contamination. Proton exchange membrane (PEM) fuel cells have a requirement for CO<10 ppm in the hydrogen fuel. Currently, the water-gas shift reaction and the methanation reaction are used to reduce the CO concentration in hydrogen produced by steam reforming, dry reforming and partial oxidation of CH_4. But these purification steps add substantial cost to the operation of

a fuel cell. In view of the stringent CO intolerance of the state-of-the-art PEM fuel cells, it is desirable to explore CO-free fuel processing alternatives.

Another research interest in CH_4 decomposition stems from the interest of new materials synthesis. Filamentous carbon, formed during CH_4 decomposition, possesses a variety of properties with prospective applications as catalyst supports, reinforcement material, selective adsorbents, and as energy storage devices.

Based on the above three research interests, CH_4 decomposition has drawn a lot of attention recently. Although CH_4 decomposition has been investigated for the above purposes in the past, little attention has been paid to catalyst deactivation. In particular, the kinetics of CH_4 decomposition, that include the initial nucleation and deactivation, have not been incorporated in published kinetic or mechanistic models of the CH_4 decomposition process on supported metal catalysts.

1.2 Motivation

The motivation for the current study of CH_4 decomposition is associated with the deactivation phenomena from previous studies of CH_4 homologation. In previous work (Zadeh and Smith, 1998), the initial high rate of CH_4 decomposition on supported Co catalysts at 723K and 101 kPa, decreased rapidly but continued despite the nominal coverage of surface Co by CH_x being greater than 1. A semi-empirical model that was developed to describe this observation assumed that the decomposition of CH_4 on a Co site was followed by the migration of the resulting CH_3 surface species from the metal to the support. The migration step was essential to explain the decreased but sustained catalyst activity observed during CH_4 decomposition. However, an alternative mechanism for CH_4 decomposition is that filamentous carbon was formed during the reaction, which is common especially on Ni catalysts at high

temperature ($\geq$ 773K). The generally accepted mechanism of filamentous carbon growth (Baker et al., 1972) implies that filamentous carbon forms without encapsulation of the catalyst metal surface that is responsible for the decomposition of the CH_4 gas. In neither of the above two mechanisms will the metal active site be occupied by the carbon species. Hence, the present work is aimed at clarifying the deactivation mechanism during the decomposition of CH_4 at moderate temperatures on low loading Co and Ni catalysts. One objective of the present study is to determine whether the carbon filament formation mechanism occurs during CH_4 decomposition under mild conditions (temperature 723K ~ 773K) on Co catalyst. The conditions at which the on-set of filamentous carbon formation occurs will be elucidated so that the kinetic model of Zadeh and Smith (1998) can be extended to account for filamentous carbon formation.

1.3 Objectives of the Research

The goal of the present work is aimed at clarifying the mechanism of catalyst deactivation during CH_4 decomposition at moderate temperatures on low loading Co and Ni catalysts. Effects of supported metal catalyst properties, such as particle size, metal-support interaction, and gas composition, in particular, were examined. Furthermore, based on the experimental observations, a kinetic model was developed to describe the experimentally observed deactivation or steady growth of filamentous carbon after an initial rate increase that was ascribed to carbon nucleation. The main objectives of the present study are:

A. To clarify the significance of carbon species migration and carbon bulk diffusion;

B. To illuminate the effect of operating parameters, temperature and gas phase composition, on the catalyst deactivation during CH_4 decomposition;

C. To determine the operating conditions for the on-set of filamentous carbon formation;

D. To elucidate the mechanism of catalyst deactivation;

E. To clarify the effect of catalyst properties, metal particle size and metal-support interaction, on the deactivation during CH_4 decomposition;

F. To develop a kinetic model that includes carbon nucleation and encapsulating carbon formation, to describe the observed CH_4 decomposition rate as either stable activity or decreasing activity after the initial rate increase.

Chapter 2 Literature Review

Effective utilization of methane remains one of the long-standing problems in catalysis (Choudhary et al., 2003a). Over the past several years, CH_4 conversion to more valuable products has attracted significant attention either through direct conversion, such as by CH_4 oxidative coupling, CH_4 aromatisation or the cyclic CH_4 homologation reaction; or by indirect conversion to syngas ($CO+H_2$) produced by conventional steam reforming, dry reforming, partial oxidation or the more recently proposed cyclic process with CH_4 cracking at high temperature or moderate temperature followed by gasification of carbon with steam or oxygen, in order to produce high purity H_2 and syngas separately (Choudhary et al.,1999, 2001a, 2001b, 2002a, 2002b, 2003a, 2003b).

In all of the above processes, the activity of the catalyst in the CH_4 activation step and the carbon species formed in this step, are important and influence the selectivity, yield to the desired products and the life time of the catalyst. Previously, CH_4 decomposition was studied as an important side reaction in a number of reactions that aim to convert natural gas to more valuable products using supported metal catalysts. Accordingly, extensive attention has been paid to the mechanism of carbon deposition and subsequently the prevention of catalyst deactivation by carbon deposition. Currently, because of the increased interest in H_2 production free of CO_2 and CO, and the synthesis of new materials as discussed in Chapter 1, CH_4 decomposition has been investigated as a primary reaction of interest. In the following sections, contributions by researchers and unresolved questions relevant to CH_4 decomposition kinetics are discussed in detail.

2.1 Applications of CH_4 Decomposition

A number of new processes have been proposed for high purity H_2 production. Sternberg (1995, 1998, 1999a, 1999b) described a non-catalytic fossil fuel decarbonization process at temperatures above 1073K, to produce particulate carbon and H_2 for use as an energy source and thereby reduce greenhouse gas emissions. Muradov (1998 and 2001a, b) proposed catalytic pyrolysis of CH_4 to produce H_2 and elemental carbon using alumina-supported 10wt% Fe_2O_3 and NiO operated at 1123K. Poirier and Sapundzhiev (1997) proposed a concept for a fuel processor based on the catalytic decomposition of natural gas to H_2 for fuel cell applications: natural gas is decomposed over a catalyst, carbon is deposited on the catalyst and H_2 is produced. Once the catalytic bed is filled with carbon, catalyst is regenerated by burning carbon in air. This processor produced a H_2 gas stream with purity greater than 95% (compared to 75% with conventional steam reforming.). Meanwhile, Amiridis and coworkers (Zhang et al., 1996a; Zhang and Amiridis, 1998; Aiello et al., 2000) also proposed the combination of CH_4 cracking-steam regeneration in two distinct steps as an alternative to conventional steam reforming. The two-step process allowed for a partial separation of the products, since only H_2 was produced during the cracking step, and probably, a better control of the selectivity during the steam gasification step. Such a separation was made practically possible because of the ability of nickel particles to form carbon nanofibres (Section 2.2.1), and thus accumulate significant amounts of carbon on the catalyst before deactivation occurred. Direct cracking of a diluted 20%CH_4 over 16.4wt% Ni/SiO_2 catalyst and regeneration was mainly studied by Amiridis and coworkers (Zhang et al., 1996a; Zhang and Amiridis, 1998; Aiello et al., 2000). Choudhary and coworkers (2002b) also examined the feasibility of cyclic production of H_2 mainly on Ni catalysts supported on SiO_2, Al_2O_3, HY and ZrO_2 and Ni/ZrO_2 were identified as promising catalysts for the cyclic stepwise steam reforming of CH_4 to H_2 and CO_2 at 773K. From the point view of CO

impurity for PEM fuel cell application, Choudhary et al. (2001a) reported that there were still low levels of CO formed, due to the interaction of surface carbon (formed from CH_4 decomposition) with the support. The amount of CO has been quantitatively analyzed (part per million levels) by methanation of the CO and subsequent analysis by flame ionization detection (FID). The CO content in the H_2 stream was dependent on the support used. The low levels of CO coupled with the stability of the catalysts for CH_4 decomposition made this an interesting conceptual process for H_2 production for fuel cell applications.

From the point view of new materials research, Kuvshinov and coworkers (Kuvshinov et al., 1998; Ermakova et al., 1999 and Ermakova et al., 2000) used high loading Ni catalysts with different preparation methods as a novel way to produce filamentous carbon and H_2 by catalytic CH_4 decomposition. Avdeeva et al. (1999) studied CH_4 decomposition on coprecipitated 60-75wt% Co-alumina catalyst at 748K to 773K. Otsuka and co-workers (1999, 2001 and 2003) reported CH_4 decomposition over Ni on different supports. Their main focus in this area was to understand what factors controlled the carbon nanofibre morphology.

2.2 Carbon Formation during CH_4 Decomposition

CH_4 decomposition is described by Equation (2.1). CH_4 decomposition is an endothermic reaction. H_2 is the only gas phase product and carbon is produced as a solid deposit during CH_4 decomposition.

$$CH_4 \longrightarrow C + 2H_2 \qquad \Delta H^0_{298} = 75.6 kJ/mol \tag{2.1}$$

2.2.1 Carbon Morphologies

Catalyzed deposition of carbon from the gas phase results in a number of different carbon morphologies, among which filaments, nanotubes and encapsulated carbon are the most

important. Carbon nanotubes and filaments are referred to as catalytic filamentous carbon (CFC) or carbon nanofibers (CN) (Shaikhutdinov et al., 1997) in the present study, which are cylindrical or tubular carbon with radii in the nanometer scale and lengths up to several micrometers. The primary differences among these three carbon deposits are shown in Table 2.1 and a schematic of parallel type and fishbone type carbon nanofibres is provided in Figure 2.1.

Table 2.1 Different morphologies of carbon deposit (Nolan et al., 1998).

Type	Shape	Orientation of graphite layer	Position of catalyst particle	H_2 effect
Filaments	Carbon cones are "stacked"	$\Theta \leq 90$ (Filaments with large orientation are often not hollow)	At their tip	H_2 is believed to satisfy the valences at cone edges (the orientation angle Θ increases)
Nanotubes	Low H_2 end member of cylindrical carbon deposit	$\Theta=0$	At their tip	Essentially a filament without graphite edges, requiring no valence-satisfying species such as H_2
Encapsulated carbon	Multilayer "shells" encapsulating catalyst particles	N/A	Surrounded by graphite carbon	N/A

Note: Orientation of graphite layer is the orientation angle Θ between the graphite basal planes and the tube axis.

Note that carbon deposition has been studied for two different reasons in the past. Conventionally, carbon formation had been studied to eliminate or reduce the formation of catalytic filamentous carbon (CFC) on catalysts in steam reforming of CH_4. Recently, a great deal of effort has been directed towards optimization of process conditions for CFC formation for H_2 production, and to tuning the properties of the CFC for desired new materials production.

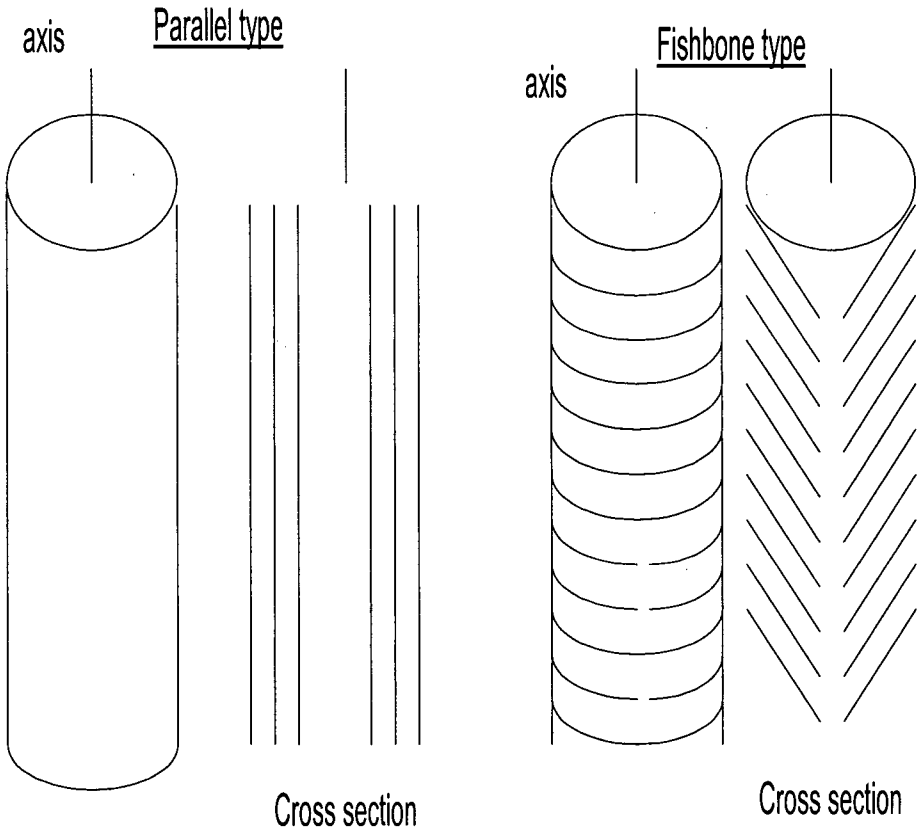

Figure 2.1 Simplified representation of the structure of parallel (left) and fishbone type (right) carbon nanofibres. The cross sections shown relate to the projections observed by TEM.

2.2.2 Mechanism of CFC Formation

The mechanism of CFC formation has attracted a lot of attention because of the unique activity behaviour observed during CFC formation. A typical CFC growth activity profile is presented in Figure 2.2. A steady-state activity can be obtained, contrary to an expected activity drop as carbon deposition on the metal catalyst surface removes catalyst sites for CH_4 decomposition.

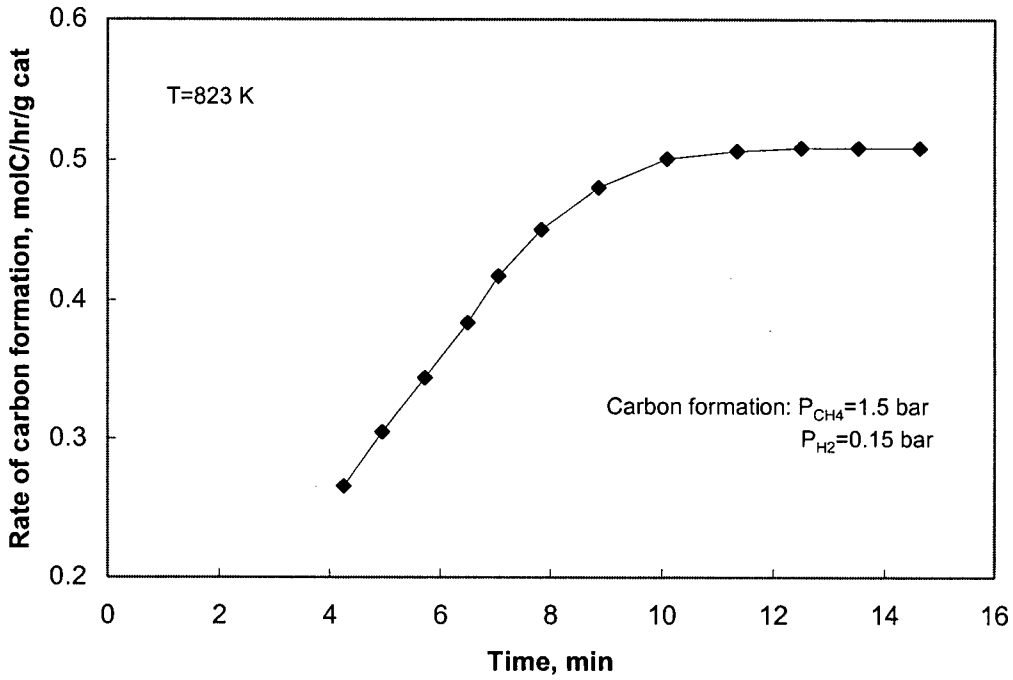

Figure 2.2 Typical rate versus time curve for CH_4 decomposition (Snoeck et al., 1997a).

Based on the qualitative and quantitative data obtained from experiments using the technique of controlled atmosphere electron microscopy (CAEM), a mechanistic interpretation on the growth of CFC was first proposed by Baker et al. (1972). They proposed that the adsorption and decomposition of the carbon-containing gas on one side of a metal particle, led to the formation of carbon atoms which then dissolved into the metal particle, diffused through the metal particle, and precipitated on the opposite side of the particle in the form of filamentous carbon. Snoeck et al. (1997a) included a carbon segregation step into the above mechanism. Figure 2.3 shows a schematic description of the CFC formation mechanism.

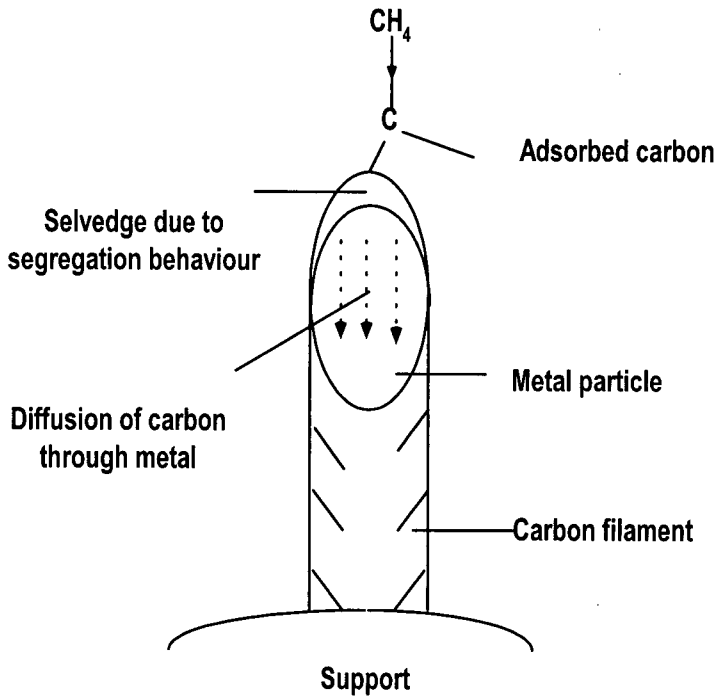

Figure 2.3 Schematic of CFC formation mechanism.

Regarding the rate determining step (RDS) in CFC formation, there is a debate in literature. The diffusion of carbon through the catalyst metal particle is generally considered to be RDS in the growth of CFC. The strongest quantitative evidence for the carbon diffusion as the RDS was the observation from several in situ electron microscopy studies that demonstrated that the activation energy E for filament growth from acetylene was in excellent agreement with the activation energy for diffusion of carbon through the bulk metal E_D (Holstein et al. 1995). The data given in Table 2.2 demonstrate the agreement. However, kinetic studies (Alstrup et al., 1993) have also shown that the first CH_4 dehydrogenation step is RDS.

The driving force for carbon diffusion from the metal-gas interface (where adsorption and decomposition of feed gas molecules takes place) to the metal-nanofiber interface (where carbon precipitates to form carbon nanofibers) has been proposed to be either an isothermal carbon concentration gradient or a temperature gradient. According to the study of Holstein et al.

(1995), however, bulk metal carbides can be ruled out as intermediates and Soret diffusion can be ruled out as a positive driving force for carbon diffusion.

Table 2.2 Comparison of activation energies for diffusion of carbon through metal, E_D, and that for carbon filament growth, E.

Metal	E_D, kJ/mol	E, kJ/mol
α-Fe	78-80	67±5
		76±8
γ-Fe	148-154	142±12
Ni	139-145	145
Co	145-162	139±7
Cr	110-117	113±15
V	116	115±12
Mo	139-172	145±17

2.2.3 Thermodynamic Properties of CFC

In earlier studies of CFC formation from CO and CH_4, attempts were made to characterize the thermodynamic properties for carbon formed by measuring equilibria of reaction. These studies observed that the equilibrium constants of reactants were smaller than the equilibrium constants corresponding to the formation of graphite. In addition, Rostrup-Nielsen (1972) observed that the deviations depended on the nickel particle size. The equilibrium constant obtained varied from catalyst to catalyst and the equilibrium correlated with the maximum nickel particle size of the catalyst. Thus the greatest deviations from graphite data were observed on catalysts with small nickel particles. The deviation from graphite data was explained by a more disordered structure of carbon formed during CFC formation and by a contribution from the surface energy of the carbon nanofibers.

2.3 Kinetic Studies of CH_4 Decomposition

For the last two decades, much attention has been paid to CFC deposited on 3d-metal catalysts (Ni, Fe, Co and their alloys) as exemplified by the studies of Baker (1989), Rostrup-Nielsen (1972) and Geus (1985). However, the factors controlling the formation of CFC are still not well understood.

2.3.1 General Activity Profile

During CFC production, the measured catalyst activity generally undergoes the following changes as the reaction proceeds: (1) an initial increase in activity; (2) a stable activity (the time for CFC formation); and (3) a decrease in activity (time of catalyst deactivation). Based on these observations, the general carbon decomposition process is assumed to involve three stages: (1) an induction period; (2) a steady-state growth and gasification of filamentous carbon; (3) catalyst encapsulation (Baker et al., 1972; Kuvshinov et al., 1998). However, these three stages are not always observed. On the one hand, some researchers reported stable activity without deactivation. For example, Snoeck and co-workers (1997a) reported that the weight versus time curve for the CH_4 cracking has only two zones: one with an increasing rate of carbon formation and one with a constant rate. The zone with decreasing rate, due to gradual deactivation of catalyst observed by Baker et al. (1972), was not been observed by Snoeck and co-workers (1997a).

Accordingly, the kinetics describing stable activity was developed based on the experimental observations of steady growth of CFC. Typically, Safvi et al. (1991), Alstrup and Tavares (1993) and Snoeck et al. (1997a and 1997b) investigated the kinetics of CH_4 decomposition over supported metal catalysts without considering catalyst deactivation. These kinetic models of steady CFC growth will be discussed in Section 2.3.2 in detail. On the other

hand, some researchers observed only deactivation instead of steady growth of CFC. Accordingly, deactivation models were developed by these investigations. Typically, Demicheli et al. (1991) and Kuvshinov et al. (1998) investigated deactivation during CH_4 decomposition using empirical models, which will be discussed in Section 2.3.3.

However, although the mechanism for CFC formation, as discussed in Section 2.2.2, has been generally accepted and kinetic models have been developed, neither the kinetic models for steady growth nor the empirical models for deactivation can describe the general activity profile. In particular, the initial rate increase observed in the beginning of the reaction has not been considered. (Studies related to the induction period will be discussed in Section 2.3.5.) Hence, a general kinetic model, especially one that includes carbon nucleation and encapsulating carbon formation, is needed.

2.3.2 Kinetic Model of Steady CFC Growth

Various kinetic models have been suggested for steady CFC growth during CH_4 decomposition. Table 2.3 gives the detailed mechanisms, rate equations and reaction conditions examined. In the simplest model it was assumed that the rate of CFC formation was proportional to the carbon activity in the gas phase, independent of the nature of the carbon containing gas and applicable to endothermic as well as to exothermic reactions (Audier and Coulon, 1985). (Note that the diffusion process was only considered as a true rate-determining step (in the sense that other steps could be considered equilibrated) at low a_c (gas), where a_c is the activity of carbon ($a_c = K_e P_{CH_4} / P_{H_2}^2$ and K_e is the equilibrium constant for the reaction: $CH_4 = C(graphite) + 2H_2$)) Lund and co-workers (Lund and Yang, 1989; Safvi et al., 1991; Chitrapu and Lund, 1992) further examined this dependence using α-Fe, γ-Fe and Ni catalysts. At low a_c, the dependence was strong, but as a_c increased it became weaker.

Accordingly, a one-dimensional model of the filament growth process, considering a disk shape metal particle, was proposed to qualitatively explain this dependency (Safvi et al., 1991). However, quantitatively the model predicted a much higher carbon growth rate than was observed. Furthermore, a two-dimensional model (Chitrapu et al., 1992) was proposed to refine this one-dimensional model by accounting for the variation in diffusion path length with filament radius using a pear shape particle. However, the results were not significantly better than those obtained via the one-dimensional approximations, and the two-dimensional model required significantly more computational effort. Hence only one-dimensional model equations are listed in Table 2.3. Note that the effort of Lund and co-workers (Safvi et al., 1991; Chitrapu and Lund, 1992) was focused on the steady-state carbon growth. The driving force for carbon diffusion was shown to be through the gradient in chemical potential (one-dimensional model, with activity of carbon equal to 1 at interface of metal and support) or concentration (two-dimensional model) of the dissolved carbon between the top and bottom surface of the particle.

Based on studies of carbon deposition on Fe films, Grabke and co-workers (1980) suggested a kinetic model for the dissociative adsorption of CH_4. In this model it was assumed that adsorbed CH_4 was stepwise dehydrogenated. Furthermore, Alstrup et al. (1993) showed that the linearized versions of the Grabke-type kinetic models could be fitted accurately to experimental results for the steady-state carbon deposition on silica-supported nickel catalyst, but only below a critical carbon activity, which depended weakly on the temperature. This linearized version of Grabke-type kinetic models is useful to determine whether the chemisorption of the CH_4 molecule or the dehydrogenation of methyl is the rate-limiting step.

More recently, Snoeck and coworkers (1997a and 1997b) proposed a rigorous CFC formation model. The coupling of the surface reaction, the segregation process, and the diffusion of carbon through the nickel particle led to a detailed model of the process of carbon filament

formation, which formed the basis for the kinetic modeling of the carbon formation and carbon gasification reaction. In this model, it was assumed that the diffusion of carbon through Ni originated from a concentration gradient, which implied a different solubility at the nickel-gas and the nickel-carbon interface. A thermodynamic basis for the different solubilities was provided. The segregation of carbon, taking place at the gas side of the Ni particle, was added as one of the steps in the global mechanism of carbon filament formation and gasification. The segregation process was described in a way similar to that of gas adsorption.

Based on the Hougen-Watson approach, the following rate equation was derived for the above mechanism (Snoeck and coworkers, 1997a and 1997b):

$$r_C = \frac{k_M^+ \cdot K_{CH_4}{}' \cdot P_{CH_4} - \frac{k_M^-{}'}{K_r'} K_C \cdot c_{C(Ni,f)} \cdot P_{H_2}^2}{(1 + K_C \cdot c_{C(Ni,f)} + \frac{K_C}{K_r'} \cdot c_{C(Ni,f)} \cdot P_{H_2}^{3/2} + K_{CH_4}{}' \cdot P_{CH_4})^2} \tag{2.2}$$

Since $c_{C(Ni,f)}$, the carbon concentration at the catalyst support side could not be measured or calculated, it was eliminated by coupling the diffusion step with the rate equation for the surface reaction during steady-state growth, i.e., $c_{C(Ni,f)} = c_{C(Ni,sat)} + \frac{d_a}{D_{s,Ni} a_{Ni}} r_C$. For the case with low carbon affinity, it was assumed that the concentration of carbon dissolved in Ni was almost uniform over the whole nickel particle for all experimental conditions and equal to the concentration of carbon at the support side of the particle: $c_{C(Ni,f)} \approx c_{C(Ni,r)} \approx c_{C(Ni,sat)}$ since $d_a / (D_{S,Ni} \cdot a_{Ni}) \leq c_{C(Ni,sat)}$. (Note: symbols see nomenclature.) For the cases that the concentration gradients through the Ni particle were non-negligible, the concentration of carbon in the Ni particle could not be assumed to be uniform and was not equal to the saturation concentration at the support side.

Also of note is the fact that the abstraction of the first H atom from molecularly adsorbed CH_4, with the formation of an adsorbed methyl group, was treated as the rate-determining step. This was contrary to theoretical studies that showed that the activation energy for the activation of gas phase CH_4 ($CH_4 + 2* \Leftrightarrow CH_3* + H*$, where * represents an active catalyst site) was less than that of adsorbed CH_4 ($CH_4** \Leftrightarrow CH_3** + H*$) over group VIII metal catalysts (Shustorovich and Bell, 1991). It is more reasonable to assume that the first step of the activation reaction can be written as $CH_4 + 2* \Leftrightarrow CH_3* + H*$, but Snoeck et al. (1997b) explained that the difference in RDS could arise from the fact that the theoretical studies and their kinetic studies (Snoeck et al., 1997 a and b) were performed in a completely different pressure range.

2.3.3 Empirical Deactivation Model

Since most kinetic studies have focused on the steady-state CFC growth, there is no kinetic model that describes the deactivation of the catalyst. Only empirical models, proposed by Demicheli et al. (1991) and Kuvshinov et al. (1998), are available to describe the deactivation of the catalyst during CH_4 cracking. Table 2.4 gives the detailed rate equations and reaction conditions examined. Demicheli et al. (1991) considered the activity factor, a, dependent on the time, temperature and CH_4 and H_2 partial pressures. Kuvshinov et al. (1998) investigated the deactivation of the catalyst proposing a carbon blocking of the surface active sites. Then, the rate of deposit was found to be proportional to the amount of CFC on the catalyst, the rate of CFC formation was in inverse proportion to the exponent of the product of the CH_4 to H_2 concentration ratio and time.

Table 2.3 Kinetic models of CFC steady growth during CH_4 cracking.

Reference	Rate equation	Mechanism	Catalysts, operation range
Safvi and co-workers (1991)	$r_C = \frac{n_M}{\rho_M L_M} = \frac{\alpha}{\gamma L_M^2}\left\{\left[\frac{\beta}{\gamma}(\gamma\omega_g - 1)\right]e^{\gamma\omega_g} - b_2\gamma\right\}$ (2.3) $b_2 = \frac{e^{\gamma\omega_L}}{\gamma}\left[\frac{\beta}{\gamma}(\gamma\omega_L - 1) - 1\right]$ (2.4) Where $\alpha = 1.43\exp(\frac{-19900}{T})$ (2.5) $\beta = 23.2$ (2.6) $\gamma = 2.42\times10^{-1}\exp(\frac{6790}{T})$ (2.7)	$n_M = -\rho_M D_s \frac{d\omega}{dz}$ (2.8) where $D_s = \alpha(1-\beta\omega)e^{\gamma\omega}$ (2.9) Boundary conditions: $a_c(z=0) = a_c(gasphase)$ (2.10) $a_c(z=L) = 1.0$	α-Fe, γ-Fe and Ni
Alstrup and Tavares (1993)	Assume CH_4 dissociative chemisorption is RDS: $r_C / P_{H_2}^2 = k_{CH_4}\theta^{*2}\frac{P_{CH_4}}{P_{H_2}^2}$ (2.11) Assume the dehydrogenation of methyl is RDS: $r_C / P_{H_2}^2 = \frac{k_{CH_3}K_{CH_3}}{K_H^{1/2}}\theta^*\frac{P_{CH_4}}{P_{H_2}^2}$ (2.12) General micro kinetic model: $r_C = k_{CH_4}\left(P_{CH_4}\theta^{*2} - \frac{1}{K_{CH_4}}\theta_{CH_3}\theta_H\right) =$ $r_C = k_{CH_3}\left(\theta_{CH_3}\theta^* - \frac{1}{K_{CH_3}}\theta_{CH_2}\theta_H\right)$ (2.13)	Based on stepwise dehydrogenation of surface species after chemisorption of the CH_4 molecule. $H_2 + 2* \Leftrightarrow 2H*$ K_H $CH_4 + 2* \Leftrightarrow CH_3* + H*$ k_{CH_4}/K_{CH_4} $CH_3* + * \Leftrightarrow CH_2* + H*$ k_{CH_3}/K_{CH_3} $CH_2* + * \Leftrightarrow CH* + H*$ $CH* + * \Leftrightarrow C* + H*$ $C* + ss1 \Leftrightarrow C_{b1} + *$ $C_{b1} + ss2 \Leftrightarrow C_{b2} + ss1$ $C_{b2} + ws \Leftrightarrow C_W + ss2$	Ni/SiO_2 $Ni_{0.99}Cu_{0.01}/SiO_2$ $Ni_{0.9}Cu_{0.1}/SiO_2$ Temperature range 723-863K P_{CH_4}: 20-80kPa P_{H_2}: 5-15kPa
Snoeck et al. (1997b)	Non-reversible model: the rate-determining step contains forward and reverse $r_C = \frac{k_M^+ \cdot K_{CH_4}' \cdot P_{CH_4} - \frac{k_M^-}{K_r''}\cdot P_{H_2}^2}{\left(1 + \frac{1}{K_r''}\cdot P_{H_2}^{3/2} + K_{CH_4}' \cdot P_{CH_4}\right)^2}$ (2.14) Reversible model: The approximate reversible version $r_C = \frac{k_M^+ \cdot K_{CH_4}' \cdot P_{CH_4} - \frac{k_M^-}{K_r''}\cdot P_{H_2}^2}{\left(1 + \frac{1}{K_r''}\cdot P_{H_2}^{3/2} + K_{CH_4}' \cdot P_{CH_4}\right)^2}$ (2.15)	$CH_4 + * \Leftrightarrow CH_4*$ K_{CH_4}' $CH_4* + * \rightarrow CH_3* + H*$ $k_M^+ \& k_M^-$ $CH_3* + * \Leftrightarrow CH_2* + H*$ K_{CH_3} $CH_2* + * \Leftrightarrow CH* + H*$ K_{CH_2} $CH* + * \Leftrightarrow C* + H*$ K_{CH} $2H* \Leftrightarrow H_2 + 2*$ $1/K_H$ $C* \Leftrightarrow C_{Ni,f} + *$ $1/K_C$ $C_{Ni,f} \Rightarrow C_{Ni,r}$ $C_{Ni,r} \Leftrightarrow C_W$ K_w	Ni catalyst promoted with low level of K 773K~823K P_{CH_4}: 1.5~10bar P_{H_2}: 0~1.5 bar

Table 2.4 Empirical models of deactivation during CH_4 cracking.

Reference	Rate equation	Mechanism	Catalysts and operation range
Demicheli et al. (1991)	$r_C = r^* a$ (2.16) $r^* = k\left(P_{CH_4} - P_{H_2}^2 / K_e\right)/(1 + K_H P_{H_2}^{0.5})^n$ (2.17) Where $a = \exp(-k_d P_{CH_4} \tau / P_{H_2})$ (2.18) $\tau = t - t^*$ (2.19) where $n = 7$	The activity factor a was dependent on the time, temperature and CH_4 and H_2 pressure. $\frac{da}{d\tau} = -r_d a^d$ (2.20) where d=1 $r_d = k_d P_{CH_4} / P_{H_2}$ (2.21)	Ni/Al_2O_3-CaO $CH_4/H_2/N_2$ mixture 838K~938K Atmospheric pressure
Kuvshinov et al. (1998)	The dependence for the CFC rate formation: $dC/dt = r_C = \left[-\frac{n+1}{2} k^* r_{max}^{1/n+2}\left(C^2 - C_{max}^2\right) + r_{max}^{1+1/n}\right]^{n/(n+1)}$ (2.22) $r_{max} = k\left(P_{CH_4} - P_{H_2}^2 / K_e\right)\left(1 + K_H P_{H_2}^{0.5}\right)^n$ (2.23) where $n = 7$	CH_4 adsorption on an ensemble of nickel atoms	High loading >30wt% Ni
Zadeh and Smith (1998)	The rate of change of coverage of different surface species follows directly from equations: $\frac{d\theta_{S_1}}{dt} = -2k_1\theta_{S_1}^2 + k_2\theta_{CH_3S_1} + k_3\theta_{HS_1}^2$ (2.24) $\frac{d\theta_{CH_3S_1}}{dt} = k_1\theta_{S_1}^2 - k_2\theta_{CH_3S_1} - k_4\theta_{CH_3S_1}$ (2.25) $\frac{d\theta_{HS_1}}{dt} = k_1\theta_{S_1}^2 - 2k_3\theta_{HS_1}^2$ (2.26) $\frac{d\theta_{CH_xS_1}}{dt} = k_4\theta_{CH_3S_1}$ (2.27) $\frac{d\theta_{CH_xS_2}}{dt} = k_5\theta_{CH_3S_2}$ (2.28) The cumulative CH_4 consumption as a function of exposure time are given by: $n_{CH_4} = -\int_0^t (mc_0) k_1 \theta_{S_1}^2 dt$ (2.29)	$CH_4 + 2S_1 \xrightarrow{k_1} CH_3S_1 + HS_1$ $CH_3S_1 + S_2 \xrightarrow{k_2} CH_3S_2 + S_1$ $2HS_1 \xrightarrow{k_3} H_2 + 2S_1$ $CH_3S_1 \xrightarrow{k_4} CH_xS_1 + \frac{3-x}{2} H_2$ $CH_3S_2 \xrightarrow{k_5} CH_xS_2 + \frac{3-x}{2} H_2$ $k_1 = k_1' P_{CH_4}$ $k_2 = k_2' \theta_{S_2}$ (2.30)	Co/SiO_2 Loading ≤ 12wt% 723 K

2.3.4 Previous Kinetic Studies of CH_4 Activation

As mentioned in Chapter 1, the motivation of the present research work stems in part from previous CH_4 non-oxidative homologation work (Zadeh and Smith, 1998). Non-oxidative homologation is a route to higher hydrocarbons via a two-step process, which involves high temperature decomposition ($CH_4 + 2S \rightarrow CH_xS + HS$) followed by low temperature hydrogenation ($CH_xS + H_2 \rightarrow S + CH_4, C_2H_6, C_3H_8$). In previous work (Zadeh and Smith, 1998), the initial high rate of CH_4 decomposition on supported Co catalysts at 623K and 101kPa, decreased rapidly but continued despite the nominal coverage of surface Co being greater than 1. To quantify these observations, a kinetic model of CH_4 activation was developed assuming decomposition of gas phase CH_4 on a Co site, followed by migration of the resulting CH_3 surface species from the Co to the support, and then followed by stepwise dehydrogenation of CH_3S_1 and CH_3S_2. In this model, the migration of carbon species from the metal site to the support site was considered essential for the active site regeneration. The simplified reaction mechanism is shown as in Table 2.4. The model was based only on data obtained from the decomposition of CH_4 in the first 2 min of reaction, and consequently pertains only to the very early stage of the reaction.

Migration of carbon species from the metal to the support as proposed by Zadeh and Smith (1998) was based on a number of observations from the literature. For example, Ferreira-Aparicio et al. (1997) proposed carbon species diffusion from active metal sites, where CH_4 was dehydrogenated, to silica and alumina supports during CH_4 decomposition over Co, Ni, Ru, Rh, Pt, Ir catalysts. Carbon species diffusion was invoked based on the observation that CH_4 was consumed in quantities greater than expected if one assumed a 1:1 CH_x: metal adsorption stoichiometry. In addition, during the decomposition reaction, a simultaneous release of CO and

H_2 occurred in the temperature range 550K - 873K as a result of the consumption of the hydroxyl groups of the support by CH_x.

An alternative explanation for active site regeneration during CH_4 decomposition is through the formation of CFC. However, the formation of CFC or the diffusion of carbon through the metal particle was not considered in the model by Zadeh and Smith (1998). Although the mechanism of CFC formation from CO, CH_4 and other hydrocarbons has been studied extensively on Ni catalysts, carbon deposition studies on supported Co catalysts are far fewer (Koerts and Santen, 1991; Guczi et al., 1997; Zadeh and Smith, 1998; Boskovic and Smith, 1996) due to the lower activity and lower capacity for carbon deposition of Co compared to Ni (Ermakova et al., 2000). However, data presented recently by Avdeeva et al. (1999) demonstrated that co-precipitated 60-75 wt% Co-alumina catalysts showed a high capacity for CFC formation during CH_4 decomposition at 773K. However it is unclear if CFC could form on the low loading Co catalysts at moderate temperature. Hence, one of the objectives of the present study is to clarify whether CFC formation can account for sustained CH_4 decomposition activity over extended time periods.

2.3.5 Induction Period of CFC

The initial rate increase observed during CFC formation is generally referred to as an induction period. Under some reaction conditions, no induction period is observed. Furthermore, under many conditions, graphitic carbon fibres do not grow, although the gas-phase composition is such that fibre growth was expected according to thermodynamics. Consequently, the cause of the initial rate increase and how the induction period affects the CFC formation is a critical question that needs to be addressed.

In existing CVD processes, carbon nucleation is considered the most important step for carbon nanotube or diamond formation on the metal surface (Liu and Dandy, 1996; Grujici et al.,

2002). However carbon nucleation has not been examined in detail for the CFC formation process over metal catalysts. Note that although the accepted mechanism for CFC, discussed in Section 2.2.2, rationalizes the steady-state growth of CFC, the important nucleation step, manifested in an initial rate increase during CFC formation, is not explained by this mechanism (De Jone and Geus, 2000). Snoeck et al. (1997a,b) mentioned that carbon nucleation is important and that the nucleation of CFC was caused by the formation of a solution of carbon in Ni that was supersaturated with respect to CFC. The degree of supersaturation was determined by the affinity for carbon formation of the gas phase. It was experimentally observed that the nucleation of CFC was much more difficult under conditions with a low affinity for carbon formation, leading to a slow nucleation and very long periods of increasing rate of carbon formation, but also to a small number of carbon filaments that was finally able to nucleate under these conditions. However, although Snoeck et al. (1997a,b) considered the nucleation of carbon, it was not included in the kinetic steps. Instead, more attention was paid to the experimental procedure. A series of experiments were sequentially performed on "used" catalyst samples, on which carbon was first deposited under standard conditions with a high affinity for carbon formation, so that the experimentally observed rates of carbon formation were all based on the same number of growing carbon filaments. Again, this model only described the steady state of carbon growth and did not describe the initial nucleation. A kinetic model that includes carbon nucleation is worthy of development.

Note that, besides carbon nucleation, two possible explanations exist for the observed initial rate increase during CH_4 decomposition. The first is related to the formation of metal carbide. Hoogenraad (1995) has studied the nucleation phase of carbon fibres by using magnetic measurements. In this study, it was assumed that metal carbide was the active site for CH_4 decomposition and metal carbide formation was considered crucial for the start of carbon fibre

growth. The study suggested that the formation of carbide causes the initial rate increase. The second opinion is that the faceting of metal particles caused the initial rate increase. It has been stressed by a number of workers that the surface structure of the metal may play a role in the growth process. Alstrup (1988) related the fact that the Ni (110) and Ni (100) surface were much more active for CH_4 dissociation than the Ni (111) surface. The above faceting of the metal particles was in line with electron microscopy observations. Faceting of the metal particle to allow for both hydrocarbon dissociation and graphite precipitation constituted a reasonable alternative for the nucleation phase. It should be noted, however, that all of these observations on the structure metal-particle faceting, inevitably have to be carried out after cooling of the sample and this could invoke crystal shape changes. To date, it remains unclear which of the explanations correctly account for the observed induction period.

2.4 Influence of Metal Catalyst Properties on Catalyst Deactivation

The mechanism of catalyst deactivation during CH_4 decomposition is complex. EXAFS and Mossbauer spectroscopies have shown that the form of catalyst remains metallic even after being encapsulated by graphite layers and detached from the alumina support with carbon fibres (Shah et al., 2001). Hence, it was postulated that the catalyst was actually not deactivated by poisoning or change in surface structure, but was isolated from methane by encapsulation and could not participate in CH_4 hydrogenation (Shah et al., 2001). Consequently, the decay constant depends on the rate of carbon build up on the surface of the catalyst, which in turn is a consequence of a number of interacting effects, including the metal type, metal particle size, metal-support interaction and the rate of carbon removal from the metal surface due to carbon bulk diffusion through metal particle, the rate of gasification due to the presence of H_2, CH_x migration rate from the metal to the support, and subsequently the formation of carbon with different morphologies. Nevertheless few studies have focused on the deactivation during CH_4

decomposition. Consequently, the mechanism and factors affecting the deactivation are not fully understood.

2.4.1 Influence of Metal Type and Metal Particle Size on Catalyst Deactivation

It is generally accepted that the active catalytic site for CH_4 decomposition and CFC growth is a metallic species. The ferrous metals of Group VIII are particularly active as catalysts for the growth of carbon filaments, the most important being (alloys of) Fe, Co and Ni. All of these metals can dissolve carbon and/or form metal carbides. Ni is the most common and active catalyst for CH_4 decomposition. Shah et al. (2001) also reported H_2 productivity results with undiluted CH_4 decomposition on 0.5%M-4.5%Fe/Al_2O_3, where M=Mo, Ni, or Pd at reaction temperature 973-1073K. Investigations of Co catalysts for CH_4 catalytic cracking are few. Only Avdeeva et al. (1999) reported filament carbon formation on a 60-75wt% Co/Al_2O_3 catalyst from CH_4 decomposition at 773K.

On all metal catalysts TEM measurements generally showed that the diameter of the CFC was closely related to the diameter of the metal particle. Also, it has been reported that the thermodynamic properties of CFC could be correlated to the metal particle size (Rostrup-Nielsen, 1972). Accordingly, coking threshold, corresponding to the operating conditions at which carbon deposition and carbon gasification rates are equal, was dependent on the metal particle size. This suggested that the metal particle size is critical to the carbon growth process.

The metal particle size effect for CH_4 decomposition kinetics has been discussed in a number of studies. Firstly, it was reported in literature that the particle diameter was critical for CFC formation (Baker, 1989). Nickel was the most active catalyst for decomposition of hydrocarbons including CH_4. The catalytic activity for the methane decomposition depended on the size of Ni metal particles; i.e., the particle size from 60 to 100 nm was most effective. However, nickel particles larger than 200 nm were incapable of producing filaments and were

covered by a carbonaceous crust that isolated them from the reaction medium (Takenaka et al., 2003). For this reason, unsupported nickel powder, liable to strong sintering in hydrocarbon medium, could not produce carbon filaments. Very small particles also appeared to inhibit graphite nucleation. Ni particles with diameters of 10-50 nm were known to initiate the growth of CFC, but the formation of CFC did not occur if the metal particle size was less than 7 nm (Kim et al., 2000). However, the carbon diffusion rate is faster on smaller particles due to the short diffusion path. For a given temperature, the rate of filament growth had an inverse square root dependence with metal particle size (Baker, 1989).

Secondly, Bartholomew (2001) reported that carbon formation and carbon gasification rates were influenced differently by modifications in metal crystallite surface chemistry, which were in turn a function of catalyst size. Also, the formation of coke and CFC involves the formation of C-C bonds on multi-atom sites, and hence, one might expect coke or carbon formation on metals to be structure sensitive. Alstrup and Travares (1993) also reported that one way to reduce the risk of carbon encapsulation and still be able to operate close to the carbon formation limit was to dilute the Ni surface of the catalyst with atoms which were much less reactive toward CH_4 than nickel, e.g., by alloying with copper, taking advantage of the different ensemble requirements for the steam reforming and the carbon formation process.

The carbon formation activity and the rate of deactivation were shown to be strongly dependent on metal particle size during the reforming of CH_4 with CO_2 (Bitter et al., 1998 and Zhang et al., 1996b). Solymosi et al. (1994) reported that the turnover frequency (TOF) for CH_4 decomposition over Pd catalysts decreased with the type of support in the order $TiO_2>Al_2O_3>SiO_2>MgO$ and this trend was interpreted as being due either to differences in Pd particle size (dispersion decreased in the same order), or the ease with which carbon migration occurred from the metal to the support. However, in this study, the effects of metal particle size

on CH_4 decomposition activity were not distinguished from support effects. However, the particle size effect on the catalyst deactivation during CH_4 decomposition was not reported.

The effect of metal loading, which is related to metal particle size, is quite unclear in the literature. Hence, a large range of metal loadings was used in literature: low loading catalysts (5wt% to 20wt% metal) were often used in studies reported in literature; catalysts with 0.1wt% loading were used by Poirier and Sapundzhiev (1997) in their fuel processor application; meanwhile, Shaikhutdinov et al. (1995) used very high loading nickel catalysts, from 30 to 95wt%, to maximize the catalyst carbon capacity. So, it is necessary to clarify the metal particle size effect on the catalyst activity and deactivation during CH_4 decomposition measured on catalysts with different metal loadings. Also of note is the fact that the effect of Co metal particle size on CFC formation has not been reported in the literature. Hence it remains unclear as to whether CFC formation during CH_4 decomposition under the mild reaction conditions employed during CH_4 homologation, can indeed explain the observed kinetics (Zadeh and Smith, 1998) on supported Co catalysts with low metal loading.

2.4.2 Metal-Support Interaction Effect on Catalyst Deactivation

Due to recent research interests, some attention also has been paid to enhancing CFC formation. Demicheli et al. (1994) reported that at low content of K, the K facilitated the formation of carbon filaments due to a reduced adhesion strength between the Ni particles and the alumina, i.e. the interaction between metal and support. This statement was based on the experimental detection of the location of potassium, at the interface between nickel and carbon, using STEM-EDX. This particular localization of the alkali could lower the adhesion strength of the graphite to the metal particle.

Snoeck et al. (1997a) also suggested that the MSI was important in explaining why full or hollow fibres were formed from supported metal particles. Briefly, at low temperature,

nucleation was slow and carbon atoms reached the entire metal-support interface via diffusion, and nucleation of a full fibre was observed. At higher temperatures, the nucleation started before the entire metal-support interface had been saturated with carbon atoms. Consequently, the metal/support interaction must be overcome to lift the particle at places where there was no excretion of carbon. They proposed this mechanism based on the observation that pear-shaped, conical or drop-wise particles accompanied the formation of hollow filaments. Similarly, Tavares et al. (1986) suggested that very small particles appeared to inhibit graphite nucleation because the enhanced MSI prevented the particle from being lifted from the surface, again preventing graphite nucleation. Furthermore, on high loaded Ni/SiO_2 and Fe/SiO_2 (80-90wt% of metal), the carbon yield was demonstrated to depend on the interaction between metal and silica. The presence of silicate in amount of ~2wt% in the $90\%Ni\text{-}10\%SiO_2$ catalyst gave rise to rapid catalyst deactivation. However, for Fe catalysts, silicate can both inhibit and promote the process of carbon formation (Ermakova and Ermakov, 2002).

2.5 Effect of Operating Conditions on Catalyst Deactivation

H_2 evolution parallels CH_4 decomposition and adsorption of H_2 onto the metal catalyst can promote gasification of deposited carbon species. The presence of H_2 can also affect the carbon morphology (Nolan et al., 1995). But the importance of operating conditions, especially the ratio of $P_{H_2}^2 / P_{CH_4}$, on the CFC formation and deactivation has not been fully recognized. Different researchers used different mixtures of CH_4 and H_2 to study CH_4 decomposition. Consequently, some researchers observed a steady CFC growth whereas activity profiles with deactivation under certain operating conditions, as shown in Figure 2.4 (Shah et al., 2001), have also been reported. Figure 2.4 shows that on the same catalyst, the decay constant is different for

two cases and the H_2 concentration or $P_{H_2}^2 / P_{CH_4}$ was quite different in these two cases. Hence, the effect of the ratio of $P_{H_2}^2 / P_{CH_4}$ on the catalyst activity and deactivation needs be addressed.

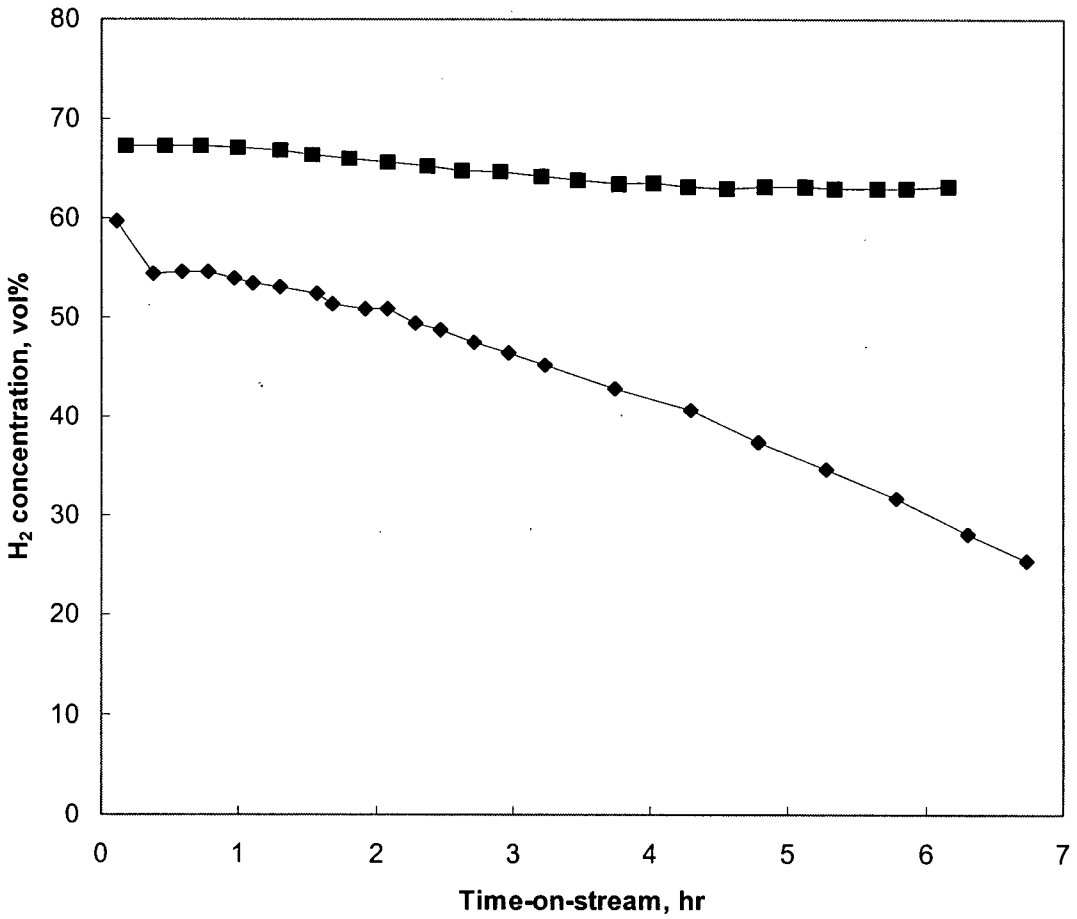

Figure 2.4 Change in H_2 production as a function of time-on-stream at 923K with 0.5%Mo-4.5%Fe/Al_2O_3 catalyst. The decrease in hydrogen production for a catalyst bed of 1 g is about 6%/hr while for a catalyst bed of 3 g is less than 1%/hr (Shah et al., 2001) (♦ 1g ; ■ 3g).

. Furthermore, a promotional effect of CO on the decomposition of ethylene over Fe to form CFC has been reported (Rodriguez et al., 1993), pointing to a strong influence of gas phase components on CFC formation.

2.6 Summary of Literature Review

Based on the literature described in this chapter, although CH_4 decomposition has been studied extensively, there remain many unresolved issues with respect to the decomposition kinetics, such as the nucleation manifested in the initial rate increase and the formation of encapsulating carbon corresponding to catalyst deactivation. Also, the effect of factors such as metal particle size and gas phase composition on the activity and deactivation of the catalyst during CH_4 decomposition remains unclear. The present work is aimed at addressing some of the above issues of deactivation during the decomposition of CH_4 at moderate temperature on low loading Co and Ni catalysts and developing a general kinetic model, which can describe the general activity profile of either steady growth or deactivation after the initial rate increase, that is ascribed to carbon nucleation.

Chapter 3 Experimental

3.1 Introduction

In this chapter the details of the experimental methods used in the present study for catalyst preparation, catalyst characterization and catalyst activity measurement during CH_4 decomposition, are presented. In Section 3.2, the preparation methods for Ni, Co catalysts supported on SiO_2 and ZrO_2, and the modified Co catalysts, are presented.

In Section 3.3 the details of the catalyst characterization methods are given. The number of catalyst active sites was measured by CO chemisorption and the metal particle size was estimated from the CO uptake. Filamentous carbon formation was detected by transmission electron microscopy (TEM). Temperature programmed reduction (TPR) and X-ray photoelectron spectroscopy (XPS) were performed on modified Co catalysts.

The experimental set-up for the CH_4 decomposition activity measurements is presented in Section 3.4. In Section 3.4.1, the details of the apparatus are presented. The method used to analyze the measured activity profile is described in Section 3.4.2. Finally, catalyst characterization data are presented in Section 3.5.

3.2 Catalyst Preparation

Co catalysts were prepared by incipient wetness impregnation of the silica support using an aqueous solution of $Co(NO_3)_2 \cdot 6H_2O$ (+98%, Aldrich). Precalcined (25 hr at 773K) silica gel (grade 62, 60-200 mesh, 15A, Aldrich 24398-1) with a BET surface area of 300 m^2/g and pore volume of 1.15 mL/g was used as the support. After impregnation, the catalysts were vacuum-dried at 383K for 37 hr and then calcined for 10 min at 723K. Note that using extended drying

times and short calcinations times have been shown to provide improved Co dispersion on SiO_2 support (Coulter and Sault, 1995).

Ni catalysts were prepared by incipient wetness impregnation of the support using an aqueous solution of $Ni(NO_3)_2 \cdot 6H_2O$ (+98%, Aldrich). After impregnation, the catalysts were dried at 383K for 37 hr and then calcined for 10 min at 723K. Besides SiO_2, ZrO_2 (Saint-Gobain Norpro Corp.) with a BET surface area of 52.9 m^2/g and pore volume of 0.3 mL/g was used as the support.

Modified Co/SiO_2 catalysts were prepared by step-wise incipient wetness impregnation. The pre-calcined (773K for 25 hr in air) silica support (Grade 62, 60-200 mesh, 15A, Aldrich 24398-1) was impregnated with an aqueous solution (de-ionized water) of $Ba(NO_3)_2$ (99.1+% Assay), or $La(NO_3)_3 \cdot 6H2O$ (99.9%, REO) or $ZrOCl_2 \cdot 8H_2O$ (99.9%, metals basis). The impregnation was followed by drying in vacuum or in air at 373K for 37 hr, and then calcining in air at 723K for 10 min. The modified SiO_2 supports contained BaO, La_2O_3 or ZrO_2, which were formed during calcination. A further impregnation was then carried out on the modified silica with an aqueous solution of $Co(NO_3)_2 \cdot 6H_2O$ (98+%, Aldrich 23926-7), followed by the same drying and calcination procedure. The modified catalyst will be designated as $Co/Me_xO_y/SiO_2$, where Me stands for Ba, Zr or La. The nominal Co loading for all modified catalysts $Co/Me_xO_y/SiO_2$ was 12 wt%. For $Co/Me_xO_y/SiO_2$ catalysts, the atomic ratio of Co to added metal (Co: Me where Me is Ba, Zr or La) was kept constant at Co: Me = 14:1 by setting the nominal metal loading for Ba, Zr and La to 2.0 wt%, 1.34 wt% and 2.02 wt%, respectively. Analysis of the calcined catalysts by X-ray diffraction (XRD) confirmed the presence of Co_3O_4 in each case and this was the only phase detected by XRD. The Co_3O_4 particle size, estimated from XRD line broadening, was 9.9 nm on SiO_2, 11.8 nm on BaO/SiO_2, 6.5 nm on the ZrO_2/SiO_2 support, and 11.7 nm on La_2O_3/SiO_2 (Appendix E).

Before being exposed to reactant, all catalysts were reduced by temperature-programmed reduction (TPR) in a 100mL/min 40%H_2/Ar to the desired temperature in one hour.

3.3 Catalyst Characterization

3.3.1 BET Surface Area and Pore Volume

Catalyst surface areas and pore volumes were measured by N_2 adsorption-desorption at 77K using a FlowSorb II 2300 Micromeritics analyzer. A 30%N_2/He mixture, fed at 15 mL/min was used for surface area measurement and a 95%N_2/He mixture fed at 20 mL/min was used for pore volume measurement. Samples were degassed at 398K for approximately 3 hours prior to measurement.

3.3.2 CO Chemisorption

The catalyst metal dispersion was determined by CO chemisorption. The CO uptake was measured gravimetrically (Perkin-Elmer TGS-2 thermogravimetric analyzer with a sensitivity of ±1 μg). About 10 mg of sample was dried at 523K for 8 hr in He. The drying temperature was chosen to avoid the transformation of Co_3O_4 to CoO, which was shown by *in situ* XRD and EXAFS measurements to occur in the temperature range 623-673K, under inert atmospheres (Khodakov et al., 1997). After drying, the catalyst was cooled to 323K and then reduced in a 40%H_2/He gas mixture flowing at 400 mL/min while heating from 323K to the desired temperature (Table 3.1) in 1 hour, followed by cooling to 323K. The degree of reduction was calculated from the catalyst weight change during TPR knowing the Co loading and assuming that Co_3O_4 was the only reducible species. Following a 5 min He purge after cooling, CO adsorption was initiated using a 12%CO/He gas mixture flowing at 400 mL/min and 101kPa total pressure. After the sample weight stabilized, the sample was flushed in pure He. No CO desorption was detected during this purge and hence the measured weight gain was attributed to

CO chemisorption at 323K. The catalyst dispersion, reported as a mole percent of reduced Co, was calculated from the CO uptake, assuming a 1:1 adsorption stoichiometry. The Co particle size was estimated from the equation d_p (nm)=0.962/Φ, where Φ is the metal dispersion (Juszczyk et al., 1993). The Ni particle size was estimated from the equation d_p (nm)=0.971/Φ, where Φ is the metal dispersion (Lesage et al., 1995).

3.3.3 Transmission Electron Microscopy (TEM)

The formation of filamentous carbon was detected by TEM (Hitachi H-800 electron microscope) examination of the used catalysts. TEM specimens were prepared by dispersing the used catalysts in ethanol and applying a drop of this dispersion onto a carbon coated copper grid, followed by drying. The microscope was operated at an acceleration voltage of 100 to 150 kV, with magnification in the range of 10,000-100,000x's. The average metal particle size was estimated directly from the number average diameter of the filaments observed by TEM, assuming that the metal particle size equals the filament diameter (Baker, 1989).

3.3.4 Temperature Programmed Reduction (TPR)

TPR was performed in a stainless steel micro-reactor. About 80mg of catalyst sample was loaded in the isothermal zone of the reactor and heated at a rate of 10 K/min to 623K in 60mL/min Ar, to desorb physically adsorbed water. After the sample was cooled to room temperature, the Ar stream was switched to 60 mL/min reducing gas 5%H_2 (99.999%, Praxair)/95%Ar (99.999%, Praxair), and the temperature was increased at a rate of 10 K/min to 1007K. The gas flow was controlled with a calibrated Brooks mass flow controller. The reactor effluent gas passed through a 4Å molecular sieve trap to remove the produced water, and was then analyzed by gas chromatography using a TCD (thermal conductivity detector).

3.3.5 X-ray Photoelectron Spectroscopy (XPS)

XPS measurements were performed in a Leybold MAX 200 instrument with hemispherical energy analyzer equipped with an achromatic Al Kα source (1486.6eV) (operated at 15 kV, 20mA emission current). The spectra are collected with a pass energy of 192eV for survey scan and a pass energy of 48eV for narrow scan. For all samples, Si 2p with binding energy (B.E.) 103.5eV was taken as an internal reference. Co 2p, O 2p and C 1s spectra were obtained by narrow scan (Appendix C). The Co $2p_{3/2}$ and $2p_{1/2}$ was fitted assuming a theoretical ratio of 2:1 and the spin-orbit coupling of Co 2p is fixed at either 15.0eV (for Co_3O_4 and metallic Co) or 15.7eV (for CoO). The $2p_{3/2}$ shake up line was fitted with one peak.

Catalysts examined by XPS were reduced to a maximum temperature of 723K, following TPR procedures described in Section 3.3.4. To minimize the exposure of the reduced or used catalysts to air, the catalyst samples were transferred from the reactor to the XPS chamber using a glove box filled with inert N_2.

3.3.6 X-Ray Diffraction (XRD)

Catalyst samples were firstly ground into powder and then coated on a glass slide. XRD patterns of catalysts were recorded with a Siemens D5000 powder diffractometer using monochromatized Cu Kα radiation (λ=1.54Å), operated at 40 kV and 30 mA. The step-scans were taken over the range of 2θ from 25 to 75° in steps of 0.04°. Diffraction patterns derived from the diffractograms were compared with standard data files. The particle size of Co_3O_4 was determined using the diffraction peak of 2θ=36.8° according to the Scherrer equation (3.1):

$$d_p = \frac{\lambda K_{const}}{\beta \cos\theta} \tag{3.1}$$

where d_p is the metal particle size, Å; λ is the wavelength (Cu Kα), 1.54 Å; K_{const} is a constant at 0.89; $\beta = \sqrt{W^2 - w^2}$, W is the full width at half maximum of the diffraction peak (FWHM), which was obtained by fitting the diffraction peak profile; w is instrumental peak broadening = 0.004 radians; θ is the diffraction angle, radians. The raw data of XRD is shown in Appendix E.

3.4 Catalyst Activity for Methane Decomposition

3.4.1 Activity Measurement

The methane decomposition rate on the catalysts of interest was measured in a fixed-bed reactor operated isothermally in differential mode. A flow diagram of the reactor and the on-line analytical equipment are shown in Figure 3.1. Gas flow rates were controlled by calibrated Brooks 5878 mass flow controllers. The stainless steel reactor (l = 60 cm, o.d. = 0.95 cm) was loaded with 0.2 g catalyst (average particle size 0.17 mm) that was supported on a quartz wool plug. A thermocouple was placed close to the top of the catalyst bed to control the reaction temperature. A Varian Star 3400CX gas chromatograph, fitted with flame ionization and thermal conductivity detectors connected in series, and equipped with a 60/80 Carbosieve G column, was used for the product and feed gas analyses. UHP grade H_2, CH_4, He, Ar (99.999%, Praxair), 5%CH_4/Ar calibrated gas (Praxair), 4.82%H_2/10.4CH_4/2.01%C_2H_4/3.75%C_2H_6/Ar calibrated gas (Praxair) and CP grade CO (Purity 99.5%, Praxair) were used in the experiments.

The methane decomposition rate was measured by the change in CH_4 flow rate (Appendix B.1). The ratio of H_2 production rate to the CH_4 decomposition rate was assumed 2:1, based on previous studies from this laboratory (Zadeh and Smith, 1998) and literature reports (Avdeeva et al., 1999). Furthermore, no higher hydrocarbons were produced under the experimental conditions of the present study.

Tests to determine the significance of external and internal diffusional effects were done following the guidelines given by Froment and Bischoff (1990). For the range of experimental conditions used in the present study, internal and external gradients in concentration and temperature were insignificant, as shown in Appendix A.

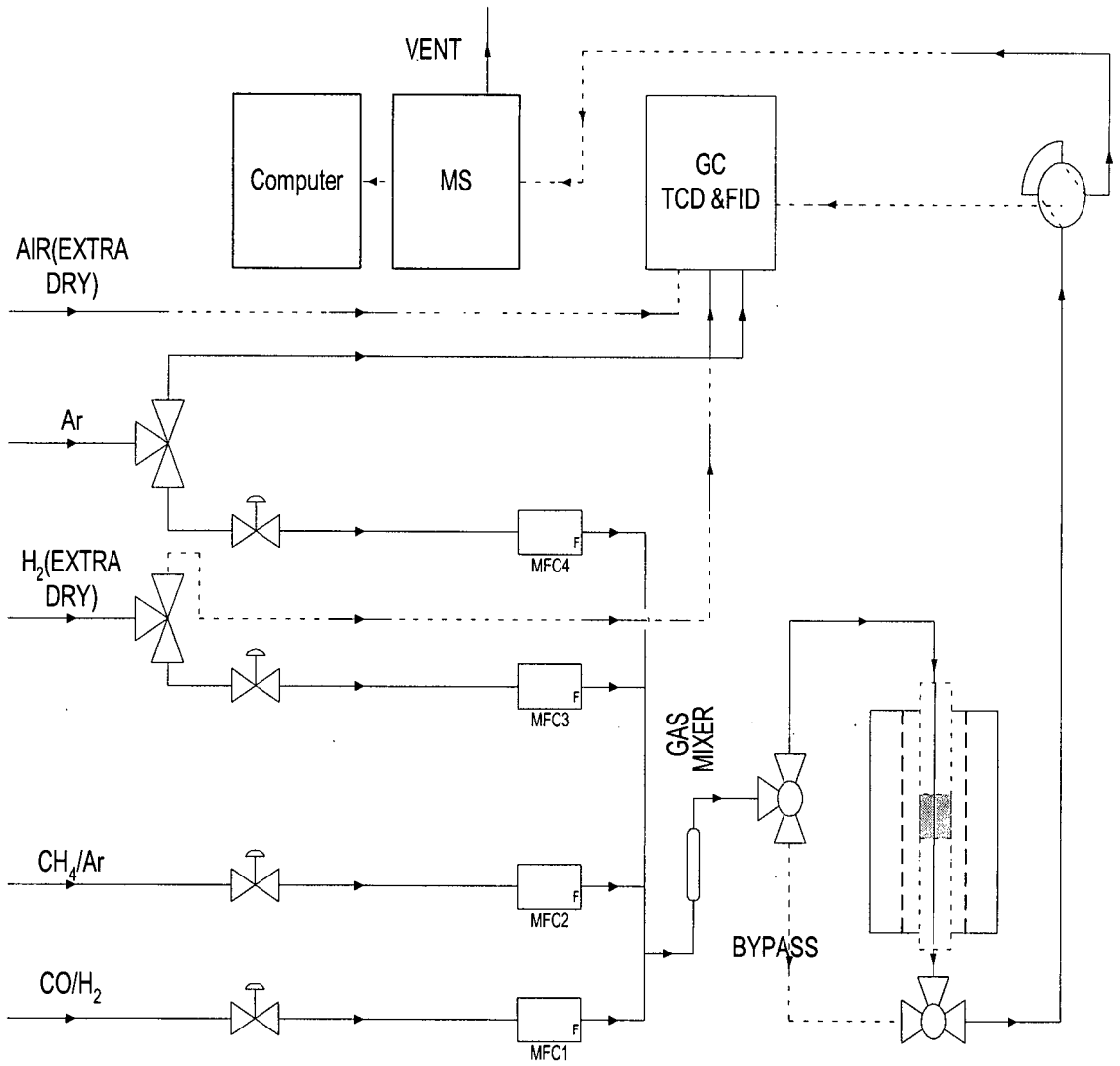

GC: gas chromatograph; TCD: thermal conductivity detector; FID: flame ionization detector; MS: mass spectroscopy; MFC: mass flow controller.

Figure 3.1 Block diagram of the experimental set-up used for CH_4 decomposition catalyst tests.

3.4.2 Description of the Measured Catalyst Activity Profile

Figure 3.2 shows typical curves of the measured CH_4 decomposition rate versus time for Co catalyst in the presence of a H_2/CH_4 feed. The activity profiles for CH_4 decomposition were of similar form for many of the catalysts investigated herein. The CH_4 decomposition rate first increases to a maximum, then decreases. The activity profiles are conveniently described by a kinetic equation of the type $r = r^* a$, where r^* is the maximum decomposition rate and a is the catalyst activity factor (Demicheli et al., 1991). If the time corresponding to the maximum is designated t^*, and if the rate is 1st order with respect to the activity factor, i.e. $da/dt = -k_d a^d$, where $d = 1$ and k_d is the decay constant, the methane decomposition kinetics after the maximum can be described by Equation (3.2):

$$r = r^* e^{-k_d (t - t^*)} \tag{3.2}$$

The maximum rate was identified directly from the activity profile. Curve fitting the decomposition rate data (after the maximum rate) versus $(t - t^*)$ using Table 2D curve software (SPSS Inc.), as shown in Figure 3.2, provided estimates of r^* and k_d. These two parameters were conveniently used to discuss the catalyst maximum activity (r^*) and decay constant, k_d, throughout the present study. For all of the data reported herein, the fits to the 1st order decay model had regression coefficients $R^2 > 0.90$. The sensitivity of r^* and k_d to the value of t^* chosen directly from the activity profile, was insignificant, as shown in Appendix G.

For the case of a measured activity profile without the maximum that occurred in the absence of H_2, the activity profile can simply be described by Equation (3.3) (Equation (3.2) with $t^* = 0$):

$$r = r^* e^{-k_d t} \tag{3.3}$$

Similarly, curve fitting of the measured CH_4 decomposition rate versus time data using Table 2D Curve software (SPSS Inc.), provided estimates of r^* and k_d.

In the present study, the decay constant k_d of a 1st order decay model was used to quantify the catalyst deactivation. In the following sections, the effect of process variables on deactivation will be discussed in terms of k_d.

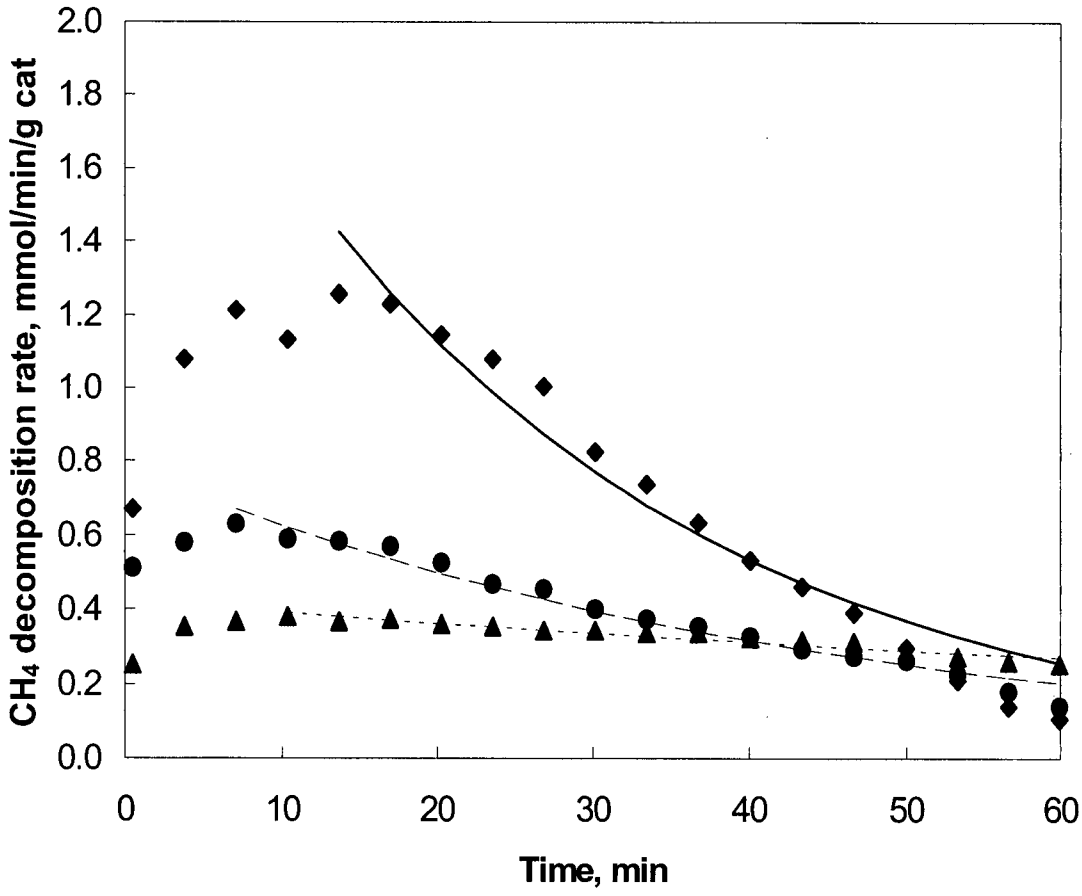

Figure 3.2 Activity of 12wt% Co/SiO_2 catalysts, with different $K_M = P_{H_2}^2 / P_{CH_4}$ ratios (Reduced at 923K, reacted at 773K, total gas flow 185 mL/min, weight of catalyst=0.2g; lines are the fit of Equation (3.2) to the experimental data points; ♦ $K_M = 0.01$ atm; • $K_M = 0.03$ atm; ▲ $K_M = 0.05$ atm).

In the present study, both decreasing activity and stable activity were observed on supported Co and Ni catalysts. The maximum activity in the case of declining activity was determined by the method described above. The maximum activity in the case of stable activity, r^*, was estimated directly from the measured stable activity.

3.5 Characterization Data

Properties of the Co/SiO_2 catalysts are listed in Table 3.1. A series of catalysts with estimated metal dispersion in the range 3.4 – 12.6% were obtained by reducing 5-30wt% Co/SiO_2 at 723K and 923K. The data of Table 3.1 show that reduction of the Co_3O_4 precursor was almost complete for all catalysts except the 30wt% Co/SiO_2 catalyst. The average Co particle size, estimated from the metal dispersion assuming pure Co particles, increased with increased Co loading (Table 3.1). The metal particle size of 11.4 nm, estimated by CO chemisorption on the 12 wt% Co/SiO_2 reduced at 723K, was in good agreement with the metal particle size (9.6 nm) estimated previously by XRD line-broadening (Zadeh and Smith, 1998), and with the 10 nm estimated from the TEM micrograph of the same catalyst after reaction.

Similarly, properties of Ni/SiO_2, Ni/ZrO_2 and modified Co catalysts $12wt\%Co/Me_xO_y/SiO_2$ are listed in Table 3.2, Table 3.3 and Table 3.4, respectively. These data will be referred to in the following chapters.

Table 3.1 Properties of Co/SiO_2 catalysts of the present study.

Co Loading	BET SA	PV	Reduction Temperature	Reduction Degree[c]	CO Uptake	Metal Dispersion	d_p (CO uptake)	d_p (TEM)
wt%	m^2/g	cc/g	K	mol%	mmol/g	%	nm	nm
5 Co	239	0.971	923	100	0.084	9.2	10.4	-
8 Co	230	1.080	923	100	0.103	7.1	13.5	-
10 Co	217	0.989	723	96.9	0.208	12.6	7.6	-
			923	100	0.094	5.4	17.8	-
12 Co	210	0.889	723	96.5	0.166	8.4	11.4	10[a]
			923	100	0.102	5.0	19.4	25[b]
30 Co	-	-	723	76.5	0.240	6.2	15.6	-
			923	89.4	0.155	3.4	28.3	26[b]

d_p: Estimated metal particle size; BET SA – surface area; PV – pore volume

[a]: Estimated from TEM image of catalyst after reaction at 723K

[b]: Measured from TEM image of catalyst after reaction at 773K.

[c]: Catalyst was reduced in 40%H_2/He from 323K to the desired temperature in one hour.

Table 3.2 Properties of Ni/SiO_2 catalysts of the present study.

Metal Loading	BET SA	PV	CO Uptake[a]	Metal Dispersion[a]	d_p (CO uptake)[a]	d_p (TEM)[b]
wt%	m^2/g	cc/g	mmol/g	%	nm	nm
2 Ni	277.6	0.690	0.012	3.6	27.2	31.7
5 Ni	250.5	0.618	0.027	3.1	30.9	33.2
8 Ni	218.5	0.566	0.036	2.6	36.8	32.5
12 Ni	234.5	0.566	0.041	2.0	43.3	50.0
15 Ni	201.5	0.485	0.050	2.0	49.5	62.5
30 Ni	163.3	0.390	0.107	2.1	47.2	50.0

BET SA – surface area; PV – pore volume; d_p – estimated metal particle size.

[a]: Catalyst was reduced in 40%H_2/He from 323K to 923K in an hour. Reduction degree was 100 mol% for all catalysts.

[b]: Measured from TEM image of catalyst after reaction at 773K.

Table 3.3 Properties of Ni/ZrO_2 catalysts of the present study.

Metal Loading	BET SA	PV	CO Uptake[a]	Metal Dispersion[a]	d_p (CO uptake)[a]
wt%	m^2/g	cc/g	mmol/g	%	nm
2 Ni	45.36	0.205	0.031	9.2	10.5
5 Ni	42.38	0.187	0.061	7.2	13.5
8 Ni	40.42	0.178	0.065	4.8	20.2
12 Ni	39.51	0.166	0.061	3.0	32.3

BET SA – surface area; PV – pore volume; d_p – estimated metal particle size.

[a]: Catalyst was reduced in 40%H_2/He from 323K to 923K in one hour. Reduction degree was 100 mol% for all catalysts.

Table 3.4 Properties of modified 12wt% Co/SiO_2 catalysts in the present study.

Catalyst	BET SA	PV	Reduction Temperature	Reduction Degree[a]	CO Uptake	Metal Dispersion	d_p (CO uptake)
	m^2/g	cc/g	K	mol%	mmol/g	%	nm
Co/SiO_2	210	0.889	723	96.5	0.166	8.4	11.4
			923	100	0.102	5.0	19.4
$Co/BaO/SiO_2$	211.1	0.468	723	88.2	0.094	5.2	18.4
			923	100	0.064	3.1	30.8
$Co/ZrO_2/SiO_2$	223.1	0.487	723	80.0	0.113	6.9	13.9
			923	100	0.105	4.5	21.4
$Co/La_2O_3/SiO_2$	197.0	0.472	723	99.9	0.120	5.9	16.3
			923	100	0.082	3.5	27.7

BET SA – surface area; PV – pore volume; d_p – estimated metal particle size.

[a]: Catalyst was reduced in 40%H_2/He from 323K to the desired temperature in one hour.

Chapter 4 Catalyst Deactivation Kinetics and Mechanism

4.1 Introduction

In this chapter, a mechanism of catalyst deactivation during CH_4 decomposition is discussed based on experimental observations. Firstly, the significance of filamentous carbon formation versus the migration of CH_x species from the metal to the support is discussed in terms of carbon removal and active site regeneration. Secondly, effects of temperature, H_2 and CO partial pressures, on the catalyst activity are presented. Based on the observations of the effect of gas phase composition on catalyst deactivation, a catalyst deactivation mechanism was developed and used to explain the experimental observations. Most importantly, the carbon formation threshold was coupled with the proposed filamentous carbon formation threshold to predict stable activity corresponding to the steady growth of filamentous carbon during catalytic CH_4 decomposition.

4.2 Activity Observations

4.2.1 Evidence and Significance of CH_x Migration and Filamentous Carbon Formation

The first question addressed in the present study arose from a previous homologation study on 12wt% Co/SiO_2. As described in Section 2.3.4, it was unclear whether filamentous carbon formed during CH_4 decomposition at low temperature, 723K. In order to detect filamentous carbon by TEM on the 12wt% Co/SiO_2 after reaction with 5%CH_4/Ar at 723K, the reaction time was extended to 120 min. Evidence of filamentous carbon growing from metal particles, corresponding to a low but stable CH_4 decomposition activity, is shown in Figure 4.1. The micrograph shows that the diameter of the filamentous carbon was about 10 nm, close to the initial metal particle size of 11.4 nm measured by CO chemisorption on the unused Co catalyst.

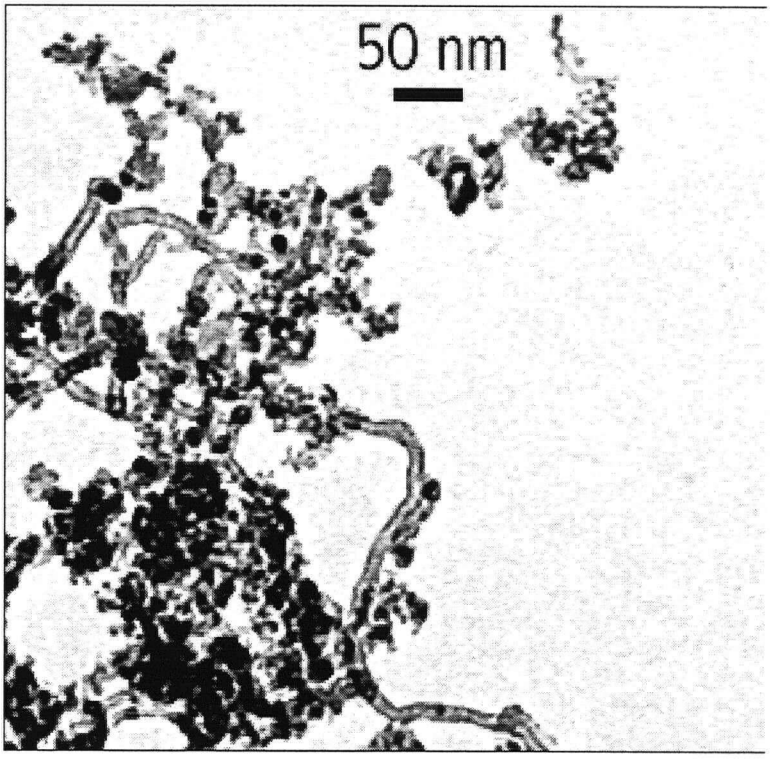

Figure 4.1 TEM image of 12wt% Co/SiO_2 catalyst (reduced at 723K) after 120 min reaction in $5\%CH_4/Ar$ at 723K, showing the presence of filamentous carbon, diameter $\approx$ 10 nm.

Additional experiments were performed to detect the migration of carbon species (CH_x), formed during CH_4 decomposition, from the Co to the SiO_2 support. The migration of these species from the Co to the SiO_2 support, where interaction with hydroxyl groups produces CO (Ferreira-Aparicio et al., 1997), was detected using mass spectroscopy by measuring the production of CO during CH_4 decomposition. Data of Figure 4.2 show that minimal amounts of CO were detected when SiO_2 alone was exposed to $5\%CH_4/Ar$ at 723K. However, CO production during CH_4 decomposition on the 12wt% Co/SiO_2 was significant, especially within the first few minutes of reaction. In accordance with the arguments presented by Ferreira-Aparicio et al. (1997) we assume that the source of CO is CH_x species that migrate from the metal onto the support where they react with hydroxyl groups to produce CO. The possibility of CO production due to CH_x and OH interaction localized near the metal particle perimeter cannot be ruled out, but the continued CO production after the initial rapid decline suggests that CH_x

migration to the support occurs, albeit to a small extent. Also note that the possibility of CO being produced from CH_4 interacting with unreduced metal oxide is small, since it is highly unlikely that the unreduced cobalt would react with methane following a one-hour reduction in 40% hydrogen at the same temperature. Furthermore, for the 12wt% Co/SiO_2 catalyst of Figure 4.2, the degree of reduction was 96.5 mol%, so that approximately 12 micromoles of oxygen would be available for reaction with CH_4 to produce an equivalent number of moles of CO. This is much less than the 77 micromoles of CO produced during the reaction period shown in Figure 4.2.

Filamentous carbon was observed under the reaction conditions shown in Figure 4.1. According to the filamentous carbon formation mechanism, carbon is removed from the metal surface by bulk diffusion through the metal particle. In addition, evidence for the migration of carbon species from the Co metal site to the support was provided by the production of CO during the CH_4 decomposition and the previously reported kinetic model that, of necessity, included a CH_x migration step from the metal to the support (Zadeh and Smith, 1998). These observations suggest that both carbon diffusion through the metal to form filamentous carbon, and the migration of CH_x from the metal to the support occur, and both contribute to the regeneration of active metal sites during CH_4 decomposition. However, the rapid decline in CO production (Figure 4.2) suggests that migration of CH_x from the metal to the support is only significant in the first 2 to 3 min of reaction. The regeneration of active metal sites for CH_4 decomposition over extended periods is mainly due to bulk diffusion of carbon through the metal particle to form filamentous carbon between the metal and support.

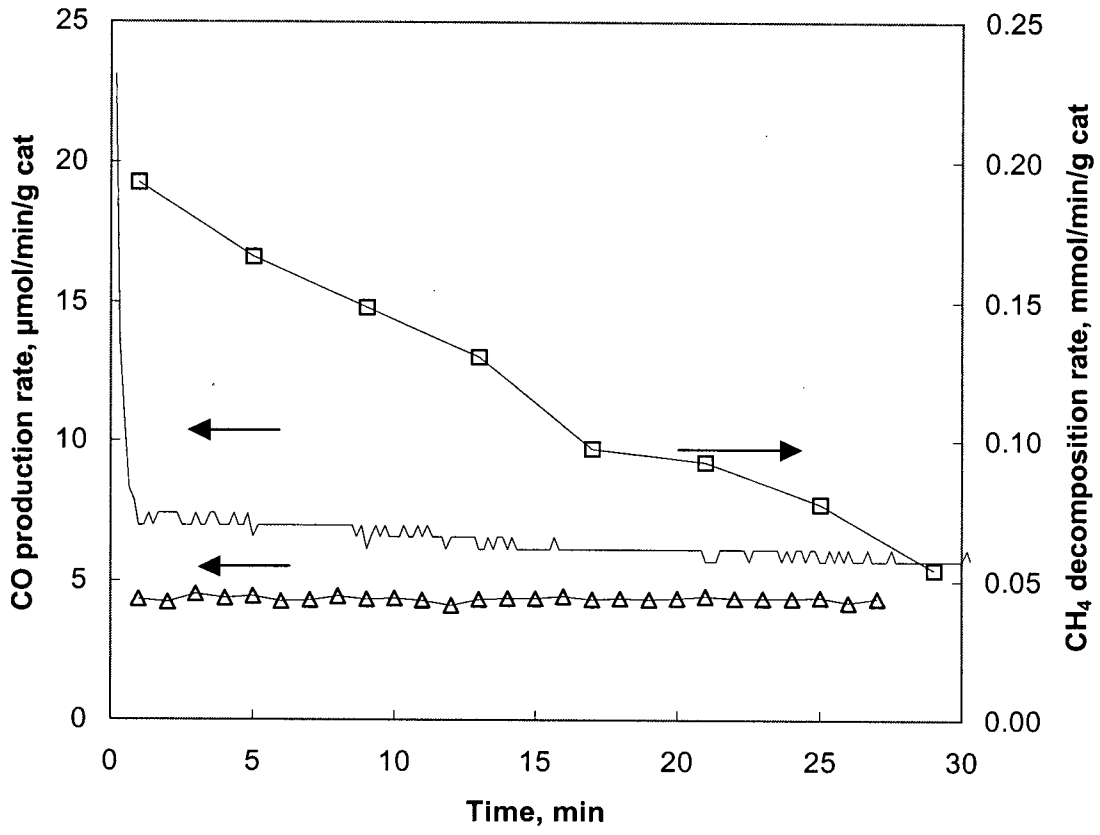

Figure 4.2 CO production rate over SiO_2 and 12wt% Co/SiO_2 (reduced at 723K) exposed to 140 mL/min of 5%CH_4/Ar at 723K (Δ CO production rate on SiO_2; — CO production rate on Co/SiO_2; □ CH_4 decomposition rate on Co/SiO_2).

4.2.2 Effect of Temperature on Activity

The effect of decomposition temperature on the catalyst activity for CH_4 decomposition was determined on 12wt% Co/SiO_2 catalysts, operated in the temperature range 723~873K. Figure 4.3 shows the catalytic activity versus time-on-stream of the 12wt% Co/SiO_2 catalyst, at different decomposition temperatures. Generally, the initial CH_4 decomposition rate was high but the catalyst deactivated rapidly. At 823K, for example, the CH_4 decomposition rate decreased to only 2.3% of its initial value after 30 minutes reaction. As discussed in Section 3.4.2, curve fitting of the measured CH_4 decomposition rate versus time data to Equation (3.3) using Table

2D Curve software, provided estimates of r^* and k_d. The influence of decomposition temperature on r^* and k_d is shown in Figure 4.4. The maximum CH_4 decomposition turn over frequency, (Max TOF, where $TOF = r^*$/active site, 1/min) increased from 1.4 to 9.4 1/min over the temperature range 723-873K with an apparent activation energy of 66.3 kJ/mol. The catalyst decay constant also increased with increasing temperature with apparent activation energy of 122.7 kJ/mol. Note that the data at 873K in Figure 4.3 show a single data point with high activity followed by a series of points at low activity. The data were not well described by the 1st order decay model. The fast decay is largely complete somewhere between point 1 and 2. However to be consistent with the other temperature data, and to capture this very rapid initial activity decay, the 1st order decay model was still used to fit the experimental data at 873K. Consequently, the estimated value of k_d reported in figure 4.4 had a large error, as shown by the error bar for that data point.

The apparent activation energy of 66.3 kJ/mol estimated for the maximum CH_4 decomposition rate on the 12 wt% Co/SiO_2 catalyst with average Co particle size of 9.5 nm, was in reasonable agreement with the 56 kJ/mol reported for CH_4 decomposition on Co/SiO_2 with metal particle size 10.3 nm (Zadeh and Smith, 1998). These values were somewhat higher than the value of 42 kJ/mol reported for the decomposition of CH_4 on Co/SiO_2 catalysts at less than a monolayer coverage (Koerts et al., 1992). Note also that these values are significantly lower than the activation energies reported for Fe and Ni catalysts when carbon diffusion through the metal is the RDS (Galuszka and Back, 1984; Holstein et al. 1995).

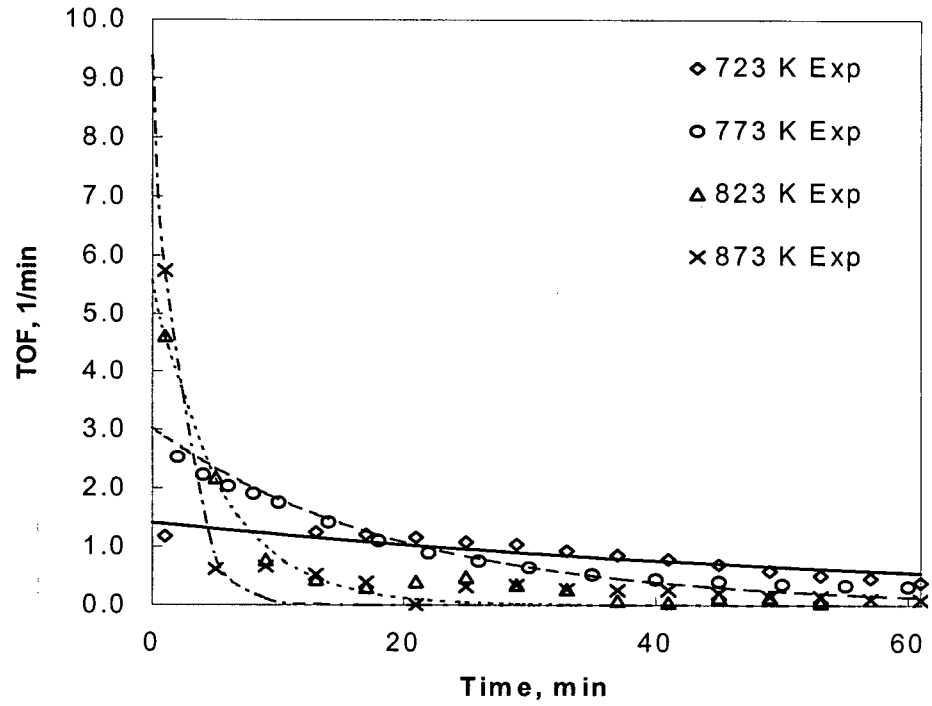

Figure 4.3 Effect of temperature on the activity of 12wt% Co/SiO_2 catalysts, reduced at 923K and reacted with $5\%CH_4/Ar$ at 140 mL/min. (Lines are 1st order decay model fit to the experimental data points).

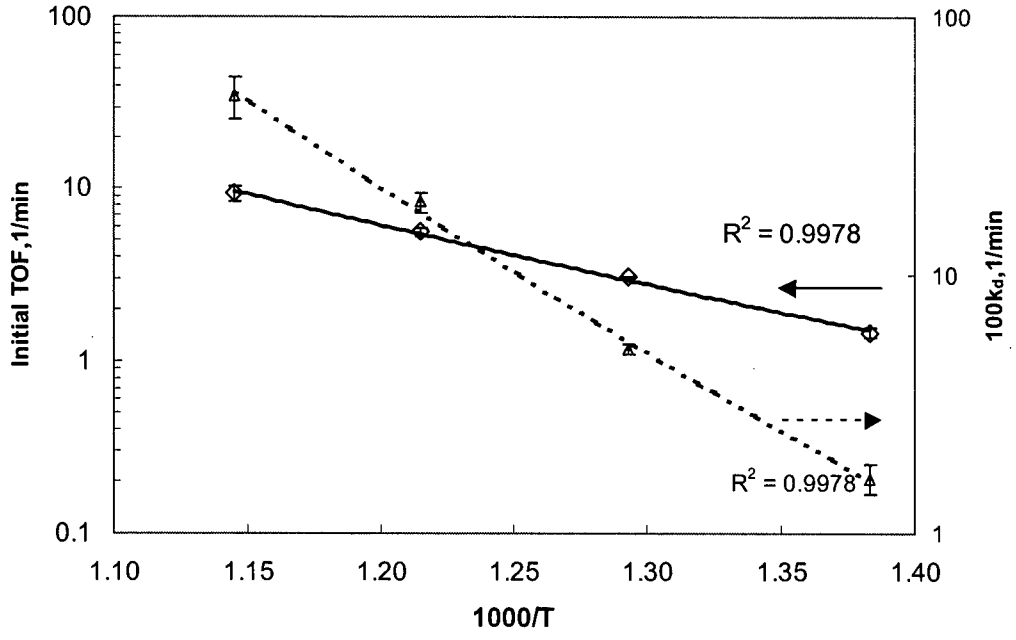

Figure 4.4 Arrhenius plots of maximum CH_4 decomposition rate (TOF, min^{-1}) (◊), and decay constant ($100\,k_d$) (Δ) versus 1000/T.

4.2.3 Effect of H_2 and CO on the Catalyst Activity

To determine the effect of adding small quantities of H_2 or CO to the CH_4 feed, a series of experiments were done to compare changes in the CH_4 decomposition activity due to the presence of 1.2%H_2 or 0.4%CO added to the 5%CH_4/Ar on 12wt% Co/SiO_2. By fitting the experimental data to the 1st order decay model, Equation (3.3), the maximum TOF and k_d were obtained and these values were plotted in Figure 4.5. Data of Figure 4.5 show that H_2 not only decreased the decay constant of the catalyst but also reduced the maximum decomposition TOF. TEM of the used catalyst after one hour reaction (Figure 4.6) showed filamentous carbon formation during CH_4 decomposition in the presence of 1.4%H_2 in the feed at 773K.

The data of Figure 4.5 also show that CO addition decreased the rate of catalyst deactivation, similar to the effect of adding H_2. However, an important difference between the effects of H_2 and CO is that the high maximum CH_4 decomposition TOF was maintained upon the introduction of CO, whereas H_2 addition reduced the maximum TOF. No higher hydrocarbons were detected upon CO addition, suggesting that no Fischer-Tropsch (FT) type reaction (from H_2+CO to higher hydrocarbons) occurred at the reaction conditions. Hence, the CO promotional effect could not be explained by assuming that FT type reactions removed H and thereby enhanced CH_4 decomposition. Furthermore, no CO decomposition was detected, based on the measured CO flow rate change through the reactor.

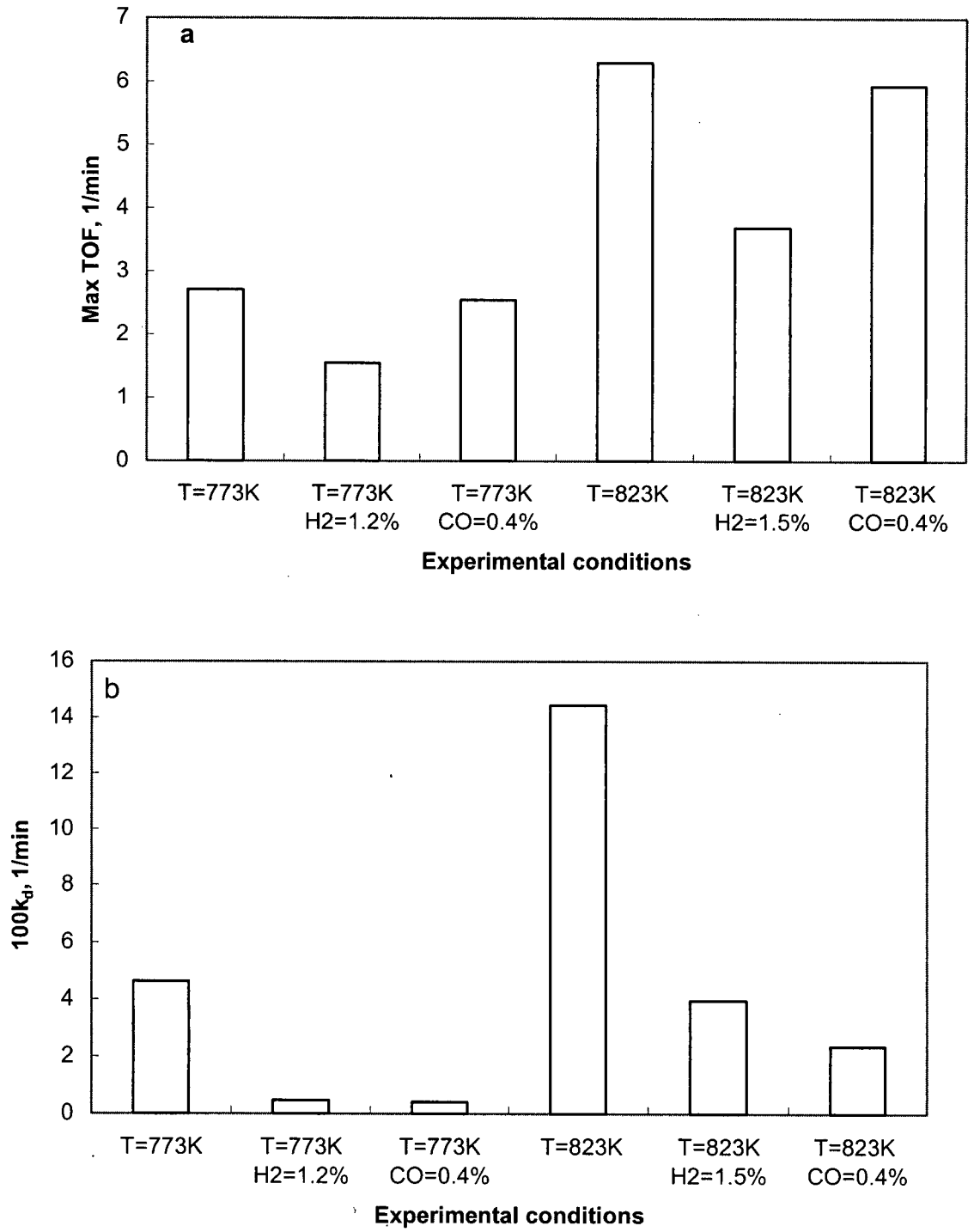

Figure 4.5 Effect of the presence of H_2 or CO on (a) the maximum activity (TOF) and (b) the decay constant ($100\,k_d$) on the 12wt% Co/SiO_2 catalyst (reduced at 923K), exposed to 5%CH_4/Ar at the reaction temperature indicated.

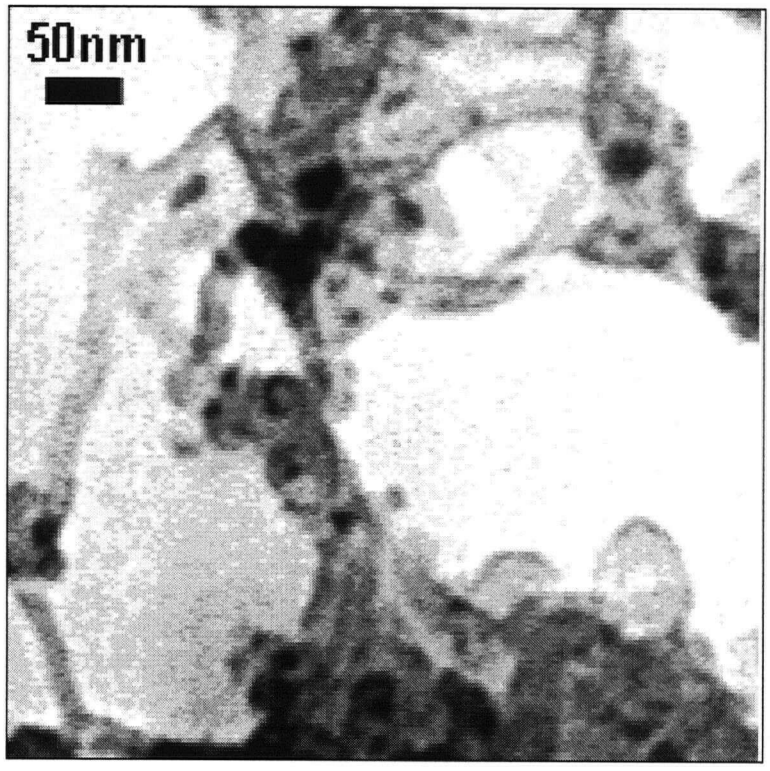

Figure 4.6 TEM micrograph of 12wt% Co/SiO_2 catalyst (reduced at 923K) after reaction in $5\%CH_4/1.4\%H_2/Ar$ at 773K for 60 min showing the presence of filamentous carbon with diameter ≈ 25nm.

Figure 4.7 presents a TEM micrograph that showed filamentous carbon formation after the catalyst was exposed to $5\%CH_4/Ar$ at 773K with 0.4%CO in the feed, corresponding to the steady CH_4 decomposition shown in Figure 4.8. Although CO is known to form filamentous carbon at higher temperature on supported metal catalysts, no filamentous carbon was detected by TEM when the Co catalyst was exposed to a 2vol.%CO in Ar. Consequently, we conclude that CH_4 decomposition was the main source of the filamentous carbon shown in Figure 4.7, corresponding to the steady CH_4 decomposition activity shown in Figure 4.8.

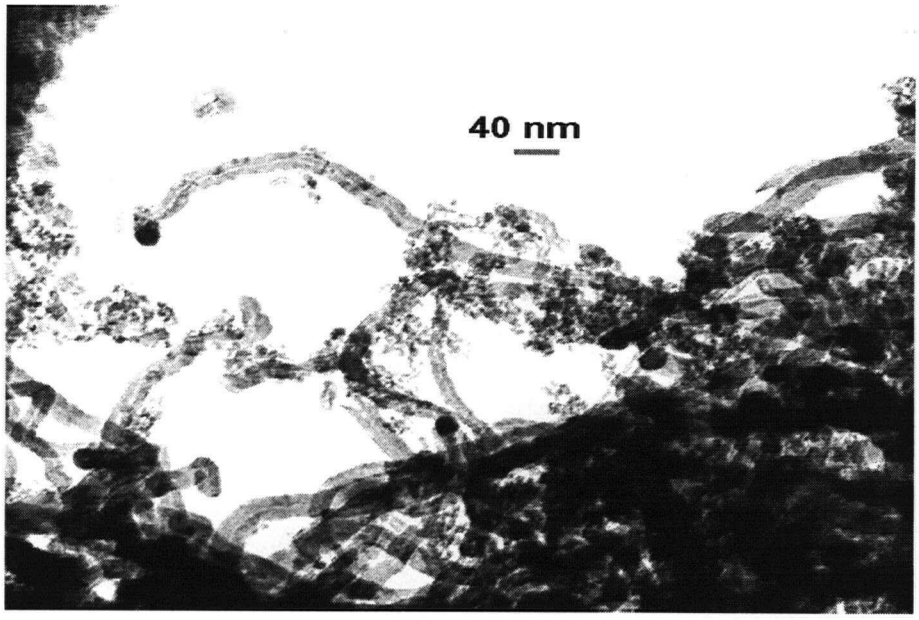

Figure 4.7 TEM micrograph of 12wt% Co/SiO_2 (reduced at 923K) after reaction in $5\%CH_4/0.4\%CO/Ar$ at 773K for 60 min showing presence of filamentous carbon with diameter ≈ 25nm.

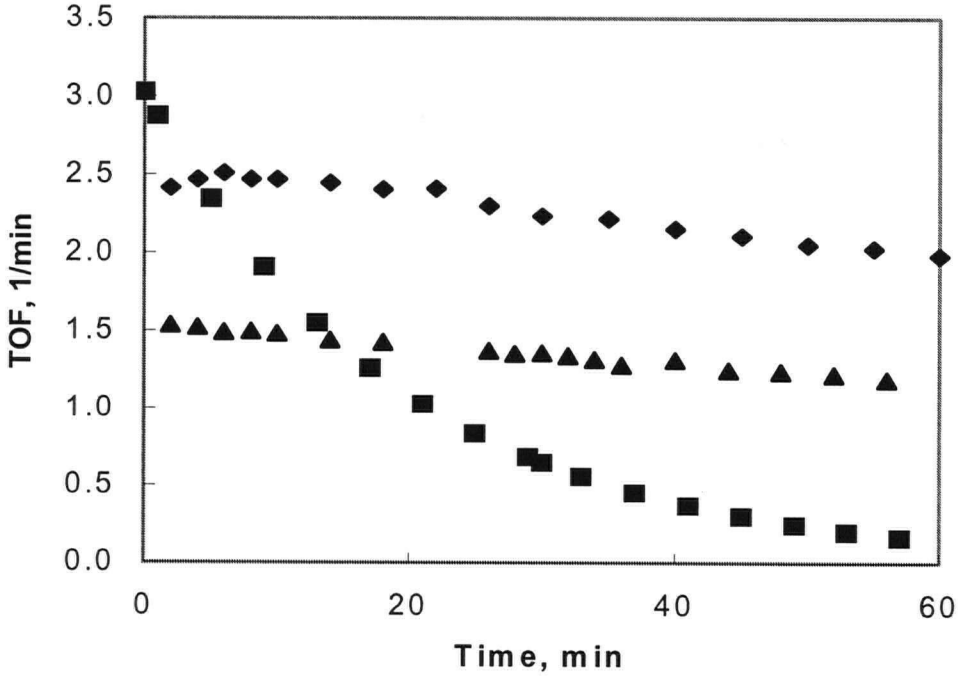

Figure 4.8 Comparison of CH_4 decomposition TOFs in the presence of CO or H_2 at 773K on 12wt% Co/SiO_2 (reduced at 923K) (The total gas flow 140 mL/min. ■ $100k_d = 4.6$ min^{-1} with $5\%CH_4$; ▲ $100k_d = 0.46$ min^{-1} with $1.4\%H_2/4\%CH_4$; ◆ $100k_d = 0.4$ min^{-1} with $0.4\%CO/ 5\%CH_4$).

In order to show the difference between activity profiles manifested by different decay constants, $100k_d$, the complete activity profiles are presented in Figure 4.8. These plots confirm that the magnitude of the decay constant reflected the slope of the activity versus time-on-stream profiles.

4.3 Prediction of Stable Activity

4.3.1 Influence of K_M on Catalyst Activity and Deactivation

In the present study, the effect of H_2 was discussed in Section 4.2.3. Additional experiments were performed, in which the $P_{H_2}^2 / P_{CH_4}$ ratio was varied and the CH_4 decomposition activity profile determined at the same temperature, 773K, on certain Co or Ni supported catalysts. The term $K_M = P_{H_2}^2 / P_{CH_4}$ is in the same form as the equilibrium constant for the methane decomposition reaction. In order to discuss the measured activity simply, the two parameters, r^* and k_d were obtained from curve fitting the activity profiles at different K_M. The data in Figure 4.9 and Figure 4.11 show that the ratio $K_M = P_{H_2}^2 / P_{CH_4}$ had a significant effect on the catalyst activity and deactivation: both catalyst activity, r^* and decay constant, k_d decreased with increasing K_M at 773K on the 12wt% Co/SiO_2 catalyst and on 5wt% Ni/SiO_2 catalyst, respectively.

4.3.2 Coking Threshold and Filamentous Carbon Formation Threshold

The point at which the CH_4 decomposition activity is zero, estimated by drawing a trendline through the data of Figure 4.9a, corresponds to the coking threshold, $K_M^* = \left(\frac{P_{H_2}^2}{P_{CH_4}} \right)$. According to Snoeck et al. (1997b), the coking threshold defines those conditions at which there is no carbon deposition and no carbon gasification on the catalyst surface, i.e., the coking

threshold corresponds to the conditions for which the rates of all consecutive steps of carbon filament formation are zero, $K_M^* = \left(\frac{P_{H_2}^2}{P_{CH_4}}\right)_{r_{C,M}=0}$. When $K_M < K_M^*$, CH_4 decomposition with carbon deposition will occur, whereas when $K_M > K_M^*$, carbon gasification occurs.

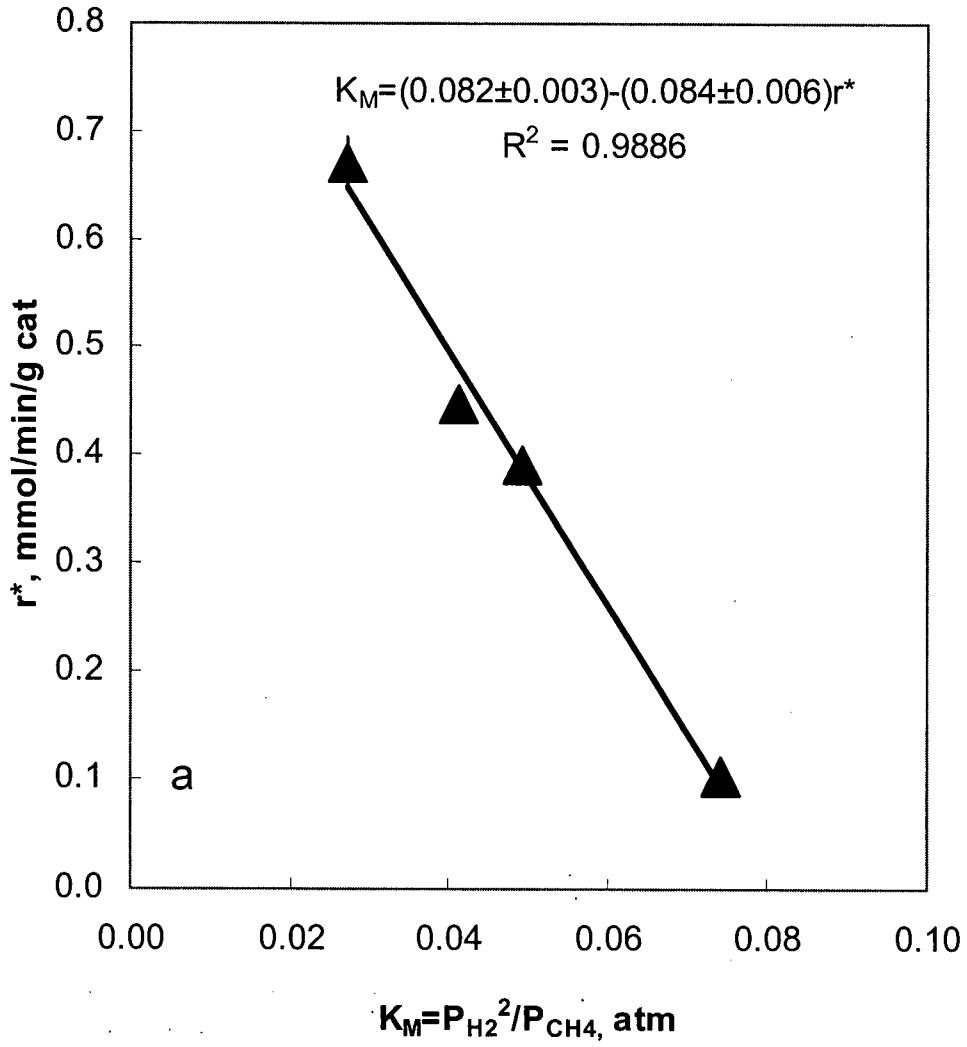

Figure 4.9a Dependence of maximum rate r^* on K_M with 12wt% Co/SiO_2 (reduced at 923K) at 773K ($K_M^* = 0.082 \pm 0.003$ atm).

Similarly, Figure 4.9b shows that $100k_d$ approaches zero with increasing K_M. The point at which $100k_d$ is zero, obtained by drawing a trendline through the data of Figure 4.9b, is defined herein as the filamentous carbon formation threshold, $K_M^f = \left(\frac{P_{H_2}^2}{P_{CH_4}}\right)$. Filamentous carbon formation threshold, K_M^f, is proposed by analogy to the coking threshold K_M^*, and also because it is generally accepted that stable activity during CH_4 decomposition corresponds to filamentous carbon formation. Figure 4.9b shows that $100k_d$ decreases with increasing K_M and the point where $100k_d$ reaches zero is defined as K_M^f, corresponding to filamentous carbon formation and stable activity (i.e. $k_d = 0$). When the value of $K_M > K_M^f$, stable activity will be observed whereas when $K_M < K_M^f$, deactivation occurs ($k_d > 0$).

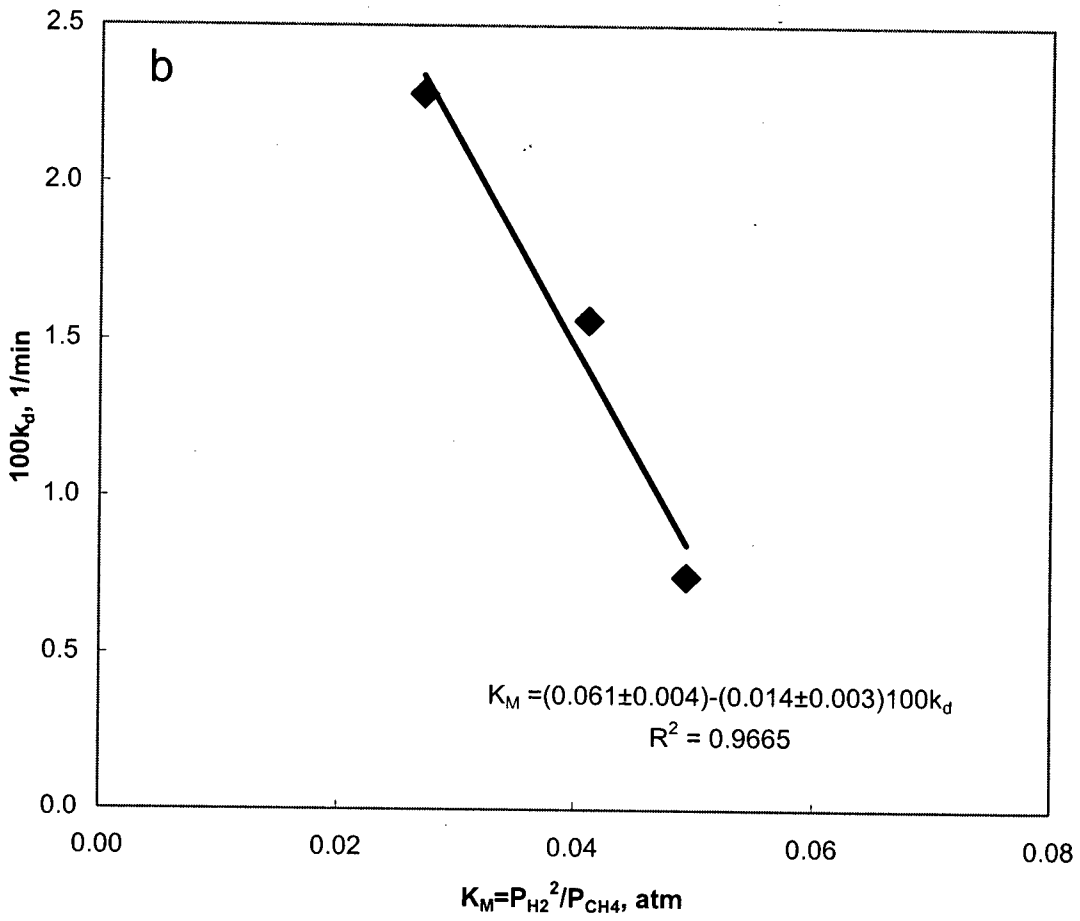

Figure 4.9b Dependence of decay constant $100\,k_d$ on K_M with 12wt% Co/SiO_2 (reduced at 923K) at 773K ($K_M^f = 0.061 \pm 0.004\,atm$).

4.3.3 Stable Catalyst Activity Prediction during CH_4 Decomposition

As discussed in Chapter 2, stable catalyst activity during CH_4 decomposition is critical for practical processes aimed at producing pure H_2 and nanofibre carbon. The two thresholds K_M^* and K_M^f can be used to predict the operating conditions (i.e. the value of K_M) needed for stable activity during CH_4 decomposition on certain catalysts at fixed temperature. Stable activity with carbon deposition would occur during CH_4 decomposition when K_M satisfies the condition: $K_M^f < K_M < K_M^*$. Figure 4.9 shows that on 12wt% Co/SiO_2 catalyst at 773K K_M^*=0.082±0.003atm and K_M^f=0.061±0.004atm. Hence, K_M must satisfy the condition:

$0.061 \pm 0.004 = K_M^f < K_M < K_M^* = 0.082 \pm 0.003$ atm, for stable activity during CH_4 decomposition to be obtained. Figure 4.10 shows that stable activity was indeed obtained when K_M=0.074atm on the same catalyst at 773K.

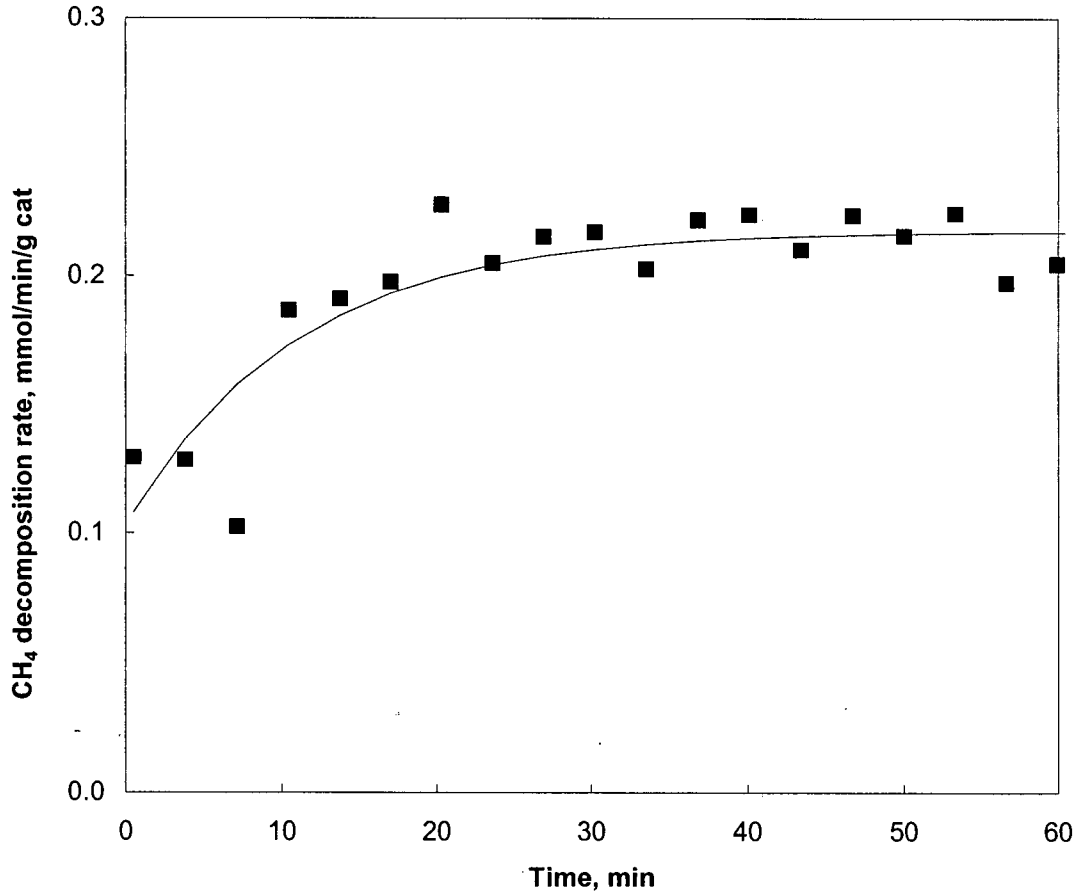

Figure 4.10 Stable activity on 12wt% Co/SiO_2 (reduced at 923K) with $K_M = 0.074$ atm at 773K.

Stable activity during CH_4 decomposition is often reported on high loading Ni catalysts (Shaikhutdinov et al., 1995), but deactivation has been observed on low loading Ni catalyst, for example 5wt% Ni/SiO_2 (the effect of metal loading on the activity will be discussed in detail in Chapter 5) in the present study. The dependence of r^* and k_d on K_M is presented in Figure 4.11a and Figure 4.11b as determined over 5wt% Ni/SiO_2 catalyst at 773K. K_M^* and K_M^f were

obtained from Figure 4.11a and Figure 4.11b, respectively. Hence, K_M^*=0.110±0.009atm and K_M^f=0.032±0.003atm. Consequently, K_M must satisfy the condition: $0.032 \pm 0.003 = K_M^f < K_M < K_M^* = 0.110 \pm 0.009$ atm for stable activity to be observed during CH_4 decomposition on 5wt% Ni/SiO_2 at 773K. Figure 4.12 shows that indeed stable activity was obtained when K_M = 0.09atm. The results presented in Figure 4.10 and Figure 4.12 show that stable activity can obtained provided K_M is chosen such that $K_M^f < K_M < K_M^*$.

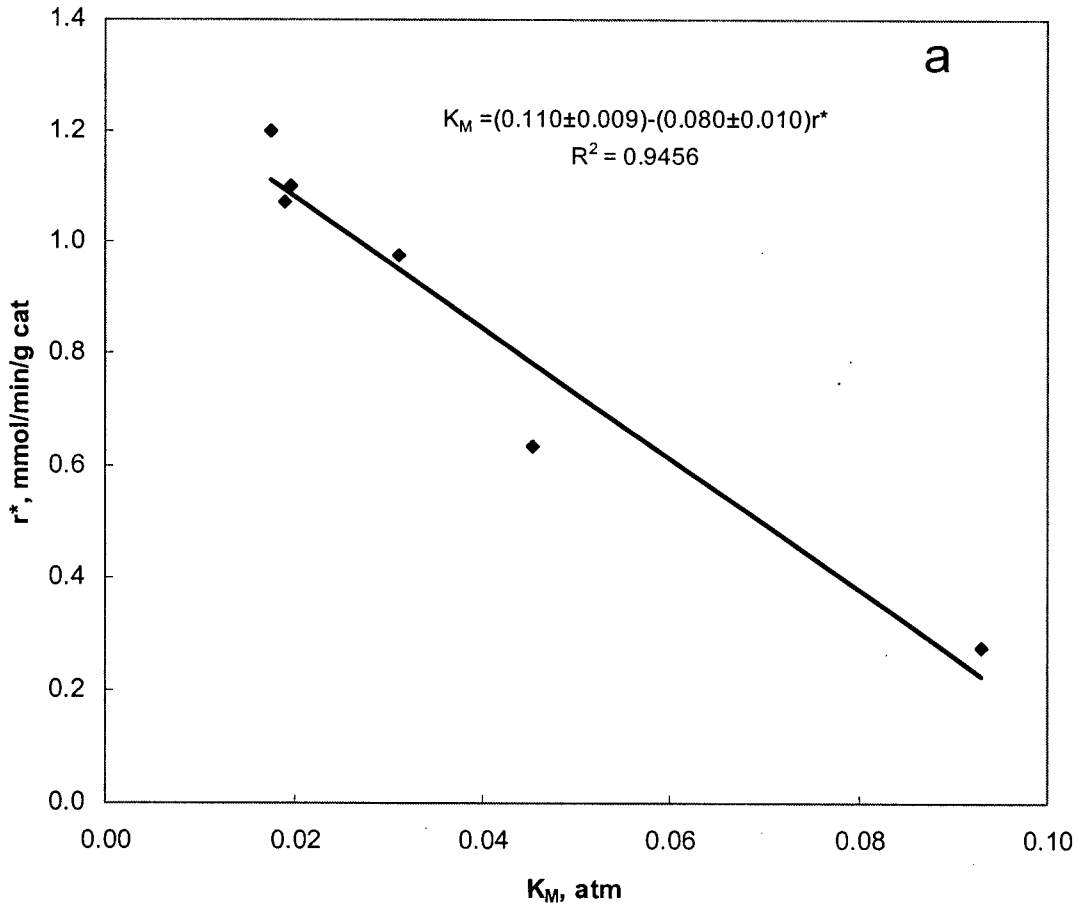

Figure 4.11a Dependence of maximum rate r^* on K_M with 5wt% Ni/SiO_2 (reduced at 923K) at 773K ($K_M^* = 0.110 \pm 0.009$ atm).

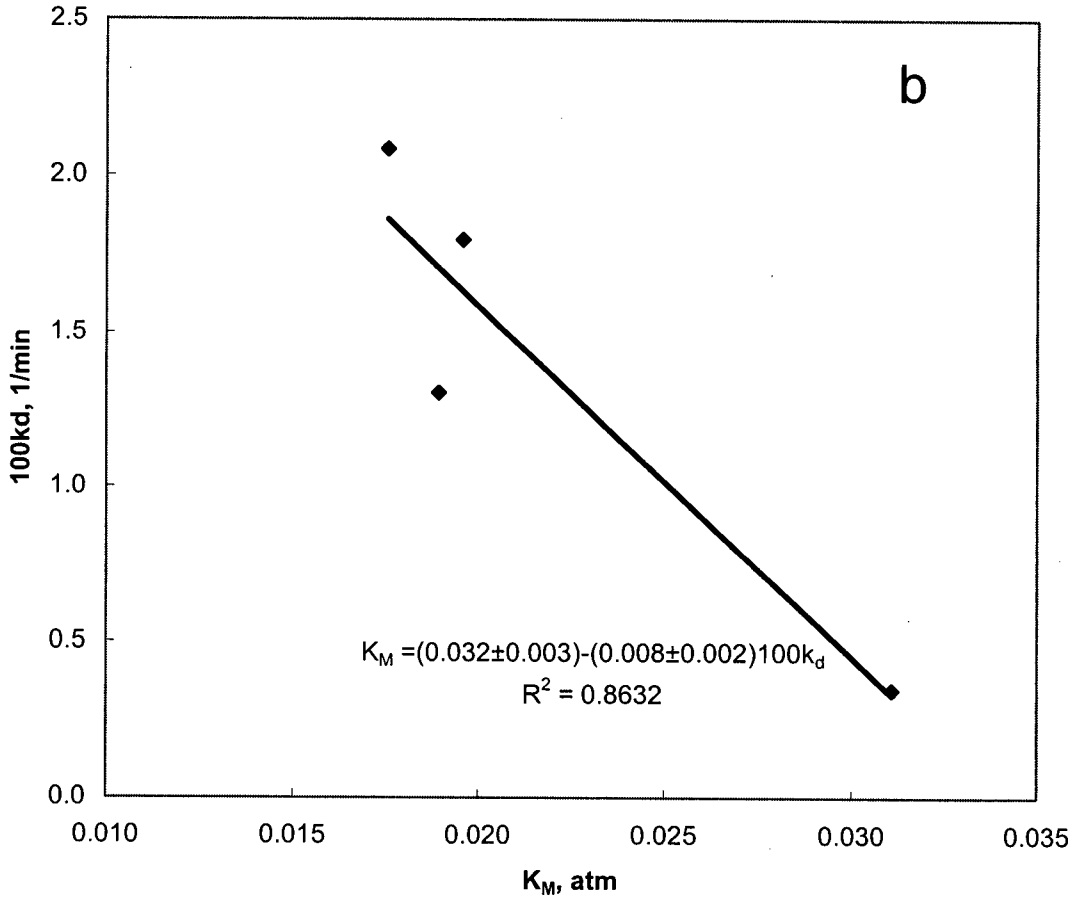

Figure 4.11b Dependence of decay constant $100k_d$ on K_M with 5wt% Ni/SiO_2 (reduced at 923K) at 773K ($K_M^f = 0.032 \pm 0.003$ atm).

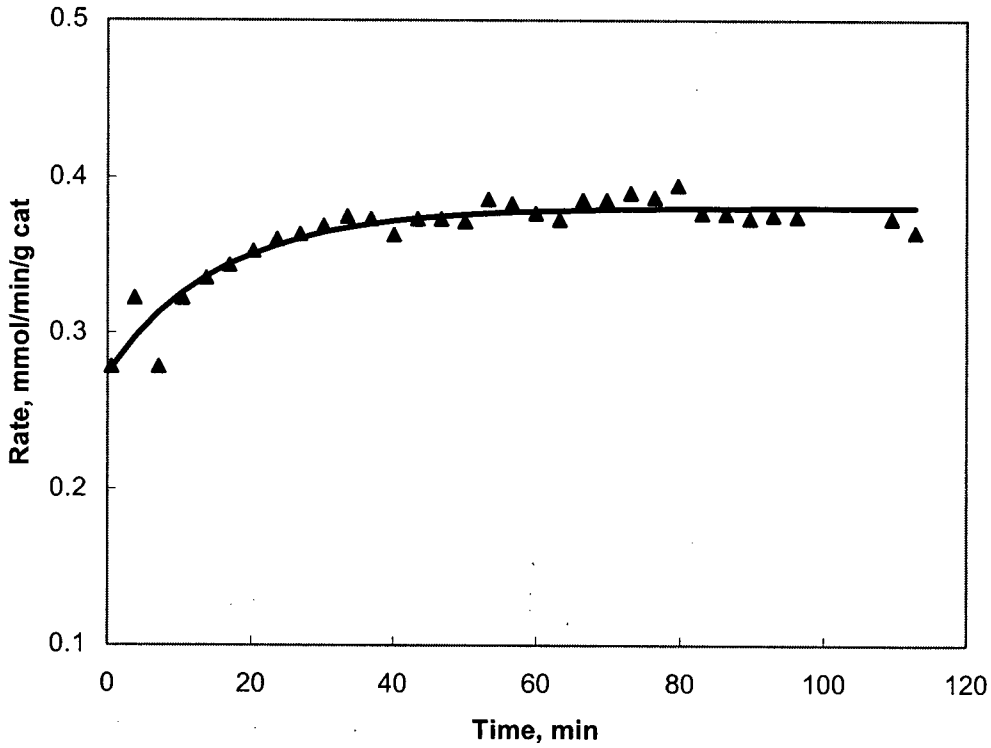

Figure 4.12 Stable activity on 5wt% Ni/SiO_2 (reduced at 923K) with $K_M = 0.09\,atm$ at 773K.

4.4 Catalyst Deactivation Mechanism

4.4.1 Catalyst Deactivation

The decomposition of CH_4 on supported Co catalysts reported herein showed that under some conditions, the catalyst deactivated. The mechanism of the deactivation is thought to be due to encapsulation of the metallic particle by graphite carbon layers (Shah et al., 2001). EXAFS and Mossbauer spectroscopies have shown that the form of catalyst remains metallic even after encapsulation (Shah et al., 2001). Hence, it was postulated that the metallic catalyst was not deactivated by poisoning or by changes in surface structure, but rather was isolated from CH_4 by encapsulation and hence could not catalyze CH_4 decomposition.

However, as already reported, stable catalyst activity was observed under certain conditions on both Co and Ni catalyst. According to the mechanism of filamentous carbon formation, as discussed in Section 2.2.2, stable activity corresponds to steady growth of filamentous carbon and TEM micrographs of used catalysts confirmed that filamentous carbon were indeed formed under these conditions (Figure 4.6 and Figure 4.7).

Based on these observations, it is necessary to account for both the encapsulating carbon formation and filamentous carbon formation during CH_4 decomposition. A mechanism that accounts for both effects is schematically represented in Figure 4.13 and is described as: 1) the single atomic carbon, resulting from reversible reaction $CH_4 \Leftrightarrow C + 2H_2$, deposits on the surface of the metal catalyst; 2) the single atomic carbon reacts through two parallel paths: 2a) encapsulating carbon formation: assuming that the encapsulating carbon can not be gasified by H_2, the number of active metal sites on the surface will decrease due to the formation of encapsulating carbon and consequently, the catalyst deactivates; 2b) the atomic carbon diffuses through the metal particle and deposits at the back of the metal particle, the catalyst active site being regenerated by the carbon bulk diffusion and hence stable catalyst activity is observed. The competition between the rate of encapsulating carbon formation and the bulk diffusion rate determines the observed rate of deactivation The decay constant of the catalyst (k_d) is a consequence of a number of interacting rates, including the net CH_4 decomposition rate, the carbon removal rate by bulk diffusion through metal particle and the encapsulating carbon formation rate.

$$k_d = -\frac{\left(dr_{f,n}/dt\right)}{r_{f,n}} \propto r_e / r_{f,n} = r_d / r_{f,n} = (r_{f,n} - r_{r,n}) / r_{f,n} \tag{4.1}$$

Equation (4.1) shows that k_d is dependent on the relative encapsulating carbon formation rate ($r_e / r_{f,n}$, the ratio of encapsulating carbon formation rate to net rate of carbon formation

rate), in which encapsulating carbon formation rate (r_e) is equal to the difference (r_d) between the net rate of carbon formation ($r_{f,n}$, the net rate of formation and gasification of carbon or coke precursor) and the rate of carbon removal from the active metal site ($r_{r,n}$, the net rate of removal by migration from metal to support or diffusion with filamentous carbon formation), i.e. $r_e / r_{f,n} = r_d / r_{f,n} = (r_{f,n} - r_{r,n}) / r_{f,n}$. In other words, the relative magnitude of the formation rates of atomic carbon, encapsulating carbon and filamentous carbon, determine the observed activity profile and consequently, carbon with different morphologies, either encapsulating or filamentous carbon, dominates on the catalyst surface.

Since the ensemble size of the encapsulating carbon formation is 6,

$$nC \cdot S \xrightarrow{k_P} nC_P \cdot S \text{ with n=6 (Chen et al., 2001)} \quad (4.2),$$

the encapsulating carbon formation rate (Chen et al., 2001) can be written as

$$r_e = k_{encap} n_s^n \quad (4.3).$$

The bulk diffusion of atomic carbon can be described as

$$\dot{r}_d = D_s \frac{(n_s / dx - n_1 / dx)}{(2/3) d_p} \quad (4.4)$$

Equation (4.4) is modified from Snoeck et al. (1997b).

where r_e, the encapsulating carbon formation rate, 1/cm^2/s; n_s, the site density of atomic carbon on the surface of metal surface, 1/cm^2; k_{encap}, rate constant of encapsulating carbon formation, cm^{10}/s; $\dot{r}_d$ is the carbon bulk diffusion rate, 1/cm^2/s; D_s, carbon bulk diffusivity, cm^2/s; d_p, metal particle size; n_1, the site density of atomic carbon on the interface between the metal and support, 1/cm^2; dx, the finite divided thickness along the carbon diffusion path.

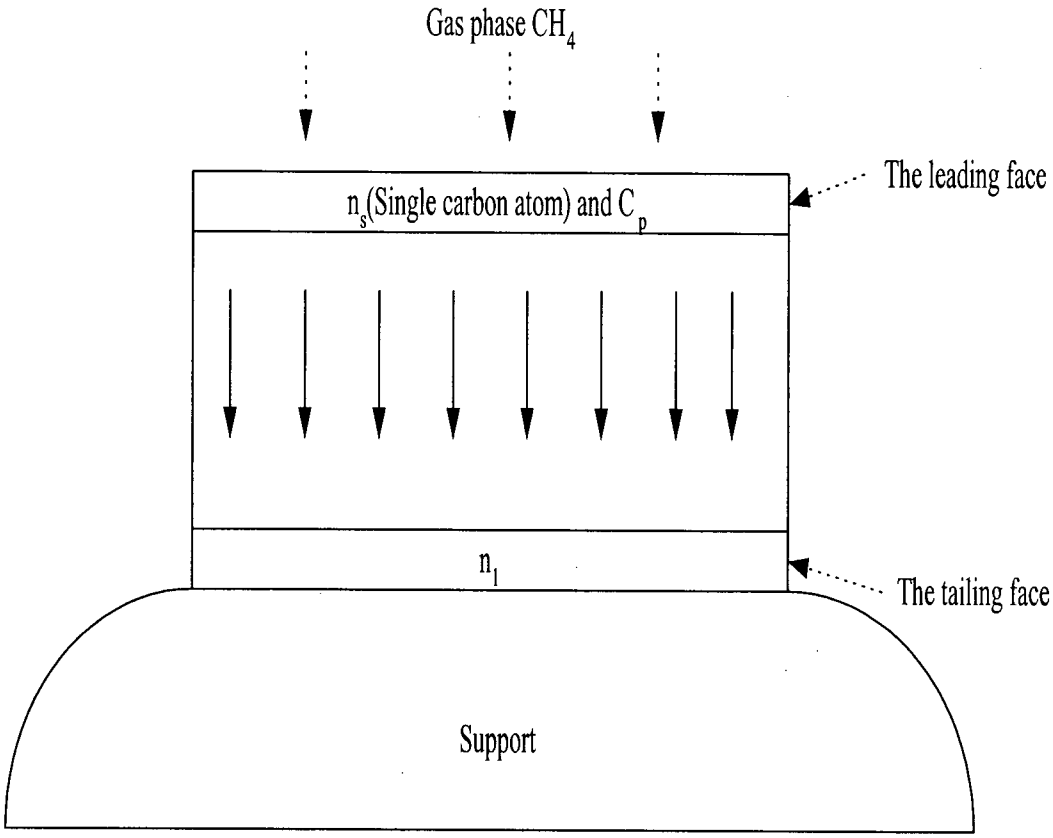

Figure 4.13 Schematic representation of catalyst deactivation mechanism during CH_4 decomposition.

4.4.2 Explanation of Temperature Effects on Catalyst Deactivation

The decay constant k_d was observed to increase with increasing decomposition temperature, and the increase followed an Arrhenius dependence on temperature with apparent activation energy of 122.7 kJ/mol (Figure 4.4). On Ni-Al_2O_3 catalysts, the apparent activation energy associated with k_d for carbon formation from CH_4-H_2 mixtures has been reported as 229 kJ/mol (Demicheli et al., 1991).

As already discussed, the rate of catalyst deactivation is a consequence of a number of interacting processes: the net rate of the CH_4 decomposition rate, the carbon removal rate by bulk diffusion through the metal particle and the encapsulating carbon formation rate. Although the net rate of CH_4 decomposition, formation of encapsulating carbon and carbon removal by diffusion all increase with temperature, the difference among them varies with temperature because of differences in their respective activation energies. According to Holstein (1994), the activation energy for filamentous carbon diffusion through Co is in the range of 145-162 kJ/mol and this activation energy is independent of reactant (either hydrocarbons or CO). The apparent activation energy for the migration of CH_x species from Co to SiO_2 support has been estimated at 48 kJ/mol (Zadeh and Smith, 1998). The present study has reported an activation energy for CH_4 decomposition of 66 kJ/mol. The activation energy for atomic carbon hydrogenation is 70 kJ/mol and the activation energy for the encapsulating carbon is 32 kJ/mol during CO methanation (Bartholomew, 2001). Consequently, an increase in reaction temperature would impact the carbon diffusivity through Co most significantly, which in turn would be expected to reduce the observed rate of catalyst deactivation. However, this is contrary to the observed effect of temperature on k_d.

Note that the competition between filamentous carbon and encapsulating carbon formation also depends on the concentration of atomic carbon at the surface, n_s. The rate of encapsulating carbon formation can be written as $r_e = k_{encap} n_s^n$ (Chen et al., 2001) whereas for bulk diffusion $r_d = D_s \frac{(n_s / dx - n_1 / dx)}{(2/3)d_p}$. As the temperature increases the atomic carbon concentration increases, manifested by the increase in the maximum decomposition rate, r^* (Figure 4.4). Consequently, at higher temperature, the increased atomic carbon concentration increases the encapsulating carbon formation rate much more significantly than the bulk diffusion. We

conclude, therefore, that the increased decay constant with temperature is associated with the resulting relative increase in the encapsulating carbon formation rate with increased temperature. This result is also in agreement with the observation that the more reactive, amorphous forms of carbon, identified at low reaction temperatures, are converted to less reactive graphitic forms at higher temperatures over a period of time (Bartholomew, 2001). Note that as the CH_4 decomposition temperature increases, the reactivity in H_2 of the carbonaceous deposit decreases (Koerts, 1991), a consequence of increased formation of un-reactive encapsulating carbon.

4.4.3 Effect of CO and K_M on Catalyst Deactivation

The data of Figure 4.5 show that the presence of either H_2 or CO in the feed reduces the decay constant. At 773K, addition of small amounts of H_2 or CO decreased the decay constant and stable activity was retained for a significant period of time during which filamentous carbon formation was detected (Figure 4.6 and Figure 4.8). However, addition of H_2 reduced the maximum TOF compared to the case without H_2 in the feed, whereas addition of CO had no significant effect on the maximum TOF. Furthermore, the data in Figure 4.9 – Figure 4.11 show that the ratio $K_M = \left(\frac{P_{H_2}^2}{P_{CH_4}} \right)$ had a significant effect on the deactivation of catalysts. Stable activity and catalyst deactivation were observed at different ratios even on the same catalyst. When the value of $K_M^f < K_M < K_M^*$, stable activity will be observed whereas when $K_M < K_M^f$, deactivation occurs.

A similar effect of H_2 during the catalytic disproportionation of CO has been reported (Nolan, 1995) and two functions of H_2 are possible: (1) to "clean" the catalytic surface by the reaction $C+2H_2 \Rightarrow CH_4$ or (2) to modify the carbon/metal interaction. As discussed for the deactivation mechanism, the relative magnitude of the rate of carbon deposition, rate of the

carbon gasification, the rate of carbon removal by the bulk diffusion through the metal particle, and encapsulating carbon formation are critical for catalyst deactivation. As the ratio of K_M increases, the H_2 partial pressure increases, which enhances the gasification of carbon. Consequently, the net rate of carbon deposition decreased, manifested by a decreasing maximum r^* and a decrease in the surface concentration of atomic carbon. The decrease in atomic carbon will cause a significant decrease in the encapsulating carbon formation rate (Equation (4.2)), compared to the small change in carbon diffusion rate (Equation (4.3)). Consequently, catalyst stability is enhanced because the formation of encapsulating carbon is less favoured.

With CO added to the CH_4 feed, two explanations for the reduction in k_d can be postulated: CO decreases the CH_4 decomposition rate ($r_{f,n}$ decreases) or CO adsorption changes the carbon-metal interface such that carbon diffusivity through the metal is increased ($r_{r,n}$ increases). The high maximum TOF upon CO addition, shown in Figure 4.5, rules out the first possibility. Hence we conclude that the reconstruction of the Co surface following CO adsorption enhances carbon diffusivity and this is consistent with the stable, high CH_4 decomposition activity reported in Figure 4.8. A similar promotional effect of CO on the decomposition of ethylene over Fe to form filamentous carbon has been reported (Rodriguez et al., 1993). The behaviour was rationalized in terms of a reconstruction of the Fe surface in the presence of co-adsorbed CO, which resulted in the formation of surfaces with differing activities.

Although the catalyst stability was improved by addition of either CO or H_2 (Figure 4.8), the mechanism of each gas is postulated to be different: CO adsorption enhances the carbon diffusion rate by surface modification, promoting filamentous carbon formation without reducing CH_4 decomposition activity whereas the presence of H_2 enhances the carbon gasification rate and thereby reduces the concentration of atomic carbon on the surface.

Consequently, catalyst stability is enhanced due to the stronger reduction in the rate of formation of encapsulating carbon relative to the carbon removal rate.

Catalyst deactivation observed during CH_4 decomposition on the Co/SiO_2 catalysts has been discussed in terms of the competition between encapsulating carbon formation and carbon diffusion from the Co surface. Another common deactivation mechanism for supported metal catalysts is by sintering of the metal particles. However, for the present reaction, this mechanism is not relevant. The initial Co particle size measured by CO chemisorption (11.4 nm, Table 3.1) is close to the size of the Co particle on the filamentous carbon tip, observed by TEM (~10nm, Figure 4.1) after 120 min reaction in CH_4 at 723K. The Co particle size measured by TEM at 773K after reaction in the presence of H_2 or CO in the feed was ~25 nm (Figure 4.6 and Figure 4.7), somewhat larger than the 19.4 nm measured by CO chemisorption of the unused catalysts. The apparent increase in particle size in this case could be due to the fact that filamentous carbon formation favoured larger metal particles and the TEM image consequently reports the larger particle size selectively, whereas CO chemisorption provides an estimate of the average metal particle size. We conclude that no significant sintering in the temperature range of 723~773K during CH_4 decomposition occurred, in agreement with the results of Avdeeva et al. (1999), who reported that the Co particle size (approx. 25 nm) did not increase at 773~823K on 60-75wt% Co-alumina catalysts exposed to CH_4 for 50 min.

4.5 Summary

The experimental observations reported herein, suggest that the migration of CH_x from the metal to the support makes a contribution to the regeneration of active metal sites in the first 2 to 3 min of reaction. The regeneration of active metal sites for CH_4 decomposition over

extended periods is mainly due to bulk diffusion of carbon through the metal particle to form filamentous carbon between the metal and support.

The effect of operating conditions such as temperature and gas phase composition, expressed as $K_M = P_{H_2}^2 / P_{CH_4}$, on CH_4 decomposition activity for supported Co catalysts was investigated in terms of r^* and k_d estimated by 1st order decay model fitting. The apparent activation energy for the maximum CH_4 decomposition rate was 66.3 kJ/mol and for the decay constant 122.7 kJ/mol on 12wt% Co/SiO_2 catalysts. The $K_M = P_{H_2}^2 / P_{CH_4}$ ratio had a critical effect on the CH_4 decomposition profile: both r^* and k_d decreased with decreasing $K_M = P_{H_2}^2 / P_{CH_4}$. Stable catalyst activity was observed under some conditions and the conditions for stable activity can be predicted from the relative magnitudes of the coking threshold, K_M^*, and the filamentous carbon formation threshold, K_M^f. Stability corresponds to the condition: $K_M^f < K_M < K_M^*$.

Based on these experimental observations, the catalyst deactivation mechanism for CH_4 decomposition incorporating competition between encapsulating carbon formation and filamentous carbon formation due to bulk carbon diffusion was proposed. The decay constant during CH_4 decomposition depends on the build up of encapsulating carbon on the surface of the catalyst, which in turn is a consequence of a number of interacting processes: carbon deposition rate, carbon removal rate by bulk diffusion through metal particle and encapsulating carbon formation rate. Accordingly, the relative magnitude of formation rates of important types of carbon including atomic carbon and encapsulating or filamentous carbon on the catalyst surface, determine whether stable activity or catalyst deactivation is observed. Consequently, either encapsulating or filamentous carbon dominates on the catalyst.

The effect of temperature and gas phase composition, K_M, on the activity profile can be explained well by the competition between the rate of encapsulating carbon formation and the rate of carbon diffusion.

Chapter 5 Effect of Catalyst Properties on Catalyst Activity

5.1 Introduction

As discussed in Section 2.4, supported metal catalyst properties such as metal particle size and metal-support interaction (MSI) have a significant effect on the catalyst activity during CH_4 decomposition. In this chapter, the observations of the dependency of the catalyst activity on the metal particle size, and stable catalyst activities over large particles of both Ni and Co are presented in Section 5.2. In Section 5.3, the dependency of coking threshold on the metal particle size (Rostrup-Nielsen, 1972) is described by the developed relationship using the experimental data of the present study. Furthermore, the effect of the metal particle size on the difference between the coking threshold and the filamentous carbon formation threshold is presented. Hence, the ease of observation of steady growth of filamentous carbon on high loading catalysts is rationalized. Finally, the effect of MSI on catalyst deactivation is discussed based on the study of modified Co catalysts.

5.2 Dependency of the Catalyst Activity on Metal Particle Size

5.2.1 Dependency of the Catalyst Activity on Co Particle Size

The influence of metal particle size (or dispersion) on CH_4 decomposition activity was measured at two different operating conditions using Co/SiO_2 catalysts with varying metal particle size (or metal dispersion) as given in Table 3.1. At each operating condition, the maximum TOF (Max TOF= r^* /the number of active site) and the decay constant ($100k_d$) were estimated by fitting the experimental data to the 1st order decay model, and the values obtained are plotted in Figure 5.1a and Figure 5.1b, respectively.

The data of Figure 5.1a show a general trend of increasing maximum TOF with increased metal particle size (or decreased Co dispersion), indicative of the structure sensitivity of the CH_4 decomposition reaction on supported metal catalysts (Boskovic and Smith, 1996). Note that the effect of metal particle size on TOF was small under the low temperature, low CH_4 partial pressure conditions of Figure 5.1a (5%CH_4/Ar at 101kPa and 723K); however at higher temperature and CH_4 partial pressure (23%CH_4/12%H_2/Ar with $K_M = 0.06$ at 101kPa and 773K), the Co particle size effect is much more significant. The data of the present study clearly show the structure sensitivity of the maximum CH_4 decomposition rate on Co/SiO_2 catalysts, since the maximum CH_4 decomposition TOF increased with increased metal particle size in the range of 7.6-28.3 nm (or decreased Co dispersion in the range of 12.6-3.4%).

The two sets of data in Figure 5.1b show a general trend of decreasing k_d with increased metal particle size (or decreased Co dispersion). Since reduced k_d implies a decrease in $r_e / r_{f,n}$ ($r_e / r_{f,n} = r_d / r_{f,n} = (r_{f,n} - r_{r,n}) / r_{f,n}$), and since the maximum rate of carbon formation increased with increasing metal particle size (Figure 5.1a), we can conclude that the filamentous carbon formation is favoured ($r_{r,n}$ increases) with increasing metal particle size. Previous studies on Ni and Fe catalysts have also shown an increase in carbon filament growth rate with particle size or decreased dispersion (Baker 1989; Galuszka and Back, 1984). Note that, unlike in previous studies, the present data were obtained on the same SiO_2 support so that support effects did not influence the effect of metal particle size (or metal dispersion).

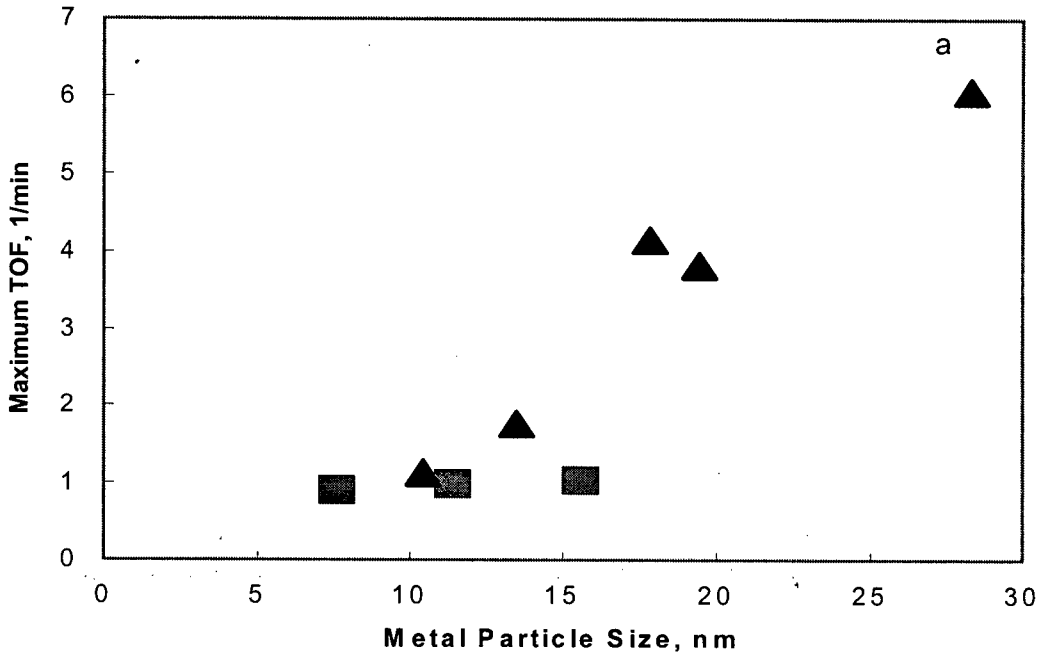

Figure 5.1a Dependence of the maximum catalyst activity (Max TOF) on Co particle size (■ 723K Reduction, 723K Reaction; ▲ 923K Reduction, 773K Reaction with $K_M = 0.06$ atm).

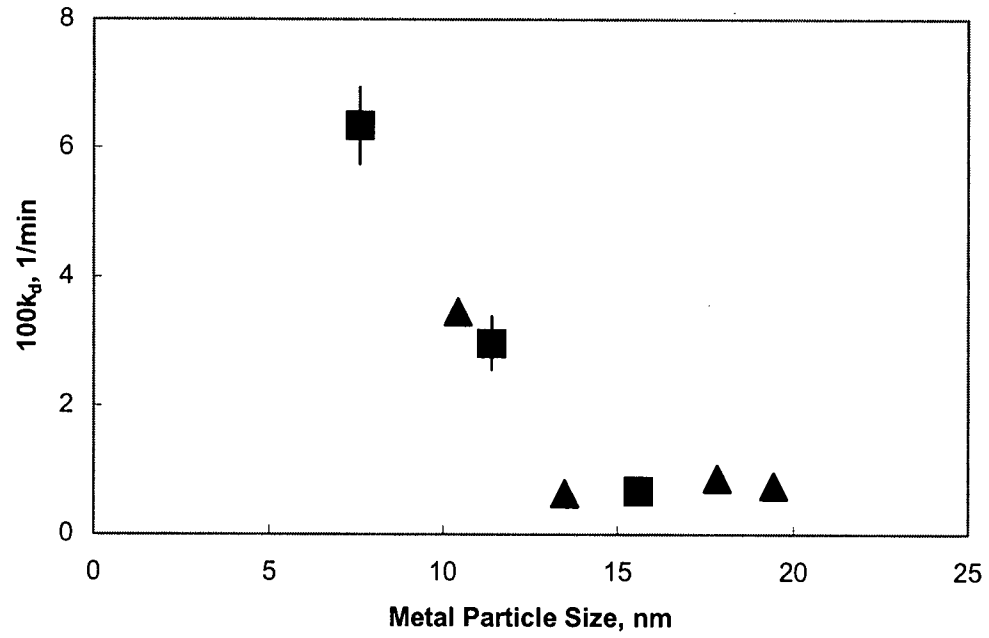

Figure 5.1b Dependence of the catalyst decay constant ($100k_d$) on Co particle size (■ 723K Reduction, 723K Reaction; ▲ 923K Reduction, 773K Reaction $K_M = 0.06$ atm).

5.2.2 Dependency of the Catalyst Activity on Ni Particle Size

Furthermore, the influence of metal particle size (or metal dispersion) on CH_4 decomposition activity was measured at one set of operating conditions using two sets of Ni catalysts, supported on SiO_2 and ZrO_2 as given in Table 3.2 and Table 3.3, respectively. The maximum TOF (Max TOF) and the decay constant ($100k_d$) were estimated by fitting the experimental data to the 1st order decay model and the values obtained are plotted in Figure 5.2a and Figure 5.2b, respectively.

The data of Figure 5.2a show a general trend of increasing maximum TOF with increasing Ni particle size (or decreasing Ni dispersion), similar to Co/SiO_2. The data of the present study clearly show the structure sensitivity of the maximum CH_4 decomposition on Ni/SiO_2 and Ni/ZrO_2 catalysts. Note that on Ni catalysts, catalyst deactivation was only observed on two catalysts with quite low loading. Data in Figure 5.2b show a similar trend of decreased $100k_d$ with increased Ni particle size (or decreased Ni dispersion).

5.2.3 Stable Catalyst Activity on Supported Co and Ni Catalysts

In the present study, stable catalyst activities were obtained on catalysts with high loading. Figure 5.3a shows that stable activity was obtained on 30wt% Co/SiO_2 with average Co particle size 26 nm. Also TEM analysis of the used 30wt% Co/SiO_2 catalyst, reacted under the conditions indicated in Figure 5.3b, confirmed that filamentous carbon was formed. Hence, stable activity corresponded to the steady growth of filamentous carbon.

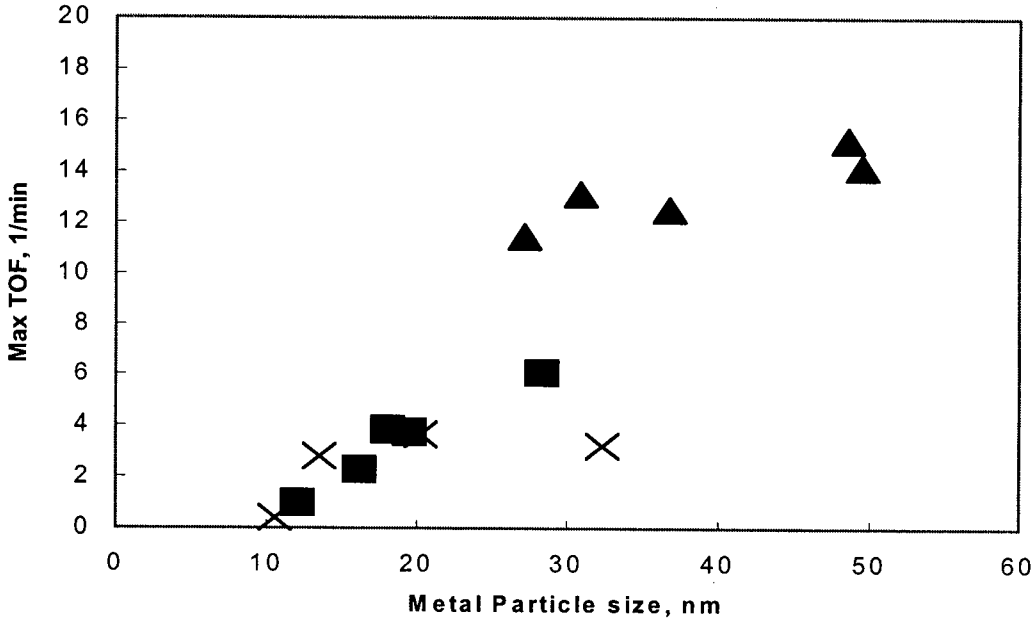

Figure 5.2a Dependence of the catalyst maximum activity (Max TOF) on metal particle size at 773K with $K_M = 0.06$ atm (■ Co/SiO_2; ▲Ni/SiO_2; × Ni/ZrO_2; catalysts were reduced at 923K).

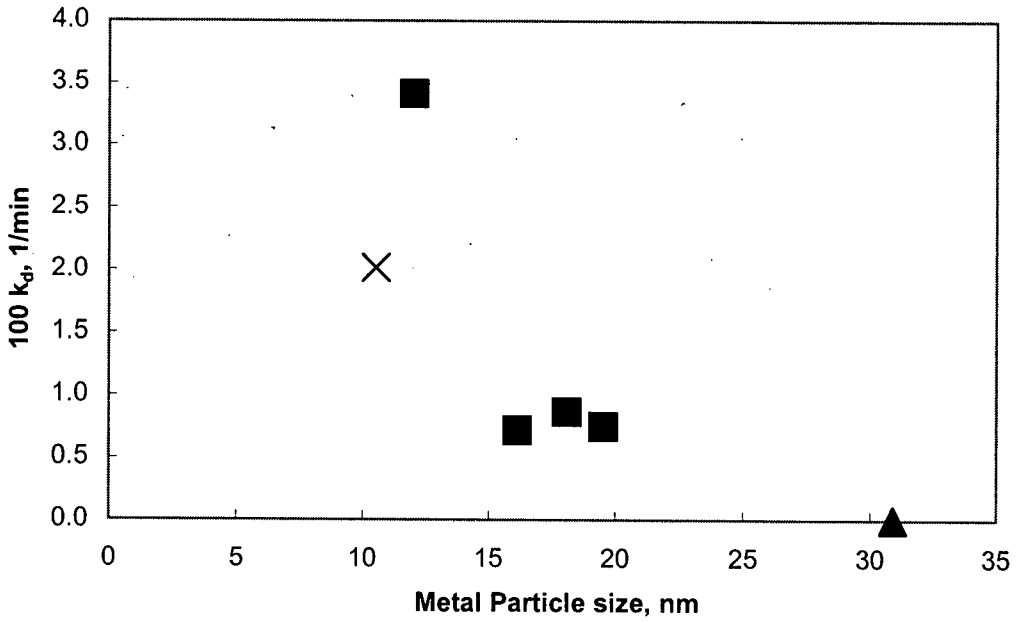

Figure 5.2b Dependence of the catalyst decay constant ($100k_d$) on metal particle size at 773K with $K_M = 0.06$ atm (■ Co/SiO_2; ▲Ni/SiO_2; × Ni/ZrO_2; catalysts were reduced at 923K).

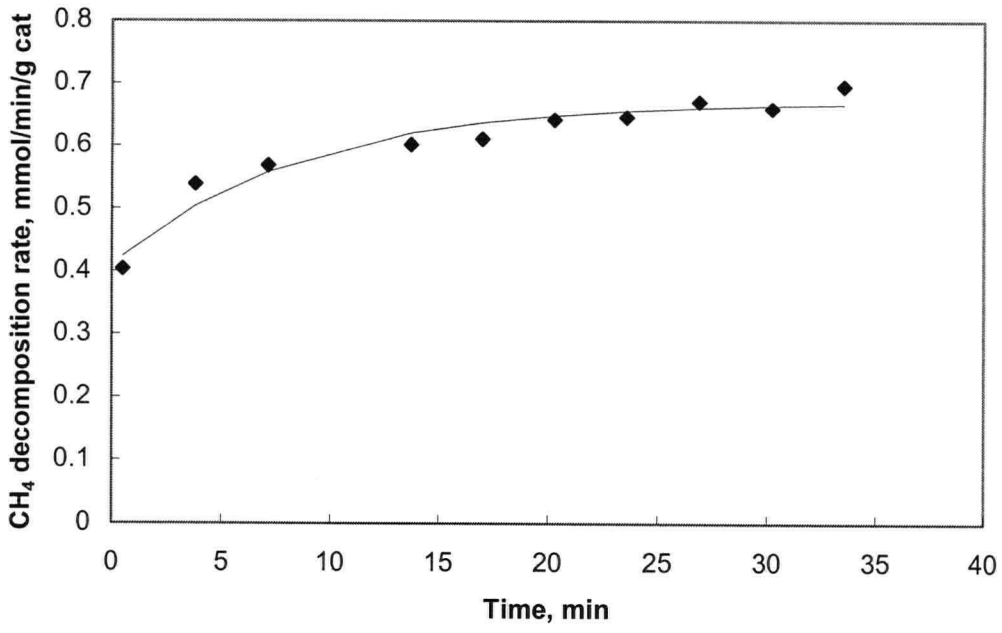

Figure 5.3a Stable catalyst activity on 30wt% Co/SiO_2 (reduced at 923K with Co particle size 26 nm) at 773K with $K_M = 0.06$ atm.

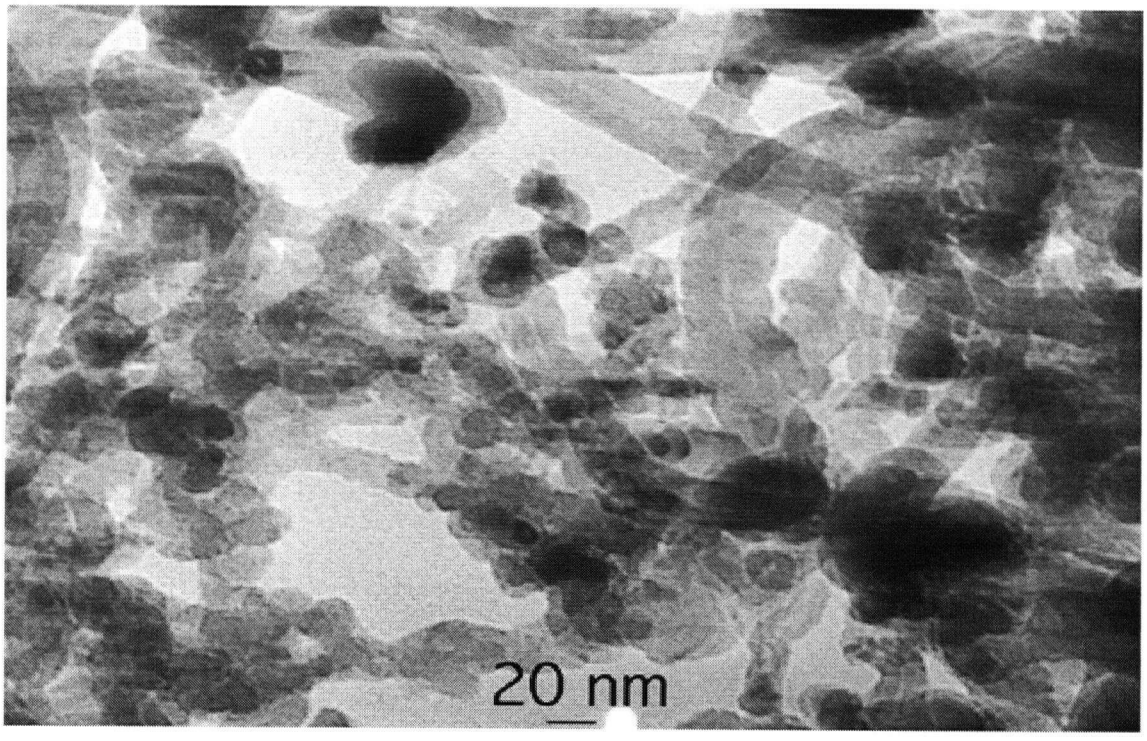

Figure 5.3b TEM micrograph of 30wt% Co/SiO_2 (reduced at 923K) after reaction at 773K with $K_M = 0.06$ atm showing the presence of filamentous carbon.

Similarly, Figure 5.4a shows that stable activity was obtained on 12wt% Ni/SiO_2 and 15wt% Ni/SiO_2 with large metal particle size, namely 43.3 nm and 49.5 nm (from CO uptake), respectively. TEM micrographs of Figure 5.4b and Figure5.4c again confirm that filamentous carbon was formed on 12wt% and 15wt% Ni/SiO_2, respectively. Similarly, Figure 5.5 shows that stable activity was obtained on the 8wt% Ni/ZrO_2 and the 12wt% Ni/ZrO_2 with large metal particle size and it can be deduced that filamentous carbon formed on 8wt% Ni/ZrO_2 and 12wt% Ni/ZrO_2. These observations suggest that stable catalyst activity corresponding to the steady growth of filamentous carbon occurs on the high loading catalyst with large metal particle size.

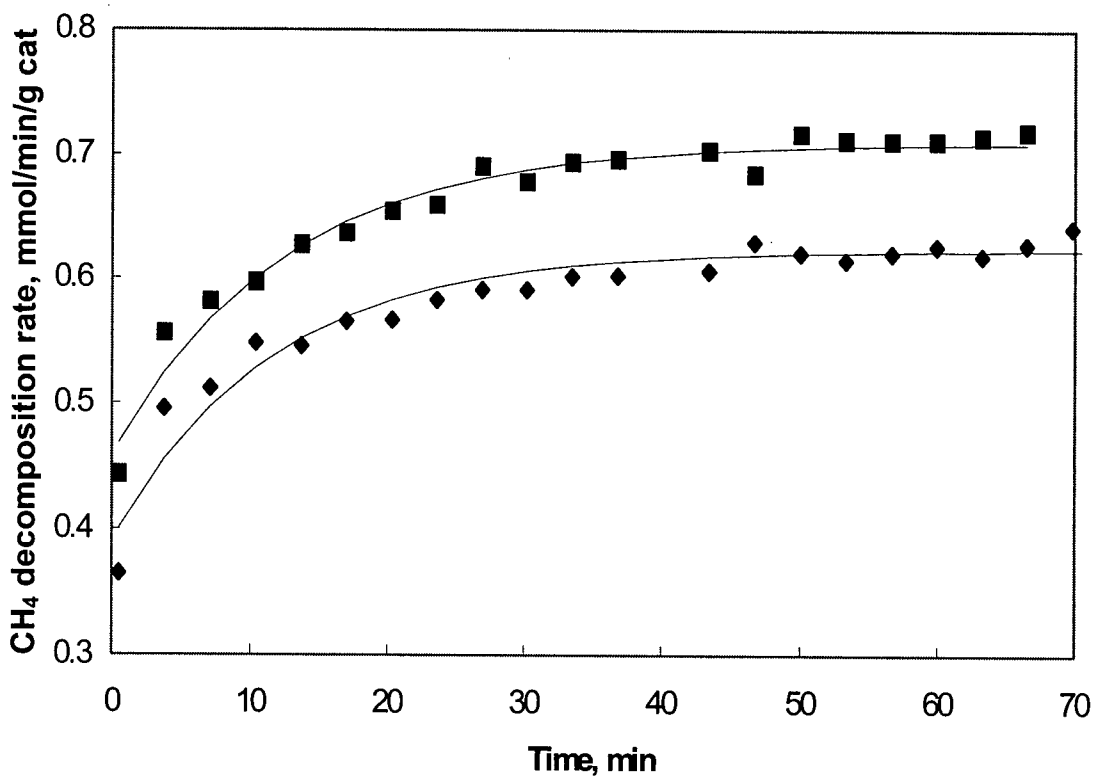

Figure 5.4a Stable catalyst activity on Ni/SiO_2 catalysts at 773K with $K_M = 0.06$ atm (♦12wt% Ni/SiO_2 with Ni particle size 43.3 nm; ■ 15wt% Ni/SiO_2 with Ni particle size 49.5 nm; catalysts were reduced at 923K).

Figure 5.4b TEM micrograph of 15wt% Ni/SiO_2 (reduced at 923K) after reacted at 773K with $K_M = 0.06$ atm showing the presence of filamentous carbon.

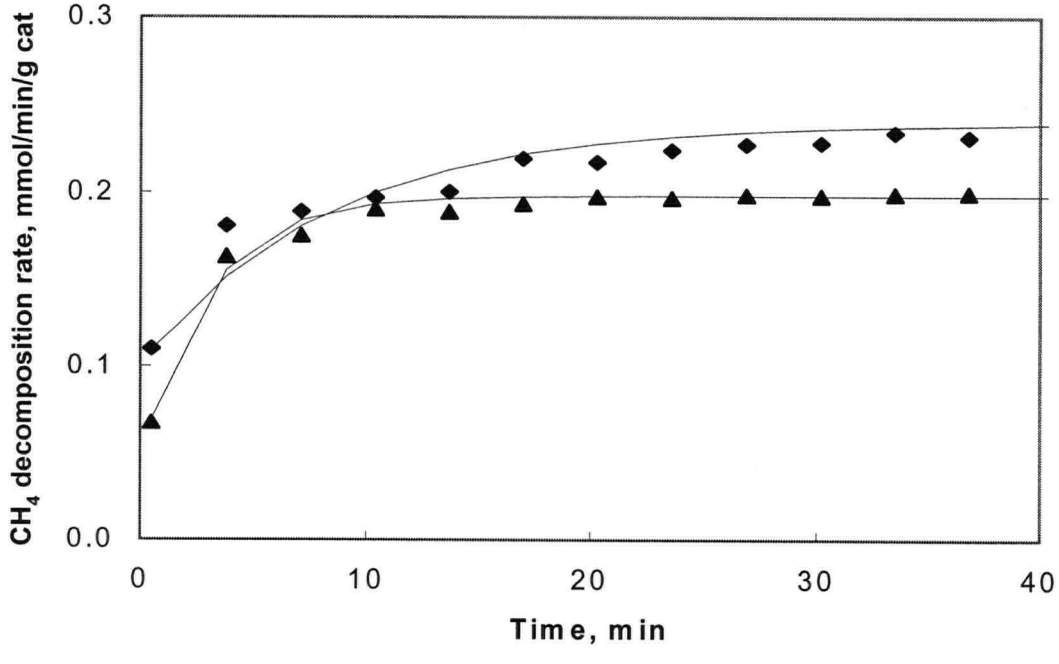

Figure 5.5 Stable catalyst activity on Ni/ZrO_2 catalysts at 773K with $K_M = 0.06$ atm (♦ 8wt% Ni/ZrO_2 with Ni particle size 20 nm; ▲ 12wt% Ni/ZrO_2 with Ni particle size 32 nm; catalysts were reduced at 923K).

Based on the above results, it can be concluded that on both Ni and Co catalysts, the maximum rate increased with increasing metal particle size and the decay constant decreased with increasing metal particle size. Furthermore, when the catalyst metal particle size is such that $k_d \rightarrow 0$, then stable catalyst activity, corresponding to the steady growth of filament carbon, is obtained during CH_4 decomposition.

5.3 Effect of Metal Particle Size on Thresholds

The two critical thresholds, coking threshold, K_M^* and the filamentous carbon threshold, K_M^f, were discussed in Section 4.3.2. According to the definition of coking threshold, K_M^* corresponds to the equilibrium constant, K_M, where the carbon deposition rate is equal to the carbon gasification rate. It has been reported (Rostrup-Nielsen, 1972) that compared to the equilibrium constants based on graphite, the K_M^* values obtained with filamentous carbon were lower and varied from catalyst to catalyst and the variations were correlated with maximum metal particle size. In the present study, the effect of metal particle size on the coking threshold is further discussed based on the data obtained in the present study. Furthermore, the effect of metal particle size on the difference between the two thresholds is discussed.

5.3.1 Dependency of K_M^* on the Metal Particle Size

As mentioned in Section 4.3.2, coking threshold K_M^* was estimated by extrapolating the plot of maximum CH_4 decomposition rate versus K_M to zero. Coking threshold is expressed as $K_M^* = \left(\frac{P_{H_2}^2}{P_{CH_4}} \right)_{rate=0}$. In the present study, different K_M^* on Co/SiO_2 catalysts with different loading were obtained (Appendix B.3). It was reported that the difference in the Gibbs free energy change between filamentous carbon and graphitic carbon formation from CH_4 or CO

decomposition can be expressed by Equation (5.1) and Equation (5.2) in terms of the equilibrium constant (Rostrup-Nielsen, 1972 and Alstrup, 1988).

$$\Delta G_C = \Delta G^0_{observed} - \Delta G^0_{graphite} \tag{5.1}$$

$$\Delta G_C = -RT \ln\left(\frac{K_{observed}}{K_{graphite}}\right) \tag{5.2}$$

On the basis of electron microscope observations that the diameter of the carbon filament was close to and not greater than that of the metal particle, Rostrup-Nielsen reported that deviations from graphite equilibrium for CO and CH_4 decomposition, on a large number of Ni catalysts could be explained by the extra energy required by the surface and defect structure of the filaments, as expressed by Equation (5.3) (Rostrup-Nielsen, 1972).

$$\Delta G_c = \mu - \mu_0 + \mu^* \tag{5.3}$$

The term $\mu - \mu_0$ corresponds to the extra surface energy due to the cylindrical form of the filament. The term μ^* corresponds to the extra energy from surface defects. A simple Kelvin equation model can be used to determine ΔG_c, as shown in Equation (5.4) or Equation (5.5):

$$\Delta G_c = (\gamma * M / \rho_c) * (1/r_M) + \mu^* \tag{5.4}$$

$$\Delta G_c = 2(\gamma * M / \rho_c) * (1/d_p) + \mu^* \tag{5.5}$$

Equation (5.4) shows that the surface energy increases with decreasing filament diameter or metal particle size. According to Equation (5.5), by linear regression of ΔG_c versus $1/d_p$, γ, the surface tension of the carbon fibres, and μ^*, the defect contribution, can be estimated from the obtained slope and intercept.

In the present study, ΔG_c on different Co and Ni catalysts was calculated from the value of K_M^* (as reported in Section 4.3.2 and Appendix B.3) and $K_{graphite} = 0.462$ atm at 773K (Rostrup-Nielsen, 1972) using Equation (5.2). The obtained values of ΔG_c are plotted versus the reciprocals of average metal particle size, in Figure 5.6. The data of Figure 5.6 show a linear relationship as described by Equation (5.5). Note that the difference between the present study and Rostrup-Nielsen's study is that the average metal particle size was used in Equation (5.4) to (5.5) not the maximum metal particle size.

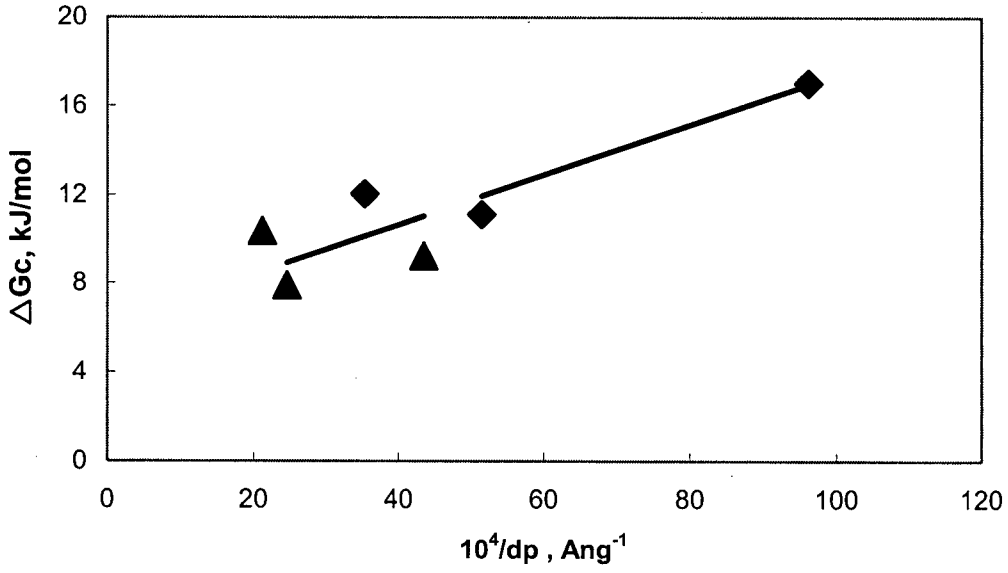

Figure 5.6 Deviation of the coking threshold from graphite equilibrium and the effect of metal crytallite size during CH_4 decomposition on Ni and Co catalysts at 773K. (♦ Co/SiO_2; ▲ Ni/SiO_2; $\Delta G_c = 0.101(10^4/d_p) + 6.68$; catalysts were reduced at 923K).

According to the intercept and slope of the data of Figure 5.6, the surface tension was estimated as 8.42 J/m^2 and the defect contribution to ΔG_c was approximately 6.68 kJ/mol at 773K, assuming the density of filamentous carbon was equal to 2.0 g/mL. The value of the surface tension is comparable to the surface tensions of about 7.9 and 7.4 J/m^2 at 773K for the CO-CO_2 and CH_4-H_2 equilibria, respectively (Rostrup-Nielsen, 1972); the defect contribution of

6.68 kJ/mol is comparable to values of 8.4 and 2.9 kJ/mol at 773K for the CO-CO_2 and CH_4-H_2 equilibria, respectively (Rostrup-Nielsen, 1972). The result from the present study confirmed that the deviation from graphite could be explained by a more disordered structure of the carbon formed, and by a contribution from the surface energy of the carbon filament. The metal (Ni or Co catalyst) appeared to have no influence on the observed equilibrium.

5.3.2 Effect of Metal Particle Size on $(K_M^* - K_M^f)$

As mentioned above, by analogy to the coking threshold, we have defined a filamentous carbon formation threshold: K_M^f, which corresponds to the term K_M where the net carbon deposition rate is equal to the carbon bulk diffusion rate. The difference between the definitions of the two thresholds is that at the coking threshold, the net carbon formation rate is equal to zero, whereas at the filamentous carbon formation threshold, the net rate is constant but not zero. As mentioned in Section 4.3.2, filamentous carbon formation threshold, K_M^f, was obtained by extrapolating the decay constant k_d at different K_M to zero. On Co/SiO_2 catalysts with different loading, different K_M^f were further obtained by extrapolation (as reported in Section 4.3.2 and Appendix B.3) and these values are plotted versus metal particle size in Figure 5.7. Furthermore, the difference between the coking threshold and filamentous carbon threshold, $(K_M^* - K_M^f)$, is plotted versus metal particle size in Figure 5.8.

At the filamentous carbon formation threshold, catalyst stable activity was obtained with carbon formation rate equal to carbon diffusion rate, with the encapsulating carbon formation rate neglected. The carbon formation rate can be simplified into $k\frac{P_{CH_4}}{P_{H_2}^2 n_s}$ when K_M approaches K_M^* (Figure 4.9a and Figure 4.11a). The diffusion rate of carbon can be described as

Equation (4.3) $\dot{r}_d = D_s \frac{(n_s/dx - n_1/dx)}{(2/3)d_p}$. The filamentous carbon formation threshold can be simplified into Equation (5.6) noting that the carbon formation rate is equal to the carbon diffusion rate:

$$K_M^f = \left(\frac{P_{H_2}^2}{P_{CH_4}}\right) \approx \frac{k(2/3)d_P}{D_s n_s (n_s/dx - n_1/dx)} \tag{5.6}$$

Note that Equation (5.6) shows that the influence of metal type on the filamentous carbon formation threshold occurs through the D_s. The data in Figure 5.7 show that the dependence of K_M^f on metal particle size is not a simple linear relationship. This can be explained by noting that n_s and $n_s - n_1$ are also dependent on metal particle size, d_P, since the activity of carbon formation is dependent on metal particle size as described in Section 5.2. However, the data in Figure 5.8 show a clear trend that the difference between the coking threshold and filamentous carbon threshold increases with increasing metal particle size on Co catalysts with different loadings. According to the discussion in Section 4.4.3, stable catalyst activity with carbon deposition during CH_4 decomposition occurs when K_M satisfies $K_M^f < K_M < K_M^*$. The increasing difference between the coking threshold and filamentous carbon formation threshold, with increased metal particle size shown in Figure 5.8, indicates that the window of suitable operating conditions for stable catalyst activity with filamentous carbon formation is wider with increasing metal particle size. This is consistent with the observation in Section 5.2 that under the same K_M, stable catalyst activity with filamentous carbon formation was obtained on larger metal particles because the condition $K_M^f < K_M < K_M^*$ can be satisfied when the difference in thresholds increases (i.e. $(K_M^* - K_M^f)$ increases).

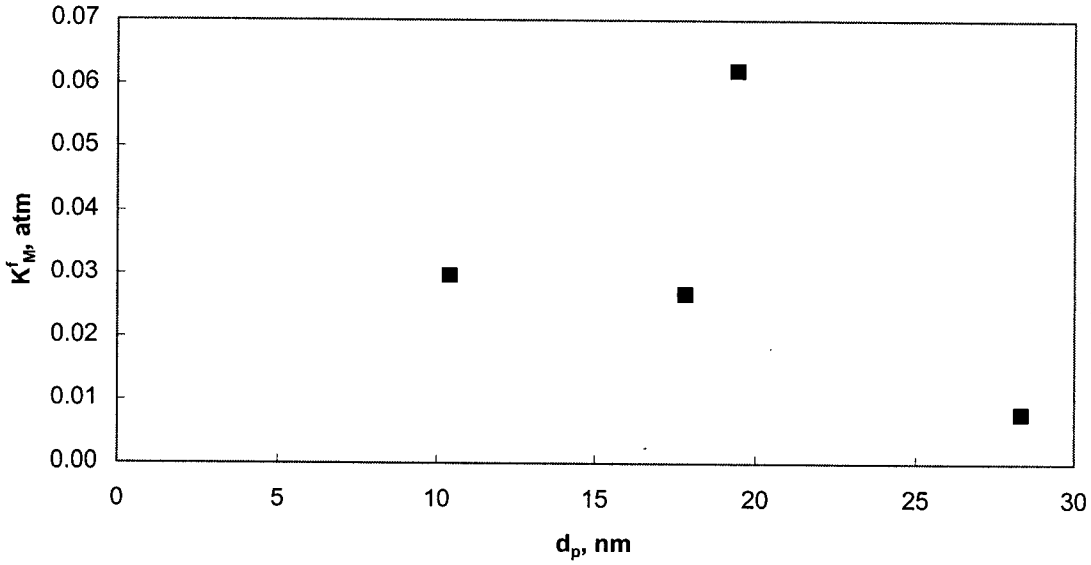

Figure 5.7 The filamentous carbon formation threshold, K_M^f, versus metal particle size on Co catalysts at 773K.

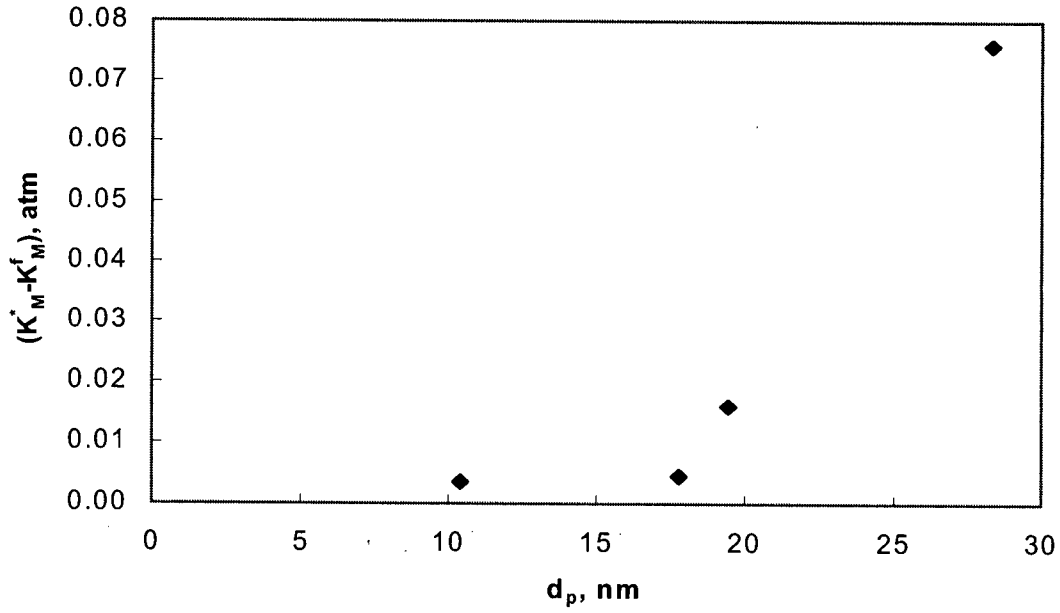

Figure 5.8 The difference between the coking threshold and the filamentous carbon formation threshold, $(K_M^* - K_M^f)$, increases with the increasing particle size of Co at 773K.

5.4 Effect of MSI on Catalyst Activity

In this section, the influence of BaO, La_2O_3 and ZrO_2 added to the SiO_2 support of the Co/SiO_2 catalyst, is reported. The catalysts with SiO_2 modified by additives BaO, La_2O_3, and ZrO_2 were designated as $Co/BaO/SiO_2$, $Co/La_2O_3/SiO_2$ and $Co/ZrO_2/SiO_2$, respectively. The $Co/BaO/SiO_2$, $Co/La_2O_3/SiO_2$ and $Co/ZrO_2/SiO_2$ catalysts were prepared by step-wise incipient wetness impregnation. Section 3.2 and Table 3.4 summarize the preparation details and characterization data of these modified catalysts. On the basis of a detailed characterization study of the modified catalysts, using TPR, XPS and CO chemisorption, the influence of the addition of BaO, La_2O_3 and ZrO_2 on the activity and deactivation of the 12wt% Co/SiO_2 catalyst during CH_4 decomposition was investigated.

5.4.1 Effect of Additives on MSI

5.4.1.1 Effect of Additives on Reduction Behavior of Co Species and MSI

In order to clarify the effect of additives, BaO, La_2O_3 and ZrO_2, on the reduction behaviour of Co_3O_4 species, the catalysts were characterized by TPR. The TPR profiles of the 12wt% Co/SiO_2 catalyst and modified catalysts $Co/BaO/SiO_2$, $Co/ZrO_2/SiO_2$ and $Co/La_2O_3/SiO_2$, are shown in Figure 5.9. Generally, the TPR profiles could be resolved into three peaks. The peak position and relative intensity of each peak, representing the relative H_2 consumption, is summarized in Table 5.1.

The TPR profile for the base 12wt% Co/SiO_2 catalyst of Figure 5.9a shows two major reduction peaks with maxima at 536K and 663K. A broad shoulder extending to 837K was also observed. The first two reduction peaks are usually identified as the two-step reduction of $Co_3O_4 \rightarrow CoO \rightarrow Co$. The stoichiometric H_2 consumption ratio associated with the two reduction steps is 1:3. However, for the Co/SiO_2 catalyst the ratio calculated from the data of Table 5.1 is

1:2.2, suggesting that not all the CoO species are reduced to Co. Rather, less reducible or irreducible species are formed during the Co_3O_4 reduction, most likely through interaction with the support, to yield, for example, Co_2SiO_4 (Riva et al., 2000; Ming et al., 1995). The broad shoulder that exists in the TPR profile at high temperature (around 837K) is assigned to the reduction of Co species that interact with the SiO_2 support (Riva et al., 2000). The H_2 consumption of this broad shoulder was 8.2% of the total H_2 consumption during TPR of the Co/SiO_2 catalyst.

For the $Co/BaO/SiO_2$ catalyst, the TPR profile of Figure 5.9b was very similar to that of the Co/SiO_2 catalyst. The low temperature reduction peaks shifted slightly to higher temperature (the first from 536K to 543K; the second from 663K to 670K). The relative H_2 consumption of the broad high temperature shoulder (around 843K) was 8.4% for the $Co/BaO/SiO_2$, essentially the same as the 8.2% obtained with Co/SiO_2. In addition, the consumption ratio of the first two peaks was 1:2.4, similar to the 1:2.2 obtained with Co/SiO_2. The result suggests that BaO changed the interaction between Co and the BaO/SiO_2 support slightly and that the reducibility of the Co species was slightly changed by the addition of the BaO to the support.

For the $Co/ZrO_2/SiO_2$ catalyst, the TPR profile of Figure 5.9c shows that the second low temperature reduction peak shifted slightly to higher temperature (the second peak from 663K to 683K), indicative of a small increase in resistance to reduction. Also, in the high temperature region, a sharp peak replaced the broad shoulder at 852K. It is further observed that the relative H_2 consumption at high temperature increased from 8.2% for the Co/SiO_2 catalyst, to 41.4% for the $Co/ZrO_2/SiO_2$ catalyst. In addition, the H_2 consumption ratio of the first two peaks was 1:3. Hence the high temperature H_2 consumption must be associated with a Co-Zr interaction that prevents the reduction of Co species generated during the calcination step. This observation confirms that a strong interaction between cobalt and zirconium replaced the cobalt-silica

interaction (Feller et al., 1999). Feller et al. claimed that the Co-Zr interaction was formed due to an interaction between the zirconium salt and cobalt ions. In the present case, the interaction probably results from residual zirconium salt not converted to ZrO_2 during the short-term calcination.

For the $Co/La_2O_3/SiO_2$ catalyst, the TPR profile of Figure 5.9d shows that the first reduction peak moved to higher temperature (from 536K to 588K) and increased in intensity relative to the first reduction peak of the Co/SiO_2 catalyst. The second reduction peak was replaced by a sharp peak at higher temperature 703K (663K for Co/SiO_2 catalyst) and the H_2 consumption ratio of the two peaks was 1:0.6. These observations are indicative of increased resistance to reduction of the oxides, especially CoO, on the La_2O_3/SiO_2 support. The relative intensity of the broad peak at high temperature decreased from 8.2% for Co/SiO_2 to 4.1% for the $Co/La_2O_3/SiO_2$ catalyst. Apparently, the addition of La_2O_3 increased the reduction temperature of both Co_3O_4 and CoO, but also resulted in Co-support species, produced during reduction, that were not subsequently reduced to Co metal. Note that the TPR of the $Co/La_2O_3/SiO_2$ catalyst also shows that if the catalyst is reduced at 723K, the degree of reduction of the Co oxide will be lower than that obtained on the Co/SiO_2.

From the TPR results, it can be concluded that the addition of BaO, La_2O_3 and ZrO_2 to the SiO_2 support, all influenced the MSI and hence the reduction behaviour of the Co species. The addition of BaO increased the interaction marginally; the addition of ZrO_2 resulted in a very strong $Co\text{-}ZrO_2/SiO_2$ interaction and Co species that could only be reduced above 850K; the addition of La_2O_3 resulted in an interaction between Co and the modified La_2O_3/SiO_2 support that increased the reduction temperature of Co_3O_4 and CoO and produced species that were not reducible during TPR.

Table 5.1 Summarized data of catalyst TPR profiles of modified Co catalysts.

Catalyst	1st Peak		2nd Peak		3rd Peak	
	Temp, K	Relative Intensity	Temp, K	Relative Intensity	Temp, K	Relative intensity
12wt% Co/SiO_2	536	28.8%	663	63.0%	837	8.2%
$Co/BaO/SiO_2$	543	27.0%	670	64.5%	843	8.4%
$Co/ZrO_2/SiO_2$	533	14.5%	683	44.1%	852	41.4%
$Co/La_2O_3/SiO_2$	588	61.7%	703	34.2%	843	4.1%

Note: In TPR, catalysts were reduced from 323K to 950K in 5%H_2/He in an hour. Catalyst reduction degrees reported in Table 3.1 and 3.4 were calculated based on the catalysts were reduced from 323K to the desired reduction temperature in 40% H_2/He in an hour.

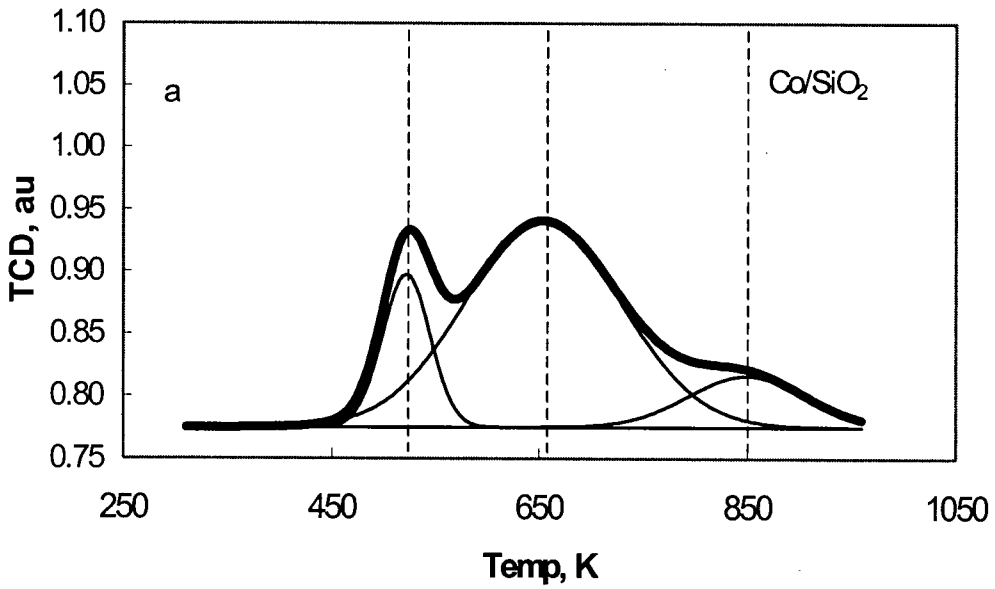

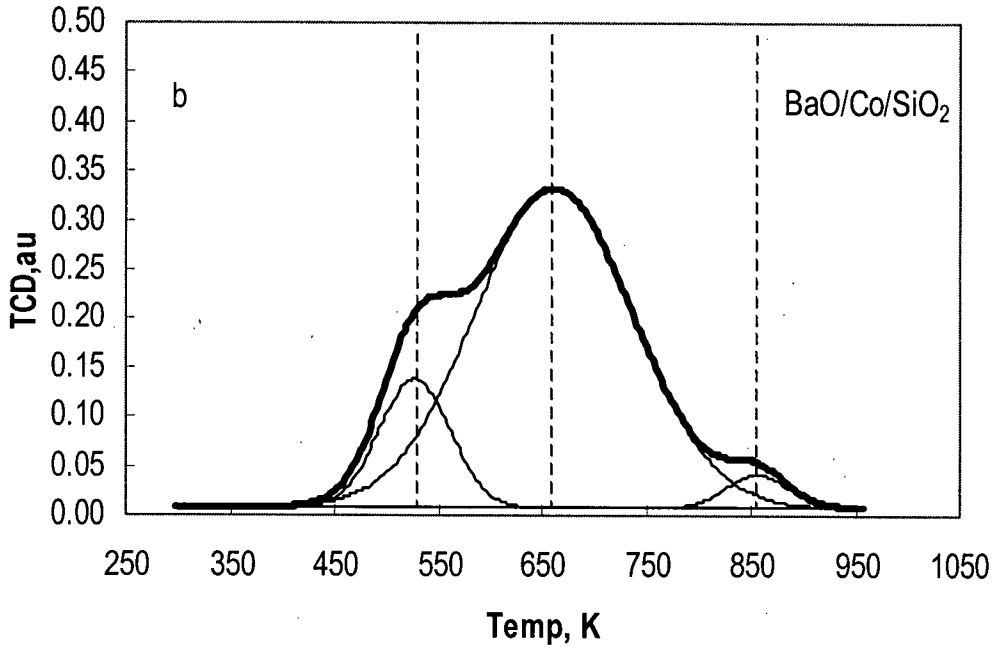
b
BaO/Co/SiO2
TCD,au
0.50
0.45
0.40
0.35
0.30
0.25
0.20
0.15
0.10
0.05
0.00
250
350
450
550
650
750
850
950
1050
Temp, K

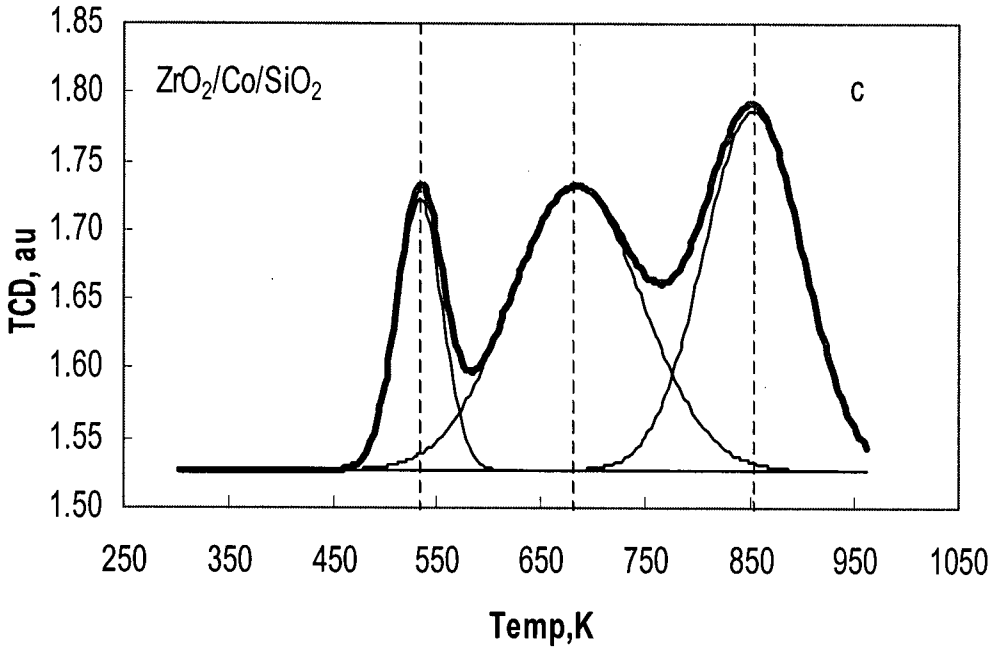
ZrO2/Co/SiO2
c
TCD, au
1.85
1.80
1.75
1.70
1.65
1.60
1.55
1.50
250
350
450
550
650
750
850
950
1050
Temp,K

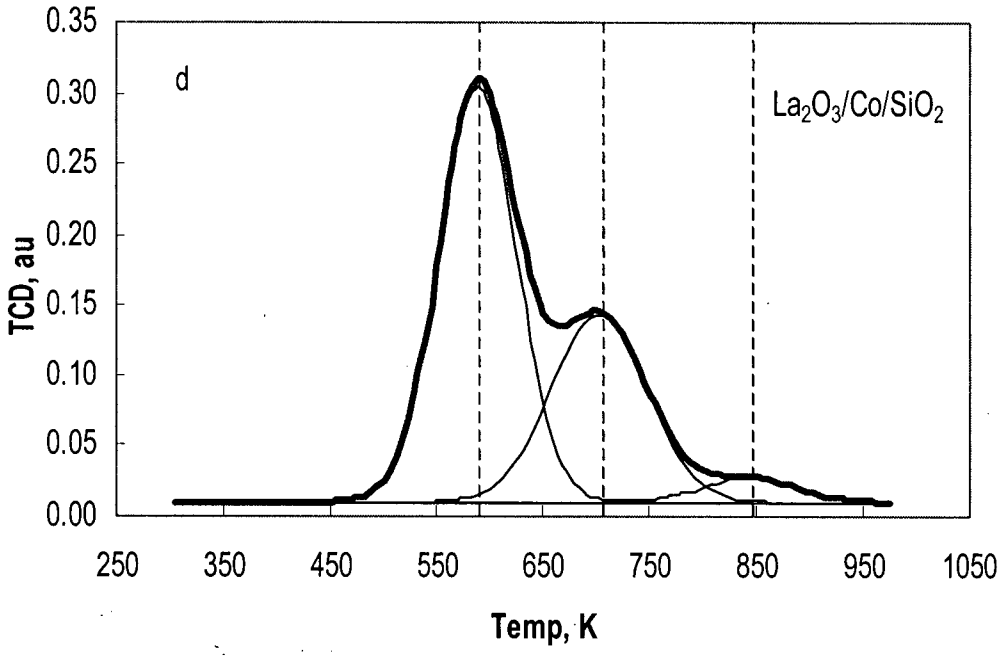

Figure 5.9 TPR profiles of modified Co catalysts. a: 12wt% Co/SiO_2; b: $Co/BaO/SiO_2$; c: $Co/ZrO_2/SiO_2$; d: $Co/La_2O_3/SiO_2$.

5.4.1.2 Effect of Additives on Surface Species

To clarify the effect of additives BaO, La_2O_3 and ZrO_2 on the distribution of surface Co species, reduced catalysts were characterized by XPS, as described in Section 3.3.5. The base Co/SiO_2 catalyst was characterized before and after reduction at 723K. Other catalysts modified by BaO, La_2O_3 and ZrO_2 were characterized by XPS after reduction at 723K. The reduction temperature of 723K was chosen because at this reduction temperature it was easier to detect different MSI effects from the TPR results compared to reduction at 923K. The effect of additives on catalyst deactivation was also significant when the catalysts were reduced at 723K as discussed in Section 5.4.3. In general, Co 2p, O 1s and Si 2p spectra were obtained from each XPS measurement. Detailed results from the XPS analysis are summarized in Table 5.2, including Co $2p_{3/2}$ binding energy (B.E.), the intensity of the shake-up shoulder relative to the Co 2p intensity, and the calculated Co: Si ratio. Among the modified catalysts, BaO was detected

by the presence of the $M_5N_{45}N_{45}$ Auger peak with kinetic energy 597.7eV; ZrO_2 was detected at a $3d_{5/2}$ B.E. of 182.6eV with energy difference 2.4eV between $3d_{5/2}$ and $3d_{3/2}$; La_2O_3 was detected at a $3d_{5/2}$ B.E. of 836.3eV.

The fitted Co 2p spectra of the various catalysts are presented in Fig. 5.10 and Table 5.2 (Comparisons between the fitted and measured spectra given in Appendix C). For the calcined Co/SiO_2 catalyst, the Co $2p_{3/2}$ B.E. was 780.3eV; The Co $2p_{3/2}$ B.E. of the reduced catalysts was in the range 780.7eV to 782.3eV (with Si 2p at 103.5 eV). Riva et al. (2000) reported the Co $2p_{3/2}$ B.E. of Co_3O_4 as 780.1eV; Co $2p_{3/2}$ B.E. of CoO as 780.5 eV; Co $2p_{3/2}$ B.E. of metallic Co as 777.8 eV with Si 2p reference at 103.3 eV (Riva et al., 2000). Meanwhile, Ming and Baker (1995) reported the Co $2p_{3/2}$ B.E. of Co_2SiO_4 as 781.3 eV with Si 2p at 103.5 eV as reference. Accordingly, for the calcined Co/SiO_2 catalyst of the present study, the Co $2p_{3/2}$ B.E. of 780.3eV is assigned to Co_3O_4 (Riva et al., 2000) and this observation is in agreement with XRD data showing the presence of Co_3O_4 after calcination. The Co $2p_{3/2}$ B.E. of the reduced catalysts was in the range 780.7eV to 782.3eV, indicative of the presence of surface Co^{2+} probably as Co_2SiO_4 (B.E. 781.3eV) (Ming and Baker, 1995) or CoO (B.E. 780.5eV) (Riva et al., 2000). The shake-up shoulder at higher B.E. for the reduced catalysts is ascribed to unreduced Co^{2+} interacting with the support. The assignment is supported by the fact that the TPR data show that CoO is reduced at low temperature (<723K). Also, steps were taken to minimize the exposure of the reduced catalysts to air (to avoid re-oxidation of Co) prior to the XPS measurement (Catalysts were sealed in inert gas after cooling be fore being loaded and transferred to the XPS using a glove box. Hence it was assumed that there was no oxidation of the reduced catalyst during the sample transfer.). To quantify the MSI, the relative intensity of the shake-up shoulder was calculated as the ratio of the fitted peak area of the shake-up shoulder to the Co $2p_{3/2}$ fitted peak area (Bianchi, 2001).

Compared to the reduced Co/SiO_2 catalyst, the spectra of the other reduced catalysts show that the relative intensity of the Co species interacting with silica was dependent upon which of BaO, ZrO_2, and La_2O_3 were present. The relative intensity of the shake-up shoulder was 12% for the reduced Co/SiO_2 catalyst. The relative intensity of the shake-up shoulder was mot available for the reduced $Co/BaO/SiO_2$ catalyst because the Co 2p and Ba 3d peaks could not be resolved. However, the conclusion that the addition of BaO had little effect on the interaction of Co species with silica could be drawn from the TPR data of Figure 5.9. Conversely, a much stronger $Co\text{-}ZrO_2/SiO_2$ interaction is apparent for the reduced $Co/ZrO_2/SiO_2$ catalyst, the relative intensity of the shake-up shoulder increasing from 12% to 28%. This result is also consistent with the increased relative H_2 consumption at high temperature (850K) that was observed during TPR. For the reduced $Co/La_2O_3/SiO_2$ catalyst, the relative intensity of the shake-up increased to 18%, again consistent with the stronger MSI identified from TPR data and ascribed to the higher resistance of the cobalt oxides to reduction at low temperature (<723K) on this catalyst.

The energy difference (ΔE) between Co $2p_{3/2}$ and $2p_{½}$ (ΔE=15eV for Co_3O_4 and metallic Co, ΔE=15.7eV for CoO) also make it possible to distinguish the different phases of Co present on the catalyst surface (Riva et al., 2000). A ΔE=15.7eV applies to Co^{2+} in general, even when cobalt forms silicate through reaction with the SiO_2 support (Riva et al., 2000). In the present study, ΔE = 15.7eV and the presence of a shake-up shoulder at higher B.E. was observed for all reduced catalysts. The ΔE=15eV listed in Table 5.2 for the unreduced Co/SiO_2 catalyst confirms that Co species were in the form of Co_3O_4 after calcination, consistent with XRD data already noted. The XPS spectrum of the un-reduced Co/SiO_2 catalyst (Figure 5.10a) also shows a very small shake-up shoulder at higher B.E., suggesting that there is very little interaction between Co species and the silica support. However, ΔE=15.7eV for the reduced Co/SiO_2 catalyst. Figure

5.10b also shows that the shake-up shoulder at higher B.E. for the reduced Co/SiO_2 catalyst was more intense than for the unreduced catalyst. The interaction between Co and SiO_2 to yield cobalt silicate must therefore occur during the catalyst reduction step.

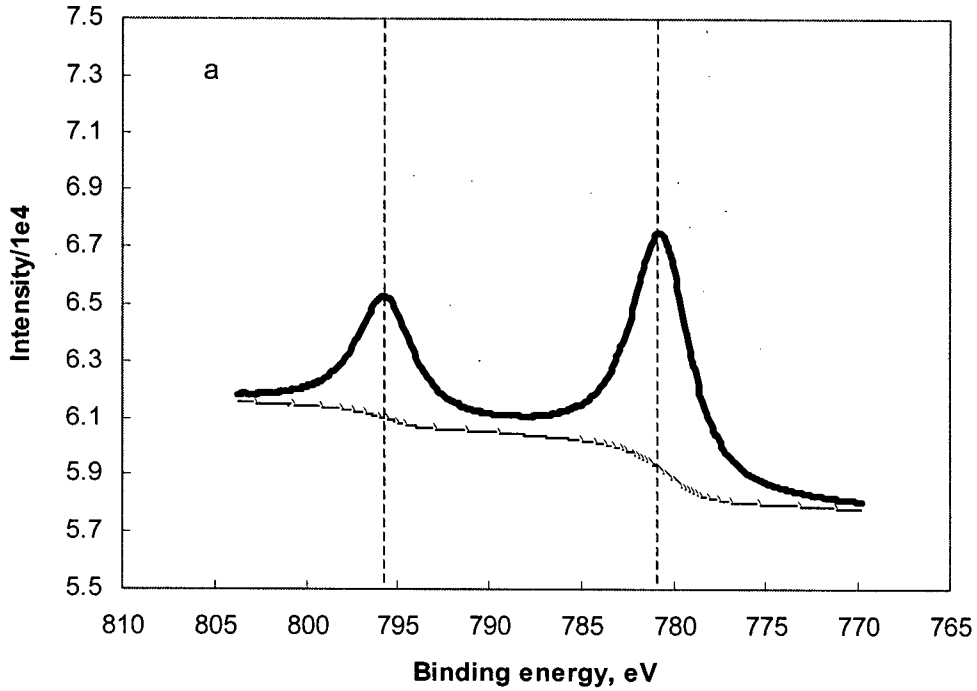

Figure 5.10 Surface Co 2p Spectra on modified catalysts. a: unreduced 12wt% Co/SiO_2; b: reduced 12wt% Co/SiO_2; c: reduced $Co/BaO/SiO_2$; d: reduced $Co/ZrO_2/SiO_2$; e: reduced $Co/La_2O_3/SiO_2$. (Note that the raw data of XPS measurement is shown in Appendix C.)

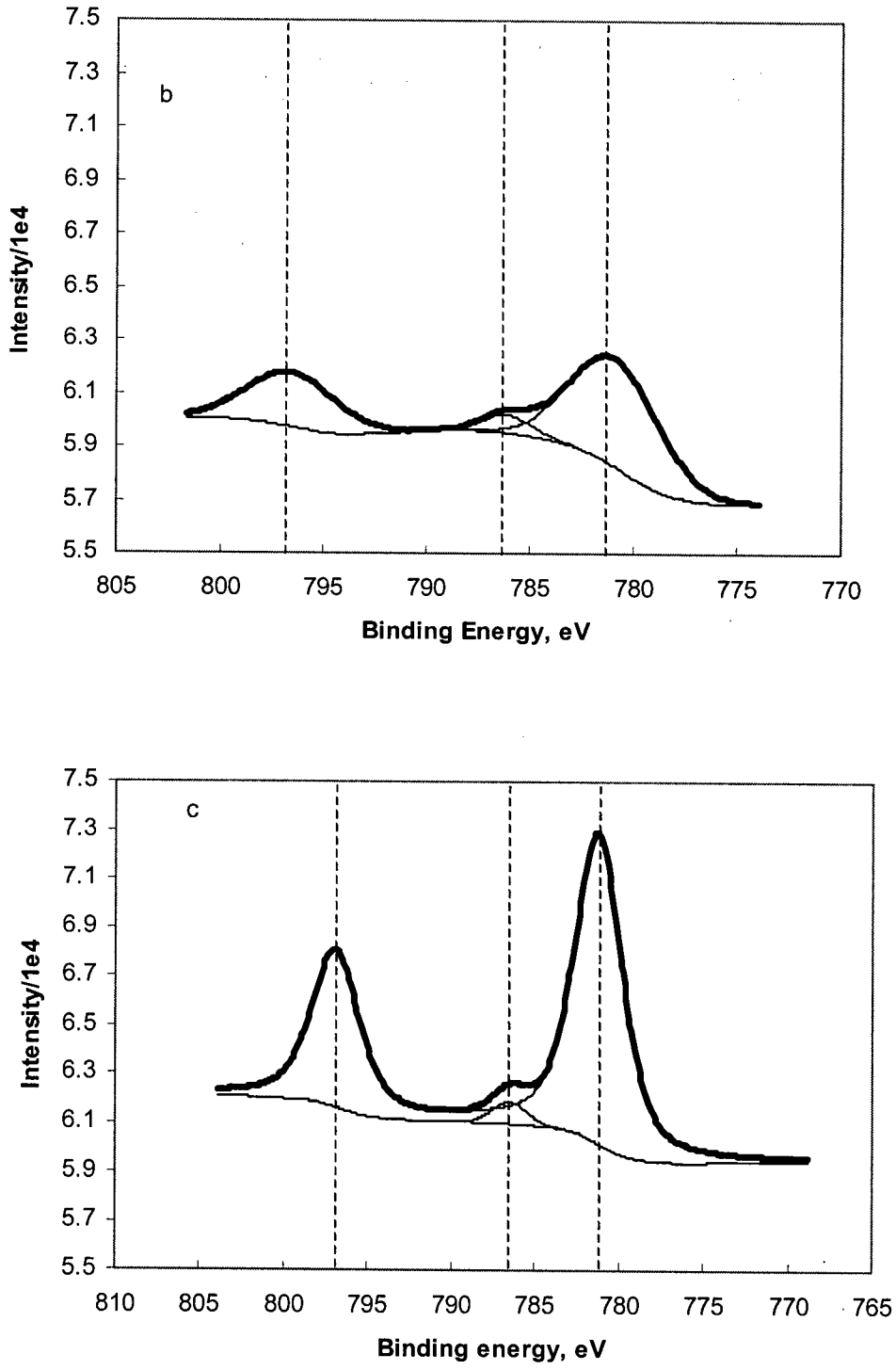

Figure 5.10 Surface Co 2p Spectra on modified catalysts. a: unreduced 12wt% Co/SiO_2; b: reduced 12wt% Co/SiO_2; c: reduced $Co/BaO/SiO_2$; d: reduced $Co/ZrO_2/SiO_2$; e: reduced $Co/La_2O_3/SiO_2$. (Note that the raw data of XPS measurement is shown in Appendix C.)

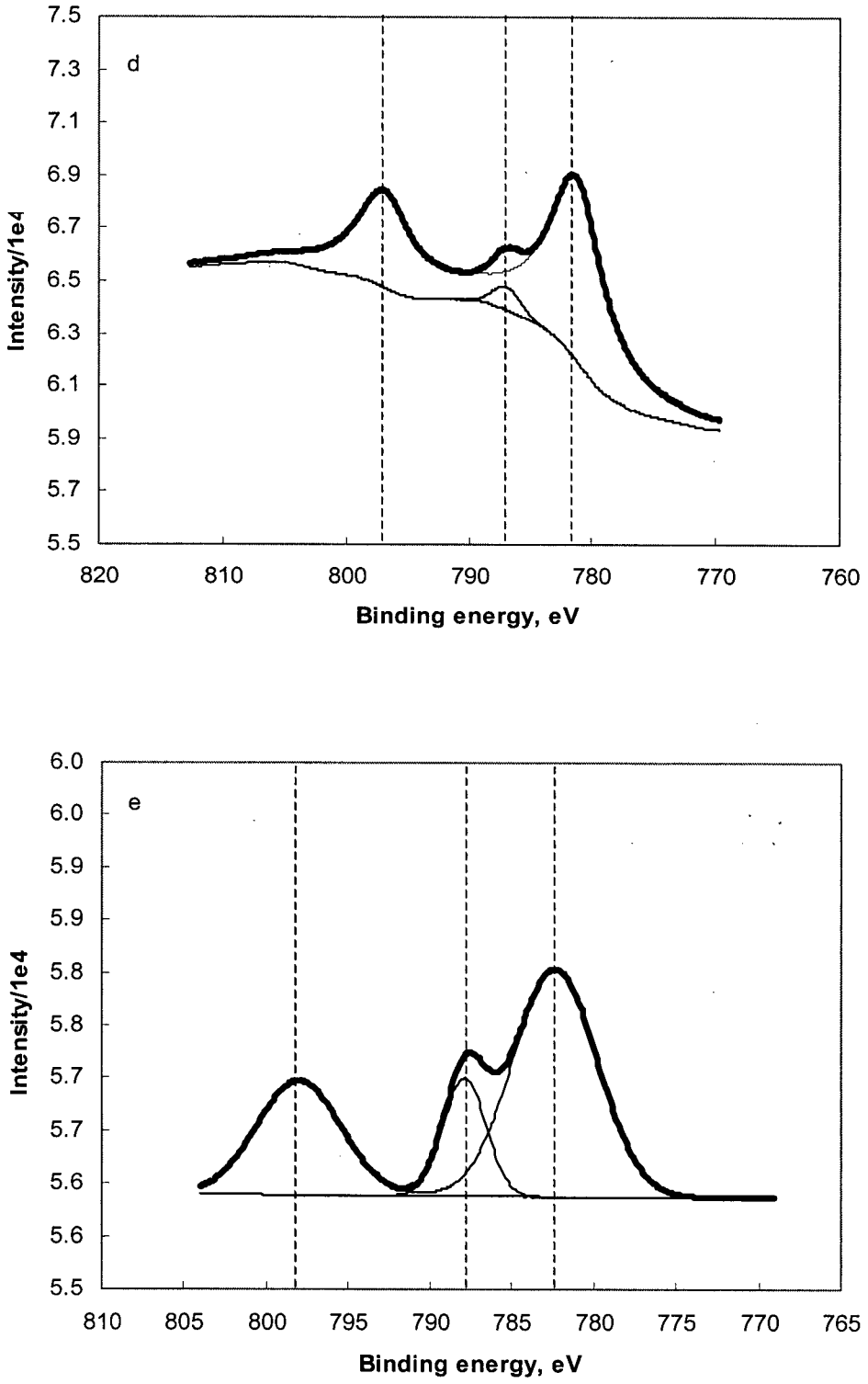

Figure 5.10 Surface Co 2p Spectra on modified catalysts. a: unreduced 12wt% Co/SiO_2; b: reduced 12wt% Co/SiO_2; c: reduced $Co/BaO/SiO_2$; d: reduced $Co/ZrO_2/SiO_2$; e: reduced $Co/La_2O_3/SiO_2$. (Note that the raw data of XPS measurement is shown in Appendix C.)

Table 5.2 Summarized data from XPS characterization of modified Co catalysts.

Catalysts	Co (eV)		Me[d] (ΔE)	O 1s	Relative intensity	100Co:Si
	Co $2p_{3/2}$	ΔE[c]	eV	eV	Shoulder/$2p_{3/2}$ %	Atomic
Co/SiO_2 without Reduction [b]	780.3	15	-	533.0		1.9
Co/SiO_2 after Reduction [b]	780.7	15.7	-	533.0	12	1.9
$Co/BaO/SiO_2$ after Reduction [b]	781.2	15.7	597.7 ($M_5N_{45}N_{45}$)	533.0	-	-
$Co/ZrO_2/SiO_2$ after Reduction [b]	781.6	15.7	182.6 ($3d_{5/2}$ ΔE=2.4)	533.0	28	2.6
$Co/La_2O_3/SiO_2$ after Reduction [b]	782.3	15.7	836.3 ($3d_{5/2}$)	533.0	18	1.1

[a] The shake-up shows the interaction of Co with silica.

[b] Catalysts were reduced from 323K to 723K in 1 hour.

[c] $\Delta E = (Co\ 2p_{1/2} - Co\ 2p_{3/2})$.

[d] Me: Ba, La or Zr.

[e] Si 2p with binding energy 103.5eV was taken as an internal reference.

5.4.1.3 Effect of Additives on Co Dispersion

The 100Co:Si ratio calculated from the XPS analysis and listed in Table 5.2 is indicative of the Co dispersion of the catalyst: a higher dispersion corresponds to higher 100Co:Si ratio. The data of Table 5.2 show that the 100Co:Si ratio was 1.9 for the Co/SiO_2 catalyst, both before and after reduction. Note that for the reduced $Co/BaO/SiO_2$ catalyst, the 100Co:Si ratio is not reported because the Co 2p and Ba 3d peaks could not be resolved (B.E. of Ba $3d_{5/2}$=779.7eV, Co $2p_{3/2}$ B.E.=778.0eV for Co^0 and 780.5eV for Co^{2+}). For the reduced $Co/La_2O_3/SiO_2$ catalyst, the 100Co:Si ratio decreased to 1.1, compared to the Co/SiO_2 catalyst, whereas for the reduced $Co/ZrO_2/SiO_2$ catalysts, the 100Co:Si ratio increased to 2.6, suggesting that ZrO_2 assisted the dispersion of Co species over the support due to the strong interaction between Co and ZrO_2. Note that although the 100Co:Si ratio determined from the XPS peak intensity data is indicative of the dispersion of the Co species on the surface, this ratio included unresolved Co^0 (B.E.

778.0eV) and Co^{2+} species. Hence the dispersion of active Co^0 as determined by CO chemisorption is considered the more accurate measure of active Co sites.

Table 3.4 summarized the active cobalt dispersion, particle size and the number of active sites as determined by CO chemisorption on the Co/SiO_2 and modified Co/SiO_2 catalysts reduced at 723K and 923K. Note that the dispersion is calculated relative to the total amount of reduced Co on the catalyst. Also note that at a reduction temperature of 723K, the TPR results show that the different MSI effects among the catalysts, as reflected in the relative intensities of the high temperature reduction peak (850K), will be important. Conversely, the TPR data show that reduction at 923K will result in complete reduction of the Co. On $Co/BaO/SiO_2$, $Co/La_2O_3/SiO_2$ and $Co/ZrO_2/SiO_2$, the CO uptake decreased compared to the Co/SiO_2 catalyst. After accounting for the degree of reduction of the Co species, the results show that the Co dispersion decreased on all the modified catalysts. Among the modified catalysts, $Co/ZrO_2/SiO_2$ had the highest dispersion. When the catalysts were reduced at 973K, however, the differences in dispersion were not as pronounced, compared to the catalysts reduced at 723K. In particular, the Co dispersion obtained on the Co/SiO_2 and the $Co/ZrO_2/SiO_2$ were approximately equal when catalysts were reduced at 973K.

5.4.2 MSI Order among the Modified Catalysts

MSI effects are known to influence the reduction of metal oxides and metal dispersion on supported metal catalysts (Haddad et al., 1996; Riva et al., 2000; Ming and Baker, 1995; Van Steen et al., 1996; Khodakov et al., 1997; Rodrigues and Bueno, 2002). A strong MSI increases the difficulty of the reduction of the precursor oxide, either by increasing the reduction temperature of existing oxides or by the production of metal-support species (such as Co_2SiO_4) that are difficult to reduce or are irreducible. Furthermore, a strong MSI decreases the mobility of the metal surface species such that the metal dispersion is enhanced. In the present study, the

strength of the MSI is of interest, and a number of techniques have been used to determine the relative strength of the MSI between Co and a SiO_2 support, modified by the addition of BaO, La_2O_3 and ZrO_2.

The interaction between Co and SiO_2 was not significantly affected by the addition of BaO to the SiO_2. The small increase in H_2 consumption during the extended high temperature TPR and the small increase in reduction peak temperatures suggest a small increase in the MSI. However, the lower relative intensity of the Co $2p_{3/2}$ shake-up shoulder as measured by XPS, suggests a small reduction in the Co-silica interaction.

The behaviour of the $Co/ZrO_2/SiO_2$ catalyst deviated significantly from the Co/SiO_2 catalyst. The addition of ZrO_2 resulted in a very strong MSI, evidenced by the increased H_2 consumption in the high temperature region (850K) of the TPR experiment. The TPR experiment also showed that the Co_3O_4 reduced to CoO was subsequently all reduced to Co. However, a significant fraction of the Co present on the catalyst after calcination could only be reduced at high temperature. Hence by reducing the catalyst at 723K, a significant portion of the cobalt remains unreduced because of the strong MSI. The strong MSI yields increased dispersion of Co surface species, as evidenced by the increased 100Co:Si ratio determined by XPS. The high shake-up peak intensity also points to a strong MSI on this catalyst. The strong MSI is also consistent with the small particle size of the Co_3O_4 precursor determined by XRD and noted previously.

For the $Co/La_2O_3/SiO_2$ catalyst, the increase in temperature associated with the reduction of both Co_3O_4 (at 588K) and CoO (at 703K) suggest a stronger interaction between these species and La, compared to Si. Although there was little decrease in the high temperature H_2 consumption, compared to Co/SiO_2, the TPR peak intensities point to a significant portion of Co_3O_4 that was reduced at low temperature, but formed species that did not reduce at high

temperature. Hence a strong MSI occurs during the reduction of this catalyst. The intensity of the Co $2p_{3/2}$ shake-up shoulder also suggests a strong MSI. However, the strong MSI did not improve Co dispersion, as indicated by the Co/Si ratio estimated by XPS. These data suggest that La_2O_3 located on top of the Co and are consistent with XPS data that confirmed the presence of La (Table 5.2) on the catalyst surface. The results obtained here do not agree with those of Haddad et al. (1996), who reported that La^{3+} moderates a strong Co-silica interaction and enhances the reducibility of the Co oxide. However, in the present work, La was added to the support prior to Co and the resulting MSI on the modified support yields a stronger MSI. The effects of aqueous impregnation of Co/SiO_2 catalysts has already been described in literature (Haddad et al., 1996), and the different sequence of impregnating steps used in the present study are the most likely source of the observed effects of La. Although the La results in a stronger MSI between Co and the modified silica support, the result is a reduced dispersion because La locates on top of the Co.

The Co dispersion, as determined from CO uptake measurements on catalysts reduced at 723K was higher on the Co/SiO_2 catalyst than either of $Co/BaO/SiO_2$, $Co/La_2O_3/SiO_2$ or $Co/ZrO_2/SiO_2$. However, based on the different MSI strengths noted in the previous paragraph, much higher dispersion would have been expected for the $Co/ZrO_2/SiO_2$ catalyst, in particular. The CO uptake measurement is assumed to titrate active sites available on the Co surface. However, it is possible that the CO uptake on Co is reduced by the presence of the modified supports. Previous studies have suggested that the perimeter of the Co particles may be decorated by the support (Zadeh and Smith, 1998), reducing CO uptake. This effect would be particularly pronounced for the $Co/ZrO_2/SiO_2$ catalyst with more highly dispersed Co. Furthermore, there might be an electronic effect associated with the modified catalysts that reduces CO uptake. The latter observation is consistent with the lower CH_4 decomposition TOF

data reported on the modified catalysts (Section 5.4.3) and shown in Figure 5.11a. The strong interaction of the Co species with Zr ensures good dispersion, but decreases reducibility. By increasing reduction temperature, more Co is reduced and the benefit of the strong interaction in aiding the dispersion of Co over the modified support is evident. The data of Table 3.4 show similar dispersion (as determined from CO uptake) for both the $Co/ZrO_2/SiO_2$ and the Co/SiO_2 catalysts when reduced at 923K.

The catalyst characterization results point to a change in the strength of the Co-support interaction when the SiO_2 support was modified by the addition of BaO, La_2O_3 or ZrO_2. The data suggest that the strength of the MSI between Co and the support can be ranked in increasing order as $Co/SiO_2 \approx Co/BaO/SiO_2 < Co/La_2O_3/SiO_2 < Co/ZrO_2/SiO_2$.

5.4.3 Catalyst Activity over Modified Co Catalysts

The effect of BaO, ZrO_2 and La_2O_3 on the CH_4 decomposition activity of the Co/SiO_2 was determined at two sets of reaction conditions, as indicated in Figure 5.11. Based on the observations in Section 5.2, that CH_4 decomposition is very dependent on the structure (Boskovic and Smith, 1996; Solymosi et al., 1994), the effect on catalyst activities must be compared based on TOFs. Following the procedures described in Chapter 3, TOF and decay constant $100k_d$, indicating the activity and stability of catalyst respectively, were obtained from the measured activity profiles and are plotted in Figure 5.11a and Figure 5.11b, respectively. In order to compare to the Co/SiO_2 catalyst, the dependency of TOFs and decay constant $100\,k_d$ on metal particle size measured on Co/SiO_2 catalysts are also plotted in Figure 5.11a and Figure 5.11b.

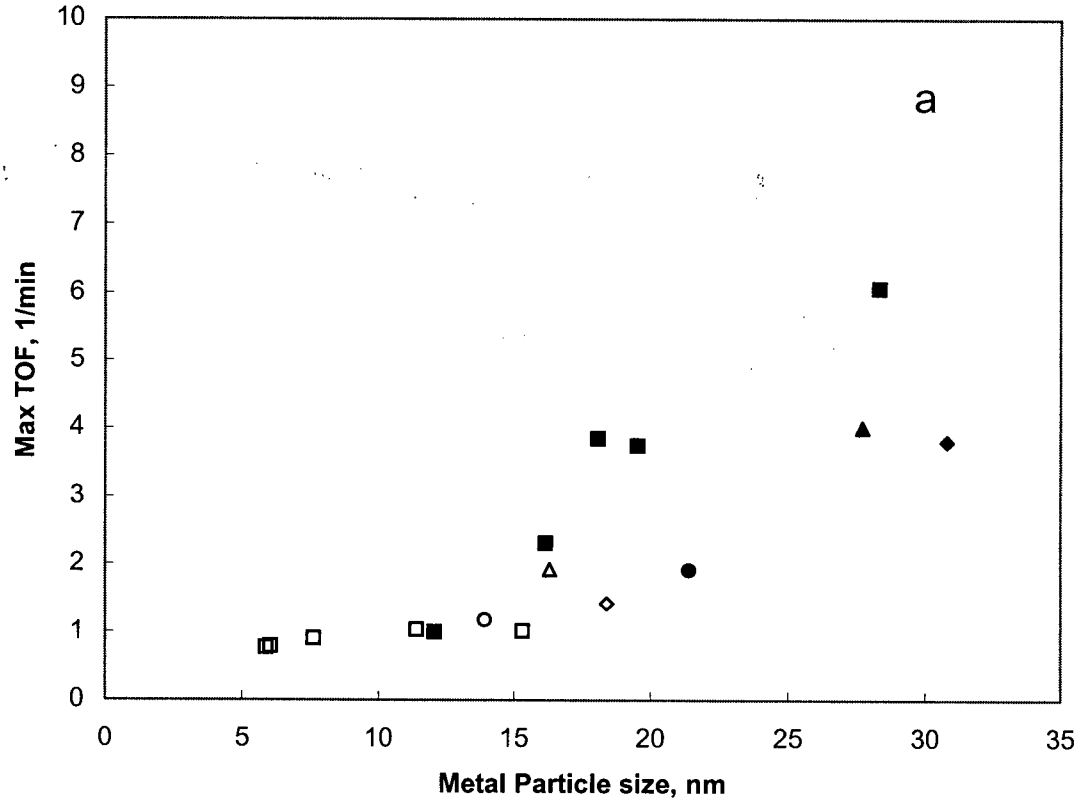

Figure 5.11a Dependence of maximum catalyst activity (TOF, r^*) on Co particle size over modified Co catalysts. (Unfilled symbol: Reduction 723K, 140 mL/min 5%CH_4/Ar at 723K; filled symbol: Reduction 923K, 185 mL/min 23%CH_4/12%H_2/Ar at 773K; □ and ■ Co/SiO_2; ◇ and ◆ Co/BaO/SiO_2; ○ and ● Co/ZrO_2/SiO_2; △ and ▲ Co/La_2O_3/SiO_2).

Figure 5.11a shows that the correlation of the CH_4 decomposition TOF with Co dispersion (or equivalent Co metal particle size) obtained on Co/SiO_2 catalysts, is also valid for the catalysts reduced at 723K in which the MSI had been modified by the addition of BaO, ZrO_2, and La_2O_3 to the SiO_2 support. The effect of using the modified support is adequately accounted for by the Co dispersion and on the promoted catalysts the same dependency on metal particle size was observed as with the Co/SiO_2 catalysts reduced at 723K. However, the modified support apparently has some impact on Co catalyst activity for the catalysts reduced at 923 K, which results in a decrease in CH_4 activity (maximum TOF) by approximately a factor of two. The

lower TOFs of the modified catalysts can be explained by the electronic effect of metallic Co and SiO_2 modified with BaO, ZrO_2, and La_2O_3. The ability of Co to dissociate CH_4 was reduced because the B.E. of Co shifted to higher B.E. for the modified catalysts.

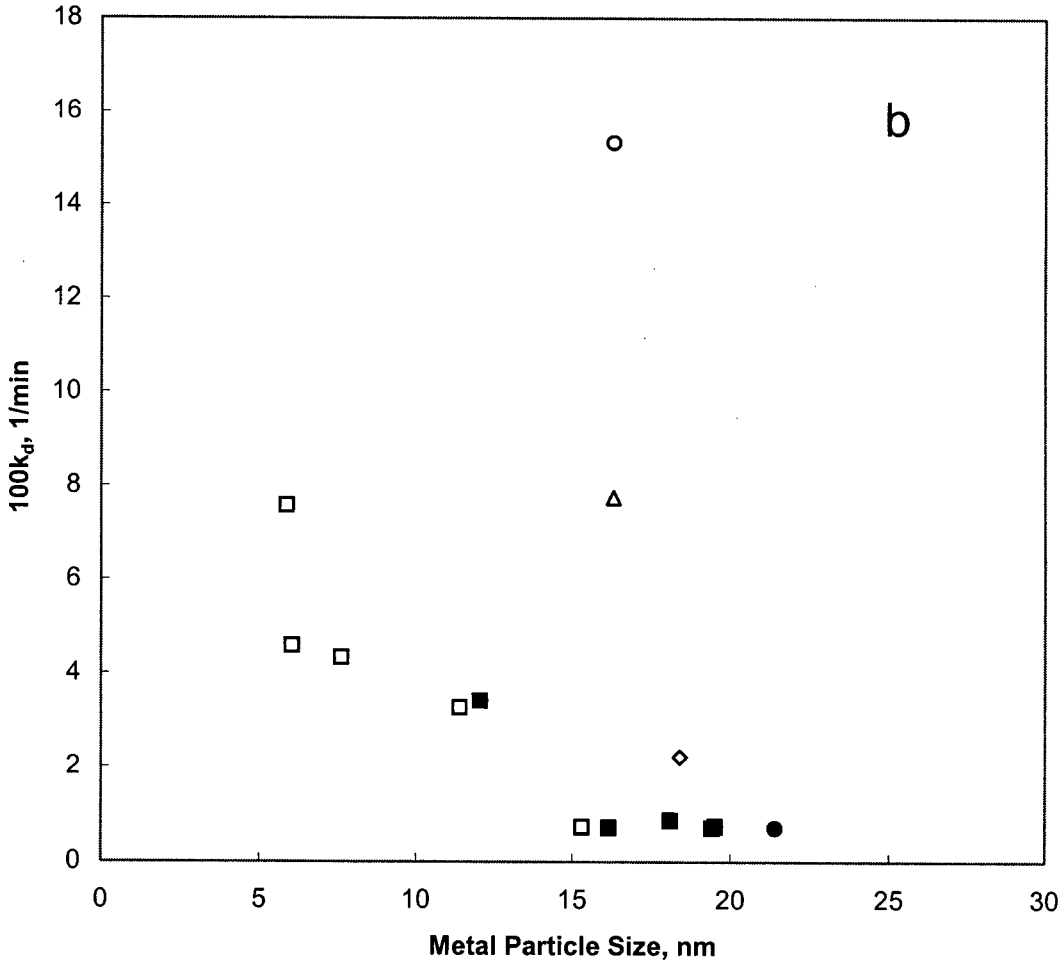

Figure 5.11b Dependence of catalyst decay constant ($100k_d$) on Co particle size over modified Co catalysts. (Unfilled symbol: Reduction 723K, 140 mL/min 5%CH_4/Ar at 723K; filled symbol: Reduction 923K, 185 mL/min 23%CH_4/12%H_2/Ar at 773K; □ and ■ Co/SiO_2; ◇ and ◆ $Co/BaO/SiO_2$; ○ and ● $Co/ZrO_2/SiO_2$; △ and ▲ $Co/La_2O_3/SiO_2$).

Data in Figure 5.11 b shows that the decay constant (k_d) decreased with increasing metal particle size on Co/SiO_2 catalysts. For the case of catalysts reduced at 723K, the decay constant determined for $Co/BaO/SiO_2$ was close to the correlation of the dependency of decay constant

obtained for the Co/SiO_2 catalyst. However, the decay constants determined for $Co/La_2O_3/SiO_2$ and $Co/ZrO_2/SiO_2$ were dramatically higher than that obtained on the Co/SiO_2 catalyst. For the case of catalysts reduced at 923K, deactivation was observed only on $Co/ZrO_2/SiO_2$ catalyst, similar to the Co/SiO_2 catalysts as shown in Figure 5.11b. Also, the decay constant determined for $Co/ZrO_2/SiO_2$ catalyst was close to the correlation obtained on the Co/SiO_2 catalysts. For $Co/BaO/SiO_2$ and $Co/La_2O_3/SiO_2$ catalyst reduced at 923K (with metal particle size 30.8 and 27.7 nm respectively), stable catalyst activities were obtained at 773K during CH_4 decomposition, as shown in Figure 5.12.

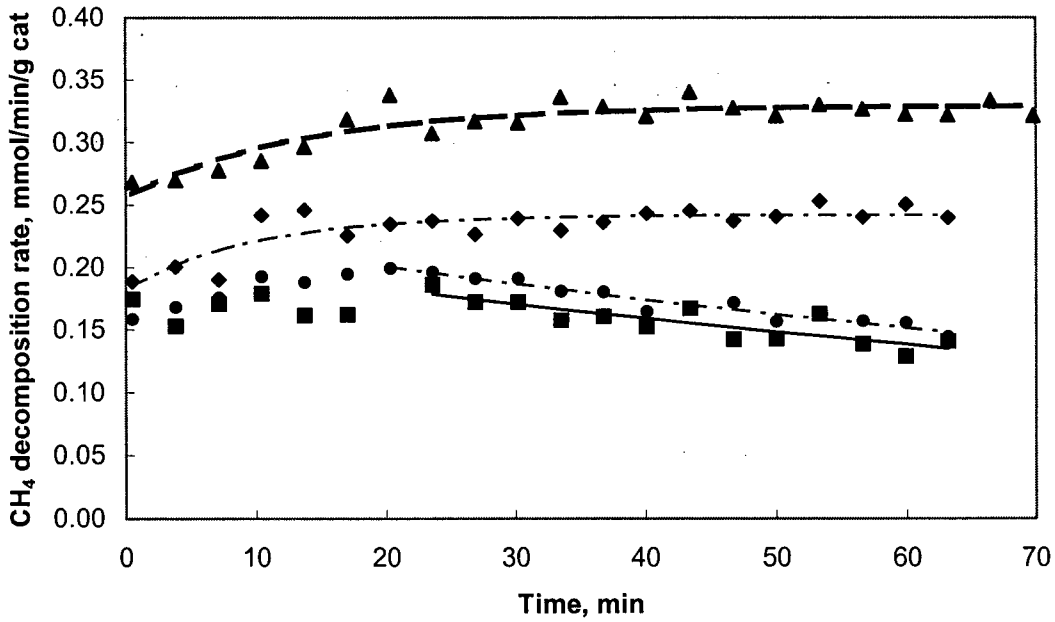

Figure. 5.12 Stable catalyst activity on modified Co catalysts. (■Co/SiO_2; ◆$Co/BaO/SiO_2$; •$Co/ZrO_2/SiO_2$; ▲$Co/La_2O_3/SiO_2$, Reduction 923K, Reaction 773K with $K_M = 0.06$ atm)

5.4.4 Effect of MSI on Catalyst Deactivation

The effect of a strong MSI on filamentous carbon formation has been reported to affect the deformation of the metal particle at the tip of the filament and also to influence the formation

of hollow or solid filaments (Snoeck et al., 1997a). In both cases, the effect is related to the strength by which the particle is held to the support. The present study suggests a third effect of the metal support interaction that leads to increased catalyst deactivation. According to the mechanism of carbon filament formation described in Chapter 4, the formation of encapsulating carbon can be ascribed to the imbalance between the rate of carbon formation and the rate of carbon removal from the metal surface. If carbon is not removed from the surface, then the active surface carbon transforms into inert, encapsulating graphitic carbon that causes deactivation. Carbon removal from the surface is a consequence of diffusion through the metal particle and excretion at the back of the particle to build graphitic layers and filaments. During this process, the metal particle is detached from the support surface. However, if the MSI is strong such that the excretion process is decreased, then the carbon removal rate will decrease significantly, resulting in a build up of encapsulating carbon and deactivation.

For the case of catalysts reduced at 723K, the data of the present study have shown that BaO had only a minor effect on the Co-support interaction, whereas the presence of La_2O_3 and ZrO_2 enhanced the MSI. Consequently, the expectation would be that the Co particle would be more difficult to detach from the La_2O_3 and ZrO_2 modified support surface and hence the carbon removal rate by filament formation would be decreased. As evidenced by the XPS data, described in Section 5.4.5, more graphitic carbon would therefore cover the surface of the catalyst and this would lead to increased deactivation. Conversely, it is easier to detach the metal particle from the support and balance the carbon formation and removal rates such that filament formation continues, in the case when the MSI is weaker, as was the case with the Co/SiO_2 and $Co/BaO/SiO_2$ catalysts. This expectation was indeed observed on the decay constant of catalyst reduced at 723K (Figure 5.11b).

Note that the catalysts used for activity measurements were reduced at 723K or 923K. The catalysts reduced at 723K yielded Co species that were not completely reduced and interacted with the support, whereas, for the catalysts reduced at 923K, more Co species interacting with the support could be reduced. Consequently, in the latter case, the correlation between decay constant and metal particle size, obtained with the Co/SiO_2 catalysts, was also followed by the $Co/ZrO_2/SiO_2$ catalyst, suggesting that the higher reduction temperature reduced the MSI and hence allowed carbon removal by filament formation. Stable catalyst activities were also obtained on $Co/BaO/SiO_2$ and $Co/La_2O_3/SiO_2$ reduced at 923K, a consequence of the large metal particle size of these catalysts (Figure 5.12).

5.4.5 Carbon Species on the Used Catalyst

Additional information about the carbon species on the catalyst surface was obtained by XPS analysis of the used catalysts. C 1s spectra on used, modified catalysts are shown in Figure 5.13. The spectra show that the shape and peak position of C 1s on $Co/BaO/SiO_2$ and $Co/La_2O_3/SiO_2$ catalysts are similar. The data also show that the line positions are shifted to low B.E. with a shoulder at low B.E. The data were fitted by two peaks at B.E. 283.4eV (carbidic carbon) and at 285eV (graphitic carbon). The relative concentration of carbon species with lower B.E. on the surface was estimated from the fitted peak area and is listed in Table 5.3. The decay constant determined for each catalyst is also listed in Table 5.3. Data in Table 5.3 show that the magnitude of k_d correlates inversely with the relative concentration of carbidic carbon observed on the used catalyst surface. For the $Co/ZrO_2/SiO_2$ catalyst, only graphitic carbon was detected corresponding to a high decay constant, $100k_d = 15.3\,\text{min}^{-1}$, as indicated in Table 5.3. For $Co/La_2O_3/SiO_2$ catalyst, 34% of the carbon was carbidic and the decay constant decreased, $100k_d = 7.7\ \text{min}^{-1}$. For the $Co/BaO/SiO_2$ catalyst, 66% of the carbon was carbidic and the decay

constant decreased further to $100k_d = 2.2\ \text{min}^{-1}$. Hence the more carbidic carbon on the catalyst surface, the lower the rate of catalyst deactivation.

According to the catalyst deactivation mechanism discussed in Chapter 4, there are two kinds of carbon on the catalyst surface: single carbon atoms which can diffuse through metal particle and encapsulating carbon which encapsulates the catalyst surface and deactivates the catalyst. Consequently, the carbidic carbon detected by XPS at low B.E. can be ascribed to the single carbon atoms that can diffuse through the metal particle. The graphitic carbon with higher B.E. can be ascribed to the encapsulating carbon that deactivates the catalyst. The competition between the filamentous carbon that is formed from the single C atoms that have diffused through the metal particle and the encapsulating carbon determine whether catalyst deactivation or stable catalyst activity is observed. Accordingly, the deactivation mechanism can explain the correlation of the magnitude of $100k_d$ with the relative concentration of carbidic carbon observed on the used catalyst surface: the more inert carbon that exists on the catalyst surface, the higher the decay constant. The distribution of carbon species confirmed that the competition between the encapsulating carbon and the filamentous carbon determines the rate of catalyst deactivation. Consequently, different carbon species, carbidic carbon or graphitic carbon dominates on the catalyst surface. For example, on $Co/ZrO_2/SiO_2$ reduced at 723K, the resistance to carbon diffusion is high because of the strong MSI. Consequently a very high decay constant results with more graphitic carbon residing on the catalyst surface.

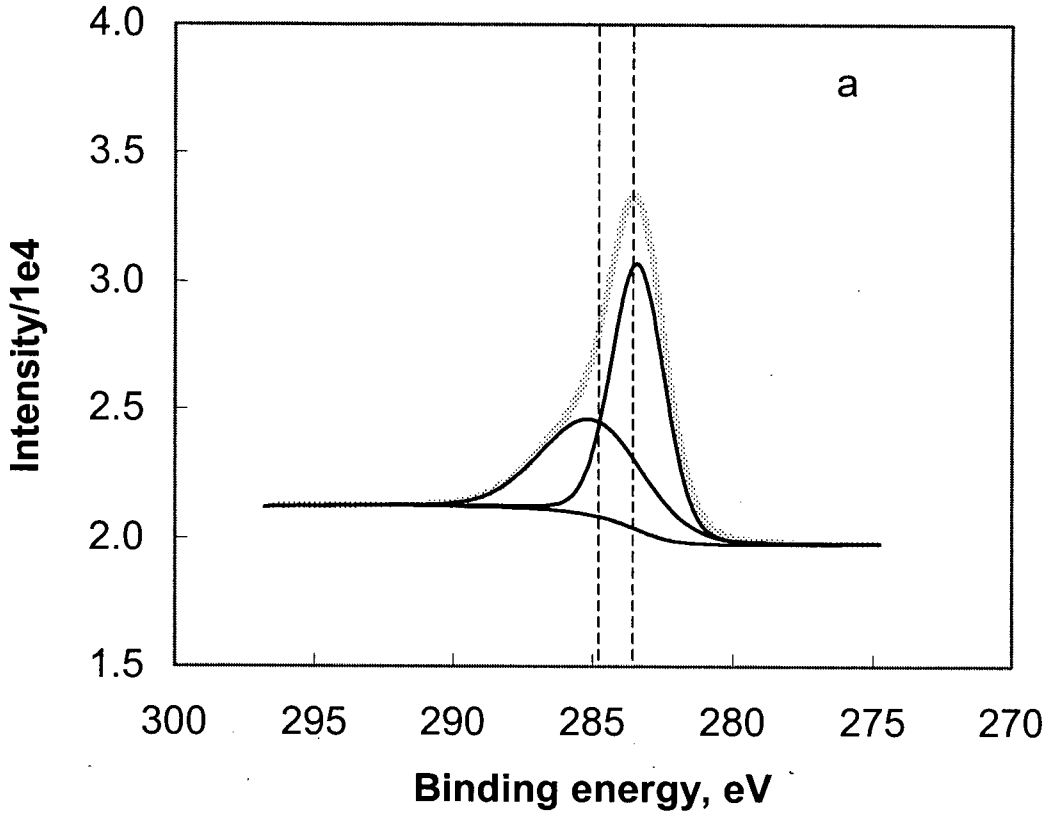
a
Intensity/1e4
4.0
3.5
3.0
2.5
2.0
1.5
300
295
290
285
280
275
270
Binding energy, eV

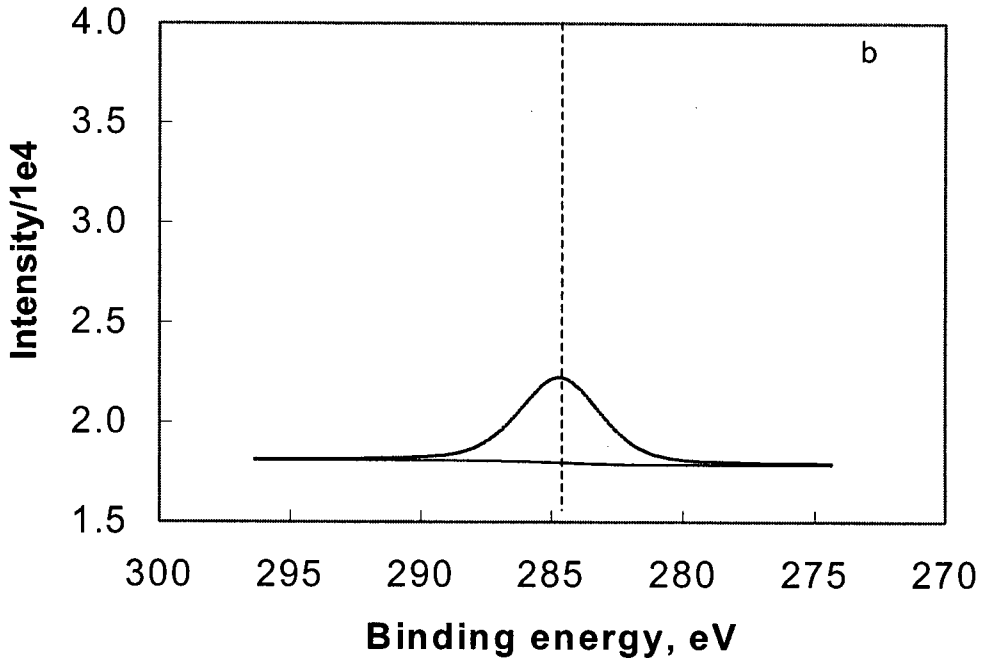
b
Intensity/1e4
4.0
3.5
3.0
2.5
2.0
1.5
300
295
290
285
280
275
270
Binding energy, eV

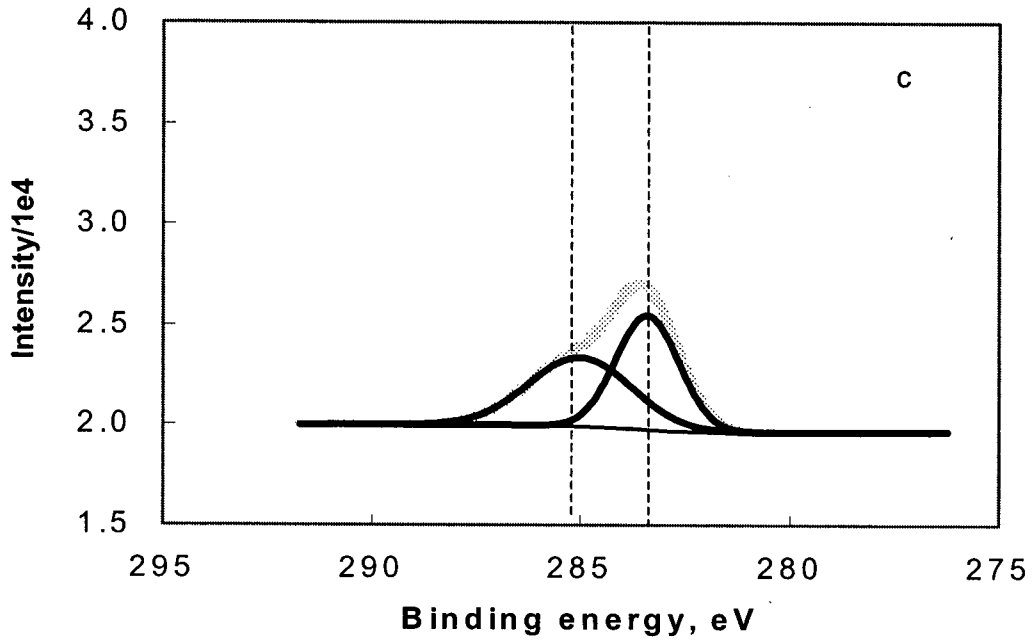

Figure 5.13 XPS spectra of C 1s on used catalysts surface. a: $Co/BaO/SiO_2$; b: $Co/ZrO_2/SiO_2$; c: $Co/La_2O_3/SiO_2$.

Table 5.3 Carbon species on the used catalysts surface from XPS measurement.

Used catalysts	C 1s 283.4eV/(285eV+283.4eV) %	Decay constant, 100 k_d 1/min
$Co/BaO/SiO_2$ after Reaction	66	2.2
$Co/ZrO_2/SiO_2$ after Reaction	0 (284.7eV)	15.3
$Co/La_2O_3/SiO_2$ after Reaction	34	7.7

5.5 Summary

The structure sensitivity of activity has been observed on the low loading Co and Ni catalysts during CH_4 decomposition: the maximum decomposition activity increased with increasing metal particle size (decreasing metal dispersion) and the decay constant decreased with increasing metal particle size (decreasing metal dispersion).

The coking threshold K_M^* obtained on Co/SiO_2 with different loading in the present study followed the linear relationship of K_M^* versus the reciprocal of the average metal particle size. A filamentous carbon formation threshold, K_M^f, has also been defined as the value of $K_M = P_{H_2}^2 / P_{CH_4}$ corresponding to the formation of filamentous carbon at a particular temperature. The difference between the coking threshold, K_M^*, and the filamentous carbon formation threshold, K_M^f, increased with the increasing metal particle size, consistent with the observation that it was easier to obtain stable activity with filamentous carbon formation on the catalyst with larger metal particle size under the same gas phase composition, K_M, and temperature.

The effect of BaO, La_2O_3 and ZrO_2, added to the SiO_2 support of Co catalysts, has also been investigated. The effect of the modified support on the catalyst reduction behaviour, dispersion and MSI was studied by TPR, XPS and CO chemisorption. The results suggest an increasing MSI among the catalysts in the order $Co/SiO_2 \approx Co/BaO/SiO_2 < Co/La_2O_3/SiO_2 < Co/ZrO_2/SiO_2$. The rate of catalyst deactivation was affected by the modified support: increased deactivation corresponded to an increased MSI. It is suggested that the latter observation is a consequence of the Co particle being held more strongly to the support, such that filament formation is reduced, which in turn results in an increase in the formation of encapsulating carbon and hence deactivation.

XPS analysis of carbon species on the used catalyst identified the presence of carbidic carbon, ascribed to single carbon atoms that diffuse through the metal particle and form filamentous carbon, and graphitic carbon, ascribed to encapsulating carbon that deactivated the catalyst. The competition between filamentous carbon formation and encapsulating carbon formation determined the rate of deactivation. Data presented herein demonstrate a correlation

between the magnitude of the catalyst decay constant and the relative concentration of carbidic carbon on the catalyst surface.

Chapter 6 Kinetic Model

6.1 Introduction

In the present study, catalyst activity-versus-time profiles have been measured on different catalysts for CH_4 decomposition. In general, the profiles have a period of initial increasing activity followed by a period of either stable activity or decreasing activity, and the profiles depend on the catalyst and process conditions. From the point of view of the catalyst, as described in Section 5.2, stable catalyst activity was obtained on Co catalysts with a large metal particle size (>26 nm). Catalyst deactivation after an initial rate increase was observed on catalysts with a small metal particle size (<26 nm). From the point view of process conditions, as described in Section 4.2, stable catalyst activity was observed when the condition $K_M^f < K_M < K_M^*$ was satisfied. On the other hand deactivation after an initial rate increase was observed when the condition $K_M < K_M^f < K_M^*$ was satisfied.

In Chapter 2, the generally accepted mechanistic steps of carbon nanofibre growth were described as: carbon atom deposition on the exposed surface of the metal catalyst; dissolution of the carbon atom and diffusion through the metal particle and finally precipitation at the back of the metal particle. However, the initial growth mechanism, corresponding to the observed zone of increasing activity, was ignored. Recently, in a review of carbon nanofibres by De Jone and co-workers (2000), it was pointed out that this generally accepted mechanism rationalized the steady-state growth of carbon nanofibres but it did not touch upon the important question of nucleation. Some speculation about carbon nucleation has been made by Snoeck and co-workers (1997a). They proposed that the dependence of the number of growing filaments on the affinity of carbon formation must be taken into account when modeling the kinetics of filamentous carbon formation. Hence, in their study the mode of experimentation, performed with used

catalysts on which carbon was previously deposited under standard conditions, ensured that the rate of growth of the carbon filaments was always based on the same number of filaments. However, to date no kinetic model has been reported for filamentous carbon formation during catalytic hydrocarbon decomposition that includes the nucleation step. On the other hand, models have been developed for carbon nanotube and diamond production during the CVD process that addressed the issue of carbon nucleation. In the present study, an initial rate increase period was observed during the initial 2-5 min of the start of the CH_4 decomposition reaction. Hence, it is necessary to include carbon nucleation and growth into the existing mechanism for carbon filament formation.

Furthermore, as described in Chapter 2, the kinetic model developed for catalytic filament formation describes only the steady growth of filamentous carbon. For the case of decreasing activity, only an empirical model exists. Based on the experimental observations of the present study, a more general kinetic model of CH_4 decomposition has to be developed, in which two important features are incorporated. The first is that carbon nucleation at the interface of the metal and support be considered in order to describe the initial rate increase observed during CH_4 decomposition; the second is that the competition between encapsulating carbon formation and carbon dissolution/diffusion on the surface of catalyst be considered to account for catalyst deactivation.

6.2 Description of the Kinetic Model

6.2.1 Terminology and Assumptions

6.2.1.1 Terminology

Some terminology needs to be defined before describing the kinetic model. Site density, is defined as the number of atomic sites per unit surface area, with units $1/cm^2$; the leading face

refers to the interface between the metal and gas phase, where single carbon atoms are formed by the reversible reaction $CH_4 \leftrightarrow C + 2H_2$; the tailing face refers to the interface between the metal and support, where the single carbon atom is excreted from the metal particle and nucleates with other carbon atoms. On the leading face, two kinds of carbon species exist: atomic carbon and encapsulating carbon: n_s, site density of single carbon atom on the leading face; n_p, site density of encapsulating carbon on the leading face. On the tailing face, three kinds of carbon species exist each with different site density as follows: n_1, site density of single carbon atom on the tailing face; n_i, site density of critical cluster on the tailing face; n_x, site density of stable cluster on the tailing face. Assuming that small clusters containing j atoms with surface concentration $n_j(t)$ may grow or decay, the growth becomes more probable than decay when the cluster size exceeds the critical number i. A critical cluster is a cluster of carbon atoms with a certain critical number i. Stable clusters are all larger clusters than the critical cluster and are considered to be stable. They may form nuclei even if some atoms leave during the subsequent growth. Note that n_{CT} of Figure 6.1 is the site density of carbon in the carbon tubes of the metal particle on the tailing face. n_{CT} is used for Model II, which will be described in Section 6.2.4.2.

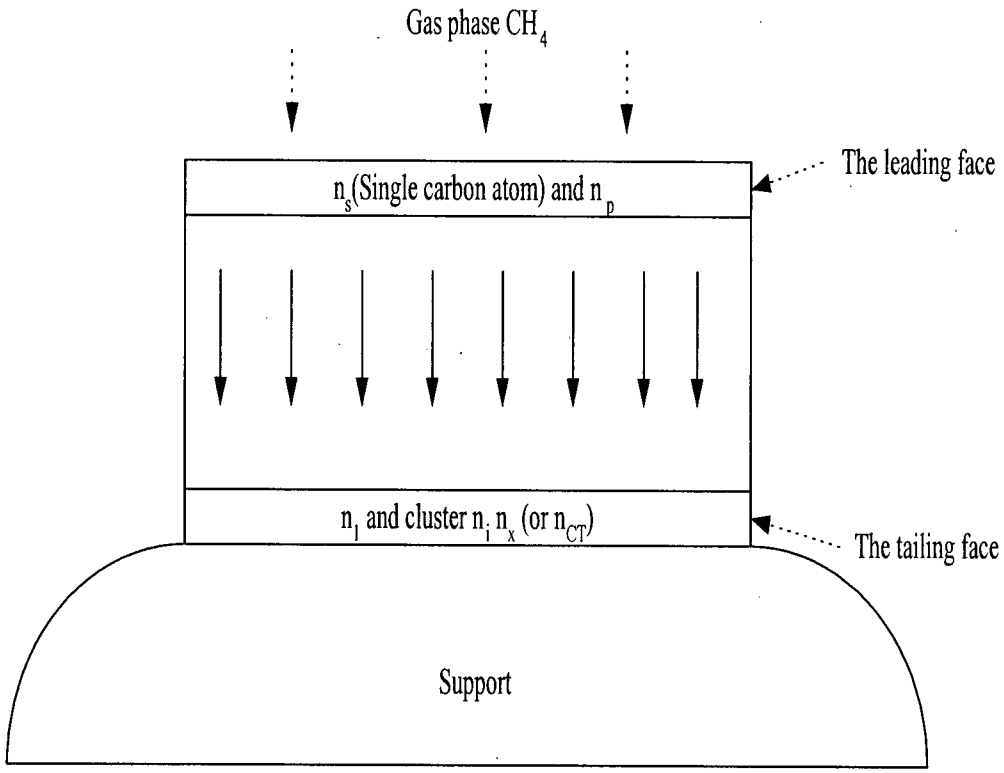

Figure 6.1 Schematic drawing of general kinetic model.

6.2.2.2 Model Assumptions

A one dimensional diffusion model was used to describe the diffusion of carbon through the metal particle. The choice was based on the results from a study of a two-dimensional model (Chitrapu et al., 1992) showing that the 2-D model was not significantly better than that obtained from a one-dimensional approximation of carbon filament formation, and that the two-dimensional model required significantly more computational effort. In the present study, the Co metal particle supported on SiO_2 was approximated as a metal slab as shown in Figure 6.1. The sides of the catalyst slab were assumed not to participate in the excretion of carbon, and hence, it was assumed that the flux of carbon in the radial direction was zero. The driving force for carbon diffusion was through the concentration gradient of single carbon atoms through the particle.

There was a uniform diffusion path length, $(2/3)d_p$. It was also assumed that all single carbon atoms had the same opportunity to nucleate. The structure of the nanofibres produced was not considered.

6.2.2 General Description of the Kinetic Model

The model is shown schematically in Figure 6.1. The model assumed that single carbon atoms were formed by CH_4 stepwise dehydrogenation at the leading face. When a single carbon atom was formed on the leading face of the metal catalyst particle, it reacted through two parallel paths: a) it diffused through the metal particle and subsequently nucleated and grew at the tailing face of the metal particle; or b) it formed encapsulating carbon and it was assumed that the encapsulating carbon could not be gasified in H_2; the number of active metal sites on the surface decreased due to the formation of encapsulating carbon and consequently, the catalyst deactivated. Hence single carbon atom diffusion through the metal slab was described using a one-dimensional model. At the leading face, stepwise dehydrogenation and encapsulating carbon formation were considered. At the tailing face, carbon nucleation and growth were considered.

The interstitial diffusion of carbon through the metal particle was described by the unsteady state diffusion equation, which was the main equation of the kinetic model:

$$\frac{\partial n_C}{\partial t} = D_s \frac{\partial^2 n_C}{\partial x^2} \tag{6.1}$$

Initial condition:

$$n_C\big|_{x=0\sim(2/3)d_p} = 0 \qquad \text{at t=0 for all x;} \tag{6.2}$$

Boundary conditions:

$$\left.\frac{dn_C}{dt}\right|_{x=0} = (r_f - r_g) - r_d - r_e \qquad \text{at } x=0 \text{ (the leading face), t>0;} \tag{6.3}$$

$$\left.\frac{dn_C}{dt}\right|_{x=(2/3)d_p} = r_d^{'} - r_{nucl} - r_{growth} \qquad \text{at } x=(2/3)d_p \text{ (the tailing face), t>0; (6.4)}$$

where

$n_c(t,x)$	Site density of single carbon atom in the metal particle, 1/cm^2;
t	Time-on-stream, s;
x	Length in the carbon diffusion direction, cm;
D_s	Diffusivity of carbon in the metal particle, cm^2/s;
d_p	Average metal particle diameter, cm;
r_f	Carbon deposition rate, 1/cm^2/s;
r_g	Carbon gasification rate, 1/cm^2/s;
$(r_f - r_g)$	Measured methane decomposition rate, 1/cm^2/s;
r_e	Encapsulating carbon formation rate, 1/cm^2/s;
r_d	Carbon diffusion rate leaving the leading face of the metal particle, 1/cm^2/s;
$r_d^{'}$	The incoming carbon diffusion rate to the tailing face of the metal particle, 1/cm^2/s;
r_{growth}	Carbon growth rate on the tailing face, 1/cm^2/s;
r_{nucl}	Carbon nucleation rate on the tailing face, 1/cm^2/s;

The initial condition is described by Equation (6.2) and the two boundary conditions are described by Equation (6.3) and (6.4). Equation (6.2) describes the initial condition that the site density of single carbon atoms is zero along the metal slab at time zero. Boundary condition (6.3) describes the site balance at the leading face at any reaction time. The site balance requires that the site density change of single carbon atoms is equal to the net carbon formation rate from CH_4 stepwise dehydrogenation and gasification ($CH_4 \leftrightarrow C + 2H_2$), minus the net carbon consumption rate determined by the encapsulating carbon formation rate and the carbon diffusion rate. It was critical to include an encapsulating carbon formation step in the boundary condition at the leading face to account for the catalyst deactivation because encapsulating

carbon cannot be gasified by H_2. The other boundary condition Equation (6.4), describes the site density balance at the tailing face. This site balance required that the site density change of single carbon atoms is equal to the incoming diffusion rate from the leading face minus the single carbon consumption rate by carbon nucleation and carbon growth. In the present study, two methods used for carbon nucleation and growth on the surface of metal substrates in CVD processes were modified to describe the carbon nucleation and excretion rate at the tailing face. The detailed description is presented in Section 6.2.4.

The above system of 2nd order partial differential equations combined with algebraic equations, consisting of the site balance equations at the leading face and tailing face have been resolved without assuming any RDS. The unsteady state diffusion equation was solved using the finite volume method. By fitting experimental CH_4 decomposition rate data to the model, parameters such as bulk carbon diffusivity D_s, surface carbon diffusivity D_1, and reaction rate constant for carbon formation k_f, gasification k_g and encapsulating carbon formation k_{encap}, were estimated. The Marquardt's compromise methodology was used for the parameter estimation. The kinetic model allowed the carbon concentration profile in the metal to be developed as a function of time, to show the changes of the driving force for carbon diffusion.

6.2.3 Description of the Boundary Conditions at the Leading Face

Equation (6.3) shows the general description of the balance of single carbon atoms on the leading face. According to the overall mechanism, reactions including CH_4 dehydrogenation, carbon gasification, and formation of encapsulating carbon were considered at the leading face.

In order to describe the net rate of carbon deposition, $(r_f - r_g)$, the following elementary steps in Equation (6.5) to (6.9) were used to describe the stepwise dehydrogenation of CH_4. Since the activation energy for the activation of gas phase CH_4 ($CH_4 + 2S \rightarrow CH_3S + HS$, where S

represents an active catalyst site) is less than that of adsorbed CH_4 ($CH_4S + S \rightarrow CH_3S + HS$) over Group VIII metal catalysts (Shustorovich and Bell, 1991), it is reasonable to assume that the first step of the CH_4 decomposition can be written according to Equation (6.5).

$$CH_4 + 2S \leftrightarrow CH_3S + HS \tag{6.5}$$

$$CH_3S + S \leftrightarrow CH_2S + HS \tag{6.6}$$

$$CH_2S + S \leftrightarrow CHS + HS \tag{6.7}$$

$$CHS + S \leftrightarrow CS + HS \tag{6.8}$$

$$2HS \xleftrightarrow{K_H} 2S + H_2 \tag{6.9}$$

Assuming that the rate of Equation (6.5) was slow, the reaction of Equation (6.9) was assumed at equilibrium with equilibrium constant K_H. Hence the concentration of HS can be expressed by Equation (6.11) obtained from Equation (6.10).

$$K_H = \frac{P_{H_2}[S]^2}{[HS]^2} \tag{6.10}$$

$$[HS] = \frac{1}{K_H^{1/2}} P_{H_2}^{1/2}[S] \tag{6.11}$$

Since Equation (6.5) is slow, the reaction steps of Equation (6.6) to (6.8) were lumped together into the reaction of Equation (6.12), which was also assumed to be at equilibrium with equilibrium constant K_{CH_3}. Hence, the concentration of CH_3S was expressed by Equation (6.15), obtained from Equation (6.12) by substitution of Equation (6.11) into Equation (6.14).

$$CH_3S + 3S \xleftrightarrow{K_{CH_3}} CS + 3HS \tag{6.12}$$

$$K_{CH_3} = \frac{[HS]^3[CS]}{[CH_3S][S]^3} \tag{6.13}$$

$$[CH_3S] = \frac{1}{K_{CH_3}} \frac{[HS]^3[CS]}{[S]^3} \tag{6.14}$$

$$[CH_3S] = \frac{1}{K_{CH_3} K_H^{3/2}} P_{H_2}^{3/2} [CS] \tag{6.15}$$

According to the reaction of Equation (6.5), the net rate of carbon deposition, $(r_f - r_g)$, is described by Equation (6.16). Hence, the net rate of carbon deposition Equation (6.17) was obtained by substitution of Equation (6.11) and (6.15) into Equation (6.16).

$$r_f - r_g = k_f P_{CH_4} [S]^2 - k_r [CH_3S][HS] \tag{6.16}$$

$$r_f - r_g = k_f P_{CH_4} [S]^2 - k_r \frac{1}{K_{CH_3} K_H^2} P_{H_2}^2 [S][CS] = k_f P_{CH_4} [S]^2 - k_g P_{H_2}^2 [S][CS] \tag{6.17}$$

The ensemble size associated with the formation of encapsulating carbon was assumed to be 6 carbon atoms, as described in Chapter 4. The encapsulating carbon formation rate was described by Equation (4.2) and Equation (4.3). The carbon diffusion rate at the leading face was described by Equation (6.18):

$$r_d = D_s \left. \frac{\partial (n_c / dx)}{\partial x} \right|_{x=0} \tag{6.18}$$

Finally the boundary condition at the leading face at t>0 was expressed by Equation (6.19):

$$\left. \frac{dn_C}{dt} \right|_{x=0} = \left. \frac{dn_s}{dt} \right|_{x=0} = (r_f - r_g) - r_d - r_e = k_f P_{CH_4} [S]^2 - k_g P_{H_2}^2 [S][CS] - D_s \left. \frac{\partial (n_C / dx)}{\partial x} \right|_{x=0} - k_{encap} n_s^6 \tag{6.19}$$

The site conservation described by Equation (6.20) was used to calculate the site density of [CS]. Assuming the concentration of HS and CH_3S is small, the site conservation Equation (6.20) was simplified into Equation (6.21).

$$[Sv]+[CS]+[CH_3S]+[HS]+[C_pS]=[Sv_0] \tag{6.20}$$

$$[Sv]+[CS]+[C_pS]=[Sv_0] \tag{6.21}$$

Assuming that the encapsulating carbon occupied the same site as the single carbon atom, the change in number of active sites was described as:

$$\frac{dS_v}{dt}=-(r_f-r_g)+r_d \tag{6.22}$$

and change in sites occupied by encapsulating carbon was described as:

$$\frac{d[C_pS]}{dt}=k_{encap}n_s^6 \tag{6.23}$$

6.2.4 Description of the Boundary Conditions at the Tailing Face

Two models were used to describe the boundary conditions at the tailing face and they are described in detail in the following Section.

6.2.4.1 Description of Kinetic Model I (Cluster Nucleation Model)

The Model I (Cluster nucleation model) describing the boundary conditions at the tailing face is derived from the nucleation model for CVD processes (Liu and Dandy, 1996). The basic idea of the nucleation model is that small clusters containing j atoms with surface concentration $n_j(t)$ may grow or decay, the growth becomes more probable than decay when the cluster size exceeds the critical number i. All larger clusters were therefore considered to be stable and hence may form nuclei, even if some atoms leave during the subsequent growth. Based on the model for CVD processes (Liu and Dandy, 1996), the induction period of carbon growth was described as: initially, atomic carbon with site density n_s ($1/cm^2$) deposited on the metal surface from stepwise CH_4 dehydrogenation, then diffused through the metal particle with diffusivity D_s and at the tailing face of the metal particle, the single carbon atom $n_1(t)$ diffused over the tailing

face with diffusivity D_1. This surface diffusion led to the formation and growth of clusters. Assuming small clusters containing j atoms with surface concentration $n_j(t)$ may grow or decay, growth becomes more probable than decay when the cluster size exceeds a certain critical size i. All larger clusters were therefore considered to be stable and hence may form nuclei. The rate of critical cluster growth depended on the rate at which single carbon atoms attached to them. The concentration of stable clusters, $n_x(t)$ increased with time.

The capture number terms, σ_i and σ_x, describe the diffusion flows of single atoms to critical clusters or stable clusters, and have been described in the relevant literature (Liu and Dandy, 1996). The capture numbers were assumed to be slowly varying quantities, with σ_i and σ_x in the range from 2 to 4 and 5 to 10, respectively (Liu and Dandy, 1996). Herein, σ_i and σ_x were assumed to be 4 and 5, respectively. The critical size i of the critical cluster was taken as 10. The surface diffusion coefficient of single atoms was expressed as D_1.

The surface concentration of single carbon atoms, n_1, was expressed by the following mass balance equation at the tailing face:

$$\left.\frac{dn_C}{dt}\right|_{x=(2/3)d_p} = \frac{dn_1}{dt} = r_d' - r_{nucl} - r_{growth} = r_d' - \sigma_x D_1 n_1 n_x - (i+1)N_r \tag{6.24}$$

The term, $\sigma_x D_1 n_1 n_x$, describes the rate of single carbon atom addition to the stable cluster n_x. The term, $(i+1)N_r$, describes the nucleation rate of single carbon atoms into critical clusters that then grow into stable clusters. The term, r_d', describes the rate of impingement of single carbon atoms from the leading face of metal particle via the bulk diffusion of interstitially dissolved carbon in metal particle as given by Equation (6.25)

$$r_d' = D_s \left. \frac{\partial (n_c / dx)}{\partial x} \right|_{x=(2/3)dp} \tag{6.25}$$

Equation (6.26) and (6.27) describe the probability of single carbon atom growth and the calculation of critical cluster site density on the tailing face. Equation (6.28) describes the growth rate of critical clusters into stable clusters.

$$n_i = \begin{vmatrix} 1/2n_1 (xstable - i) & xstable > i \\ 0 & xstable < i \end{vmatrix} \tag{6.26}$$

where $$xstable = \sigma_i D_1 \int_0^t n_1(t)\,dt \tag{6.27}$$

$$N_r = \frac{dn_x}{dt} = D_1 n_1 n_i \tag{6.28}$$

6.2.4.2 Description of Kinetic Model II (Boltzmann Nucleation Model)

The second method used in the present study to describe the boundary conditions at the tailing face is referred to as the Boltzmann nucleation model, which is modified from the atomic-scale analysis of CVD of carbon nanotubes (Grujicic et al., 2002). In the atomic-scale analysis of CVD of Carbon nanotubes (Grujicic et al., 2002), the carbon nucleation and carbon growth was described using elementary reaction steps, listed in Table 6.1. Similar to the Cluster Nucleation Model, C atoms with site density n_s (1/cm^2) deposit on the metal surface from the gas phase, diffuse through the metal particle with diffusivity D_s, and subsequently nucleate and grow at the tailing face.

Table 6.1 Activation energy of carbon nucleation steps.

Reaction I: Nucleation of the outer carbon tube wall	
n C(s)→n C(CT) n>10	E =149.4 kJ/mol
Reaction II: Growth of the outer carbon tube wall	
C(s)+n(CT)→ (n+1)C(CT)	E =128.7 kJ/mol

Reaction I states that when the number of nearest-neighbour carbon atoms reaches (or exceeds) a critical value, carbon atoms arrange themselves into a graphite-like structure to nucleate the outer wall of the carbon tube. The critical number of carbon atoms required for nucleation was assumed to be 10 and was assumed to be independent of processing conditions. The activation energy term, E, for nucleation, was taken from the work of Lee et al. (1999). The activation energy was estimated by subtracting an average energy of the ten adjacent single atoms from that for the ten corresponding atoms in the newly nucleated wall of the carbon tube. The nucleation reaction is assumed to be irreversible. Equation (6.29) describes the nucleation rate of a single carbon atom at the tailing face.

$$r_{nucl} = 10 k_{nucl} n_1^{10} \tag{6.29}$$

Reaction II describes the case when a single carbon atom is adjacent to a nucleus of a (non-innermost) wall of a carbon tube, it can attach to the nucleus giving rise to growth. An average value of the activation energy used herein was obtained from the work of Lee et al. (1999). The activation energy was estimated by subtracting the average energy of a single carbon atom from that for a carbon atom at the edge of a nucleus of the newly nucleated wall of a carbon tube. The growth process is also considered to be irreversible. Equation (6.30) describes the carbon growth rate and Equation (6.31) describes the changing rate of carbon nuclei.

$$r_{growth} = k_{growth} n_{CT} n_1 \tag{6.30}$$

$$\frac{d n_{CT}}{d t} = k_{nucl} n_1^{10} \tag{6.31}$$

Finally, the boundary condition at the tailing face was expressed as Equation (6.32), by substitution of Equation (6.25), Equation (6.29) and (6.30) into Equation (6.4)

$$\left.\frac{dn_C}{dt}\right|_{x=(2/3)d_p} = \frac{dn_1}{dt} = r_d^{'} - r_{nucl} - r_{growth} = D_s \left.\frac{\partial(n_C / dx)}{\partial x}\right|_{x=(2/3)d_p} - 10k_{nucl} n_1^{10} - k_{growth} n_{CT} n_1 \tag{6.32}$$

6.3 Kinetic Model I and Kinetic Model II Fit to Literature Data

Very few literature studies have reported the rate of reaction during the initial stage of carbon deposition during CH_4 decomposition or related reaction. Figure 6.2 shows experimental data during the initial stage of reaction and carbon deposition, reproduced from the literature (Sacco et al., 1984) for various reactants. All the experiments were performed with 6×6×0.25 mm polycrystalline Fe foil. Data in Figure 6.2 show the weight gain of a Fe foil versus time-on-stream for small time intervals during the initial 5 min of reaction. A set of carbon deposition rates was then estimated by differentiating the data of Figure 6.2. These rates are plotted in Figure 6.3, showing that the carbon deposition rate first decreased then increased to high carbon deposition rates for two of the three cases. In only one case was the initial rate decrease not obtained and those data are similar to the observations of the present study.

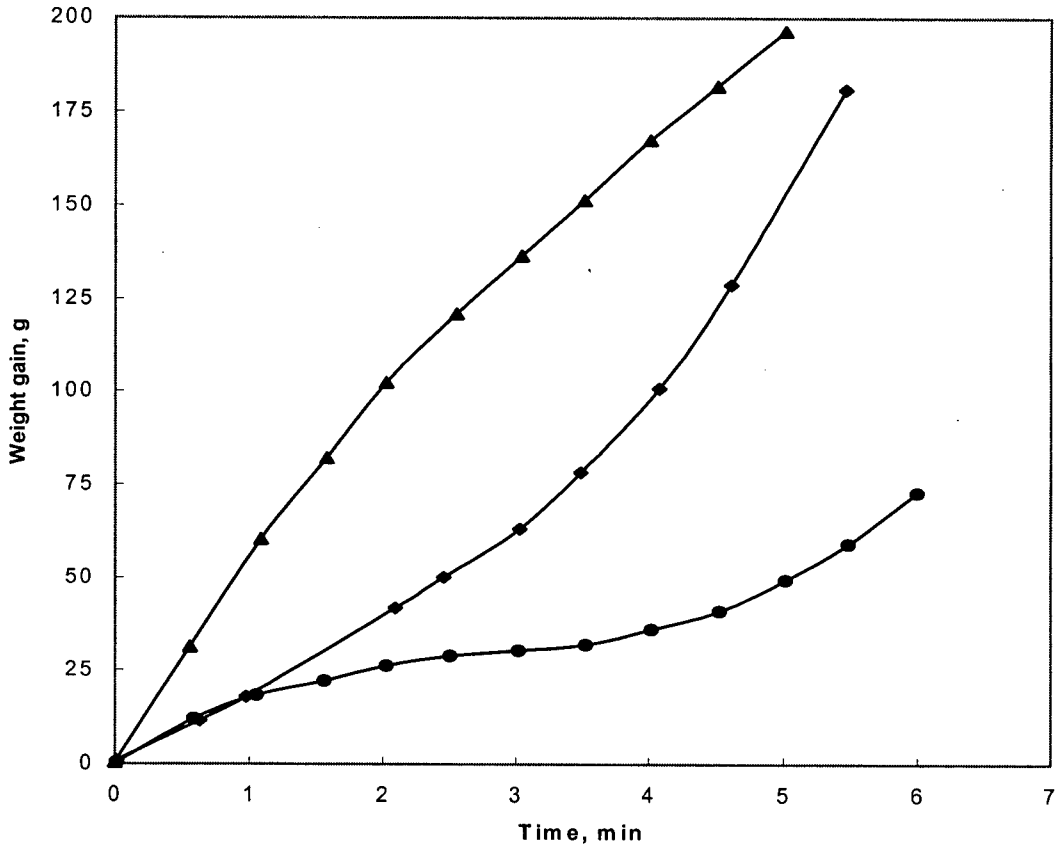

Figure 6.2 Initial weight gain versus time for various H_2, CO, CO_2, CH_4 and H_2O at 900K and 101kPa on Fe foil(▲ $P_{CO}P_{H_2} = 0.13\,\text{bar}^2$, $P_{CO_2}P_{CO}^2 = 0.21$ bar^3; ♦ $P_{CO}P_{H_2} = 0.12\,\text{bar}^2$, $P_{CO_2}P_{CO}^2 = 2.0\,\text{bar}^3$; ● $P_{CO}P_{H_2} = 0.06\,\text{bar}^2$, $P_{CO_2}P_{CO}^2 = 2.1$ bar^3).

The initial rate decrease followed by a rate increase shown in Figure 6.3 can be well explained by the proposed general kinetic model. The initial rate decrease corresponds to the initial unsteady state carbon diffusion stage of the reaction during which critical clusters have not yet formed. The diffusion rate decreases with time-on-stream because the single carbon atom accumulating at the tailing face has not yet been excreted and the driving force for diffusion, the difference in single carbon atom concentration between the leading and tailing face of the particle, decreases with time. As diffusion proceeds, the single carbon at the tailing face starts to nucleate, excrete and grow at the tailing face. During this period, the site density of single carbon atoms at the tailing face decreases and the driving force for the carbon diffusion increases. The

increased carbon deposition rate corresponds to the period of carbon nucleation. The reason that for one set of data in Figure 6.3 the initial rate decrease was absent might be because the carbon nucleation rate was high due to the high initial carbon deposition rate. Consequently, the carbon nucleation started earlier and was not detected. The observations made in the present study also correspond to this scenario.

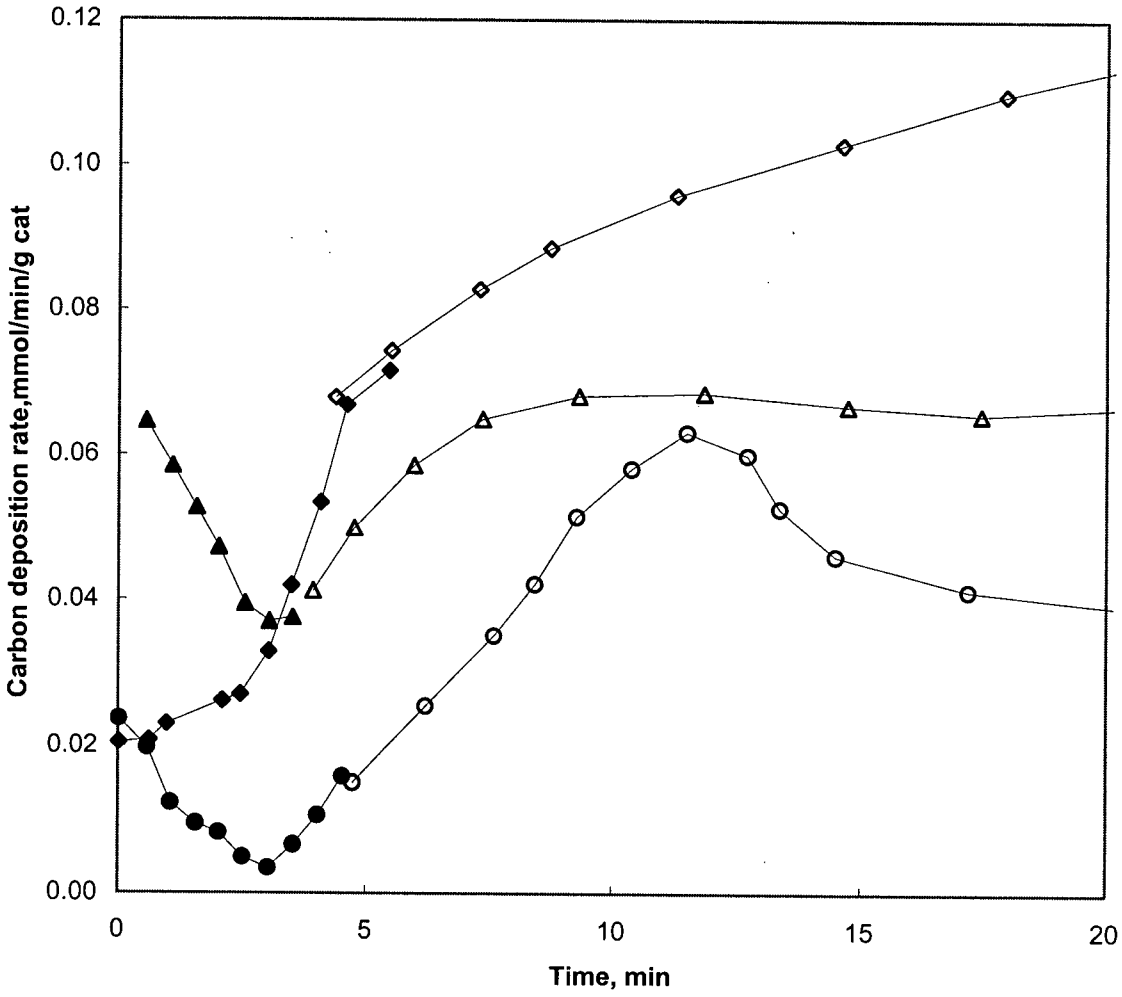

Figure 6.3 Carbon deposition rate versus time for various H_2 CO, CO_2, CH_4 and H_2O at 900K and 101kPa. (Filled symbol is for the initial period measured at small time interval; unfilled symbol is measured at the larger time interval; △ and ▲ $P_{CO}P_{H_2} = 0.13$ bar^2, $P_{CO_2}P_{CO}^2 = 0.21$ bar^3; ◇and◆ $P_{CO}P_{H_2} = 0.12$ bar^2, $P_{CO_2}P_{CO}^2 = 2.0$ bar^3; ○ and ● $P_{CO}P_{H_2} = 0.06$ bar^2, $P_{CO_2}P_{CO}^2 = 2.1$ bar^3).

In order to further check the proposed kinetic models, one set of data of Figure 6.3 with stable activity ($P_{CO}P_{H_2} = 0.13\,\text{bar}^2$, $P_{CO_2}P_{CO}^2 = 0.21$ bar^3) was selected and fitted to the two kinetic models Kinetic Model I and Kinetic Model II, described in Section 6.2. Note that because of the complexity of the gas phase composition, the kinetics of the carbon deposition and gasification surface reactions are not included in these models. Rather, it is assumed that there is no change in n_s during the reaction. To simplify, encapsulating carbon formation is assumed neglected on the leading face. (Also note that x refers to the direction of the depth of the Fe foil.) Model parameters were estimated using Marquart's Compromise with an initial guess of parameters. The computer code used to perform the numerical calculations is listed in Appendix F. The fitted parameters are listed in Table 6.2. From the model fitting, the site density profiles along the depth of Fe foil were obtained and the changes in site density for different carbon clusters were also obtained. The fitting results of Kinetic Model I and Kinetic Model II are presented in Figure 6.4 and Figure 6.5.

Table 6.2 Parameters from the kinetic models fit to the data for the initial stage of carbon deposition.

	$n_s \times 10^{-17}$	$D_S \times 10^6$	$D_1 \times 10^{20}$		R^2	F-value
	1/cm^2	cm^{2}s^{-1}	cm^{2}s^{-1}			
Model I	6.635±0.04	2.660±0.02	7.699±0.02		0.69	14.6
Model II	7.812±0.020	3.861±0.010	$k_{nucl} \times 10^{175}$, cm^{18}s^{-1}	$k_{growth} \times 10^{-10}$, cm^{2}s^{-1}	0.37	2.3
			3.486±0.014	4.786±0.020		

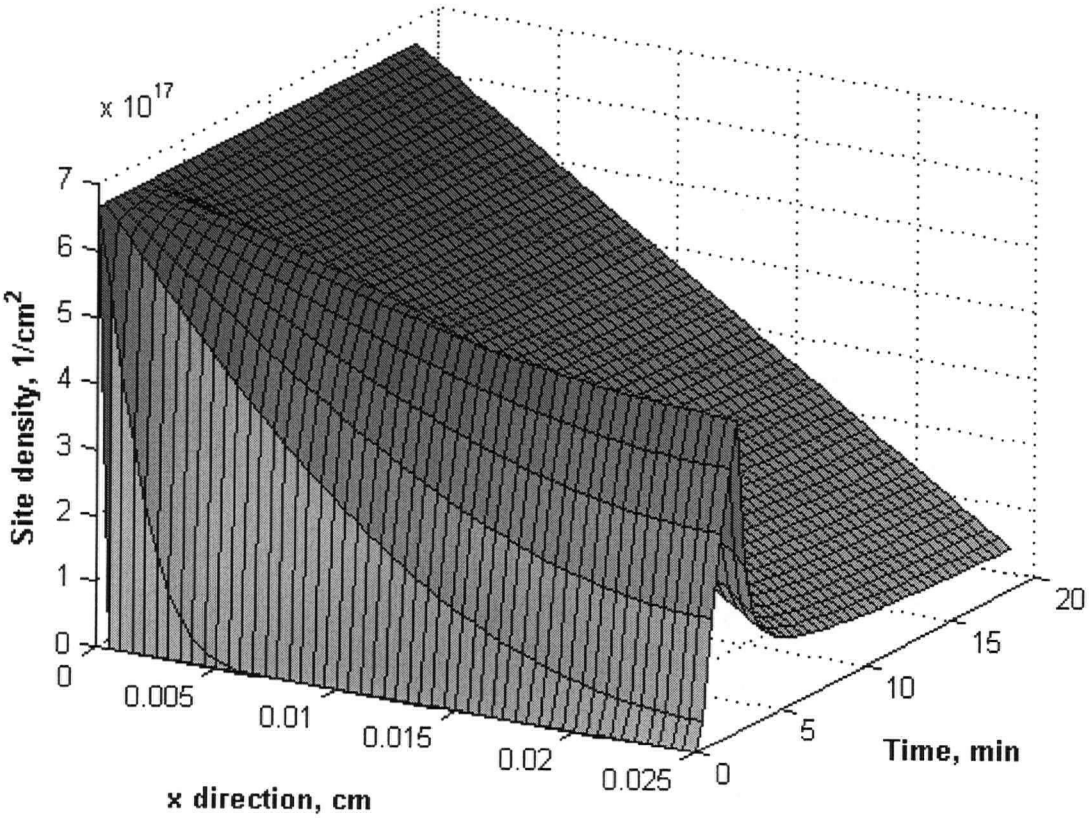

Figure 6.4a Single carbon atom profile along the depth of Fe foil obtained by fitting literature data to the Kinetic Model I.

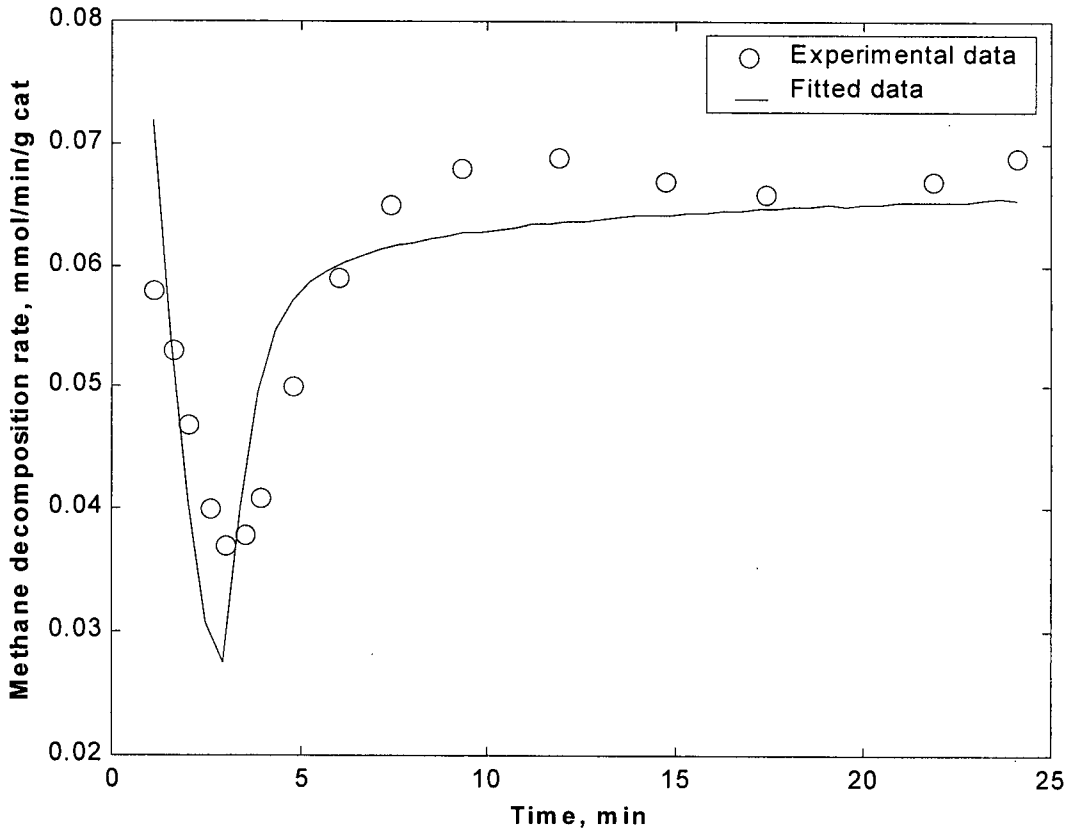

Figure 6.4b Carbon deposition rate obtained by fitting literature data to the Kinetic Model I.

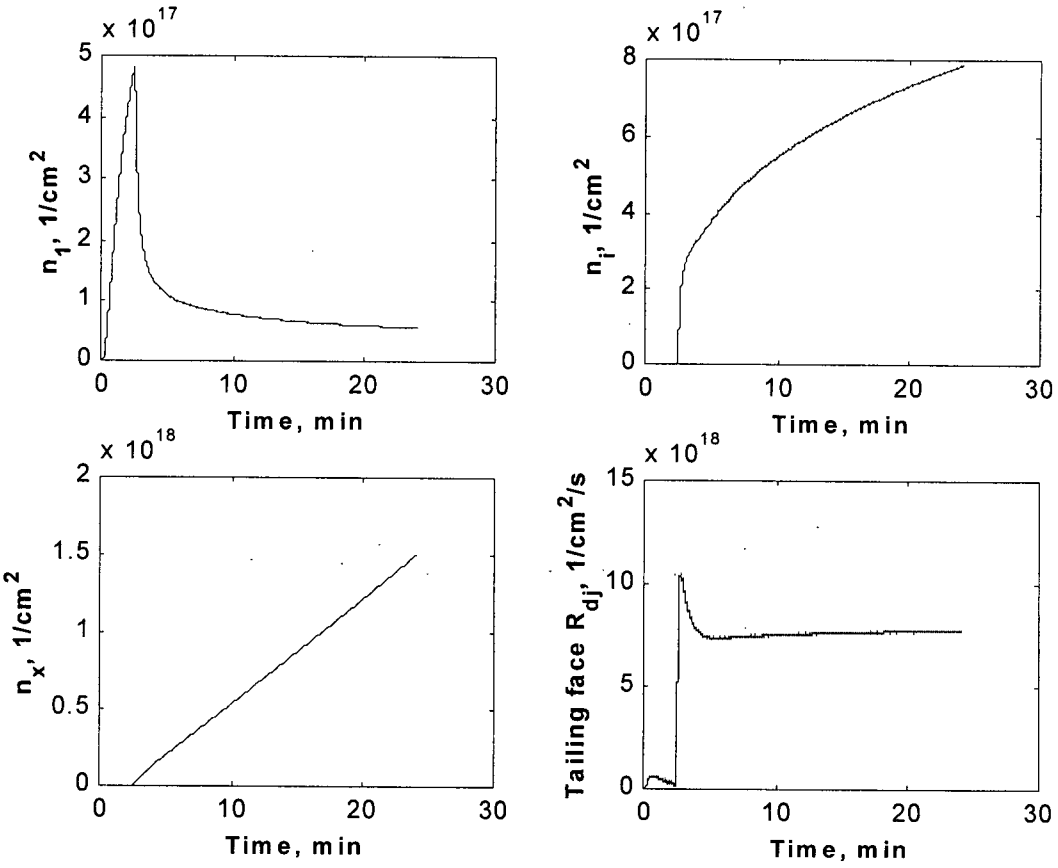

Figure 6.4c Site density changes as a function of time-on-stream obtained by fitting literature data to the Kinetic Model I.

Figures 6.4a, b and c show the literature results fitted to the Kinetic Model I. Figure 6.4a shows the change in single carbon atom site density along the depth of Fe foil with time-on-stream. The profile of single carbon atom site density was very steep at the very beginning of the reaction. The profile then levelled off since the diffusion driving force decreased when single carbon atoms accumulated at the tailing face. The profile then became steep again due to an increased driving force for diffusion since the single carbon atom site density decreased as the carbon nucleation and growth at the tailing face occured. Finally, the profile stabilized corresponding to stable carbon growth at the tailing face. Figure 6.4b shows the fitted carbon deposition rate on the Fe foil had three stages with respect to time-on-stream: an initial rate

decrease, a rate increase and a stable rate consistent with the profile changes described in Figure 6.4a. The period corresponding to an initial rate decrease is associated with the unsteady state carbon diffusion, with single carbon atoms accumulating at the tailing face of the particle. The period of rate increase corresponds to carbon nucleation. The final, stable carbon deposition rate corresponds to the steady growth of carbon. Data in Figure 6.4c shows the changes in n_1, n_i, and n_x with time-on-stream and the carbon diffusion rate at the tailing face. The profile of n_1 also shows three stages: an initially increase, a decrease and a constant value. The profile of n_i also shows three stages: an initial stage when n_i is equal to zero, a sharp increase and then a steady increase. The profile of n_x shows two stages: initial equal to zero, then steady increases. The profile of carbon diffusion rate at the tailing face shows an initial low rate followed by a rapid increase and then a decrease to a stable value. The three stages were therefore assigned as: Stage (i): corresponding to the unsteady state diffusion, n_1 increases and n_i, and n_x are equal to zero since single carbon atoms are accumulating on the tailing face and have not yet nucleated into carbon clusters. Consequently, the carbon diffusion rate at the tailing face is low; Stage (ii): carbon nucleation and growth have begun. Then n_1 decreases, while n_i, and n_x increase. Consequently, the carbon diffusion rate increases since the driving force for diffusion increased. Stage (iii): Carbon nucleation and growth at the tailing face reach a steady value and the carbon diffusion rate at the tailing face decreases to a stable level.

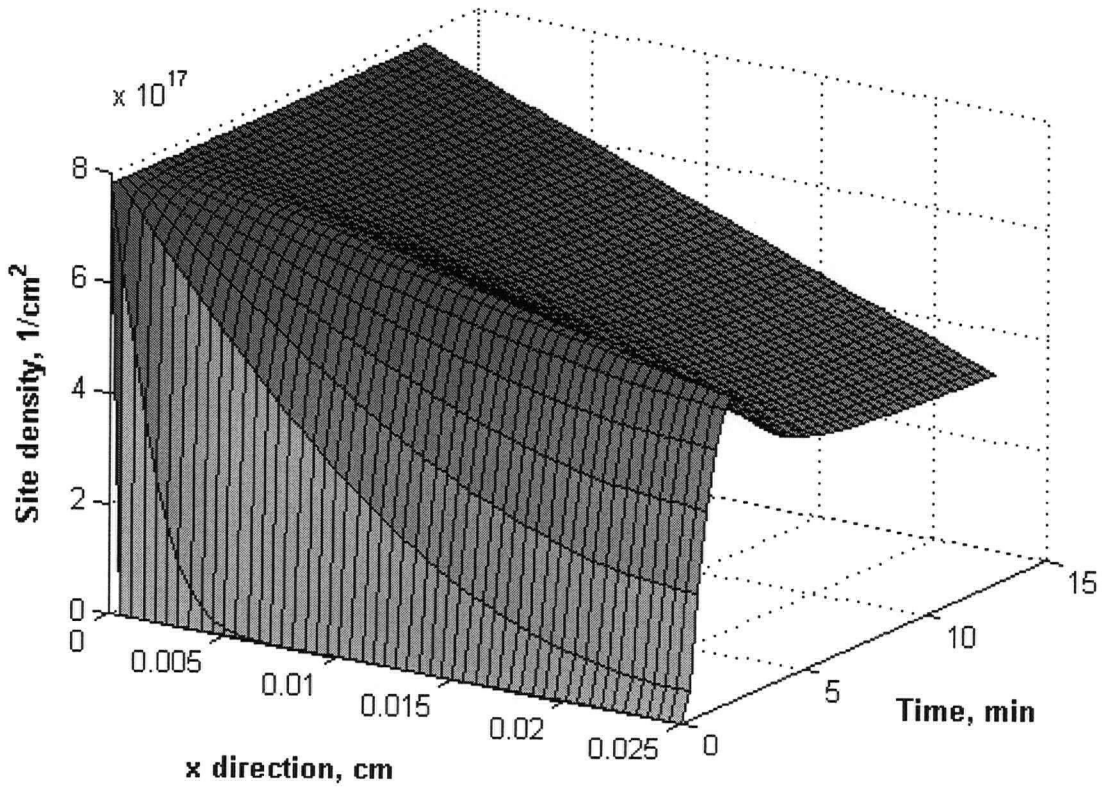

Figure 6.5a Single carbon atom profile along the Fe foil obtained by fitting literature data to the Kinetic Model II.

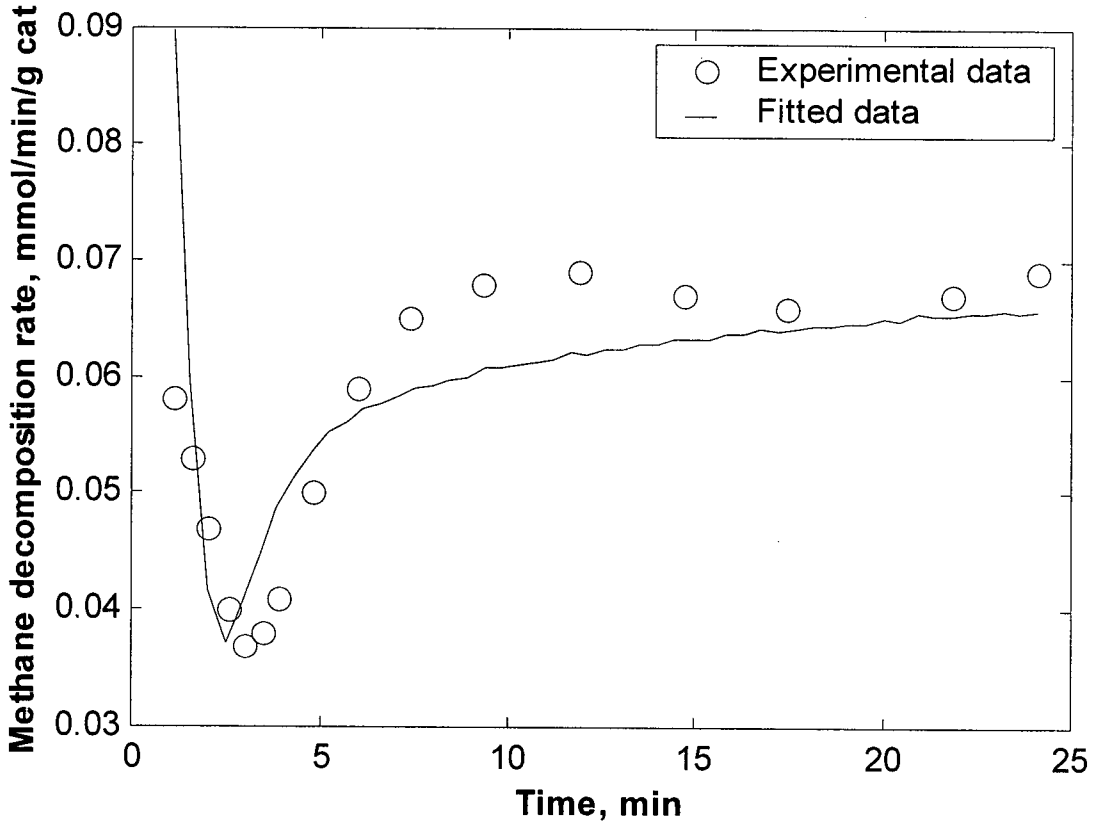

Figure 6.5b Carbon deposition rate obtained by fitting literature data to the Kinetic Model II.

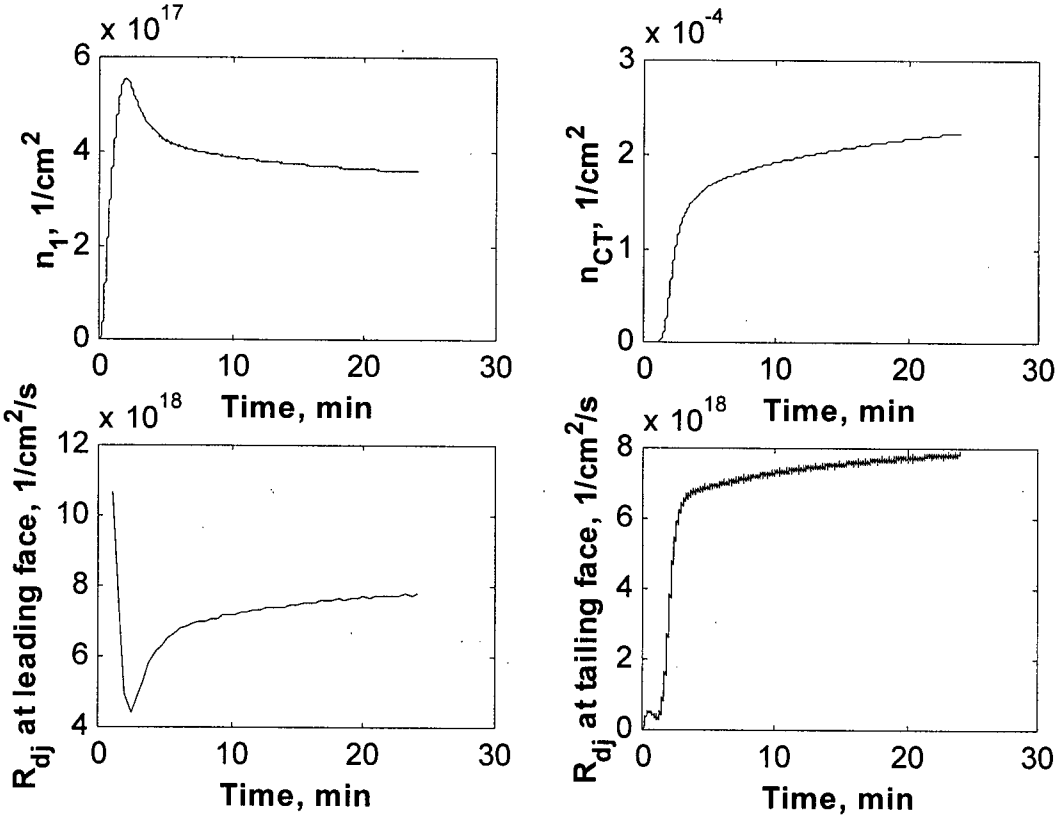

Figure 6.5c Detailed information obtained by fitting literature data to the Kinetic Model II.

Similarly, Figure 6.5a, b and c show the results obtained from literature data fitted to the Kinetic Model II. Again, the site density profiles along the Fe foil with time-on-stream were obtained and are plotted in Figure 6.5a. Figure 6.5b shows the fitted carbon deposition rate on Fe foil with time-on-stream. Detailed information about changes in n_1, and n_{CT} with time, and the carbon diffusion rate at the tailing face, are presented in Figure 6.5c. Similarly, three stages during the initial reaction are apparent. However, as described in Section 6.2, there is a difference between Model I and Model II. In Model II, there is continuous nucleation and growth of carbon nanofibres at the tailing face. The nucleation and growth of carbon start from time zero, although the initial diffusion rate is low.

The model parameter values listed in Table 6.2 show that the fitting of Kinetic Model I is better than Kinetic Model II based on a comparison of the F-statistics. Also, only one parameter, surface diffusivity D_1, was used to describe the carbon nucleation and carbon growth in Kinetic Model I. Consequently, in the following Section, only Kinetic Model I was used to describe the experimental data obtained in the present study.

6.4 Kinetic Model I Fit to Co/SiO_2 Catalyst Activity Data

6.4.1 Typical Examples of Kinetic Model I Fit on Co/SiO_2 Catalysts

As mentioned in the model description, the proposed kinetic model can describe the steady growth of filamentous carbon and deactivation, after the initial rate increase that is a consequence of the nucleation. In this section, two typical profiles obtained during CH_4 decomposition, which show deactivation and steady carbon growth, are fitted by Kinetic Model I.

Figure 6.6a, b and c show the fit of Kinetic Model I to the experimental data on 30wt% Co/SiO_2 with steady carbon growth. Similar to Figure 6.4a and Figure 6.5a, the carbon site density profiles in Figure 6.6a show three stages: steep profiles level off, corresponding to the initial unsteady state diffusion; the profile then becomes steep with the start of carbon nucleation and growth; finally, a stable profile, corresponding to the steady growth of carbon nanofibers, is apparent. Figure 6.5b shows that the steady growth of carbon nanofibres after the initial rate increase, was well described by the Kinetic Model I. Figure 6.5c shows similar information as described in Figure 6.3c. However, the difference between Figure 6.5c and Figure 6.3c is that the profile for n_s, the site density of single carbon atoms at the leading face, changes with time-on-steam in Figure 6.5c because the surface reaction was included in the former calculation.

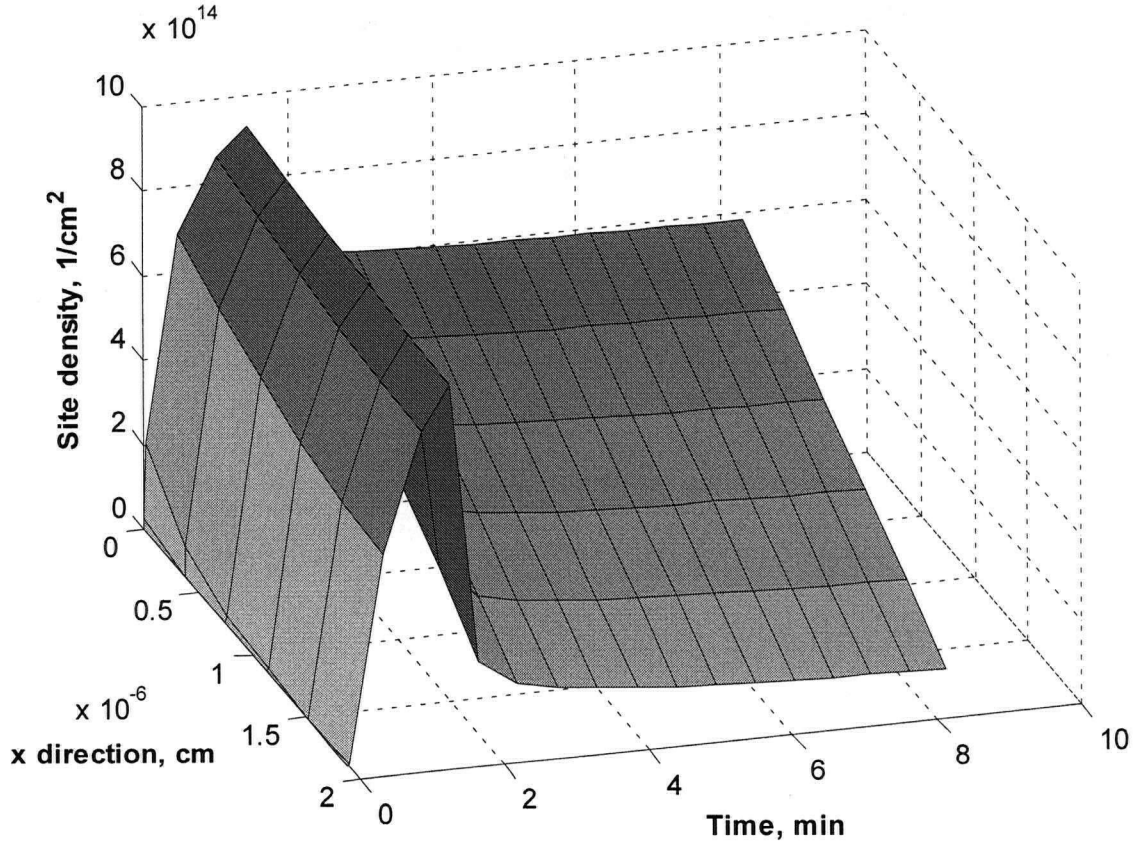

Figure 6.6a Single carbon atom profile along diffusion path with steady carbon growth on 30wt% Co/SiO_2 (923K reduction, 773K reaction with $K_M = 0.06$ atm) fitted to the Kinetic Model I.

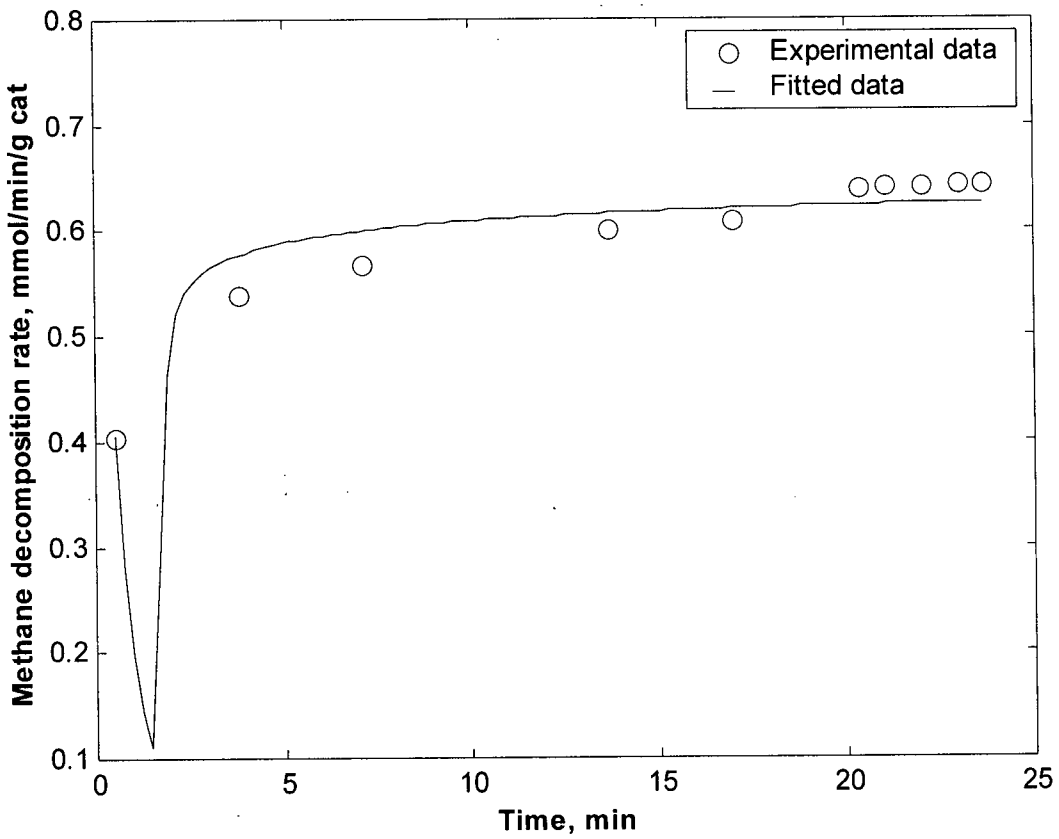

Figure 6.6b Carbon deposition with steady carbon growth on 30wt% Co/SiO_2 (923K reduction, 773K reaction with $K_M = 0.06$ atm) fitted to the Kinetic Model I.

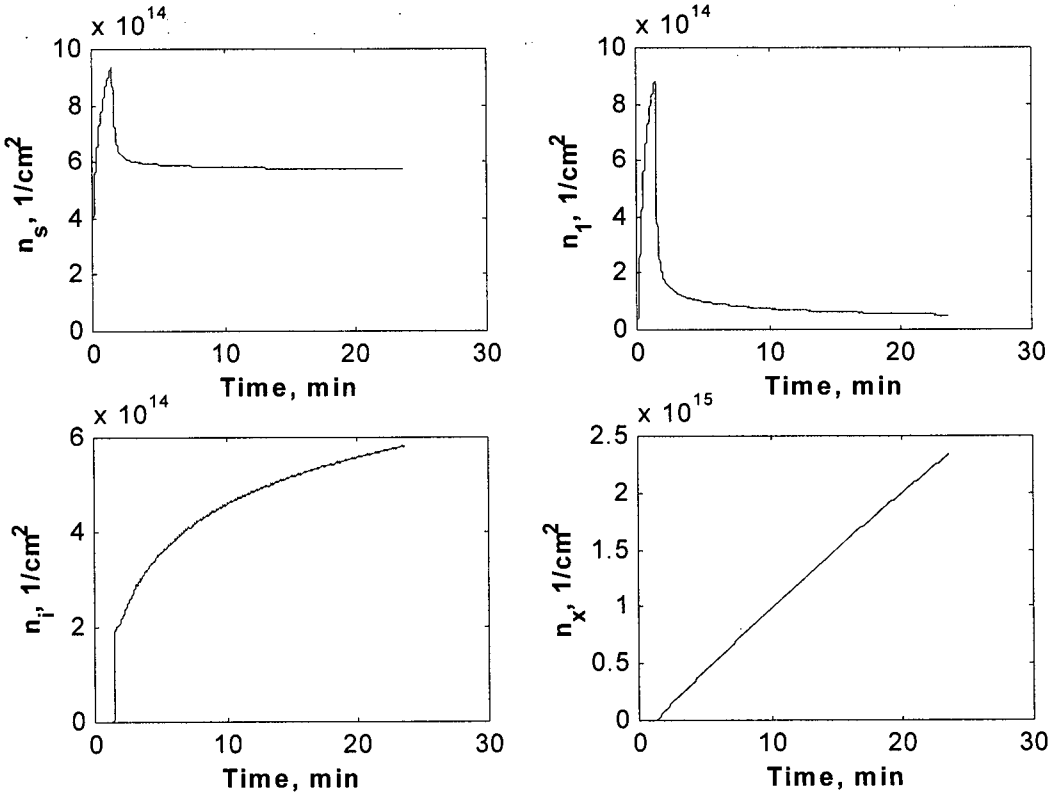

Figure 6.6c Detail information obtained from experimental data with steady carbon growth on 30wt% Co/SiO_2 (923K reduction, 773K reaction with $K_M = 0.06$ atm) fitted to the Kinetic Model I.

Figure 6.7a, b and c show the fit of the Kinetic Model I to the experimental data on 10wt% Co/SiO_2, with deactivation after the initial rate increase. The site density profiles along the diffusion path at different reaction times. Figure 6.7a also shows the presence of three stages of reaction during CH_4 decomposition. Figure 6.7b shows that the catalyst deactivation after the initial rate increase was well described by the kinetic model I. The information described in Figure 6.7c is similar to Figure 6.6c except that in this instance n_s decreases with increasing reaction time. The density of active sites and sites occupied by the encapsulating carbon are described in Figure 6.7d. The available active sites decrease with time-on-stream. Meanwhile, the active sites occupied by encapsulating carbon increase with time-on-stream and this increase is that causes the catalyst to deactivate in this example.

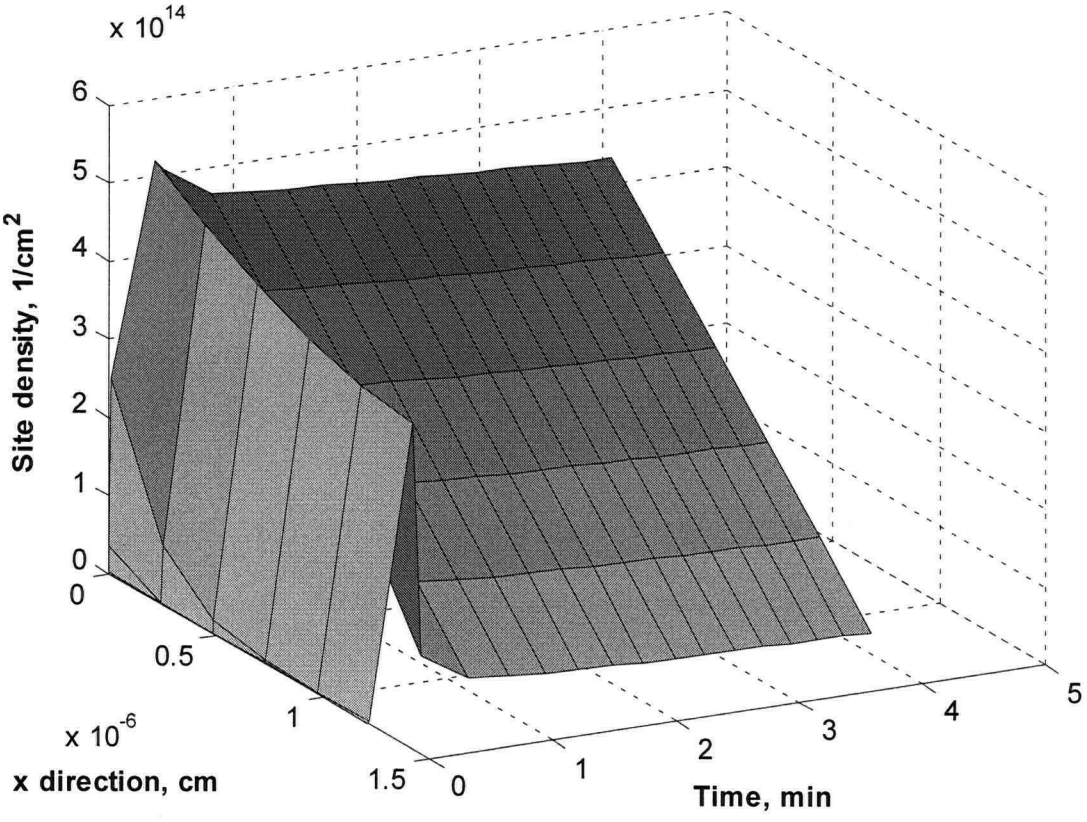

Figure 6.7a Single carbon atom profile along diffusion path with deactivation on 10wt% Co/SiO_2 (923K reduction, 773K reaction with $K_M = 0.06$ atm) fitted to the Kinetic Model I.

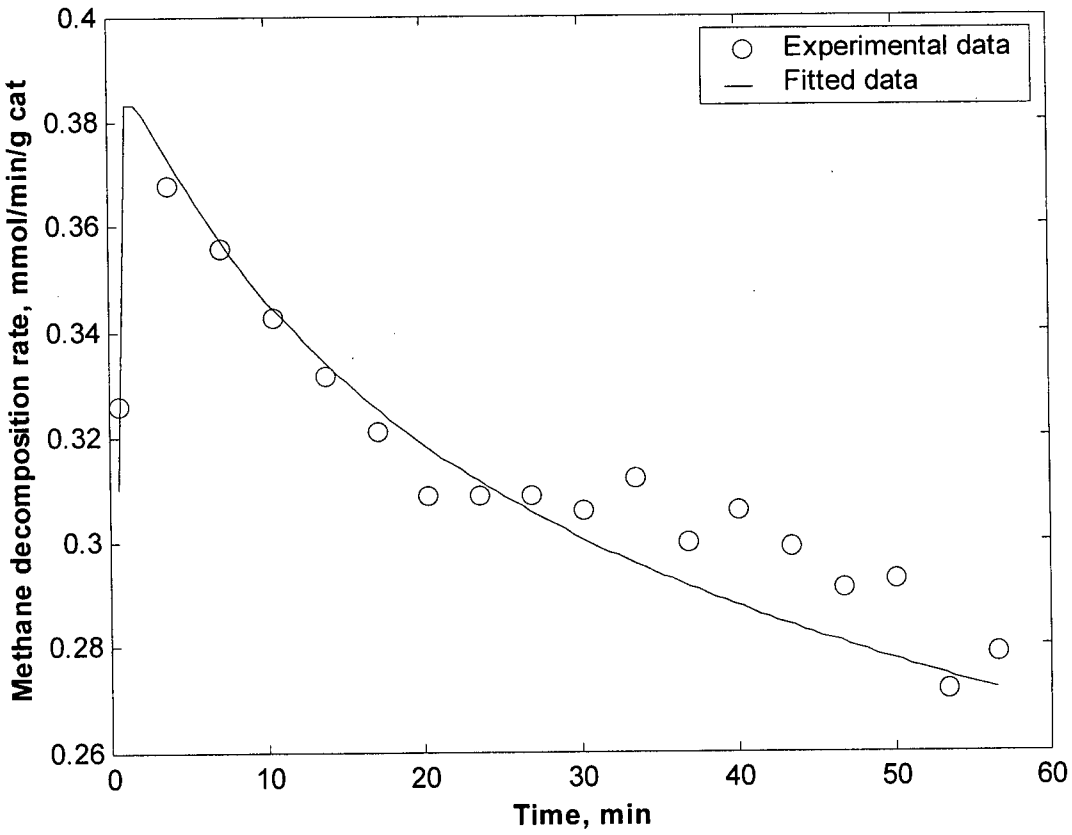

Figure 6.7b Carbon deposition with deactivation on 10wt% Co/SiO_2 (923K reduction, 773K reaction with $K_M = 0.06$ atm) fitted to the Kinetic Model I.

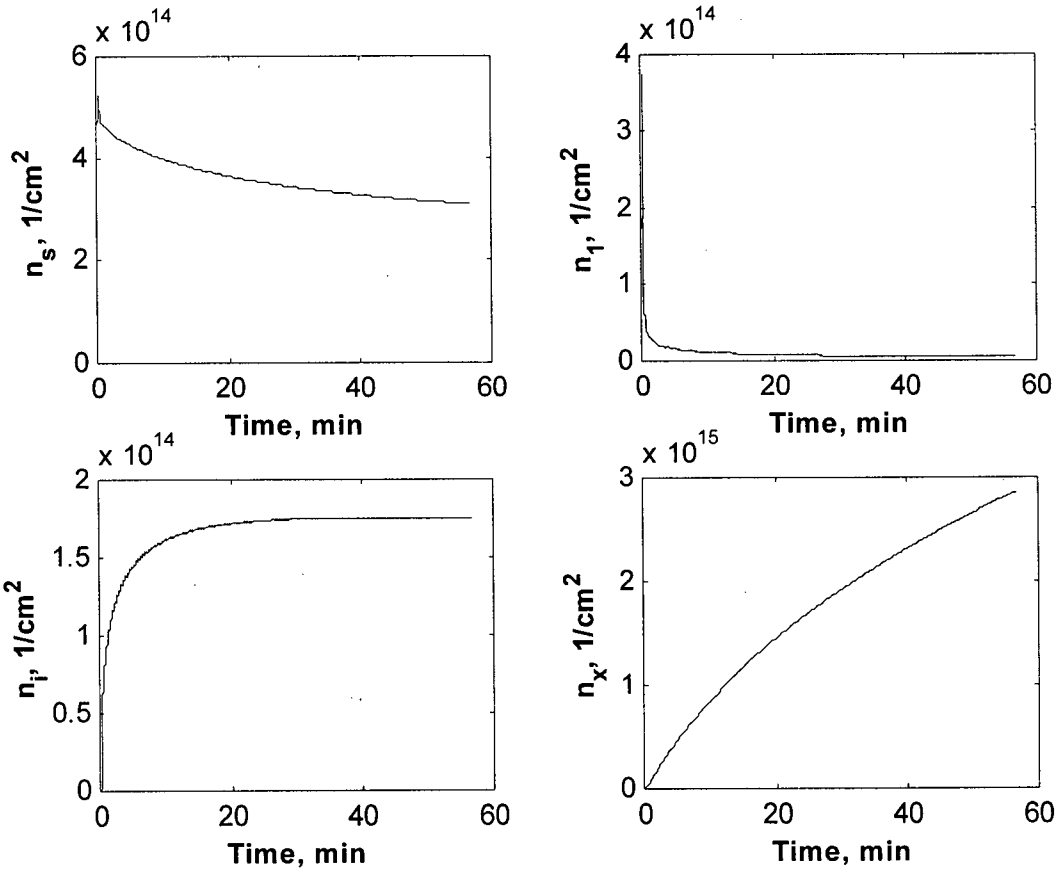

Figure 6.7c Detailed information obtained from experimental data with deactivation on 10wt% Co/SiO_2 (923K reduction, 773K reaction with $K_M = 0.06$ atm) fitted to the Kinetic Model I.

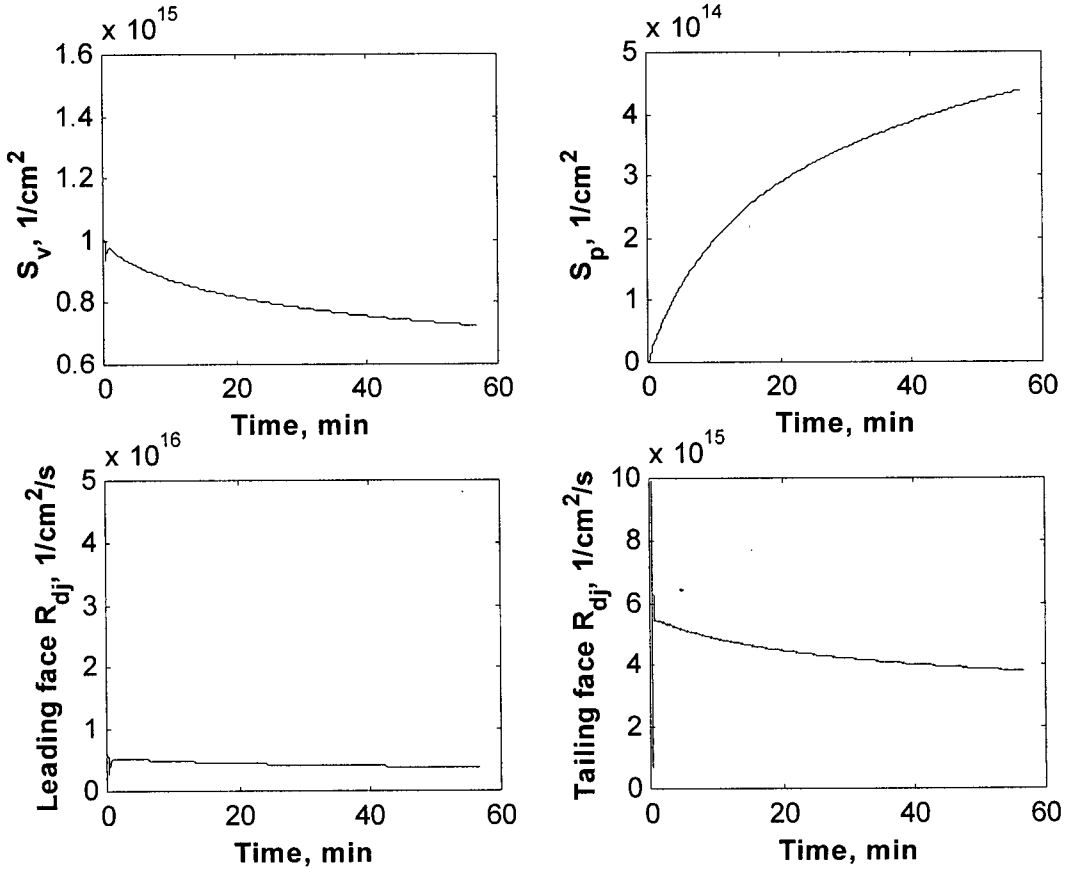

Figure 6.7d Detailed information obtained from experimental data with deactivation on 10wt% Co/SiO_2 (923K reduction, 773K reaction with $K_M = 0.06$ atm) fitted to the Kinetic Model I.

6.4.2 Effect of Metal Particle Size

To better understand the effect of metal particle size on filamentous carbon formation kinetics, experimental data on Co/SiO_2 catalysts with different Co loadings under the same CH_4 decomposition conditions, $K_M = 0.06 atm$ and T=773K, were fitted to the proposed Kinetic Model I. The estimated parameter values obtained in each case are listed in Table 6.3. Also, typical parameters are plotted versus metal particle size in Figure 6.8a, b, c, d and e.

Table 6.3 Effect of metal particle size on kinetic parameters estimated at 773K over Co/SiO_2 catalysts (923K reduction, 773K reaction with $K_M = 0.06$ atm).

Catalyst / Parameters	wt% Co	8	10	12	30
d_p	nm	13.5	17.8	19.4	28.0
$D_s \times 10^{14}$	cm^2/s	4.05±0.20	6.08±0.001	5.90±0.23	13.6±0.23
$D_i \times 10^{16}$	cm^2/s	4.54±0.38	6.16±0.02	0.96±0.04	0.517±0.01
$k_f \times 10^{19}$	$Pa^{-1}cm^2s^{-1}$	14.2±0.42	8.80±0.04	7.02±0.004	4.10±0.16
$k_g \times 10^{22}$	$Pa^{-2}s^{-1}cm^2$	2.82±0.24	2.11±0.04	0.77±0.0004	0.24±0.001
$k_{encap} \times 10^{75}$	$cm^{10}s^{-1}$	17.7±0.64	2.95±0.01	0.55±0.00003	$1.13\times10^{-4}\pm1.01\times10^{-7}$
R^2	%	0.68	0.84	0.78	0.92

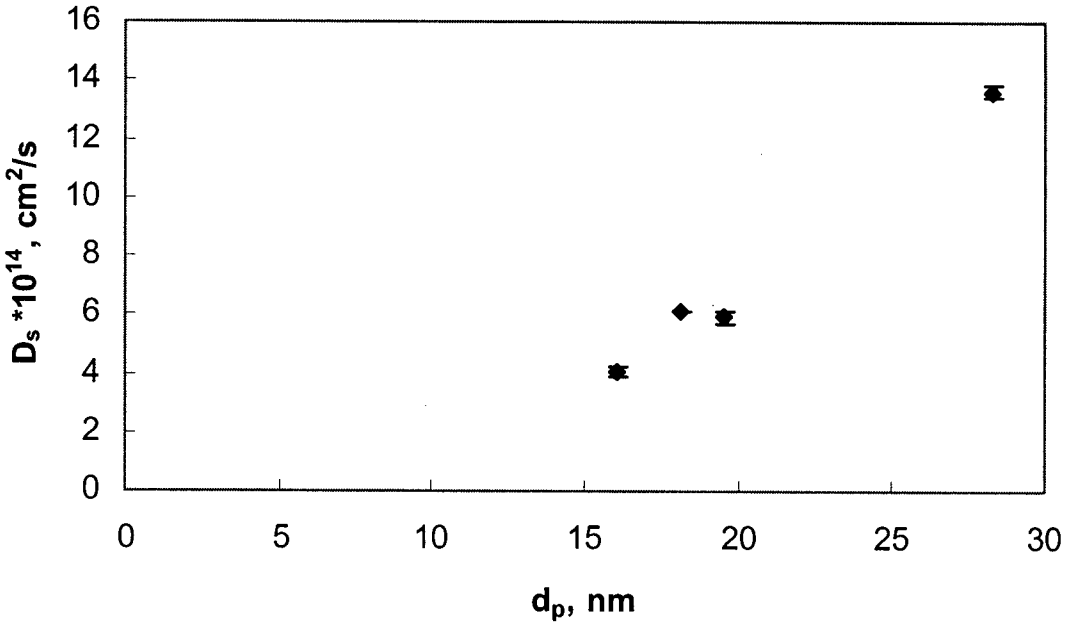

Figure 6.8a Effect of metal particle size on D_s, the carbon diffusivity through Co.

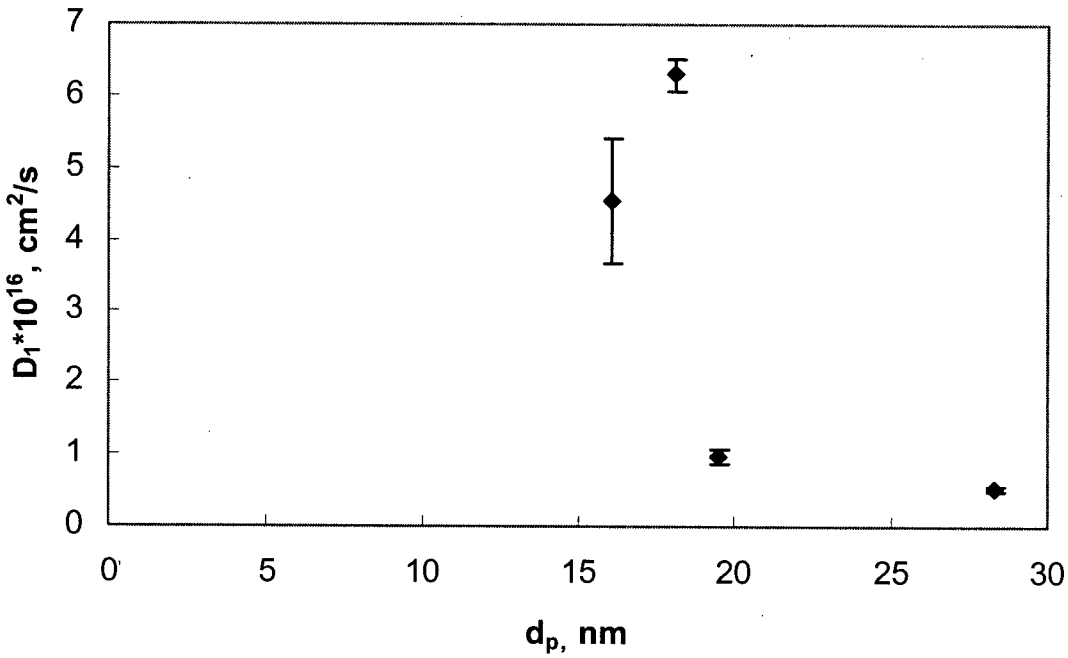

Figure 6.8b Effect of metal particle size on D_1, the carbon surface diffusivity at the tailing face.

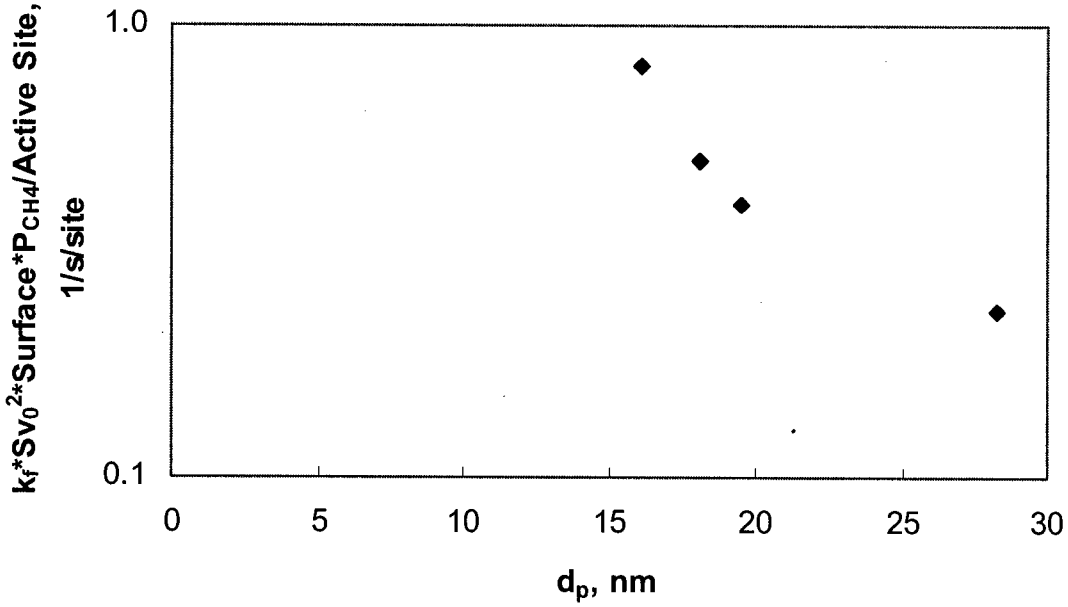

Figure 6.8c Effect of metal particle size on $k_f Sv_0^2 P_{CH_4} \cdot Surface/Active\ Site$, the initial TOF for CH_4 decomposition.

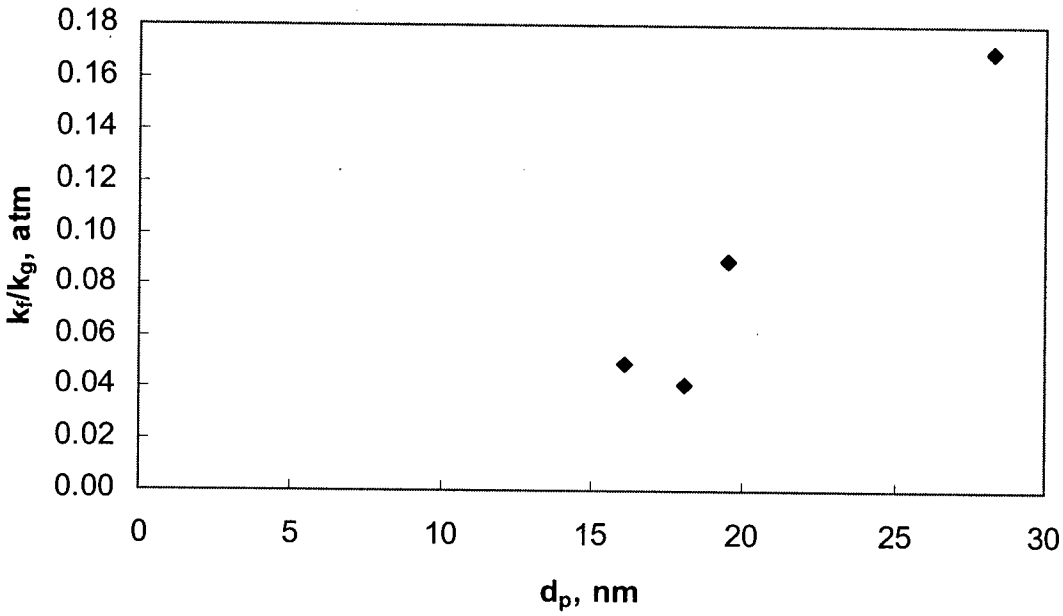

Figure 6.8d Effect of metal particle size on k_f / k_g, equilibrium constant for carbon CH_4 decomposition.

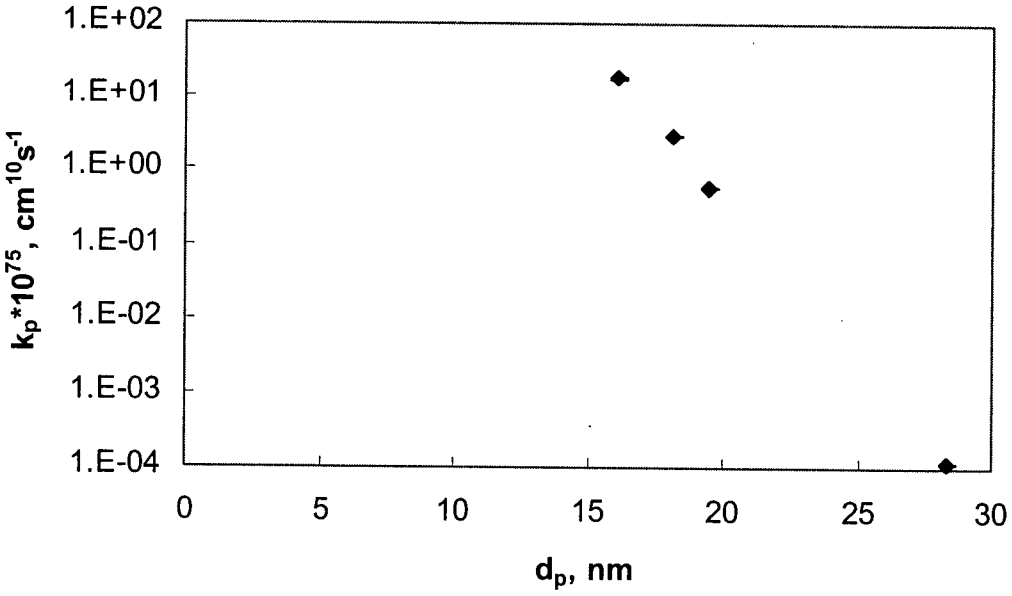

Figure 6.8e Effect of metal particle size on k_{encap}, rate constant for encapsulating carbon formation.

The modeling results of Table 6.3 and of Figure 6.8a show that the carbon diffusivity through Co was in the range of 4.05×10^{-14} to 1.36×10^{-13} cm^2/s. The range of values was two order of magnitude lower than that reported with Co foil at 773K, $D_s=6.94\times10^{-12}$ cm^2/s (Yokoyama et al., 1998). However, the carbon diffusion coefficient is dependent upon the carbon activity. Safvi et al. (1991) reported values from 1×10^{-9} to 1×10^{-6} cm^2/s as carbon activity ranged from 0 to 35 on γ-Fe at 1033K. In the present study, the carbon activity of the gas phase was approximately 7.0. However, the carbon activity for the data reported by Yokoyama et al. (1998) was unclear. Furthermore, modeling results of Figure 6.8a show that the diffusivity, D_s, increased with increasing metal particle size. One possible explanation of this observation is that carbon diffusion is structure sensitive and that the (100) and (110) surfaces are more suitable for carbon diffusion (Yang and Chen, 1989). The (100) and (110) faces are apparently favoured at the gas/metal interface whereas the (111) face is favoured at the graphite/ metal interface, based on a study of carbon filament growth on fine particles of α-Fe, Co and Ni catalyst from CH_4 at 700°C (Yang and Chen, 1989). In the present study, the decreased carbon diffusivity, D_s, with decreasing metal particle size might be explained by the fact that the formation of (100) and (110) faces was less favourable on the small metal particles due to the presence of defect sites that result in high coordination sites on small metallic particle.

Modeling results of Figure 6.8b show that the carbon surface diffusivity, D_1, decreased with increasing metal particle size, resulting in a weaker ability for carbon nucleation. This observation may be explained by noting that (111) face was favourable on the small metal particles due to the presence of defect sites that result in high coordination sites on small metallic particle.

Modeling results of Figure 6.8c show the initial TOF for methane dissociation, $k_f Sv_0^2 P_{CH_4} \cdot Surface/Active\ Site$ *(1/s/site*, where the units of $k_f Sv_0^2 P_{CH_4}$ are $1/cm^2/s$; *Surface* is the surface area of metallic particle calculated from CO uptake, $cm^2/gcat$; *Active Site* is the active metallic site obtained from CO uptake during CO chemisorption, mmol/gcat.) increased with increasing metal particle size. This observation is indicative of a structure sensitive CH_4 decomposition on supported Co catalysts. The result obtained here agrees with that of Wei and Iglesia (2003), who reported that on all noble metals, turnover rate increased with increasing metal dispersion obtained for CH_4-CO_2 and CH_4-H_2O reactions, suggesting that the coordinatively unsaturated surface atoms prevalent in small crystallites are significantly more active than those in the low-index planes predominately exposed on large crystallites. Wei and Iglesia (2003) also pointed out that similar effects have been predicted theoretically for model metal surfaces by Szuromi et al. (1985). Szuromi et al. (1985) have suggested that it was the presence of high coordination sites that was crucial for the lowering of activation barriers for the carbon-hydrogen bond cleavage process, and theoretical calculations show that the activation barrier is lower on a step on Ni (211) than Ni (111), and certain defect sites on small metallic particles might have lower activation energies for CH_4 dissociative adsorption (Beebe et al., 1987). Hence, the initial TOF for methane dissociation, $k_f Sv_0^2 P_{CH_4} \cdot Surface/Active\ Site$, decreased with the increasing metal particle size and this observation can be explained by the fact that, analogous to the activity for CH_4 decomposition on Ni, the initial TOF is high on the coordinatively unsaturated surface atoms prevalent in small Co crystallites; the initial TOF is low on the low-index planes that predominate on large Co crystallites. Note that in Section 5.2 it was observed that the maximum TOF increased with increasing metal particle size. There is a difference between the initial TOF reported in Figure 6.8c obtained by modelling and maximum TOF obtained from experimental observations. The initial TOF, determined by the number of

metallic sites on catalyst initially, whereas the maximum TOF, obtained after the initial rate increase, reflects the carbon formation rate determined by a number of complex reaction steps such as the carbon deposition, the carbon diffusion, encapsulating carbon formation and carbon nucleation.

Modeling results of Figure 6.8d show that the equilibrium constant, expressed as k_f / k_g (atm), increased with metal particle size. This is consistent with the discussion in Section 5.3 that demonstrated that the equilibrium constant increases with increasing metal particle size, or the diameter of the carbon nanofibre.

Finally, the results of Figure 6.8e show that the encapsulating carbon formation rate constant, k_{encap}, decreased with increasing metal particle size. It is suggested that encapsulating carbon formation was not favoured on the surfaces of large metal particles. Yang and Chen (1989) reported results that encapsulating carbon formation was dependent on the exposed face of the metal: the encapsulating carbon formation favoured binding on Ni (111) followed in the order (111) > (311) > (100) > (110). Hence, the encapsulating carbon formation rate constant, k_{encap}, decreased with increasing metal particle size is likely a result of the low-index planes (100) and (110) being predominate on large crystallites.

6.5 Summary

A general kinetic model of CH_4 decomposition on supported metal catalysts has been developed based on experimental observations and a deactivation mechanism. The initial increase in activity was described by carbon nucleation. In addition, the developed model described not only the catalyst deactivation but also the steady activity observed in some cases after the initial rate increase. The carbon nucleation at the tailing face was described using two methods: Cluster nucleation (Model I) and Boltzmann nucleation (Model II). The fit of literature

data to Kinetic Model I and Model II confirm the presence of carbon nucleation at the tailing face. The experimental kinetic data on supported Co catalysts were well described by the kinetic model. The site density profile along the metal particle was also obtained in the present study. Furthermore, the effect of metal particle size on the activity of CH_4 decomposition has been quantified by fitting the experimental data to the proposed kinetic model.

Chapter 7 Conclusions and Recommendations

7.1 Conclusions

The kinetics of CH_4 decomposition on supported Co and Ni catalysts has been investigated. The catalyst activity and deactivation were discussed in terms of the maximum rate and decay constant of a 1st order decay model. The experimental observations presented herein suggest that the migration of CH_x from the metal to the support made a small contribution to the regeneration of active metal sites only in the first 2 to 3 min of reaction. In agreement with previous studies on Fe and Ni, filamentous carbon formation reduced the rate of catalyst deactivation during CH_4 decomposition by removing carbon from the metal surface. The presence of H_2 or CO reduced the net rate of carbon deposition and increased the net rate of carbon removal by diffusion through the Co, respectively. Hence, stable CH_4 decomposition activity and filamentous carbon formation were observed on supported Co catalysts with low metal loading in the presence of H_2 or CO. The increased decay constant with temperature was ascribed to rapid ageing of the carbon species deposited on the catalyst surface as reaction temperature increased. Based on the above observations, it was concluded that catalyst deactivation was a consequence of the competition between the rate of encapsulating carbon formation and the rate of carbon diffusion. Stable activity or catalyst deactivation during CH_4 decomposition was observed, depending on which of these two rates was greater.

The structure sensitivity of the CH_4 decomposition reaction has been observed on low loading Co and Ni catalysts: the maximum decomposition activity increased with increasing metal particle size (decreasing metal dispersion) and the decay constant decreased with increasing metal particle size (decreasing metal dispersion).

The coking threshold K_M^* obtained on Co/SiO_2 with different loading in the present study followed the linear relationship of K_M^* versus the reciprocal of the average metal particle size. A filamentous carbon formation threshold, K_M^f, has also been defined as the value of $K_M = P_{H_2}^2 / P_{CH_4}$ corresponding to the formation of filamentous carbon at a particular temperature. The difference between the coking threshold, K_M^*, and the filamentous carbon formation threshold, K_M^f, increased with the increasing metal particle size, consistent with the observation that it was easier to obtain stable activity with filamentous carbon formation on the catalyst with larger metal particle size under the same gas phase composition, K_M, and temperature.

The effect of BaO, La_2O_3 and ZrO_2, added to the SiO_2 support of Co catalysts, has also been investigated. The effect of the modified support on the catalyst reduction behaviour, dispersion and MSI was studied by TPR, XPS and CO chemisorption. The results suggest an increasing MSI among the catalysts in the order $Co/SiO_2 \approx Co/BaO/SiO_2 < Co/La_2O_3/SiO_2 < Co/ZrO_2/SiO_2$. The rate of catalyst deactivation was affected by the modified support: increased deactivation corresponded to an increased MSI. It is suggested that the latter observation is a consequence of the Co particle being held more strongly to the support, such that filament formation is reduced, which in turn results in an increase in the formation of encapsulating carbon and hence deactivation.

XPS analysis of carbon species on used catalysts identified the presence of carbidic carbon, ascribed to single carbon atoms that diffuse through the metal particle and form filamentous carbon, and graphitic carbon, ascribed to encapsulating carbon that deactivated the catalyst. The competition between filamentous carbon formation and encapsulating carbon formation determined the rate of deactivation. Data presented herein demonstrate a correlation

between the magnitude of the catalyst decay constant and the relative concentration of carbidic carbon on the catalyst surface.

A general kinetic model of CH_4 decomposition on supported metal catalysts has been developed based on experimental observations and the deactivation mechanism described above. The model described not only the catalyst deactivation but also the steady activity observed in some cases after the initial rate increase. The initial rate increase was described by including the rate of carbon nucleation at the tailing face of the metal particle in model using two methods: Cluster nucleation (Model I) and Boltzmann nucleation (Model II). The fit of literature data to Model I and Model II confirmed the presence of carbon nucleation at the tailing face. The experimental kinetic data on supported Co catalysts were well described by the kinetic model. The site density profile along the metal particle was also obtained and the effect of metal particle size on the CH_4 decomposition activity has been quantified by fitting the experimental data to the proposed kinetic model.

7.2 Recommendations

In the present study, the carbon deposition rate was obtained from the gas phase analysis and consequently, the initial carbon deposition rate was not measured for small time intervals. It is suggested that in the future, the carbon deposition rate be measured from the weight change of catalyst at small time intervals in order to develop more reliable parameter estimates for the nucleation steps of the model.

It should be noted that this study has addressed the transient nucleation and growth stage in filamentous carbon on the tailing face of the metal particle. However, some limitations remain: One assumption made in present model is that there was no steric limitation during

nucleation. The metal particle was assumed infinite. The growth of carbon nanofibres is not described at atomic level. More predictable results can be provided if the above issues were addressed further.

References

Aiello, R., Fiscus, J.E., Zur Loye, H.C., and Amiridis, M.D. (2000). "Hydrogen Production via the Direct Cracking of Methane over Ni/SiO_2: Catalyst Deactivation and Regeneration." *Applied Catalysis A: General* 192(2), 227-234.

Alstrup, I., and Tavares, M.T. (1993). "Kinetics of Carbon Formation from CH_4+H_2 on Silica-Supported Nickel and Ni-Cu Catalysts." *Journal of Catalysis* 139(2), 513-524.

Alstrup, I.. (1988). "A New Model Explaining Carbon Filament Growth on Nickel, Iron, and Nickel-Copper Alloy Catalysts." *Journal of Catalysis* 109(2), 241-251.

Audier, M., and Coulon, M. (1985). "Kinetic and Microscopic Aspects of Catalytic Carbon Growth. " *Carbon* 23, 317.

Avdeeva, L.B., Kochubey, D.I., and Shaikhutdinov, S.K. (1999). "Cobalt Catalysts of Methane Decomposition: Accumulation of The Filamentous Carbon." *Applied Catalysis a-General* 177(1), 43-51.

Baker, R.T.K. (1989). "Catalytic Growth of Carbon Filaments." *Carbon* 27(3), 315-323.

Baker, R.T.K., Barver, M.A., Harris, P.S., Feates, F.S., and Waite, R.J. (1972). "Nucleation and Growth of Carbon Deposits from the Nickel Catalyzed Decomposition of Actylene.." *Journal of Catalysis* 26, 51-62.

Bartholomew, C.H. (2001). "Mechanisms of Catalyst Deactivation." *Applied Catalysis A: General,* 212(1-2), 17-60.

Beebe, T.P., Wayne, Jr.D., and Kay, B.D., (1987). "Kinetics of the Activated Dissociative Adsorption of Methane on the Low Index Planes of Nickel Single Crystal Surfaces." *Journal of Chemical Physics* 87(4), 2305-2315.

Bianchi, C.L. (2001). "TPR and XPS Investigations of Co/Al_2O_3 Catalysts Promoted with Ru, Ir and Pt.", *Catalysis Letters* 76, 155-159.

Bitter, J.H., Seshan, K., and Lercher, J.A. (1998). "Mono and Bifunctional Pathways of CO_2/CH_4 Reforming over Pt and Rh Based Catalysts." *Journal of Catalysis* 176(1), 93-101.

Boskovic, G., Zadeh, J.S.M., and Smith, K.J. (1996). "K Promotion of Co Catalysts for the Two-Step Methane Homologation Reaction." *Catalysis Letters* 39(3-4), 163-168.

Chen, D., Lodeng, R., Anundskas, A., Olsvik, O., and Holmen, A. (2001). "Deactivation during Carbon Dioxide Reforming of Methane over Ni Catalyst: Microkinetic Analysis." *Chemical Engineering Science* 56(4), 1371-1379.

Chitrapu, P., Lund, C.R.F., and Tsamopoulos, J.A. (1992). "A Model for the Catalytic Growth of Carbon Filaments." *Carbon* 30(2), 285-293.

Choudhary, T.V., Aksoylu, E., Goodman, D.W. (2003a). "Nonoxidative Activation of Methane." *Catalysis Reviews* 45(1), 151-203.

Choudhary, T.V., and Goodman, D.W. (1999). "Stepwise Methane Steam Reforming: a Route to CO-Free Hydrogen." *Catalysis Letters* 59(2-4), 93-94.

Choudhary, T.V., and Goodman, D.W. (2002a). "CO-Free Fuel Processing for Fuel Cell Applications." *Catalysis Today* 77(1-2), 65-78.

Choudhary, T.V., Sivadinarayana, C., Chusuei, C.C., Klinghoffer, A., and Goodman, D.W. (2001a). "Hydrogen Production via Catalytic Decomposition of Methane." *Journal of Catalysis* 199(1), 9-18.

Choudhary, T.V., Sivadinarayana, C., Goodman, D.W. (2003b). "Production of CO_x-free Hydrogen for Fuel Cells via Step-wise Hydrocarbon Reforming and Catalytic Dehydrogenation of Ammonia." *Chemical Engineering Journal* 93(1), 69-80.

Choudhary, V.R., Banerjee, S., and Rajput, A.M. (2001b). "Continuous Production of H_2 at Low Temperature from Methane Decomposition over Ni-Containing Catalyst Followed by Gasification by Steam of the Carbon on the Catalyst in Two Parallel Reactors Operated in Cyclic Manner." *Journal of Catalysis* 198(1), 136-141.

Choudhary, V.R., Banerjee, S., and Rajput, A.M. (2002b). "Hydrogen from Step-Wise Steam Reforming of Methane over Ni/ZrO_2: Factors Affecting Catalytic Methane Decomposition and Gasification by Steam of Carbon Formed on the Catalyst." *Applied Catalysis A: General* 234(1-2), 259-270.

Coulter, K. E., and Sault, A.G. (1995). "Effects of Activation on the Surface Properties of Silica-Supported Cobalt catalysts" *Journal of Catalysis* 154, 56-64.

Dautzenberg F.M. (1988). "Characterization and Catalyst Development." Chapter 11, ACS Symp. Series, *196th ACS Meeting*, Loas Angelos Calit, 99-119.

De Jong, K.P., and Geus, J.W. (2000). "Carbon Nanofibers: Catalytic Synthesis and Applications." *Catalysis Reviews-Science and Engineering* 42(4), 481-510.

Demicheli, M.C., Duprez, D., Barbier, J., Ferretti, O.A., and Ponzi, E.N. (1994). "Deactivation of Steam-Reforming Model Catalysts by Coke Formation. 2. Promotion with Potassium and Effect of Water." *Journal of Catalysis* 145(2), 437-449.

Demicheli, M.C., Ponzi, E.N., Ferretti, O.A., and Yeramian, A.A. (1991). "Kinetics of Carbon Formation from CH_4-H_2 Mixtures on Nickel Alumina Catalyst." *Chemical Engineering Journal and the Biochemical Engineering Journal* 46(3), 129-136.

Ermakova, M.A., and Ermakov, D.Y. (2002). "Ni/SiO_2 and Fe/SiO_2 Catalysts for Production of Hydrogen and Filamentous Carbon via Methane Decomposition." *Catalysis Today* 77(3), 225-235.

Ermakova, M.A., Ermakov, D.Y., and Kuvshinov, G.G. (2000). "Effective Catalysts for Direct Cracking of Methane to Produce Hydrogen and Filamentous Carbon. Part I. Nickel Catalysts." *Applied Catalysis A: General* 201(1), 61-70.

Ermakova, M.A., Ermakov, D.Y., Kuvshinov, G.G., and Plyasova, L.M. (1999). "New Nickel Catalysts for the Formation of Filamentous Carbon in the Reaction of Methane Decomposition." *Journal of Catalysis* 187(1), 77-84.

Feller, A., Claeys, M., Van Steen, E. (1999). "Cobalt Cluster Effects in Zirconium Promoted Co/SiO_2 Fischer-Tropsch Catalysts." *Journal of Catalysis* 185(1), 120-130.

Ferreira-Aparicio, P., Rodrigues-Ramos, I., Fuerrero-Ruiz, A. (1997). "Methane Interaction with Silica and Alumina Supported Metal Catalysts." *Applied Catalysis A: General* 148, 343-356.

Froment, G.F, Bischoff, K.B. (1990). "Chemical Reactor Analysis and Design.", *Wiley*, New York.

Galuszka, J., Back, M.H. (1984). "Iron Surface Morphology Factor in the Growth of Filamentous Carbon." *Carbon* 22(2), 141-145.

Geus, J.W. (1985). *Eur. Patent* 0,198,558, B1.

Grabke, H.J., Muller.E.M., and Konczos, G. (1980). "Adsorption, Segregation and Reactions of Non-Metal Atoms on Iron Surfaces." *Materials Science and Engineering* 42(1), 91-99.

Grujicic, M., Cao, G., Gersten, B. (2002). "An Atomic-Scale Analysis of Catalytically-Assisted Chemical Vapor Deposition of Carbon Nanotubes." *Materials Science and Engineering B-SOLID* 94 (2-3), 247-259.

Guczi, L., Sarma, K.V., and Borko, L. (1997). "Low-Temperature Methane Activation under Nonoxidative Conditions over Supported Ruthenium-Cobalt Bimetallic Catalysts." *Journal of Catalysis* 167(2), 495-502.

Haddad, G.J., Chen, B., and Goodwin, J.G. (1996). "Characterization of La^{3+}-Promoted Co/SiO_2 Catalysts." *Journal of Catalysis* 160(1), 43-51.

Holstein, W.L. (1995). "The Roles of Ordinary and Soret Diffusion in the Metal-Catalyzed Formation of Filamentous Carbon." *Journal of Catalysis* 152(1), 42-51.

Hoogenraad, M.S., (1995). Ph.D. thesis, *Utrecht University*.

Juszczyk W., Karpinski Z., Lomot D., Pielaszek J., Paal Z. and Stakheev A.Y. (1993). "The Structure and Activity of Silica-Supported Palladium-Cobalt Alloys I. Alloy Homogeneity, Surface Composition, and Activity for Neopentane Conversion." *Journal of Catalysis* 142, 617-629.

Khodakov, A.Y., Lynch, J., Bazin, D., et al. (1997). "Reducibility of Cobalt Species in Silica-Supported Fischer-Tropsch Catalysts." *Journal Catalysis* 168(1), 16-25.

Kim, J.H., Suh, D.J., Park, T.J., and Kim, K.L. (2000). "Effect of Metal Particle Size on Coking during CO_2 Reforming of CH_4 over Ni-Alumina Aerogel Catalysts." *Applied Catalysis A: General* 197(2), 191-200.

Koerts, T., and Vansanten, R.A. (1991). "A Low-Temperature Reaction Sequence for Methane Conversion." *Journal of the Chemical Society-Chemical Communications* (18), 1281-1283.

Koerts, T., Deelen, M.J.A.G., and Vansanten, R.A. (1992). "Hydrocarbon Formation from Methane by a Low-Temperature 2-Step Reaction Sequence." *Journal of Catalysis* 138(1), 101-114.

Kuvshinov, G.G., Mogilnykh, Y.I., and Kuvshinov, D.G. (1998). "Kinetics of Carbon Formation from CH_4-H_2 Mixtures over a Nickel Containing Catalyst." *Catalysis Today* 42(3), 357-360.

Lee, C.J., Kim, D.W., Lee, T.J., et al. (1999). "Synthesis of UniformLy Distributed Carbon Nanotubes on a Large Area of Si Substrates by Thermal Chemical Vapor Deposition." *Applied Physics Letters* 75(12), 1721-1723.

Lesage, P., Clause, O., Moral, P., Didillon, B., Candy, J.P., and Basset, J.M. (1995). "Surface Organometallic Chemistry on Metals: Preparation of Bimetallic Catalysts by Controlled Hydrogenolysis of $Sn(n\text{-}C_4H_9)$ on a Ni/SiO_2 catalyst." *Journal of Catalysis* 155, 238-248.

Liu, H.M., Dandy, D.S. (1996). "Nucleation Kinetics of Diamond on Carbide-Forming Substrates during Chemical Vapor Deposition. 1. Transient Nucleation Stage." *Journal of the Electrochemical Society* 143(3), 1104-1109.

Lund, C.R.F., Yang, R.T. (1989). "Solid-State Diffusion during Carbon Gasification and Filament Growth.", *Carbon* 27(6), 956-958.

Ming, H., Baker B.G. (1995). "Characterization of Cobalt Fisher-Tropsch Catalysts I. Unsupported Cobalt-Silica Gel Catalysts." *Applied Catalysis A: Genera,* 123, 23-36.

Muradov, N. (2001a). "Hydrogen via Methane Decomposition: an Application for Decarbonization of Fossil Fuels." *International Journal of Hydrogen Energy* 26(11), 1165-1175.

Muradov, N.Z. (1998). "CO_2-Free Production of Hydrogen by Catalytic Pyrolysis of Hydrocarbon Fuel." *Energy & Fuels* 12(1), 41-48.

Muradov, N.Z. (2001b). "Thermocatalytic Production of Hydrogen via Pyrolysis of Hydrocarbon Fuels: from Methane to Residual Oil." *Abstracts of Papers of the American Chemical Society* 221, U494-U494.

Nolan, P.E., Lynch, D.C., and Cutler, A.H. (1998). "Carbon Deposition and Hydrocarbon Formation on Group VIII Metal Catalysts." *Journal of Physical Chemistry B* 102(21), 4165-4175.

Nolan, P.E., Schabel, M.J., Lynch, D.C., and Cutler, A.H. (1995). "Hydrogen Control of Carbon Deposit Morphology." *Carbon*, 33(1), 79-85.

Otsuka, K., Kobayashi, S., and Takenaka, S. (2001). "Catalytic Decomposition of Light Alkanes, Alkenes and Acetylene over Ni/SiO_2." *Applied Catalysis A: General* 210(1-2), 371-379.

Otsuka, K., Ogihara, H., and Takenaka, S. (2003). "Decomposition of Methane over Ni Catalysts Supported on Carbon Fibers Formed from Different Hydrocarbons." *Carbon* 41(2), 223-233.

Otsuka, K., Seino, T, Kobayashi, S., et al. (1999). "Production of Hydrogen through Decomposition of Methane with Ni-supported Catalysts", *Chemistry Letters* 11, 1179-1180.

Poirier, M.G., Sapundzhiev, C. (1997). "Catalytic Decomposition of Natural Gas to Hydrogen for Fuel Cell Applications." *International Journal of Hydrogen Energy* 22(4), 429-433.

Rase H.F. (1990). "Fixed-Bed Reactor Design and Diagnostics: Gas-Phase Reaction." *Butterworth.*

Riva R., Miessnerm, H., Vitali, H.and Piero G.D. (2000). "Metal-Support Interaction in Co/SiO_2 and Co/TiO_2." *Applied Catlysis A: General* 196, 111-123.

Rodrigues, E.L. and Bueno, J.M.C. (2002). "Co/SiO_2 Catalysts for Selective Hydrogenation of Crotonaldehyde II: Influence of the Co Surface Structure on Selectivity." *Applied Catalysis A: General* 232, 147-158.

Rodriguez, N.M., Kim, M.S., and Baker, R.T.K. (1993). "Promotional Effect of Carbon-Monoxide on the Decomposition of Ethylene over an Iron Catalyst." *Journal of Catalysis* 144(1), 93-108.

Rostrup-Nielsen, J.R (1972). "Equilibria of Decomposition Reactions of Carbon Monoxide and Methane over Nickel Catalysts." *Journal of Catalysis* 27, 343-356.

Sacco, A.Jr., Thacker, P., Chang, T.N., and Chiang, A.T.S. (1984). "The Initiation and Growth of Filamentous Carbon from α-Iron in H_2, CH_4, H_2O, CO_2 and CO Gas Mixtures." *Journal of Catalysis* 85, 224-236.

Safvi, S.A., Bianchini, E.C., Lund, C.R.F. (1991). "The Dependence of Catalytic Carbon-Filament Growth-Kinetics upon Gas-Phase Carbon Activity." *Carbon* 29(8), 1245-1250.

Shah, N., Panjala, D., and Huffman, G.P. (2001). "Hydrogen Production by Catalytic Decomposition of Methane." *Energy & Fuels* 15(6), 1528-1534.

Shaikhutdinov, S.K., Avdeeva, L.B., Goncharova, O.V., Kochubey, D.I., and Novgorodov, B.N. (1995). "Coprecipitated Ni-Al and Ni-Cu-Al Catalysts for Methane Decomposition and Carbon Deposition .1. Genesis of Calcined and Reduced Catalysts." *Applied Catalysis A: General* 126(1), 125-139.

Shaikhutdinov, S.K., Avdeeva, L.B., Novgorodov, B.N., Zaikovskii, V.I., and Kochubey, D.I. (1997). "Nickel Catalysts Supported on Carbon Nanofibers: Structure and Activity in Methane Decomposition." *Catalysis Letters* 47(1), 35-42.

Shustorovich, E., and Bell, A.T. (1991). "An Analysis of Fischer-Tropsch Synthesis by the Bond-Order-Conservation-Morse-Potential Approach." *Surface Science* 248(3), 359-368.

Snoeck, J.W., Froment, G.F., and Fowles, M. (1997a). "Filamentous Carbon Formation and Gasification: Thermodynamics, Driving Force, Nucleation, and Steady-State Growth." *Journal of Catalysis* 169(1), 240-249.

Snoeck, J.W., Froment, G.F., and Fowles, M. (1997b). "Kinetic Study of the Carbon Filament Formation by Methane Cracking on a Nickel Catalyst." *Journal of Catalysis* 169(1), 250-262.

Solymosi, F., Erdohelyi, A., and Cserenyi, J. (1994). "Methane Decomposition and Reaction of Hydrocarbon Fragments over Pd Catalysts." *Abstracts of Papers of the American Chemical Society* 207, 28.

Steinberg, M. (1995). "The Hy-C Process (Thermal-Decomposition of Natural-Gas) Potentially the Lowest Cost Source of Hydrogen with the Least CO_2 Emission." *Energy Conversion and Management* 36(6-9), 791-796.

Steinberg, M. (1998). "Production of Hydrogen and Methanol from Natural Gas with Reduced CO_2 Emission." *International Journal of Hydrogen Energy* 23(6), 419-425.

Steinberg, M. (1999a). "Natural Gas is a Key to Fossil Fuel CO_2 Global Warming Mitigation." *Abstracts of Papers of the American Chemical Society* 217: 22

Steinberg, M. (1999b)."Fossil Fuel Decarbonization Technology for Mitigating Global Warming." *International Journal of Hydrogen Energy* 24(8), 771-777.

Szuromi, P.D., Engstrom, J.R., and Weinberg, W.H. (1985). "The Adsorption and Reaction of Normal Alkanes on the Iridium (110)-(1×2) Surface." *Journal of Physical Chemistry* 89, 2497.

Takenaka S, Kato E, Tomikubo Y, Otsuka K. (2003). "Structural change of Ni species during the methane decomposition and the subsequent gasification of deposited carbon with CO2 over supported Ni catalysts." *JOURNAL OF CATALYSIS* 219 (1): 176.

Tavares, M.T., Bernardo, C.A., Alstrup, I, Rostrup-Nielsen, J.R. (1986). "Reactivity of Carbon Deposited on Nickel-Copper Alloy Catalysts from the Decomposition of Methane." *Journal of Catalysis* 100(2), 545-548.

Van Steen, E., Sewell, G.S., Makhothe, R.A., Micklethwaite, C., Manstein, H., Le Lange, M. and O'Connor, C.T. (1996). "TPR Study on the Preparation of Impregnated Co/SiO_2 Catalysts." *Journal of Catalysis* 162, 220-229.

Wei, J. and Iglesia E. (2003). "Structural Requirements and Activation Pathways in Reactions of Methane Catalyzed by Supported Metals." *18th North American Catalysis Society Meeting,* Cancun, Mexico, 286.

Yang, R.T. and Chen, J.P. (1989). "Mechanims of Carbon Filament Growth on Metal Catalysts." *Journal of Catalysis* 115, 52-64.

Yokoyama, H., Numakura, H., and Koiwa, M. (1998). "The Solubility and Diffusion of Carbon in Palladium." *Acta Materialia* 46(8), 2823-2830.

Zadeh, J.S.M., and Smith, K.J. (1998). "Kinetics of CH_4 Decomposition on Supported Cobalt Catalysts." *Journal of Catalysis* 176(1), 115-124.

Zhang, T.J., Amiridis, M.D. (1998). "Hydrogen Production via the Direct Cracking of Methane over Silica-supported Nickel Catalysts." *Applied Catalysis A: General* 167(2), 161-172.

Zhang, T.J., Wilson, C., Agler, H., and Amiridis, M.D. (1996a). "Deactivation and Subsequent Regeneration of Silica-Supported Nickel Catalysts during Methane Cracking." *Abstracts of Papers of the American Chemical Society* 211, 7.

Zhang, Z.L., Tsipouriari, V.A., Efstathiou, A.M., and Verykios, X.E. (1996b). "Reforming of Methane with Carbon Dioxide to Synthesis Gas over Supported Rhodium Catalysts .1. Effects of Support and Metal Crystallite Size on Reaction Activity and Deactivation Characteristics." *Journal of Catalysis* 158(1), 51-63.

Appendices

Appendix A Differential Reactor

A.1 Introduction

In investigating heterogeneously catalyzed reactions, an important, early objective is to determine whether intrinsic catalyst activity has been measured. Heat or mass transfer effects, caused by intrareactor, interphase, or intraparticle gradients, can disguise the results and lead to misinterpretations. Before accurate and intrinsic catalyst kinetic data can be established, these disguises must be eliminated by adjusting the experimental conditions. In order to make sure the activity measured is the intrinsic activity, the effect of external mass transfer and internal diffusion must be minimized. The guidelines for catalyst testing described by Dautzenberg (1988), by Rase (1990) and by Froment and Bischoff (1990) were followed in the present study and are described in the following sections.

A.2 Catalyst Testing Parameters

The available catalyst and reactor parameters are presented in Table A.1.

Table A.1 Parameters of catalyst and reactor.

	Symbol & value
Diameter of reactor	$D=7.5\times10^{-3}$ m
Diameter of catalyst particle	$d_p'=1.7\times10^{-4}$ m
Length of reactor	$L_R=6\times10^{-1}$ m
Length of catalyst bed	$L=1\times10^{-2}$ m

A.3 Reactor Flow Pattern: Plug Flow Operation

Even when plug flow is believed to prevail, great care must be exercised to ensure that the flow pattern is ideal. The diameter of the PFR (D) must be at least 10 times the catalyst particle diameter (d_p') (D/d_p' >10). This eliminates the influence of the reactor walls on the flow pattern. In the present study, D/d_p'=44, which satisfied the condition D/d_p'>10.

Furthermore, axial gradients may exist by virtue of conversion. These effects are minimized by selecting the correct ratio of bed length to particle diameter (L/d_p'). For gas-solid systems the catalyst bed length (L) should be at least 50 times greater than the particle diameter (L/d_p'>50). For the experimental set-up of the present study L/d_p'=59, which satisfied the criteria L/d_p'=50. Furthermore, Table A.2 gives the alternative steps to calculate the required L/d_p' for laboratory fixed-bed reactors:

Table A.2 Steps for ensuring plug flow operation in laboratory reactors.

1. Determine the viscosity of the fluid medium at reactor conditions: Assuming viscosity of fluid medium equal to pure Ar, $\mu = 2.1\times10^{-5} Ns/m^2$
2. Calculate the superficial fluid velocity (u): $u = \frac{V}{\left(\frac{\pi D^2}{4}\right)} = \frac{180cc/\min\times10^{-6}/60*(673/273)}{\frac{3.14\times(7.5\times10^{-3})^2}{4}} = 0.17m/s$ (A.1)
3. Calculate the particle Reynolds number: $N_{Re_p} = \frac{ud_p'\rho}{\mu}$ (A.2) Herein, $\rho = 1.784kg/m^3$; Accordingly, $N_{Re_p} = \frac{ud_p'\rho}{\mu} = \frac{0.17m/s\times0.17\times10^{-3}m\times1.784kg/m^3}{2.1\times10^{-5}Ns/m^2} = 2.46$
4. Calculate the Peclet number:

$$N_{P_e} = (0.087)N_{\mathrm{Re}_P}^{0.23}\left(\frac{L}{d'_p}\right) \text{ (for gas-phase operation)} \quad \text{(A.3)}$$

Herein, $\frac{L}{d'_p} = 59$ then $N_{P_e} = (0.087)N_{\mathrm{Re}_P}^{0.23}\left(\frac{L}{d'_p}\right) = 0.087 \times (2.46)^{0.23}(59) = 6.31$

5. Calculate $N_{P_{e\min}}$:

$$N_{P_{e\min}} = 8n \ln \frac{1}{1-X} \quad \text{(A.4)}$$

Herein n=1, then $N_{P_{e\min}} = 8n \ln \frac{1}{1-X} = 8 \times \ln \frac{1}{1-0.1} = 0.84$

6. Acceptable deviation from plug flow can be assumed if:

$$N_{Pe} > N_{Pe\min} \quad \text{(A.5)}$$

Herein, $N_{Pe} = 6.31 > N_{Pe\min} = 0.84$, which is acceptable deviation from plug flow.

7. The minimum L/d'_p follows from:

$$\frac{L}{d'_p} > 92.0 N_{\mathrm{Re}_P}^{-0.23} n \ln \frac{1}{1-X} \text{ (for gas-phase operation)} \quad \text{(A.6)}$$

Herein, $\frac{L}{d'_p} = 59 > 92.0 N_{\mathrm{Re}_P}^{-0.23} n \ln \frac{1}{1-X} = 92.0 \times (2.46)^{-0.23} \times 1 \times \ln \frac{1}{1-0.1} = 7.88$

The above calculations show that L/d'_p of the present study satisfied the required L/d'_p for laboratory plug flow operation of fixed-bed reactors.

A.4 Reactor Isothermal Operation

The extent to which catalyst activity measurements are disturbed by intrareactor, interphase, and intraparticle effects of heat transport was assessed by evaluating the experimental catalyst performance using the mathematical criteria in Table A.3. In all cases, the criteria for isothermal operation were met.

Table A.3 Criteria for Isothermal Operation.

Intrareactor	
$\frac{\lvert\Delta H\rvert R_V r_i^2}{k_b T_w} < 0.2\frac{RT_w}{E}$ (A.7)	$\frac{\lvert\Delta H\rvert R_V r_i^2}{k_b T_w} = \frac{75600\times0.03\times455\times(3.75\times10^{-3})^2}{1.2\times773} = 1.56\times10^{-2} < 0.2\frac{RT_w}{E} = 0.2\times\frac{8.314\times773}{42000} = 3.06\times10^{-2}$
Interphase	
$\frac{\lvert\Delta H\rvert R' \rho_P d_P'}{h_s T_b} < 0.3\frac{RT_b}{E}$ (A.8) $h_s = \frac{0.357}{\left(\frac{d_p' G}{\mu}\right)^{0.359}} c_P G$ (A.9)	$\frac{\lvert\Delta H\rvert R' \rho_P d_P'}{h_s T_b} = \frac{75600\times0.03\times455\times1.7\times10^{-4}}{22.5\times773} = 0.01 < 0.3\frac{RT_b}{E} = 0.3\times\frac{8.314\times773}{42000} = 4.59\times10^{-2}$ $h_s = \frac{0.357}{\left(\frac{d_p' G}{\mu}\right)^{0.359}} c_p G = \frac{0.357}{\left(\frac{1.7\times10^{-4}\times0.12}{2.1\times10^{-5}}\right)^{0.359}}\times520\times0.12 = 22.5 J/m^2/s/K$
Intraparticle	
$\frac{\lvert\Delta H\rvert R' \rho_P r_P^2}{k_P T_S} < 0.75\frac{RT_S}{E}$ (A.10)	$\frac{\lvert\Delta H\rvert R' \rho_P r_P^2}{k_P T_S} = \frac{75600\times0.03\times455\times(8.5\times10^{-5})^2}{1.7\times10^{-2}*773} = 5.67\times10^{-4} < 0.75\frac{RT_S}{E} = 0.75\times\frac{8.314\times773}{42000} = 1.15\times10^{-1}$

Where $\rho_P = 455 kg/m^3$; $c_P = 520 J/kg/K$; E =42kmol/mol; $\lvert\Delta H\rvert = 75.6 kJ/mol$; $k_b = 1.2 W/m/K$;

$k_p = 1.7\times10^{-2} W/m/K$; T =773K; $G = u\times\rho = 0.07\times1.784 = 0.12$ kg/m^2/s.

$R' = 1.8 mmol/\min/gcat = 0.03 mol/s/kgcat$; $R_V = R'\times\rho = 0.03*455 mol/s/m^3$.

A.5 Diagnostic Tests for Interphase (External) Transport Effects

A check for external transport limitations was performed using guidelines described by Froment and Bischoff (1990). In a flow system, the flow rate can be varied while the space velocity is kept constant. If the conversion remains constant, the influence of interphase and intrareactor effects may be assumed to be negligible. Figure A.1 shows the conversion hardly changed with varied flow rates while space velocity was kept constant. The diagnostic test confirms that there was no external transport limitation at the conditions of the present study.

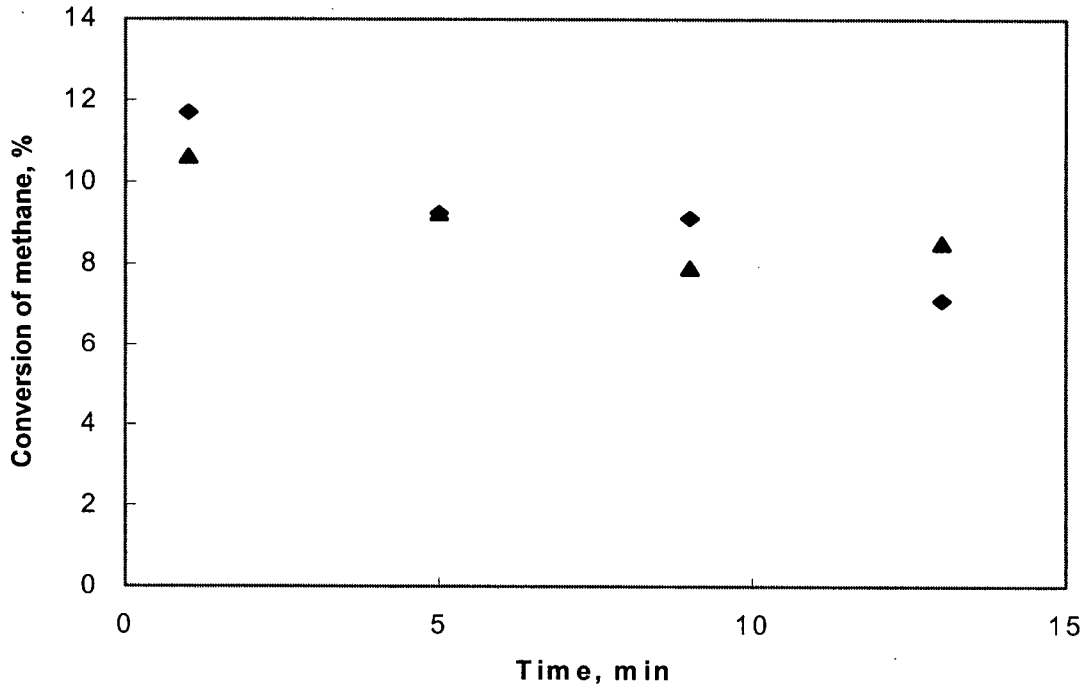

Figure A.1 Diagnostic tests for interphase (external) transport effect (▲140mL(STP)/min; ♦210 mL(STP)/min, SV=19,000hr^{-1}, T=673K, 5%CH_4/Ar, 12wt% Co/SiO_2).

A.6 Diagnostic Tests for Internal Transport Effect

Changing the catalyst particle size can be used to test intraparticle effects. If there is no change in catalyst activity with change in particle size (assuming the exposed surface area of active catalyst is constant), the catalyst is considered to be free of intraparticle gradients. Figure A.2 shows that the conversion does not change with the change of catalyst particle size during CH_4 decomposition over Co catalyst. This result confirmed that there was no intraparticle effect in the present study.

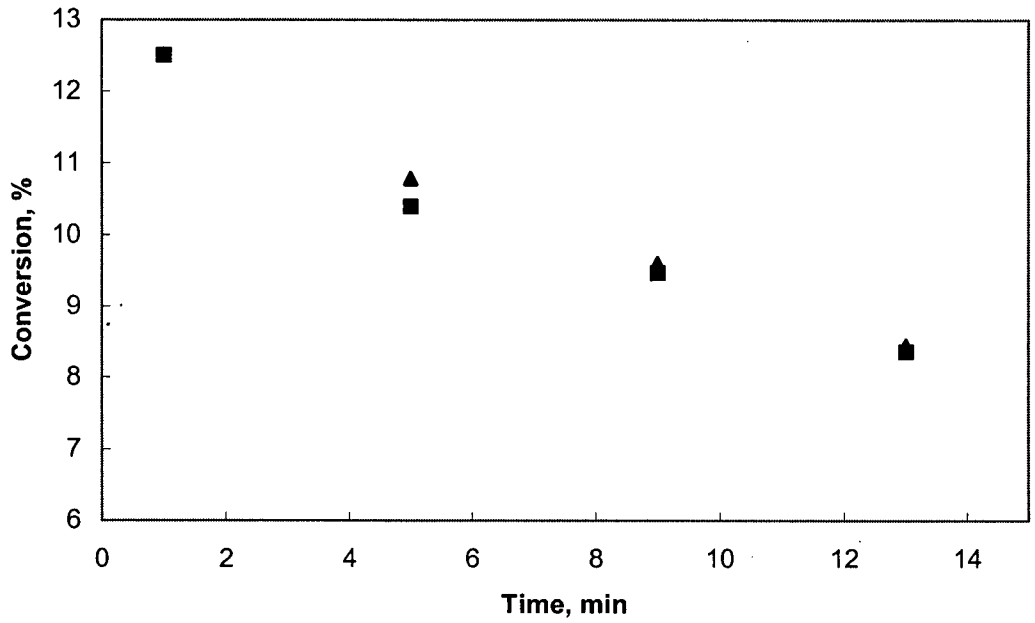

Figure A.2 Diagnostic tests for intraparticle transport effects (▲Particle size=170μm, ■Particle size=90μm, T=673K, 140mL/min, 5%CH_4/Ar, SV=19,000hr^{-1}, 12wt% Co/SiO_2).

Based on the above observations, it can be concluded that for the range of experimental conditions of present study, there were no internal or external gradients of concentration or temperature.

A.7 Reactor Differential Operation

Differential operation is reached when the conversion over the catalyst bed is so small that the change in composition over the catalyst bed does not influence the rate of carbon formation. It is the limited to the linear part of the conversion versus space-time curve. Also, the flow of fluid through a packed bed generally results in a decreasing gradient of total pressure. This can produce an axial change of reactant partial pressure. In order to ensure isobaric operation, the particle diameter should be selected carefully. This differential operation allows one to assume that temperature, pressure and concentration are constant through the thin catalyst bed layer. In this sense the differential reactor is the simplest gradientless reactor.

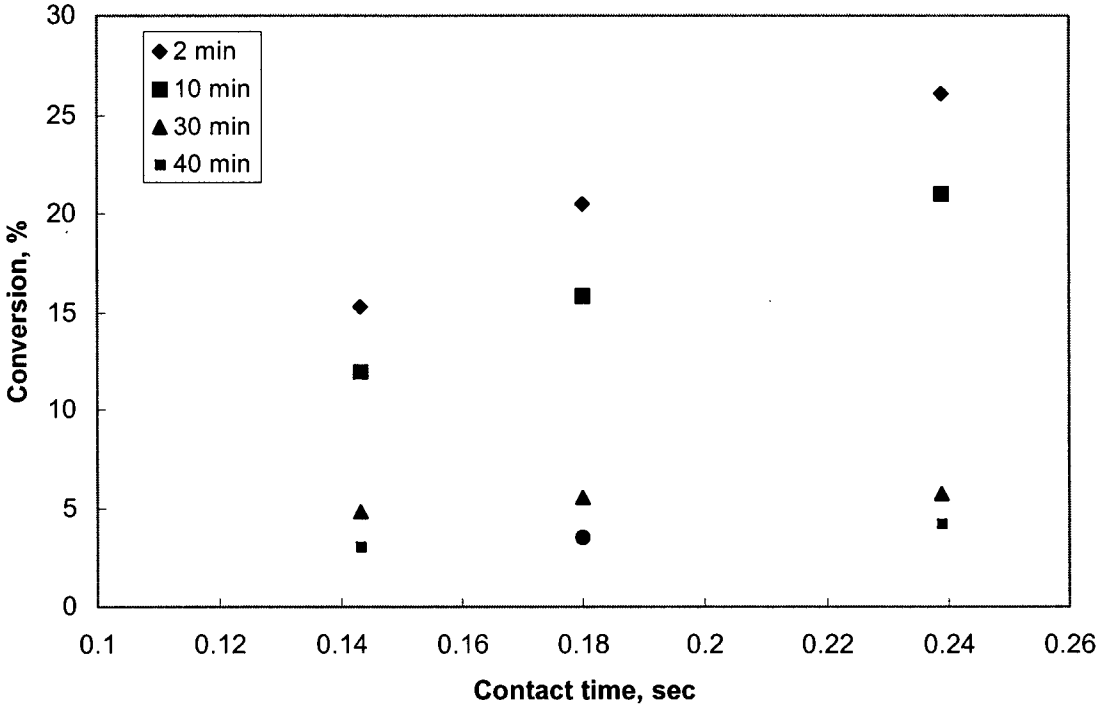

Figure A.3 Diagnostic tests for differential operation.

Differential operation was checked by a number of experimental tests. The results of CH_4 conversion versus contact time at different time-on-stream, shown in Figure A.3, confirmed that operating conditions of the current study was limited to the linear part of the conversion versus space-time curve. For the most severe conditions, the conversion of methane, based on the feed flow rate through the catalyst bed, was below 15%.

Appendix B Example of Activity Calculation and Curve Fitting

B.1 Example of Activity Calculation

Table B.1 Example of activity calculation spreadsheet.

Run	Y144 650 Rdn 500Rxn 5wt%Co SiO_2 CH_4=182 H_2=10 Ar=48 varain GC					Rxn at 500 and Rdn from 50 TO 650°C in an hour	
Catalyst	0.05	5wt% Co/SiO_2					
Reduction	650	°C					
Feed Flow Meter (set point)	182	cc/min					
Cat wt	0.25g						
CH_4 in CH_4/Ar feed content	0.57	(FID)					
Rxn Temp	500	°C					
	CH_4/Ar	Ar	H_2	Total			
Meter Feed Flow	182	48.00	10.00				
Corrected Meter Flow, sccm	127.61	80.53	15.33	223.47	cc/min		
Measured Total Flow							
	CH_4	Ar	H_2				
Feed mol frac	0.57	0.36	0.07				
Feed mmol/min	5.69	3.59	0.68	9.97	mmol/min		
Experiment		H_2TCD	CH_4 FID[a]				
Calibration Factors		2.62E-13	2.27E-12	CH_4 from FID	H_2		CH_4 from FID [c]
Sampling No.	Time min	moles/area	moles/area	fraction of moles	fraction of moles	CH_4 X[b]	mmol/ min/g
S1	0.5	2729588	2023387	0.56	0.09	1.38	0.31
S2	3.8	2976535	2017234	0.56	0.10	1.68	0.38
S3	7.1	3126477	2007769	0.56	0.10	2.14	0.49
S4	10.4	3168554	2005892	0.56	0.10	2.23	0.51
S5	13.7	3117019	2005129	0.56	0.10	2.27	0.52
S6	17.0	3045161	2009570	0.56	0.10	2.05	0.47
S7	20.3	2953359	2014678	0.56	0.09	1.80	0.41
S8	23.6	2855800	2019168	0.56	0.09	1.58	0.36
S9	26.9	2775058	2024542	0.56	0.09	1.32	0.30

S10	30.2	2674955	2028177	0.56	0.09	1.14	0.26
S11	33.5	2619172	2032761	0.57	0.08	0.92	0.21
S12	36.8	2564711	2030958	0.57	0.08	1.01	0.23
S13	40.1	2490466	2034264	0.57	0.08	0.85	0.19
S14	43.4	2451519	2037638	0.57	0.08	0.68	0.16
S15	46.7	2420696	2039165	0.57	0.08	0.61	0.14
S16	50.0	2389595	2039240	0.57	0.08	0.60	0.14
S17	53.3	2362315	2040876	0.57	0.08	0.52	0.12
S18	56.6	2410885	2039089	0.57	0.08	0.61	0.14
S19	59.9	2329779	2042022	0.57	0.07	0.47	0.11
S20	63.2	2311303	2041744	0.57	0.07	0.48	0.11
S21	66.5	2306260	2041338	0.57	0.07	0.50	0.11

Note:

[a]: CH_4 FID calibration factors=Moles of CH_4 in the sampling valve/area in FID (calibrated gas);

[b]: Conversion of CH_4= 100*(molar fraction of CH_4 in inlet-molar fraction of CH_4 in outlet)/molar fraction of CH_4 in inlet ;

[c]: Decomposition rate of CH_4=Conversion of CH_4*total molar flow rate/weight of catalyst.

B.2 Examples of Curve Fitting Results

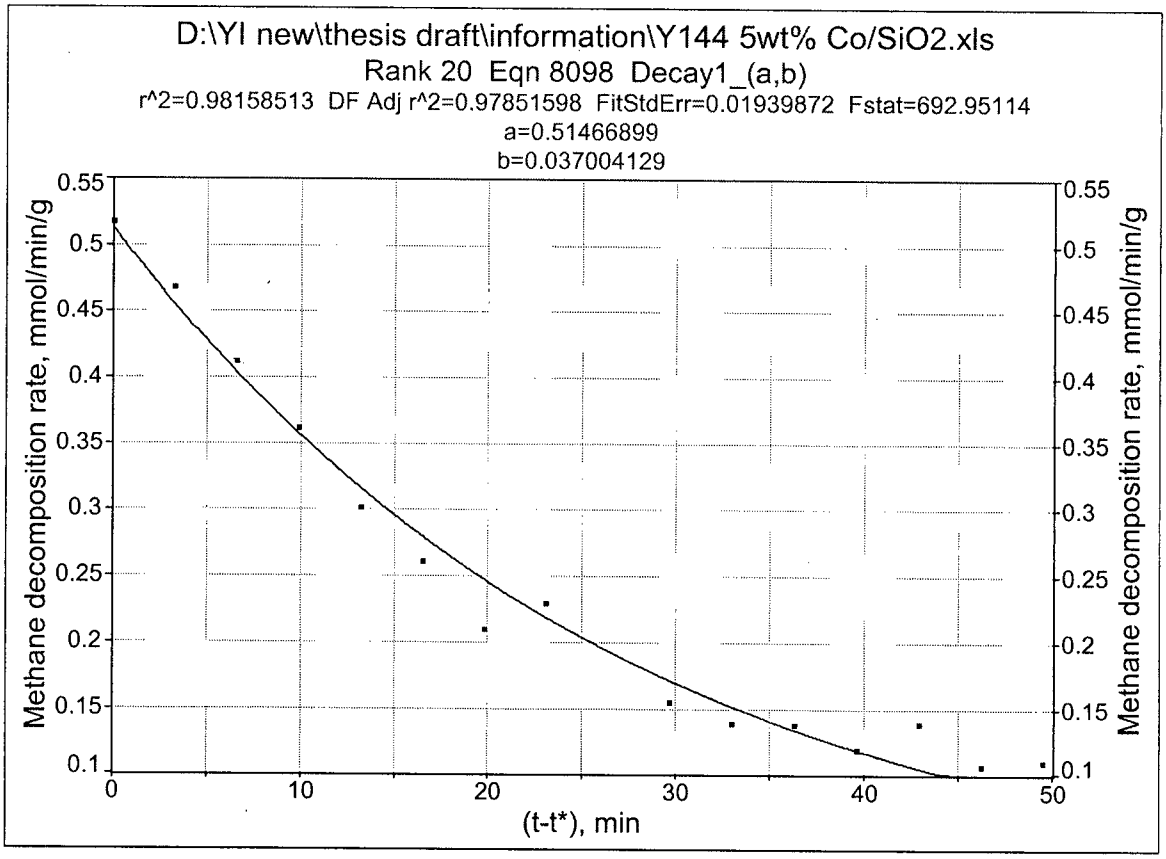

Rank 20 Eqn 8098 Decay1_(a,b)

r^2 Coef Det	DF Adj r^2	Fit Std Err	F-value
0.9815851279	0.9785159825	0.0193987197	692.95114099

Parm	Value	Std Error	t-value	95% Confidence Limits		P>|t|
a	0.514668986	0.012766141	40.31515693	0.487089414	0.542248557	0.00000
b	0.037004129	0.001649077	22.43930035	0.033441515	0.040566743	0.00000

Area Xmin-Xmax	Area Precision
11.681120496	1.485066e-19

Function min	X-Value	Function max	X-Value
0.0824192932	49.500000000	0.5146689856	1.302334e-10
1st Deriv min	X-Value	1st Deriv max	X-Value
-0.019044878	1.302334e-10	-0.003049854	49.500000000
2nd Deriv min	X-Value	2nd Deriv max	X-Value
0.0001128572	49.500000000	0.0007047391	1.302334e-10

Procedure	Minimization	Iterations
LevMarqdt	Least Squares	8

r^2 Coef Det	DF Adj r^2	Fit Std Err	Max Abs Err
0.9815851279	0.9785159825	0.0193987197	0.0371376971

Source	Sum of Squares	DF	Mean Square	F Statistic	P>F
Regr	0.26076467	1	0.26076467	692.951	0.00000
Error	0.0048920342	13	0.00037631033		
Total	0.2656567	14			

Description: Y144 5wt% Co/SiO2

X Variable: time

Xmin:	0.0000000000	Xmax:	49.500000000	Xrange:	49.500000000
Xmean:	24.640000000	Xstd:	16.256198818	Xmedian:	23.100000000
X@Ymin:	46.200000000	X@Ymax:	0.0000000000	X@Yrange:	46.200000000

Y Variable: rate, mmol/min/g

Ymin:	0.1070120911	Ymax:	0.5181675635	Yrange:	0.4111554724
Ymean:	0.2448871252	Ystd:	0.1377515113	Ymedian:	0.2102216655
Y@Xmin:	0.5181675635	Y@Xmax:	0.1101102729	Y@Xrange:	0.4080572906

B.3 Calculation of K_M^* and K_M^f

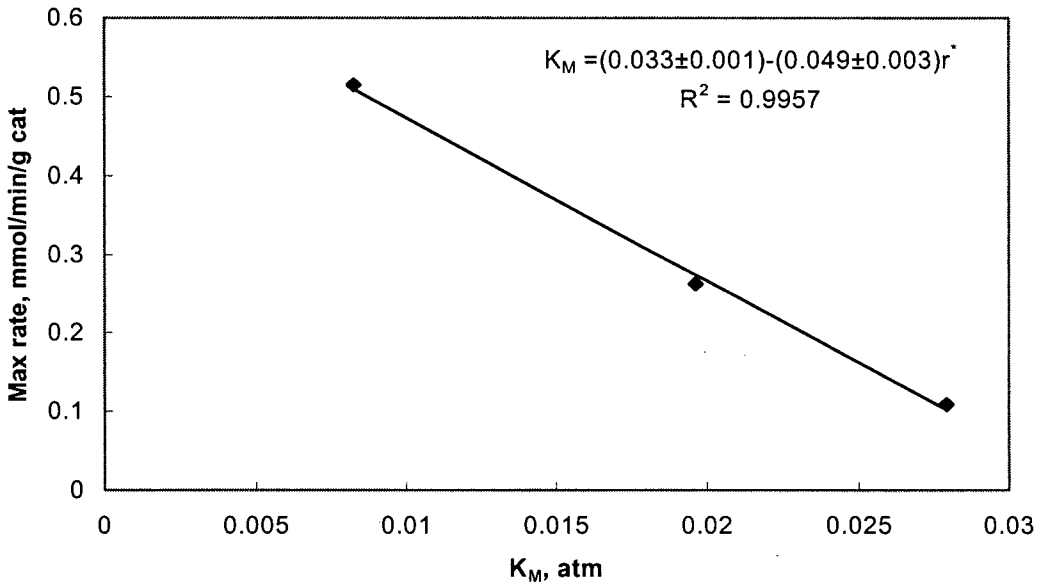

Figure B.1 Maximum CH_4 decomposition rate versus K_M at 773K on 5wt% Co/SiO_2 (reduced at 923K) with $K_M^* = 0.033 \pm 0.001$ atm.

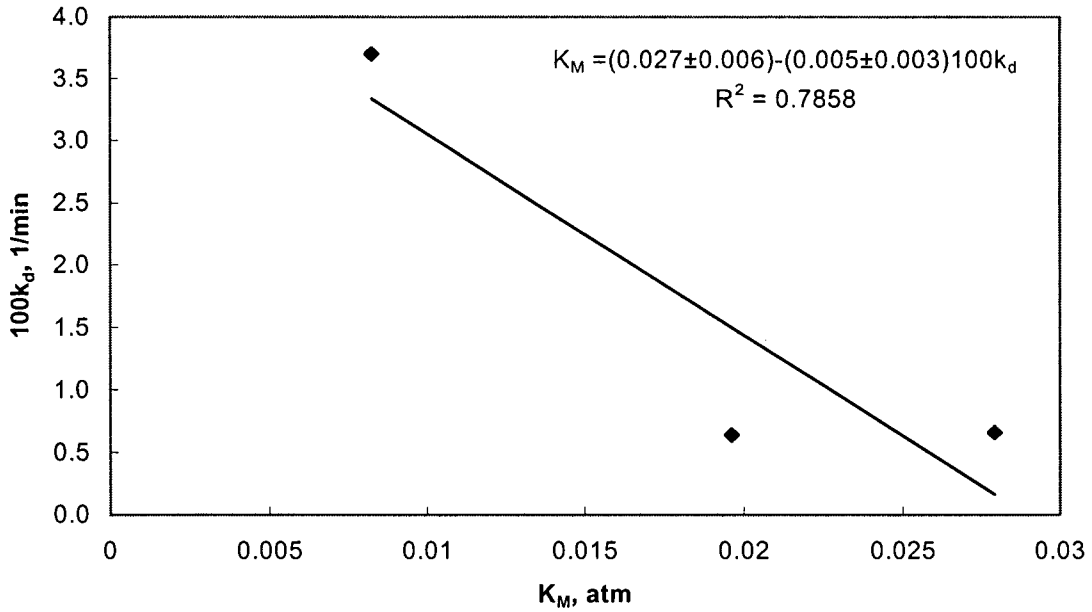

Figure B.2 Decay constant versus K_M at 773K on 5wt% Co/SiO_2 (reduced at 923K) with $K_M^f = 0.027 \pm 0.006$ atm.

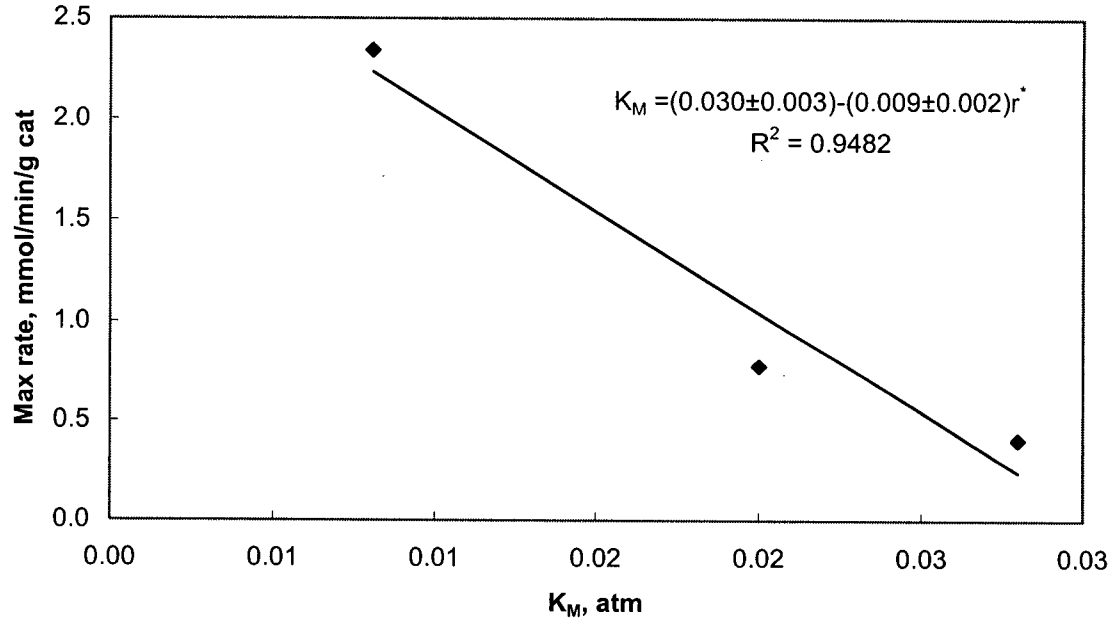

Figure B.3 Maximum CH_4 decomposition rate versus K_M at 773K on 10wt% Co/SiO_2 (reduced at 923K) with $K_M^* = 0.030 \pm 0.003$ atm.

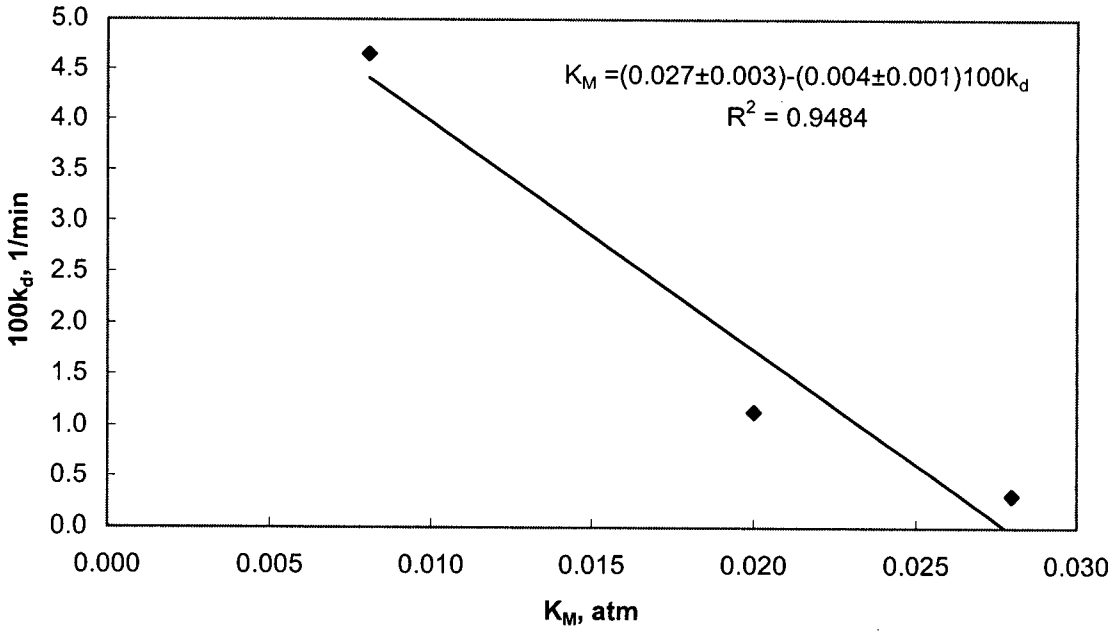

Figure B.4 Decay constant versus K_M at 773K on 10wt% Co/SiO_2 (reduced at 923K) with $K_M^f = 0.027 \pm 0.003$ atm.

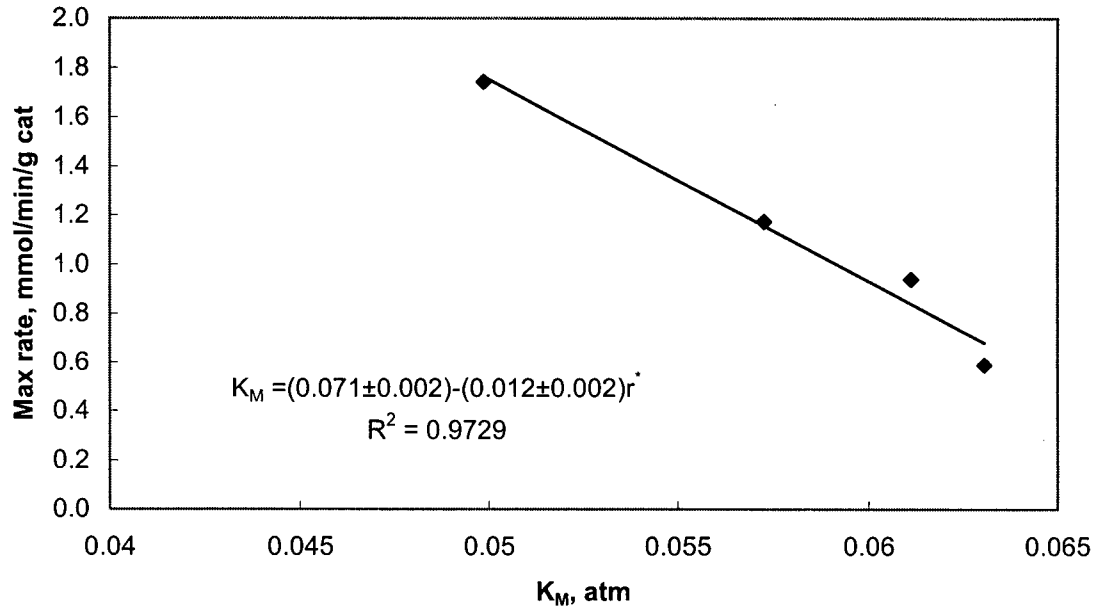

Figure B.5 Maximum CH_4 decomposition rate versus K_M at 773K on 30wt% Co/SiO_2 (reduced at 923K) with $K_M^* = 0.071 \pm 0.002$ atm.

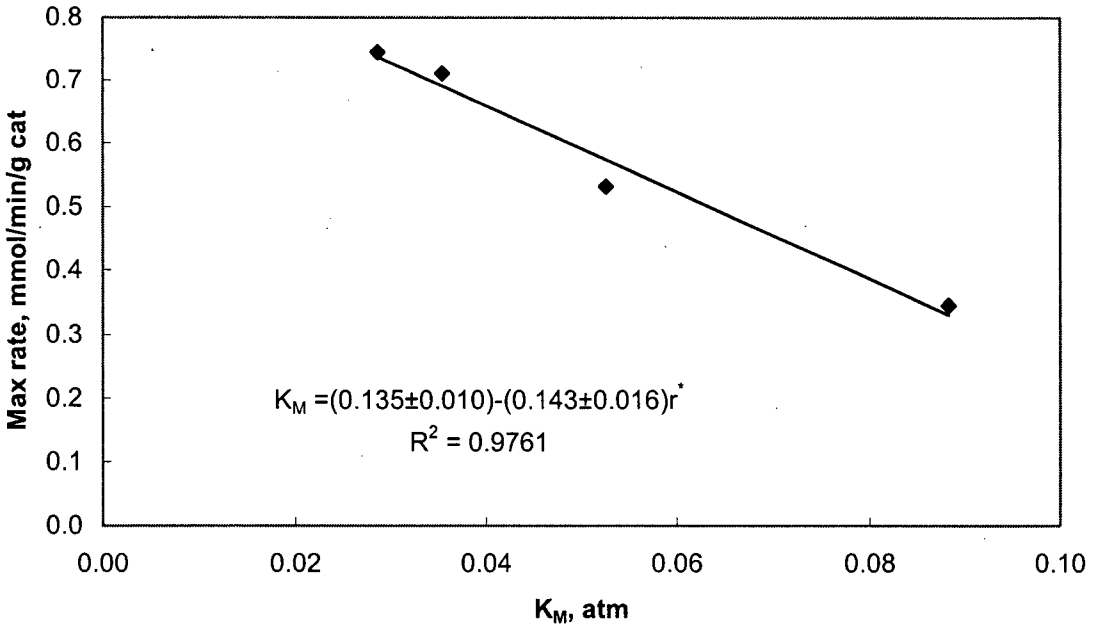

Figure B.6 Maximum CH_4 decomposition rate versus K_M at 773K on 15wt% Ni/SiO_2 (reduced at 923K) with $K_M^* = 0.135 \pm 0.010$ atm.

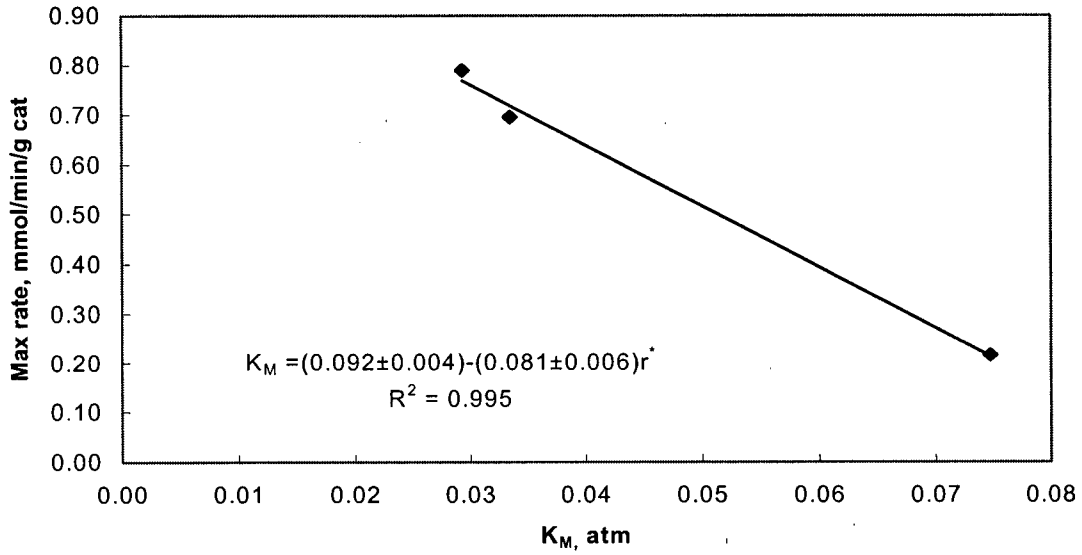

Figure B.7 Maximum CH_4 decomposition rate versus K_M at 773K on 30wt% Ni/SiO_2 (reduced at 923K) with $K_M^* = 0.092 \pm 0.004$ atm.

Note that the simple linear correlation described the data of Figure B.1, Figure B.5 to Figure B.7 quite well. To be consistent, the linear correlation was also used to describe the data of Figure B.2, Figure B.3 and Figure B.4 although the middle point was below the line in each case. This approach provided reasonable estimates of the x-axis intercept, as shown by the deviation errors of estimation of K_M^* and K_M^f, listed in the caption of each figure.

B.4 Carbon Diffusivity Data

Table B.2 Carbon diffusivity data (Yokoyama et al., 1998).

Host	D_0 (m^2/s)	E_D (kJ/mol)	Temperature range, K		Ref
Pd	1.99526×10^{-5}	132	1223	1378	Present work
r-Fe	6.60693×10^{-5}	157	1198	1371	Smith
	2.34423×10^{-5}	148	1123	1578	Agren
Co	1.77828×10^{-4}	174	1125	1370	Smith
	8.12831×10^{-6}	149	723	1073	Cernak et. al.
Ni	3.38844×10^{-5}	149	1125	1372	Smith
	3.01995×10^{-5}	149	843	1123	Cermak and Mehrer

Appendix C XPS Spectra

C.1 XPS Survey Scan Spectra

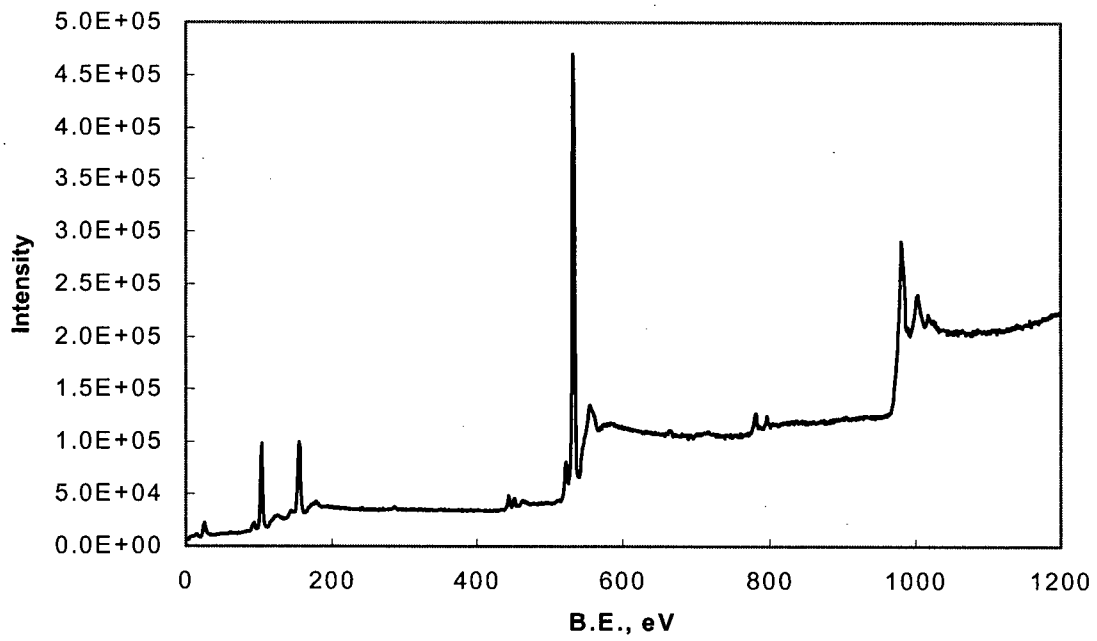

Figure C.1 Survey scan spectrum on $Co/BaO/SiO_2$ after reduction.

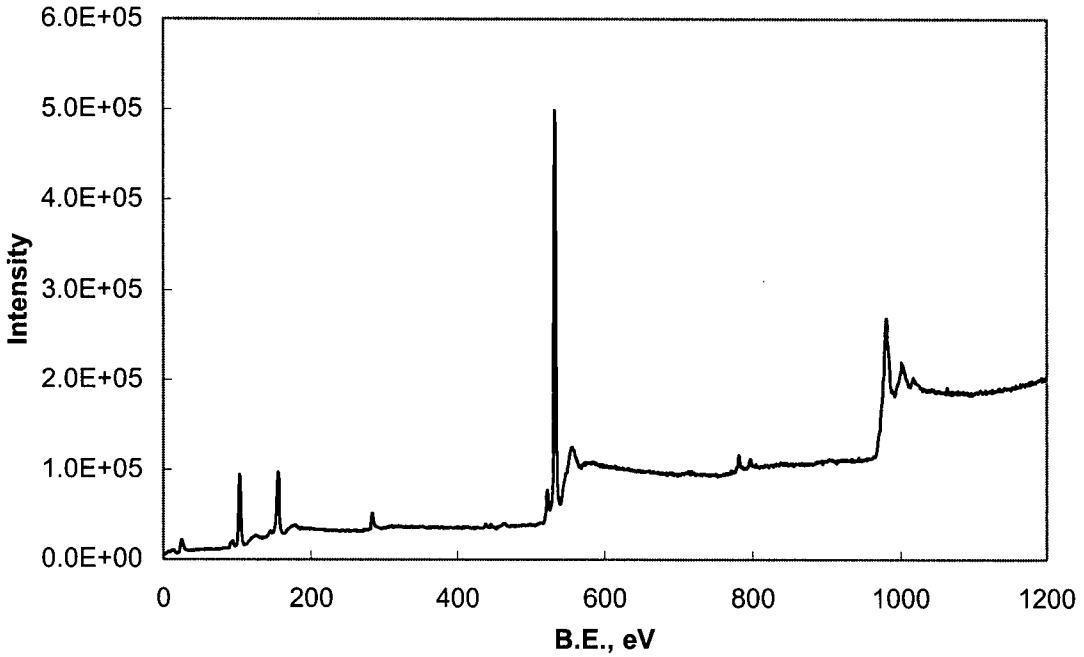

Figure C.2 Survey scan spectrum on $Co/BaO/SiO_2$ after reaction.

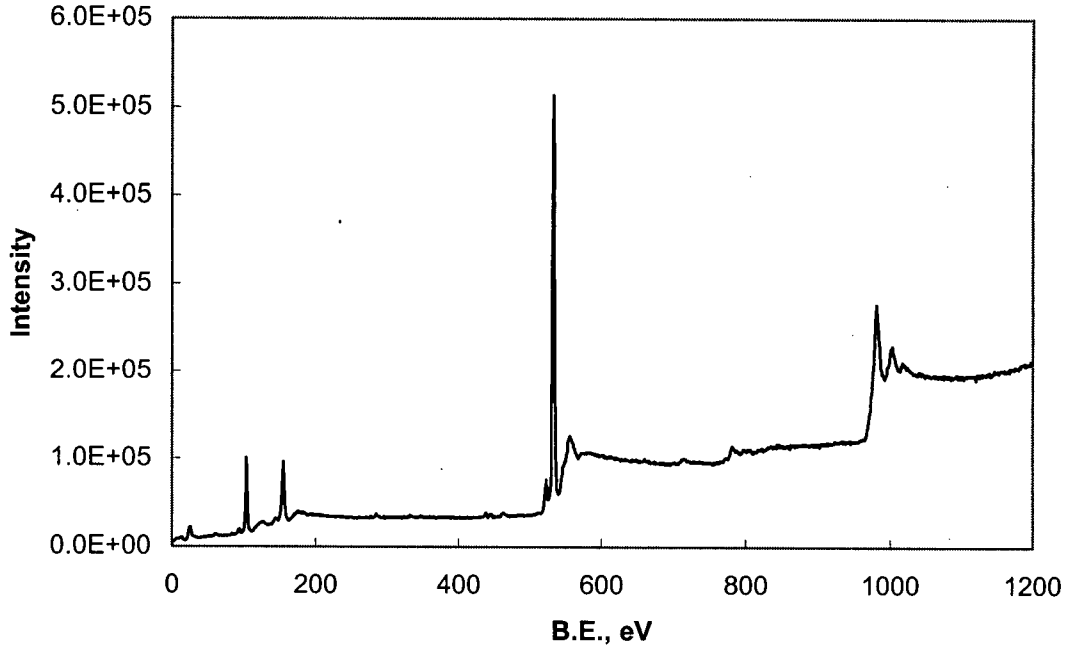

Figure C.3 Survey scan spectrum on $Co/ZrO_2/SiO_2$ after reduction.

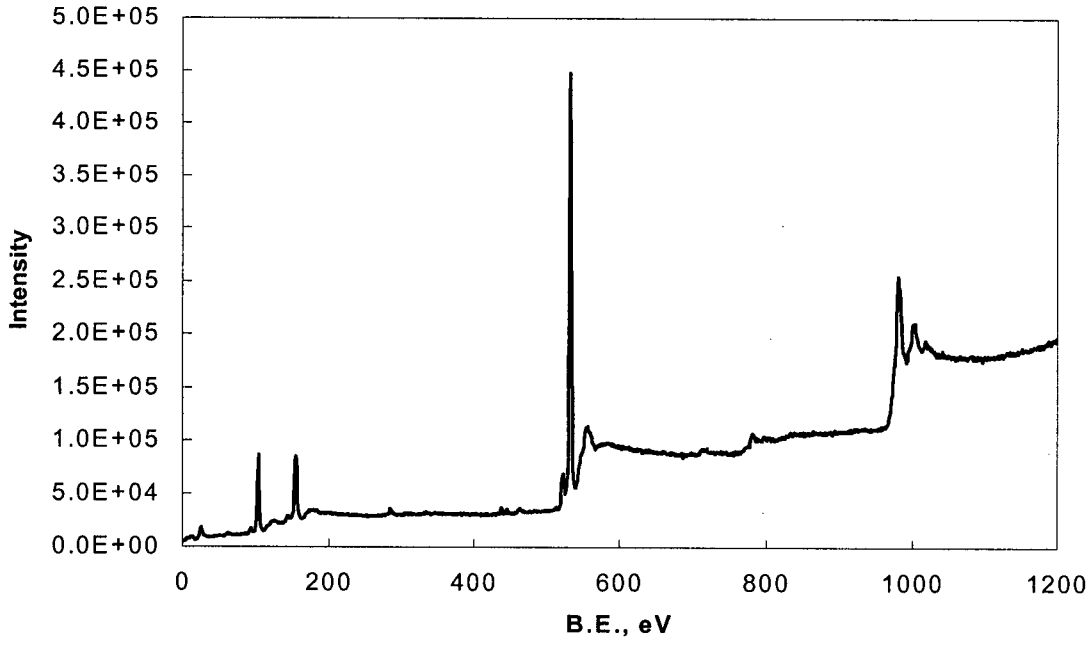

Figure C.4 Survey scan spectrum on $Co/ZrO_2/SiO_2$ after reaction.

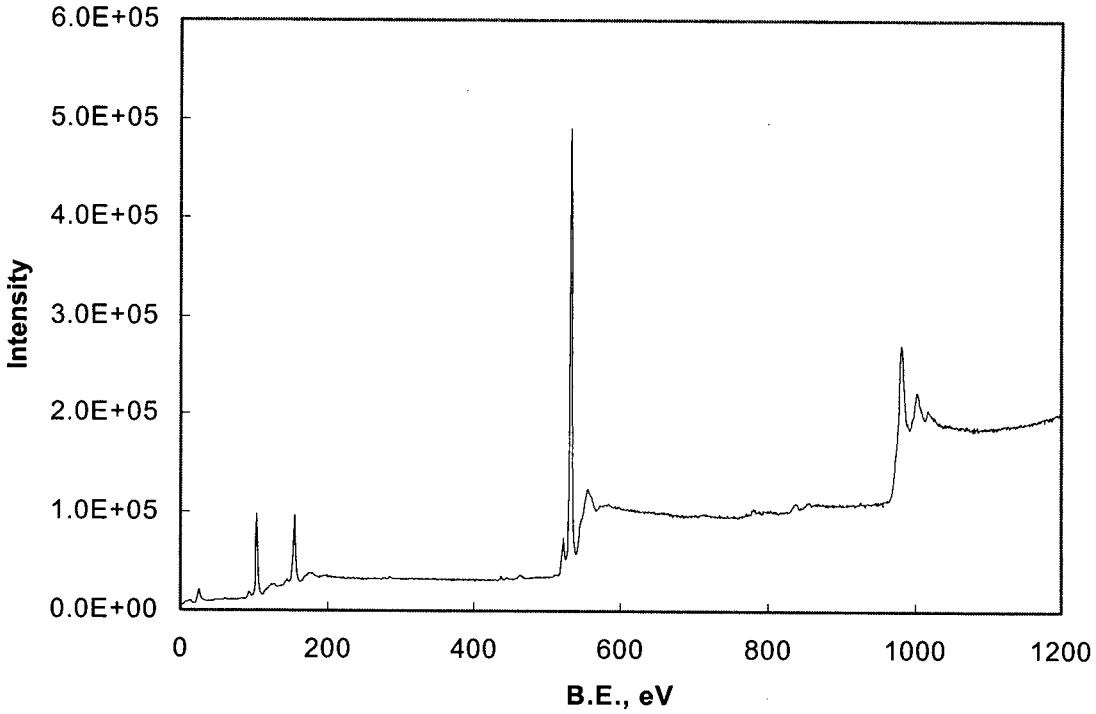

Figure C.5 Survey scan spectrum on $Co/La_2O_3/SiO_2$ after reduction.

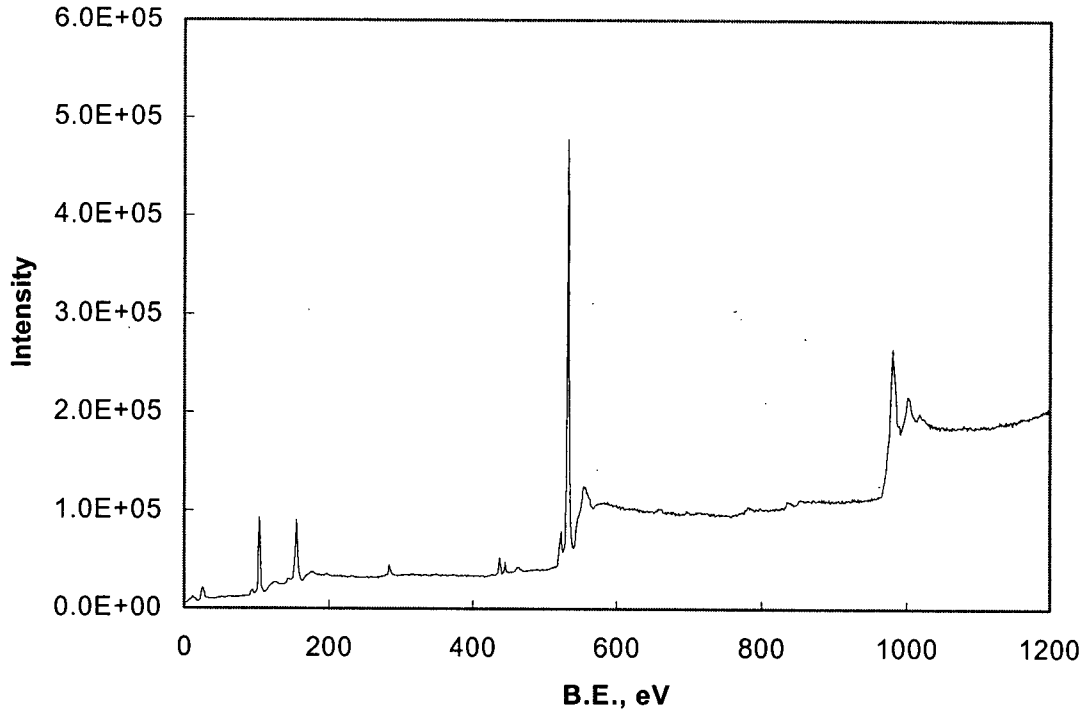

Figure C.6 Survey scan spectrum on $Co/La_2O_3/SiO_2$ after reaction.

C.2 XPS Narrow Scan Co 2p Spectra

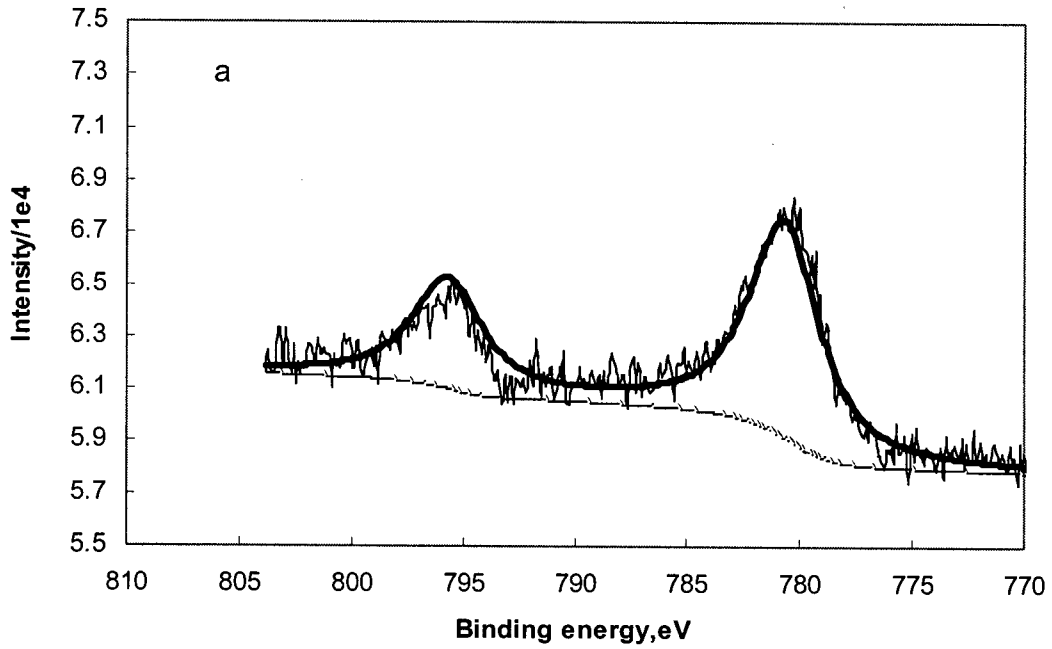

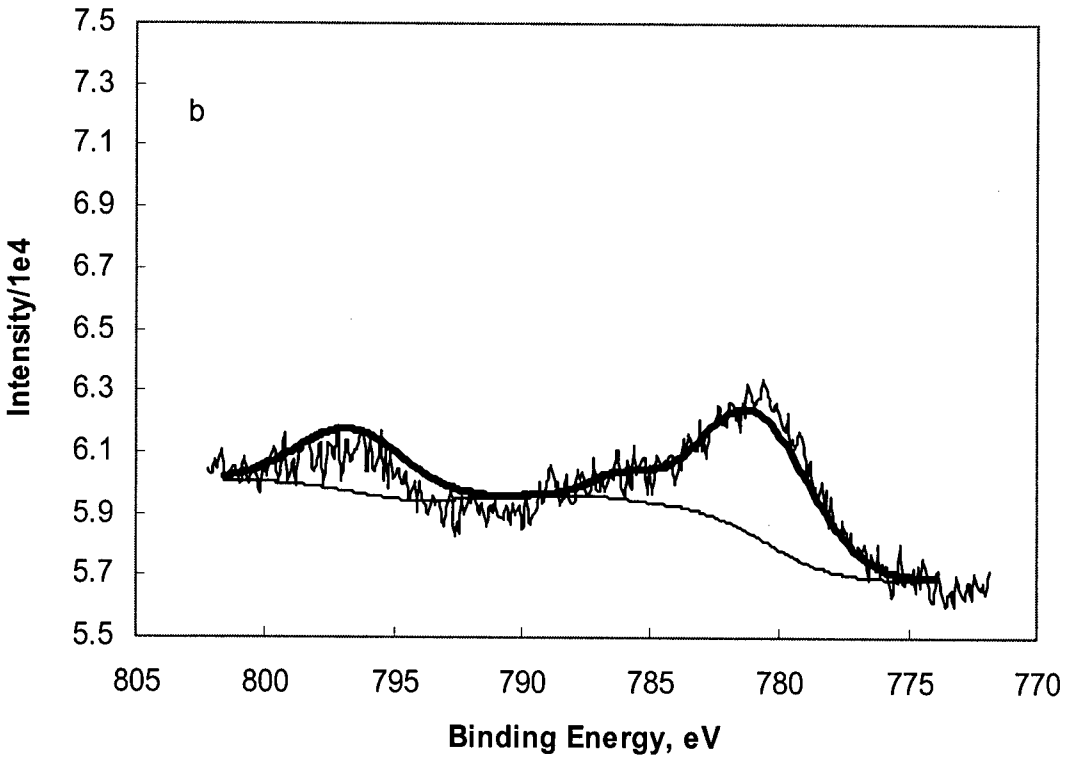

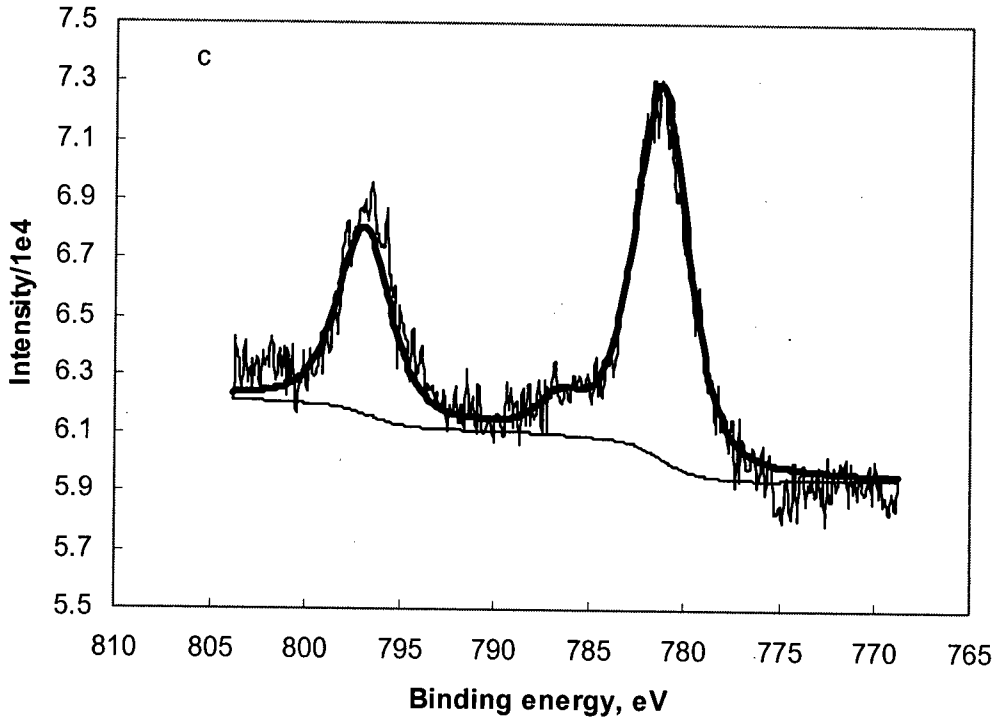
c
Intensity/1e4
7.5
7.3
7.1
6.9
6.7
6.5
6.3
6.1
5.9
5.7
5.5
810
805
800
795
790
785
780
775
770
765
Binding energy, eV

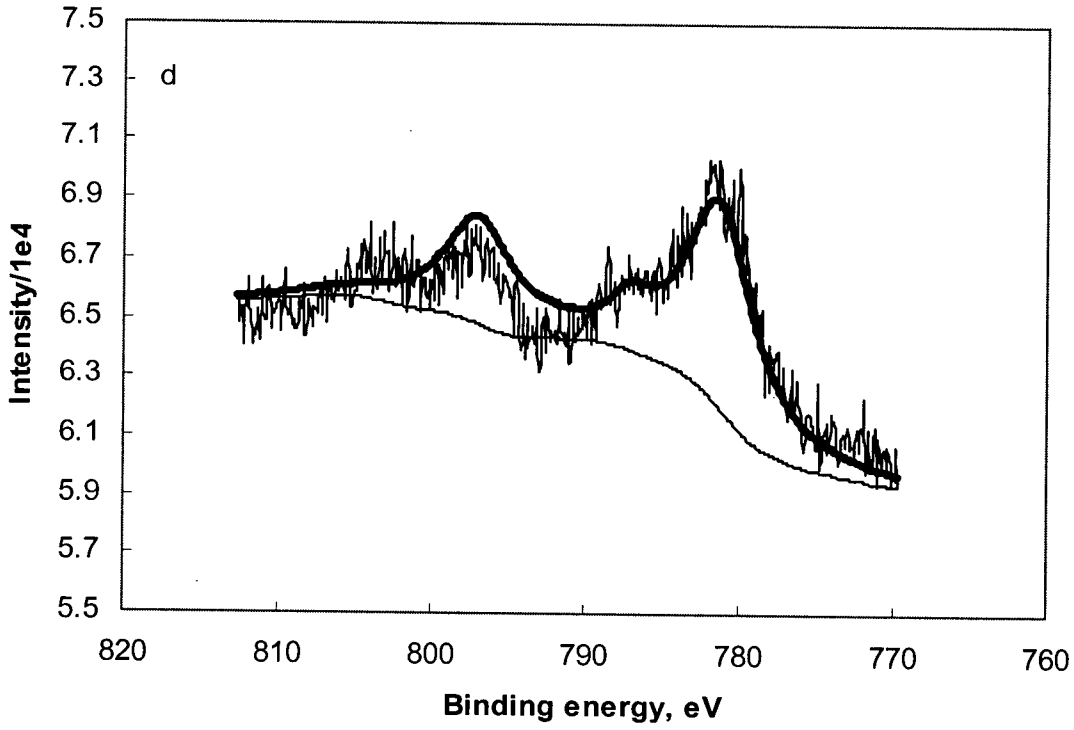
d
Intensity/1e4
7.5
7.3
7.1
6.9
6.7
6.5
6.3
6.1
5.9
5.7
5.5
820
810
800
790
780
770
760
Binding energy, eV

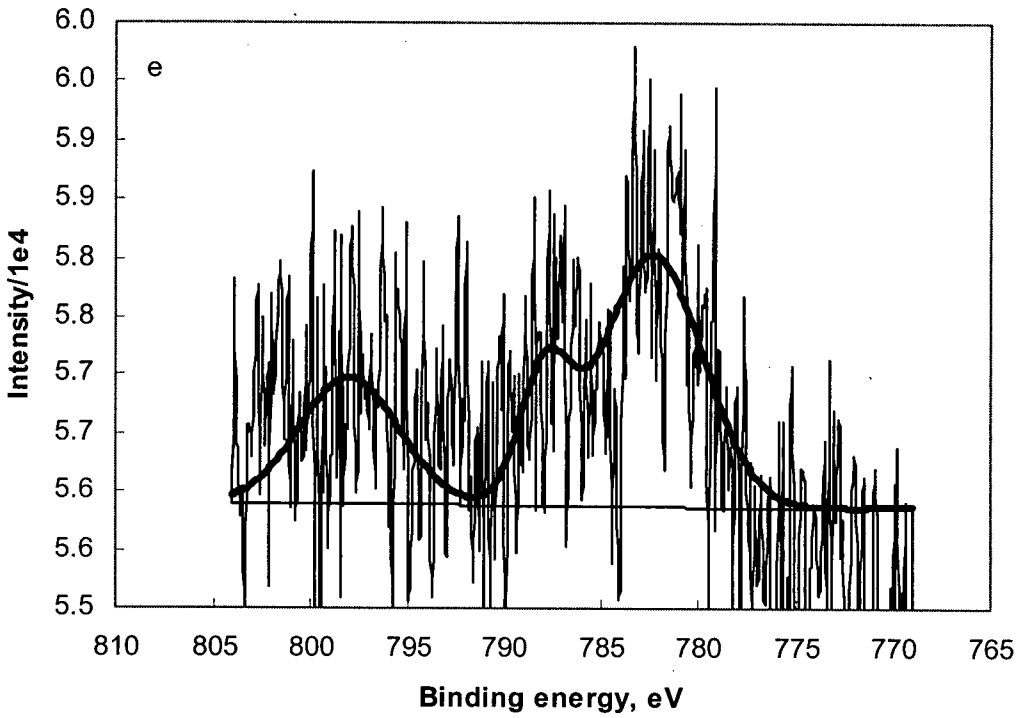

Figure C.7 Comparison of raw data and fit data of surface Co 2p Spectra on modified catalysts. a: unreduced 12wt% Co/SiO_2; b: reduced 12wt% Co/SiO_2; c: reduced $Co/BaO/SiO_2$; d: reduced $Co/ZrO_2/SiO_2$; e: reduced $Co/La_2O_3/SiO_2$.

C.3 XPS Narrow Scan C 1s Spectra

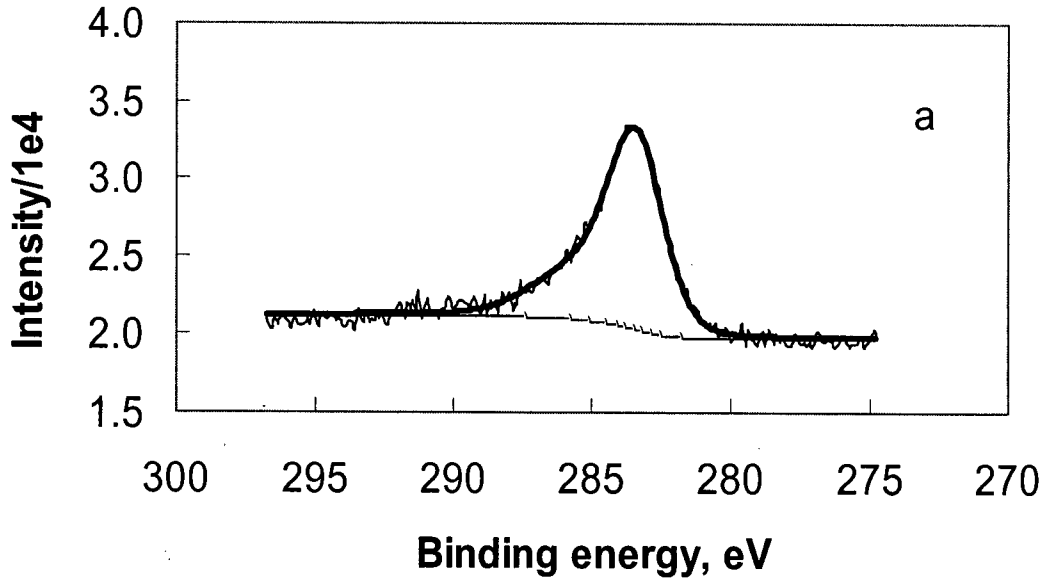

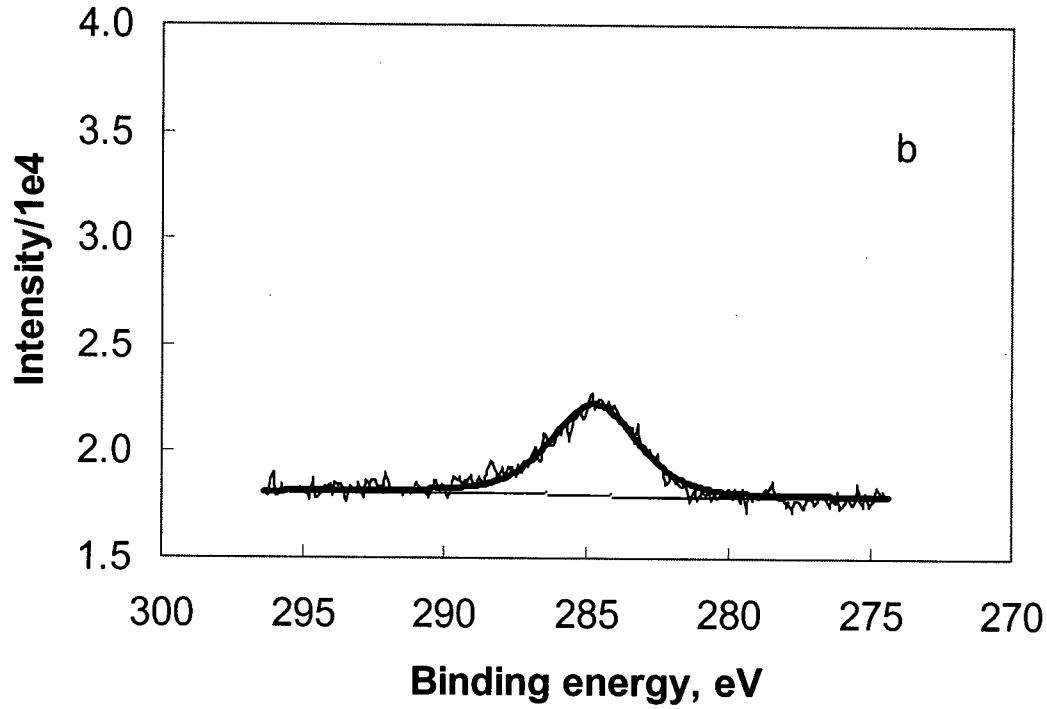

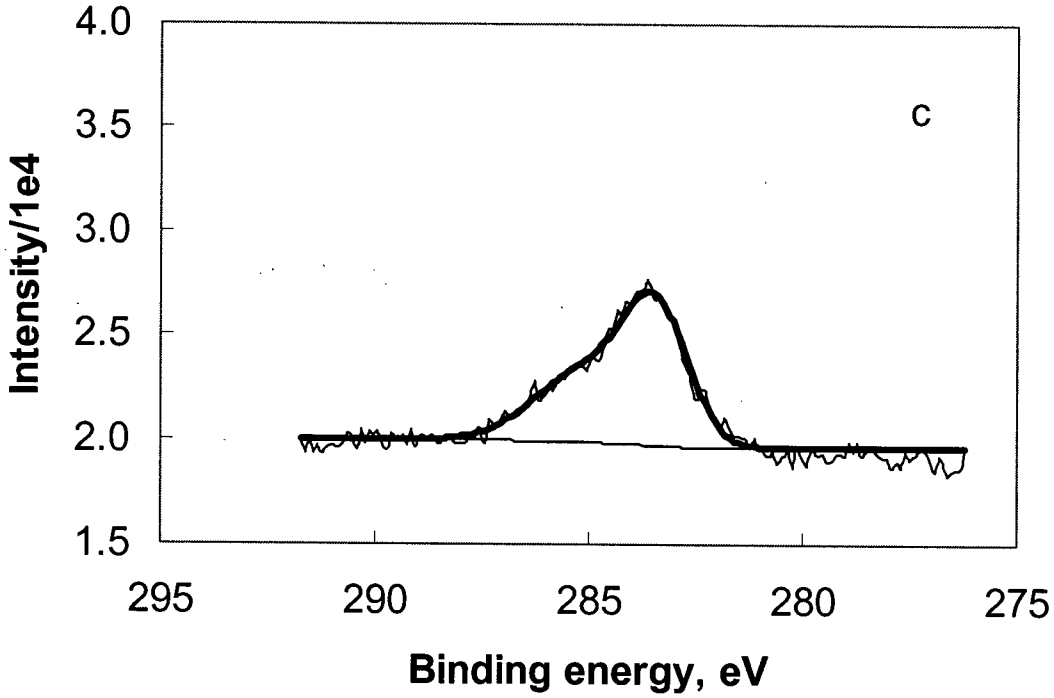

Figure C.8 Comparison of raw data and fit data of C 1s spectra on used catalysts surface. a: $Co/BaO/SiO_2$; b: $Co/ZrO_2/SiO_2$; c: $Co/La_2O_3/SiO_2$.

C.4 XPS Narrow Scan O 1s Spectra

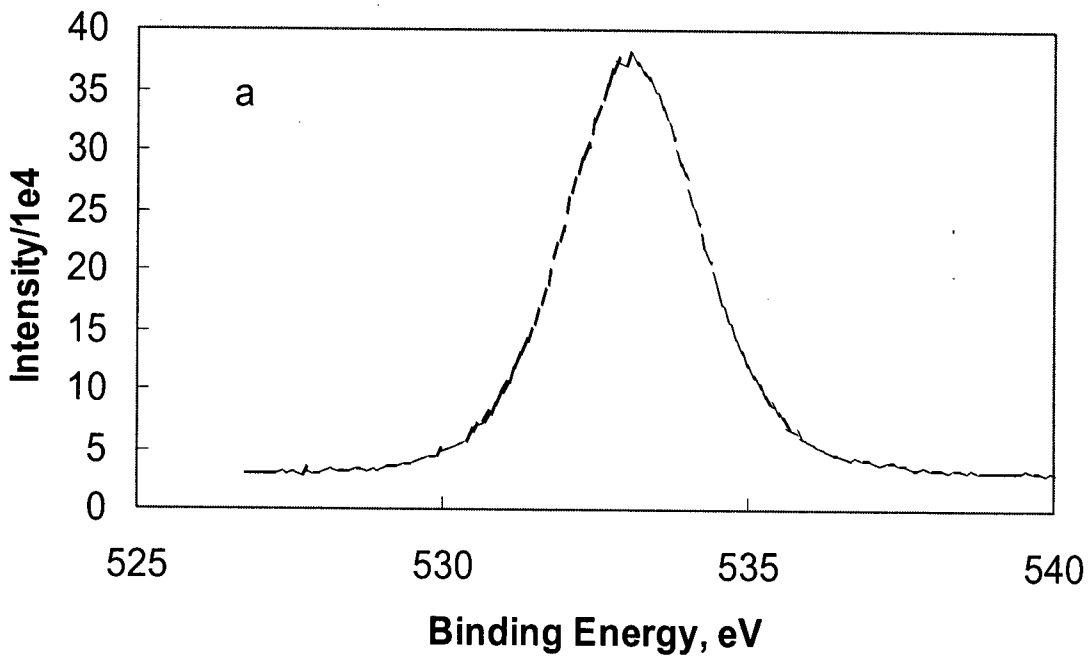

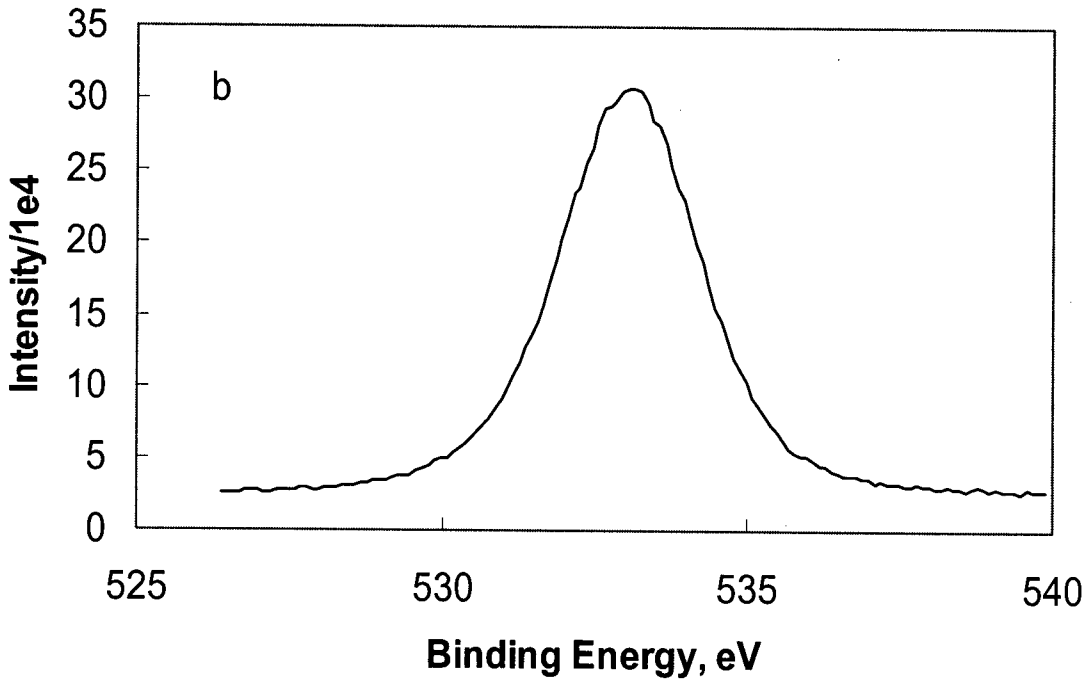

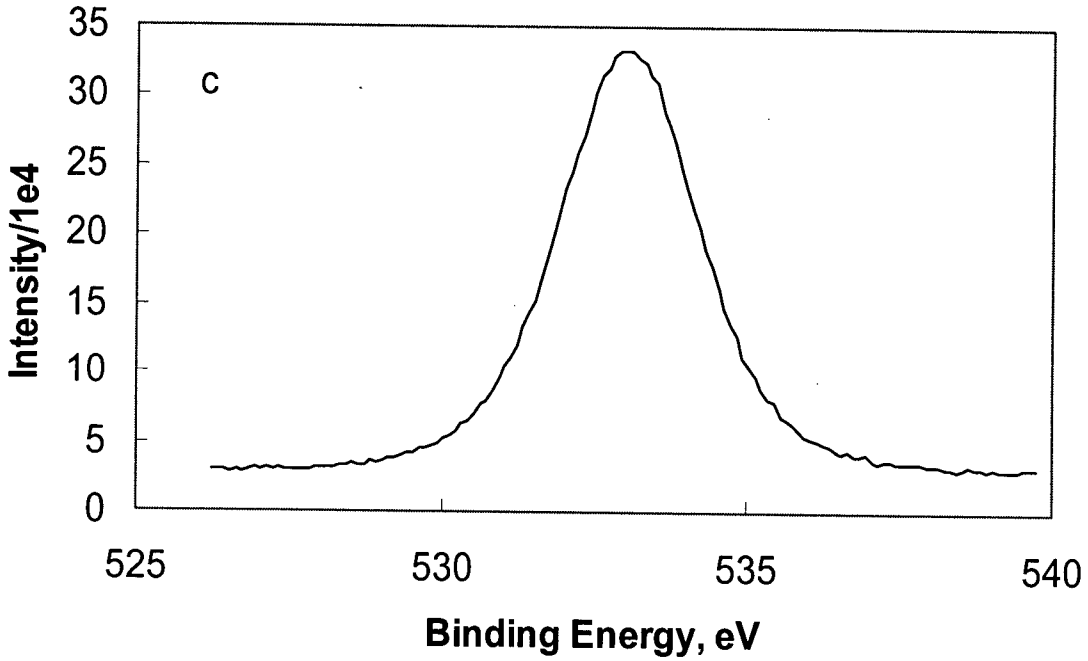

Figure C.9 XPS O 1s spectra on used catalysts surface. a: $Co/BaO/SiO_2$; b: $Co/ZrO_2/SiO_2$; c: $Co/La_2O_3/SiO_2$.

Appendix D Gas Flow and GC Calibration

D.1 Gas Flow Calibration

In the present study, four mass flow controllers were used in the activity test. The calibrated gas, full range and the sensor conversion factor of the calibrated gas were listed in Table D.1. Sensor conversion factors for specified gases were listed in Table D.2.

Table D.1 Description of Mass flow controller

Channel Number	Calibration gases	Full Range, SCCM	Sensor conversion factor of calibrated gas
1	O_2	20	0.99
2	CH_4	200	0.81
3	10% H_2S / 90% H_2	60	0.99
4	He	300	1.39

Table D.2 Sensor conversion factors for specified gases

Gases	Sensor conversion factor
Ar	1.40
He	1.39
H_2	1.01
H_2S	0.85
10% H_2S / 90% H_2	0.99*
CH_4	0.81
CO	0.99
N_2	1.005
O_2	0.99

*Sensor conversion factor for gas mixture=100/(10/0.85+90/1.01)=0.99

Table D.3 Calibration of gas flow for each flow controller

Gas (Channel)	Calibration equation
5.16% CH_4/Ar (Ch 2)	Flow=1.7295×Reading
5.2 % CH_4/Ar (Ch 2)	Flow=1.6507×Reading-7.2505
4.82% H_2, 10.4% CH_4, 2.01% C_2H_4, 3.75% C_2H_6 /Ar (Ch2)	Flow=1.4935×Reading
Pure CH_4 (Ch 2)	Flow=1.0×Reading
H_2 (Ch 3)	Flow=1.0677×Reading
Ar (Ch 4)	Flow=0.7759×Reading+32.029

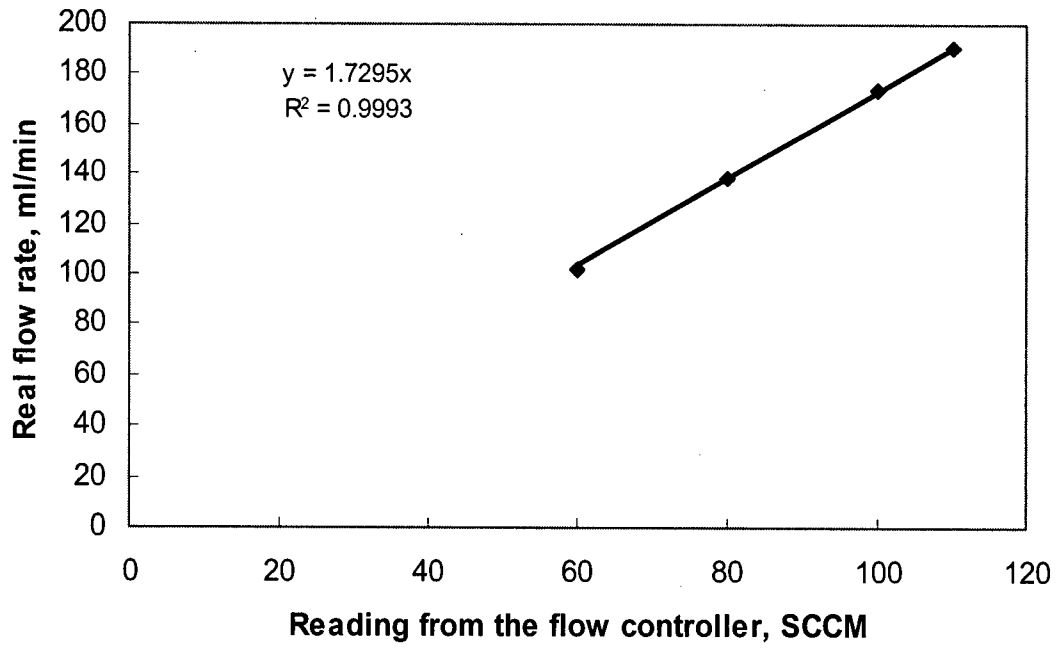

Figure D.1 Measured flow versus calibrated reading. (5.16%CH_4/Ar in Ch 2).

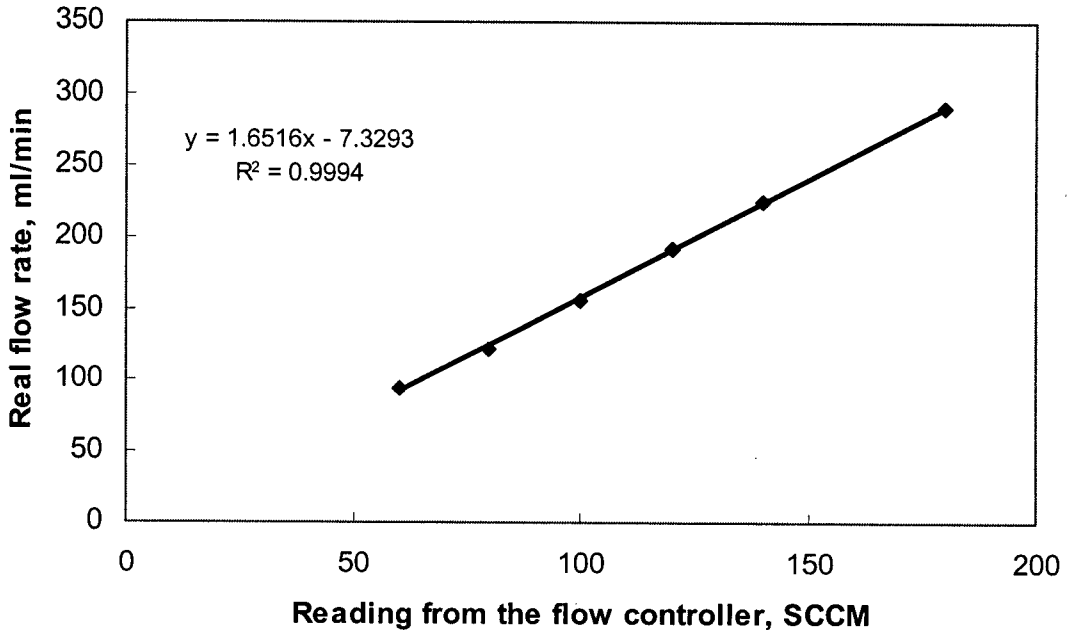

Figure D.2 Measured flow versus calibrated reading. (5.2%CH_4/Ar in Ch 2).

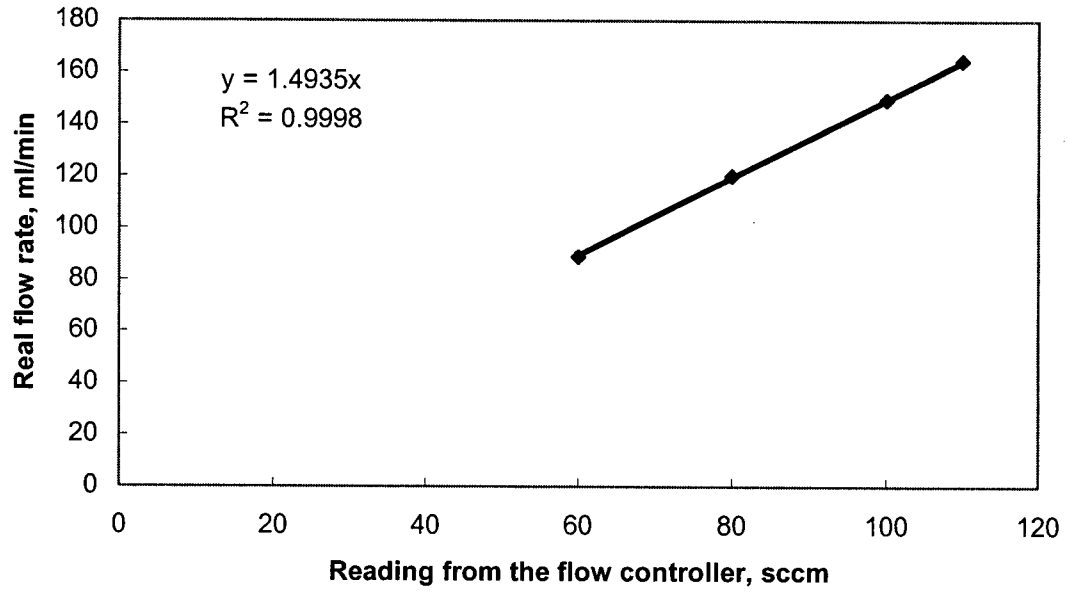

Figure D.3 Measured flow versus calibrated reading. (4.82%H_2/10.4%CH_4/Ar in Ch 2).

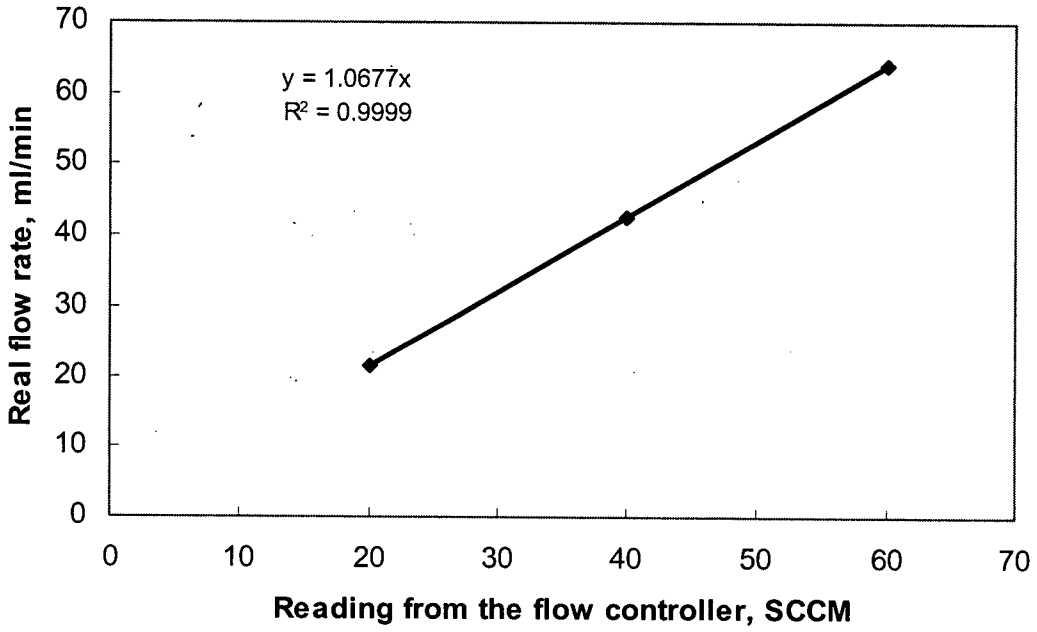

Figure D.4 Measured flow versus calibrated reading. (Pure H_2 in Ch 3).

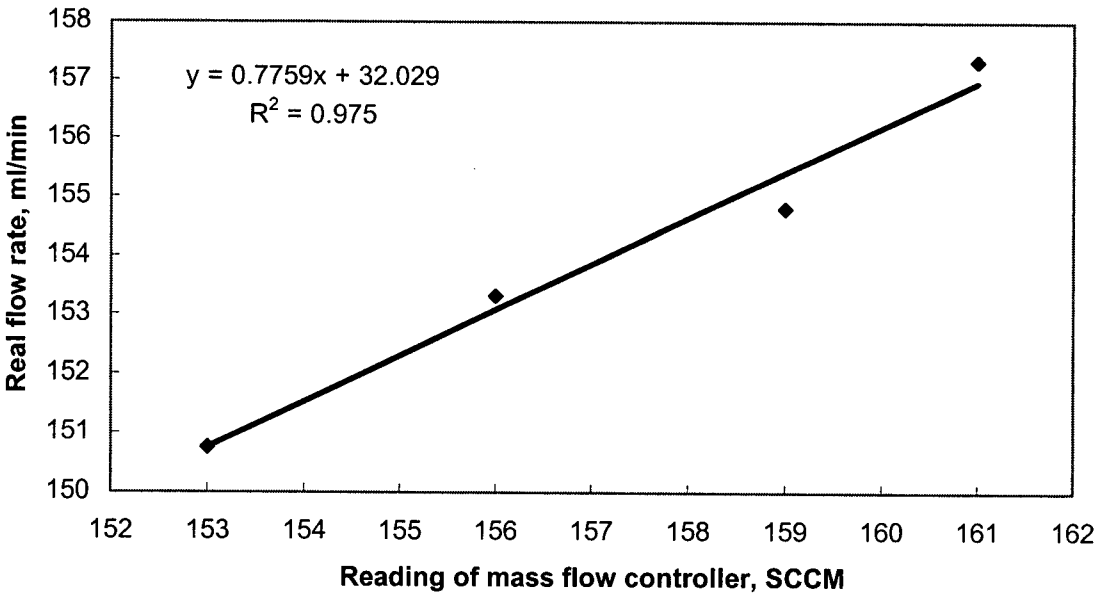

Figure D.5 Measured flow versus calibrated reading. (Ar in Ch 4).

D.2 GC Calibration

D.2.1 GC Set up

THE SAMPLING LOOP VOLUME IS 250 µL.

GC SET UP INFORMATION:

GC COLUMN: 60/80 CARBOSIEVE G 5' R59225 SUPELCO

INITIAL COLUMN TEMP 100°C

INITIAL COL HOLD TIME 3.00 MIN

INJECTOR TEMP 100°C

AUXILIARY TEMP 200°C

INITIAL AUX HOLD TIME 0.00

Detector temp 150°C

TCD A ATTEN RANGE A/Z SIG

32 0.5 yes pos

FILAMENT TEMP 175°C

FID B ATTEN RANGE A/Z

16 8 yes

PLOT SPEED 1.0 CM/MIN

ZERO OFFSET 15%

PLOT SIGNAL A

TIME TICKS YES

INSTR EVEN CODES YES

USER NUMBER 0-0

PRINT USER NUMBER NO

PRINT REPORT YES

PRINT RUN LOG NO

PLOT

PRGM TIME SPEED SIG

1 1.5 1.0 B

INITIAL RELAYS –1-2-3-4

RELAYS

PRGM TIME STATE

1	0.50	2
2	0.70	-2
3	3.00	-2

RUN MODE 1-ANALYSIS
PEAK MEASUREMENT PARAMETER 1-AREA
LONG REPORT FORMAT NO
RESULT CALCULATION TYPE1-AREA%
DIVISOR 1.000
AMOUNT STANDARD 1.0
MULTIPLIER 1.0
RESULT UNITS
REPORT UNIDENTIFIED PEAKS YES
UNINDENTIFIED PEAK FACTOR 0.0
SAMPLE ID
SUBSTRACT BLANK BASELINE YES
PEAK REJECT VALUE 10000
SIGNAL TO NOISE RATIO 5
TANGENT PEAK HEIGHT 10
INITIAL PEAK WIDTH 2
SEQUENCE AUTOMATION
RUNS OF TABLE SINGLE
STOP AUTOMATION AFTER ERROR 0

PRGM	METHOD	RUNS
1	1	5

D.2.2 GC Calibration

A calibrated gas chromatograph (GC) with a thermal conductivity detector (TCD) and a flame ionization detector (FID) were used for the sampling and analysis of CH_4 decomposition activity. For calibration, an analyzed gas mixture (Praxair) of 4.82% H_2, 10.4 %CH_4, 2.01% C_2H_4, 3.75% C_2H_6 balanced with Ar was used. By repeat analyses, calibration factors (Moles of component in the sampling loop/Peak area) were obtained. Retention time and response factor were listed in Table D.4.

Table D.4 Response factor and retention time of GC.

Component	Retention time, min	Response factors, moles/area
H_2	1.04	2.62×10^{-13}
CH_4	2.09	2.27×10^{-12}

Appendix E XRD Results

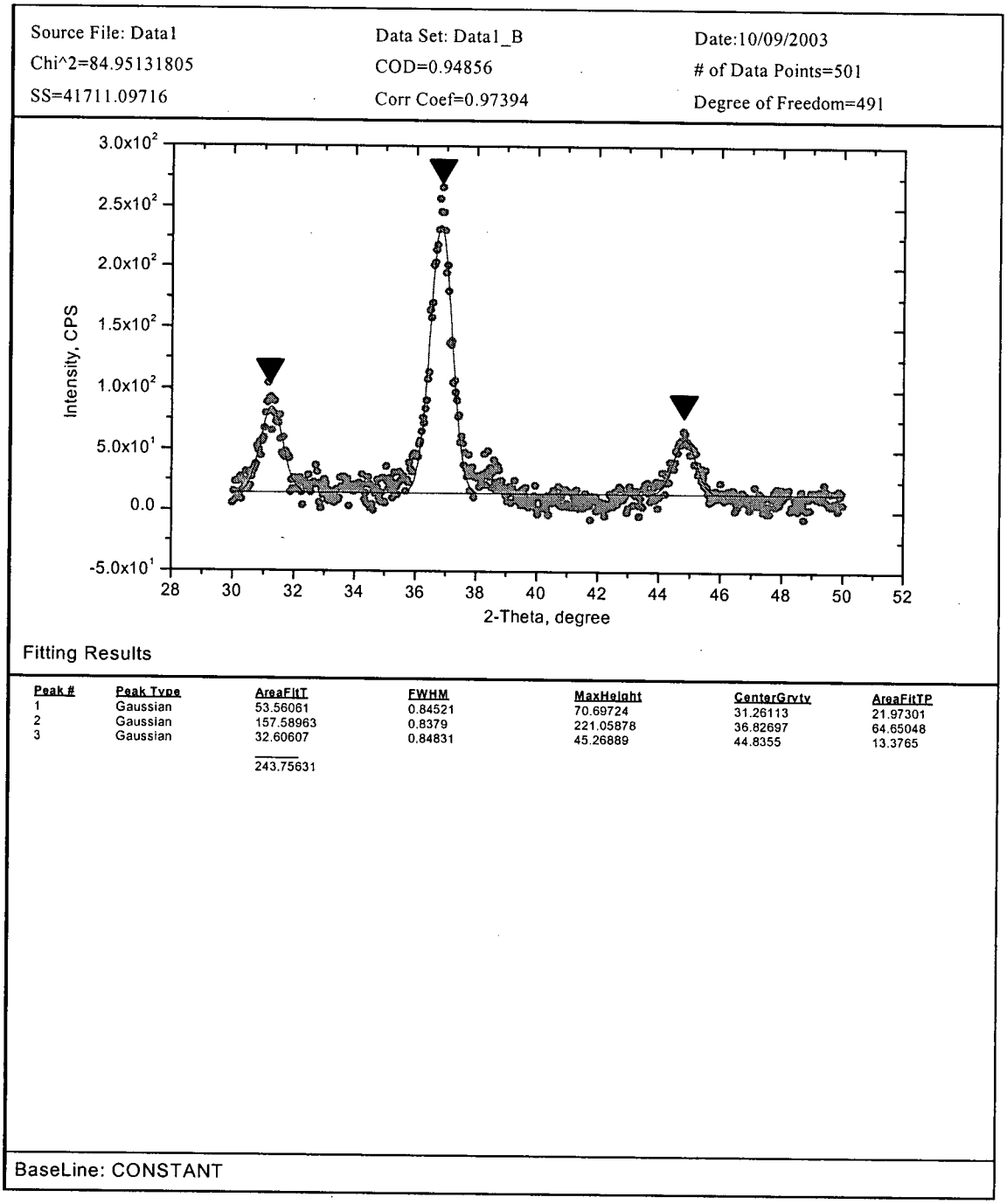

Figure E.1 XRD Pattern of 12wt% Co/SiO_2 after calcinations (▼Co_3O_4).

Source File: Data1 | Data Set: Data1_B | Date:10/09/2003
Chi^2=183.8792100 | COD=0.94416 | # of Data Points=501
SS=89916.93368 | Corr Coef=0.97168 | Degree of Freedom=489

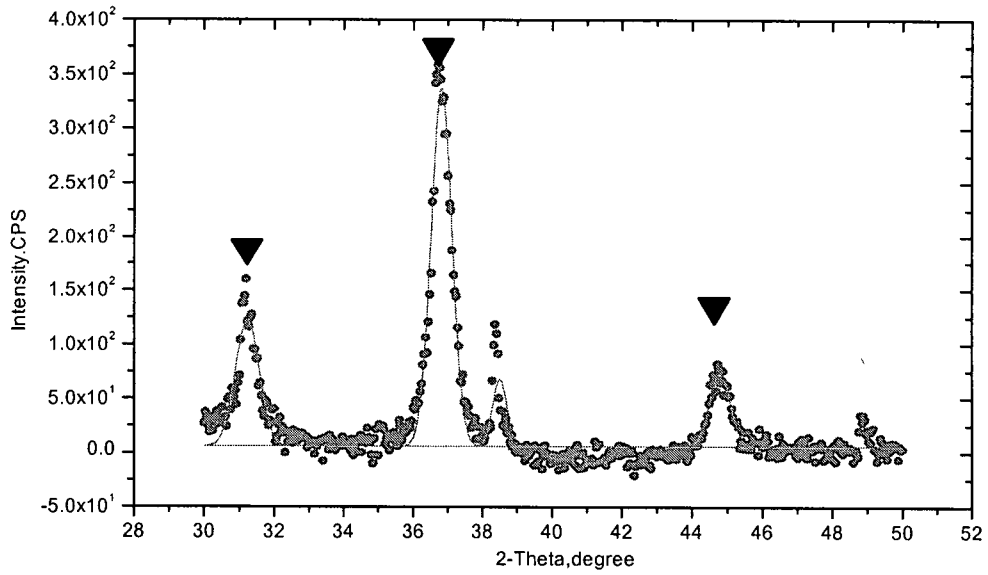

Fitting Results

Peak #	Peak Type	AreaFitT	FWHM	MaxHeight	CenterGrvty	AreaFitTP
1	Gaussian	84.45406	0.80458	116.08286	31.23026	23.57943
2	Gaussian	204.43427	0.70305	331.23504	36.81559	57.07769
3	Gaussian	28.44771	0.48024	61.96795	38.5	7.94255
4	Gaussian	40.83239	0.68246	67.76251	44.79096	11.40033
		358.16844				

BaseLine: CONSTANT

Figure E.2 XRD Pattern of 12wt% Co/BaO/SiO_2 after calcinations (▼Co_3O_4).

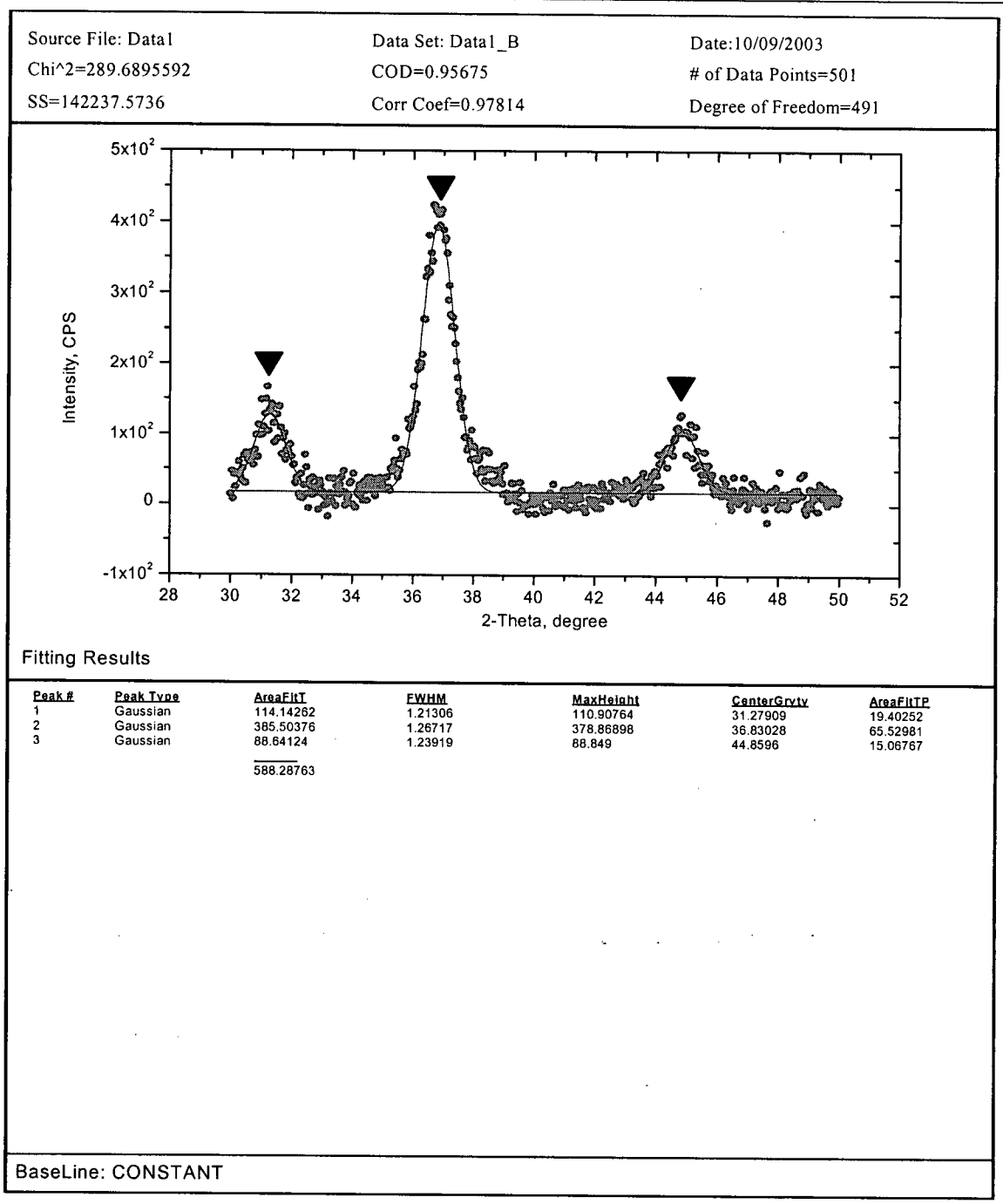

Figure E.3 XRD Pattern of 12wt% $Co/ZrO_2/SiO_2$ after calcinations (▼Co_3O_4).

Source File: Data1 | Data Set: Data1_B | Date:10/09/2003
Chi^2=123.5918852 | COD=0.94636 | # of Data Points=501
SS=60683.61563 | Corr Coef=0.97281 | Degree of Freedom=491

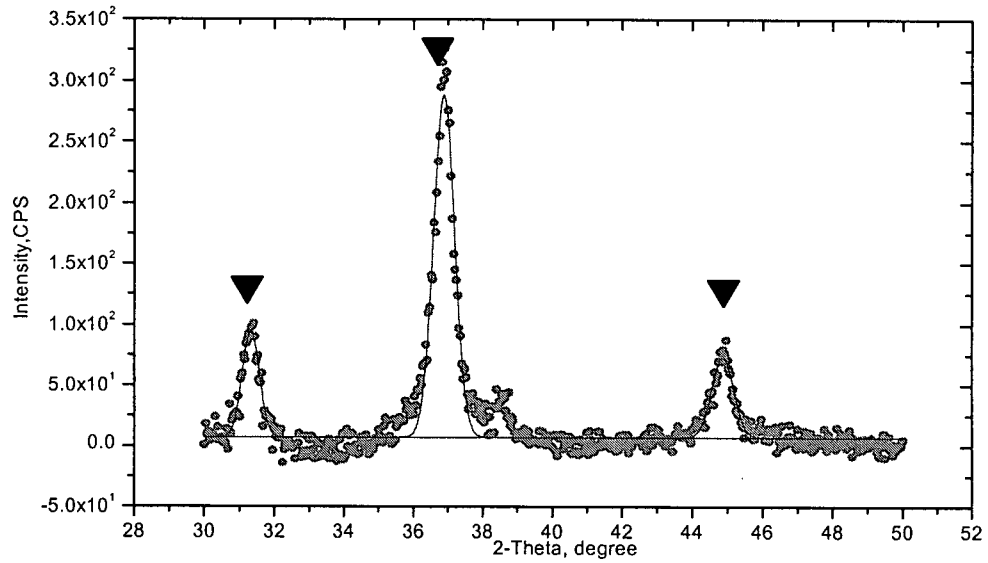

Fitting Results

Peak #	Peak Type	AreaFitT	FWHM	MaxHeight	CenterGrvty	AreaFitTP
1	Gaussian	46.97437	0.57013	87.33545	31.32547	17.84837
2	Gaussian	174.78516	0.71022	280.87968	36.88327	66.41133
3	Gaussian	41.42623	0.71731	66.03809	44.8636	15.7403
		263.18576				

BaseLine: CONSTANT

Figure E.4 XRD Pattern of 12wt% $Co/La_2O_3/SiO_2$ after calcinations (▼Co_3O_4).

43-1003 Quality: C
CAS Number:
Molecular Weight: 240.80
Volume[CD]: 528.30
Dx: 6.055 Dm:
S.G.: Fd3m (227)
Cell Parameters:
a 8.084 b c
α β γ
SS/FOM: F30=317(.0032, 30)
I/Icor: 4.30
Rad: CuKa1
Lambda: 1.54056
Filter:
d-sp: calculated

Co3 O4
Cobalt Oxide
Ref: Grier, D., McCarthy, G., North Dakota State University, Fargo, North Dakota, USA, ICDD Grant-in-Aid, (1991)

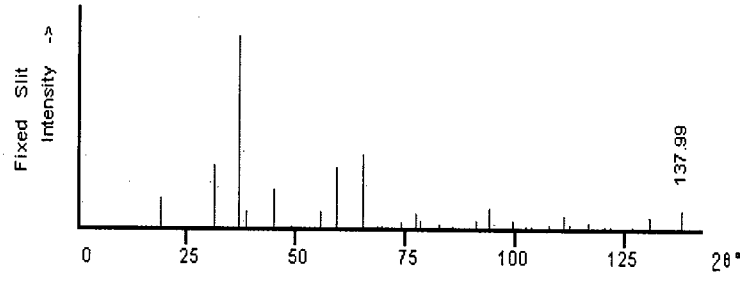

2θ	int-f	h	k	l	2θ	int-f	h	k	l	2θ	int-f	h	k	l
19.000	16	1	1	1	69.741	<1	4	4	2	103.58	<1	6	4	4
31.271	33	2	2	0	74.117	3	6	2	0	107.90	2	8	2	2
36.845	100	3	1	1	77.338	8	5	3	3	111.20	7	7	5	1
38.546	9	2	2	2	78.403	4	6	2	2	112.33	2	6	6	2
44.808	20	4	0	0	82.625	2	4	4	4	116.91	3	8	4	0
49.081	<1	3	3	1	85.759	1	5	5	1	120.48	<1	9	1	1
55.655	9	4	2	2	90.963	4	6	4	2	121.69	<1	8	4	2
59.353	32	5	1	1	94.096	11	7	3	1	126.71	1	6	6	4
65.231	38	4	4	0	99.331	4	8	0	0	130.73	6	9	3	1
68.628	1	5	3	1	102.51	<1	7	3	3	137.99	10	8	4	4

Figure E.5 Standard XRD pattern for Co_3O_4.

Table E.1 Calculation of Co_3O_4 particle size for different catalysts.

Catalyst	2θ	FWHM	d_p, nm[a]
12wt% Co/SiO_2	36.82	0.84	9.9
$Co/BaO/SiO_2$	36.82	0.70	11.8
$Co/ZrO_2/SiO_2$	36.83	1.27	6.5
$Co/La_2O_3/SiO_2$	36.88	0.71	11.7

[a]: $d_p = 0.89*\lambda/(\beta*\cos\theta)$.

Appendix F Program of General Kinetic Model

F.1 Simple Model I without Surface Reaction

```
clear all
global PCH4 PH2 x y
global Ds criticalsigmai stablesigmax criticalI ns D1 weight
global time dp tsetfinal nyfinaln Cayfinal dx xdirection ac kp
% "empirical.m" is matlab routine that uses Marquardt method
% to estimate parameters in the non linear regression.
% Finite differences are used to estimate the differential needed;
% ODE is solved by matlab builtin function ODE45;

% Dependent variable is a set of methane decomposition rate, mmol/min/g
% Independent variables is a set of time,unit is min

% It includes 4 subroutines as follows:
% 'sumf.m' evaluate the sum of squares for specified a;
% 'nucleation' evaluate the rate of methane decomposition using given parameeter a
% 'coeff.m' evaluate augmented matrix;
% 'molfun.m' gives the r.h.s. functions of ODEs;
% 'gaussj.m' is a function m-file that uses Gauss elimination with
%  scaled partial selection to solve linear equation.

criticalI=10;                          % Assuming crtitical cluster size=10
criticalsigmai=10;stablesigmax=1;
dp=0.25/10; % depth of Fe foil ,in cm
weight=6e-3*6e-3*0.25e-3*7874*1000;    % Weight of foil,g
% Independent and dependent variables
x=[1.1 1.6 2.0 2.6 3.0 3.5 3.9 4.8 6.0 7.4 9.3 11.9 14.7 17.4 21.8 24.1];
y=[0.058 0.053 0.047 0.040 0.037 0.038 0.041 0.050 0.059 0.065 0.068 0.069 0.067 0.066 0.067
    0.069];
n=length(x);
% a=[ns,Ds,Di]
a0=[6.428 2.64 7.699]                  % Initial guess

tol=1e-6;maxit=100;
relax=1.0;
iter=0; maxda=1e10;

a=a0;m=length(a);
I=eye(m,m);relax=1.0;
% Step 2 and 3:Set initial lamda==1e-3 and calculate the sum of squares
lamda=1e-3;
S=feval('sumf',a);
while iter<maxit & maxda>tol
  % Step 4th : evaluate the augmented coeffient matrix
```

```
  alpha=coeff('nucleation',x,y,a);
  da=gaussj(alpha);
  acoeffold=alpha(1:m,1:m);
  b=alpha(:,m+1);
  % Step 5th: evaluate the new augmented coeffient matrix
  acoeff=acoeffold+I*lamda;
  alpha=[acoeff b];
  % Step 6th: calculate new da
  da=gaussj(alpha);
  % Step 7 th and 8th: calculate new a and Snew
  anew=a+relax*da;
  Snew=feval('sumf',anew);

  % Set suitable lambda to satisfy Snew > S
  while Snew > S
    lamda=10*lamda;
    acoeff=acoeffold+I*lamda;
    alpha=[acoeff b];
    da=gaussj(alpha);
    % Step 6th: calculate new da
    anew=a+relax*da;
    % Step 7 th and 8th: calculate new a and Snew
    Snew=feval('sumf',anew);
  end
  % Set and begin next newton's regression
  a=anew;lamda=0.1*lamda;S=Snew;
  iter=iter+1;
  maxda=max(abs(da./a))
  da
end

if maxda <= tol
  fprintf('\n Sucessful solution in %2.0f iterations!\n',iter)
  i=[1:length(a)];result=[i;a];
  for j=1:n
    f(j)=nucleation(x(j),a);
  end

  % Statistical calculations:
  % r^2 Coeef Det
  % Sum of squares due to error
  SSE=sum((y-f).^2);
  % Sum of squares about mean
  yavg=sum(y)/n;
  SSM=sum((y-yavg).^2);
  % Degree of freedom:
  DOF=n-m;
```

```
% Coefficient of determination
r2=1-SSE/SSM;
% DF Adj r2m degree of freedom adjusted r2
DOFr2=1-(SSE*(n-1))/(SSM*(DOF-1));
% Fit Standard Error
StdErr=(SSE/DOF)^0.5;

% F statistic value
F_stat=((SSM-SSE)/(m-1))/(SSE/DOF);
% Standard error
alpha=coeff('nucleation',x,f,a);
alpha1=alpha(1:m,1:m);
Coviance=inv(alpha1'*alpha1);
for i=1:m
  Cii(i)=Coviance(i,i);
end
% Based on DOF=14 , confidence level=0.05
tvalpha=2;
coefficientSE=tvalpha*(Cii.*SSE/DOF).^0.5
% Final standard error
% Calculation for plotting
newn=100;
dxf=(x(length(x))-x(1))/50;
xfine=[x(1):dxf:x(length(x))];

for j=1:length(xfine)
  finalratem(j)=nucleation(xfine(j),a);
  if xfine(j)==1.1
    timefinal=time;
    finalresult=Cayfinal;
  else
    timefinal=[timefinal;time];
    finalresult=[finalresult;Cayfinal];
  end
end
Num=size(finalresult,2);
n1final=finalresult(:,Num-2);        % nc at the tailing face corresponding to xfine
xfinal=criticalsigmai*Di.*finalresult(:,Num-1);    % Calculation of xstable
nxfinal=finalresult(:,Num); % nx at the tailing face corresponding to xfine
% Caculation of diffusion rate at the tailing face
Rdjtailfinal=Ds.*(finalresult(:,Num-3)-finalresult(:,Num-2))./dx./dx;
% Calculation of diffusion rate profile
for j=2:Num-3
  Rdjfinal(:,j)=Ds/dx/dx.*(finalresult(:,j-1)-finalresult(:,j));
end
% No surface reaction, assuming the surface carbon concentration is constant
Rdjfinal(:,1)=0;
% Calculation of ni
```

```
for j=1:length(timefinal)
  if xfinal(j) > criticalI
    ni(j)=0.5*n1final(j)*(xfinal(j)-criticalI);
  else
    ni(j)=0;
  end
end
dn3=Di.*n1final.*ni';                    % Calculation of nucleation rate
% Changing rate of n1 at the tailing face
dn2=Rdjtailfinal-stablesigmax*Di.*n1final.*nxfinal-(criticalI+1)*criticalsigmai*dn3;
Rdjfinal(:,Num-2)=dn2;

% Plot reslt
figure(1)
colormap('default')
surf(xdirection,timefinal(1:100:1000),finalresult(1:100:1000,1:Num-2))
xlabel('x direction, cm')
ylabel('Time, min')
zlabel('Site density, 1/cm^2')

figure(2)
plot(x,y,'ko')
xlabel('Time, min')
ylabel('Methane decomposition rate, mmol/min/g cat')
Legend('Experimental data','Fitted data')
hold on
plot(xfine,finalratem,'k-')
hold off

figure(3)
subplot(2,2,1),plot(timefinal,n1final,'k-')
xlabel('Time, min')
ylabel('n_1, 1/cm^2')
subplot(2,2,3),plot(timefinal,nxfinal,'k-')
xlabel('Time, min')
ylabel('n_x, 1/cm^2')
subplot(2,2,2),plot(timefinal,ni','k-')
xlabel('Time, min')
ylabel('n_i, 1/cm^2')
subplot(2,2,4),plot(timefinal,Rdjfinal(:,Num-3),'k-')
xlabel('Time, min')
ylabel('Tailing face R_d_j, 1/cm^2/s')

figure(4)
subplot(2,2,1),plot(timefinal,xfinal,'k-')
xlabel('Time,  min')
ylabel('xstable, 1/cm^2')
subplot(2,2,2),plot(timefinal,dn2,'k-')
```

```
  xlabel('Time, min')
  ylabel('dn2, 1/cm^2/s')

  subplot(2,2,3),plot(timefinal,dn3,'k-')
  xlabel('Time, min')
  ylabel('dn3, 1/cm^2/s')

  Surface=6*6/10/10/weight;
  subplot(2,2,4),plot(xfine,finalratem/Surface/1e3*6.02e23,'k-')
  xlabel('Time, min')
  ylabel('diffusion rate at leading face, 1/cm^2/s')

  figure(5)
  colormap('cool')
  surf(xdirection,timefinal(1:500:20000),finalresult(1:500:20000,1:Num-2))
  xlabel('x direction, cm')
  ylabel('Time, min')
  zlabel('Site density, 1/cm^2')

else
  error('Marquardts method did not converge')
end
% Print and plot results:
fprintf('\n Sucessful solution in %2.0f iterations!\n',iter)
i=[1:length(a)];result=[i;a];

fprintf('\n Parameter:\n')
fprintf('     a(%1.0f) = %8.3e\n',result)

fprintf('\n\n  Numeric summary:\n')
fprintf('  SSE=%8.6f              SSM=%8.6f\n',SSE,SSM)
fprintf('  r^2 Coef Det=%8.6f      DF Ajsr2=%8.6f\n',r2,DOFr2)
fprintf('  fit Std Err=%8.6f       F-value=%8.6f\n',StdErr,F_stat)

fprintf('\n\n\n Result of constants :\n')
fprintf('     ns = %8.3e        Std= %8.3e\n\n',ns,coefficientSE(1)*ns/a(1))
fprintf('     Ds = %8.3e cm^2/s  Std= %8.3e\n',Ds/60,coefficientSE(2)*Ds/a(2)/60)
fprintf('     D1 = %8.3e cm^2/s  Std= %8.3e\n',Di/60,coefficientSE(3)*Di/a(3)/60)

fprintf('\n\n\n Result of constants :\n')
fprintf('     ns = %8.3e        Std= %8.3e\n\n',ns,coefficientSE(1))
fprintf('     Ds = %8.3e cm^2/s  Std= %8.3e\n',Ds/60,coefficientSE(2)/60)
fprintf('     D1 = %8.3e cm^2/s  Std= %8.3e\n',Di/60,coefficientSE(3)/60)
```

```
function rate=nucleation(tset,a)
% m file for nucleation
global Ds ns Di
global dx
global time tsetfinal Cayfinal dx xdirection ac weight
global criticalsigmai stablesigmax D1 nx ni criticalI ns Ds dp Rdj ac tsetold Cayold

% Initial condition of nucleation rate, nx, ni
Nr=0;nx=0;ni=0;
% Calculation of surface diffusion coefficient
% Base on iron case
ns=a(1)*1e17;
Di=a(3)*1e-16*60*1e0*1e-4;          % cm^2/s
Ds=a(2)*1e-14*1e4*60*1e4;           % cm^2/s
Surface=6*6/10/10/weight;           % cm^2/g catalyst
% y is a vector, y(1) is the x/sigmai/D; y(2)is n1 ;y(3)is the nx;
m=50+1;                             % Finite grid of depth of Fe foil;
xmax=dp;                            % Assuming 6m is the maximum distance i.e. infinite
mm=m-1;                             % n is the number of x points
dx=xmax/mm;xdirection=0:dx:xmax;
% Calculate a vector of Caj at time 0
% Initial condition at t=0 with all x>0, Ca=Ca0
if tset==1.1
  y0=[0 0];                 % Initial condition for xstable/Di/criticalsigmai,nx
  Ca0=0;                    % Concentration of carbon site density at the leading face;
  Ca1=ns;                   % Concentration of carbon site density at the tailing face;
  % Set initial conditions of nc along the Fe foil
  for j=2:length(xdirection)
    Caj(j)=Ca0;
  end
  Caj(1)=Ca1;               % boundary condition at surface at t=0, Ca=Ca1
  Cay=[Caj y0];
  % Using ode23 solve the odes
  [time,Ca]=ode23('molfun',[0 tset],Cay);
  % Initial conditions for next time frame;
  Cayold=Ca(size(Ca,1),:);
  % Initial time for next time frame
  tsetold=tset;
else
  [time,Ca]=ode23('molfun',[tsetold tset],Cayold);
end
if tset~=tsetold
  Cayold=Ca(size(Ca,1),:);
  tsetold=tset;
end
Cayfinal=Ca;
% Caculate the methane decomposition rate at the leading face
rate=Rdj/6.02e23*1e3*Surface; % mmol/min/cm^2  into mmol/min/g catalyst
```

```
rate=rate;
[tset rate]
```

```
function Caprime=molfun(t,Cay)
global criticalsigmai stablesigmax D1 nx ni criticalI ns Ds dp Rdj ac weight

global dx
% molfun.m is a function file which can calculate the rhs of pde, at any time t,
% the pde can be discretized at position i by using a central difference in space

% Input arguments:
%       t- time,vector
%       Cay- a vector of concentration at different x space direction at
%                same time direction t,and with xstable/Di/criticalsigmai,nx at the tailing face
% Output arguments:
%       Caprime- a vector of first directive of Ca at different x space direction
%                  at the same time direction t

% Length of vector Cay
m=length(Cay);
mm=m-3;
Ca=Cay(1:mm+1);     % nc along the length of Fe foil
n=Cay(m-2:m);       % n1,n1 integral,n3 at the tailing face
Caprime(1)=0;       % Assuming the concentration of ns is constant;
% Calculate the rhs of unsteady state of carbon diffusion;
for i=2:mm
  Caprime(i)=Ds*(Ca(i-1)-2*Ca(i)+Ca(i+1))/dx^2;
end
% Carbon diffusion rate at the tailing face;
Rdjtail=Ds*(Ca(mm)-Ca(mm+1))/dx/dx;
% Directives of xstable/Di/criticalsigmai
dn1=n(1);
% Calculation of xstable
xstable=criticalsigmai*Di*n(2);
% Calculation of ni
if xstable > criticalI
  ni=0.5*n(1)*(xstable-criticalI);
else
  ni=0;
end
% Nucleation rate
dn3=Di*n(1)*ni;
% Site balance of n1 on the tailing face
dn2=Rdjtail-stablesigmax*Di*n(1)*n(3)-(criticalI+1)*criticalsigmai*dn3;% rate of n1
% First derivatives of nc at the tailing face;
Caprime(mm+1)=dn2;
% Vector of rhs of ODE
Caprime=[Caprime';dn1;dn3];
% Calculation of methane decomposition rate, mmol/min/g
Rdj=Ds*(Ca(1)-Ca(2))/dx/dx;
Surface=6*6/10/10/weight;% cm^2/g catalyst
```

```
rate=Rdj/6.02e23*1e3*Surface;
% [t xstable n(1) n(3) rate Ca(1)-Ca(2) dn2 Rdj Rdjtail ni ns-n(1)]
```

F.2 Simple Model II without Surface Reaction

```
clear all
global PCH4 PH2 x y knucleation kgrowth
global dx weight
global Ds criticalsigmai stablesigmax criticalI ns D1 kgowth knucleation
global time dp tsetfinal nyfinaln Cayfinal dx xdirection ac

% "empirical.m" is matlab routine that uses Marquardt method
% to estimate parameters in the non linear regression.
% Finite differences are used to estimate the differential needed;
% ODE is solved by matlab builtin function ODE;

% Dependent variable is a set of methane decomposition rate, mmol/min/g
% Independent variables is a set of time,unit is min

% It includes 4 subroutines as follows:
% 'sumf.m' evaluate the sum of squares for specified a;
% 'nucleation' evaluate the rate of methane decomposition using given parameeter a
% 'coeff.m' evaluate augmented matrix;
% 'molfun.m' gives the r.h.s. functions of ODEs;
% 'gaussj.m' is a function m-file that uses Gauss elimination with
%  scaled partial selection to solve linear equation.

criticalI=10;                                % Assuming crtitical cluster size=18
criticalsigmai=10;stablesigmax=1;
dp=0.25/10;                                  % Depth of Fe foil ,in cm
weight=6e-3*6e-3*0.25e-3*7874*1000;          % Weight of foil,g
% Given independent and dependent variable values for the regression:
x=[1.1 1.6 2.0 2.6 3.0 3.5 3.9 4.8 6.0 7.4 9.3 11.9 14.7 17.4 21.8 24.1];
y=[0.058 0.053 0.047 0.040 0.037 0.038 0.041 0.050 0.059 0.065 0.068 0.069 0.067 0.066 0.067
      0.069];
% y is in micromol/min
n=length(x);
% User defined the number of parameters going to be fitted:
% Step 1st: set initial of parameter
% a0=[sv0 Ds knucl kgrowth]
a0=[8.616 3.734 3.803 4.916]

tol=1e-6;maxit=100;
relax=1.0;
iter=0; maxda=1e10;

a=a0;m=length(a);
I=eye(m,m);relax=1.0;
% Step 2 and 3:Set initial lamda==1e-3 and calculate the sum of squares
lamda=1e-3;
S=feval('sumf',a);
```

```
while iter<maxit & maxda>tol
  % Step 4th : evaluate the augmented coeffient matrix
  alpha=coeff('nucleation',x,y,a);
  da=gaussj(alpha);
  acoeffold=alpha(1:m,1:m);
  b=alpha(:,m+1);
  % Step 5th: evaluate the new augmented coeffient matrix
  acoeff=acoeffold+I*lamda;
  alpha=[acoeff b];
  % Step 6th: calculate new da
  da=gaussj(alpha);
  % Step 7 th and 8th: calculate new a and Snew
  anew=a+relax*da;
  Snew=feval('sumf',anew);

  % Set suitable lambda to satisfy Snew > S
  while Snew > S
    lamda=10*lamda;
    acoeff=acoeffold+I*lamda;
    alpha=[acoeff b];
    da=gaussj(alpha);
    % Step 6th:calculate new da
    anew=a+relax*da;
    % Step 7 th and 8th: calculate new a and Snew
    Snew=feval('sumf',anew);
  end
  % Set and begin next newton's regression
  a=anew;lamda=0.1*lamda;S=Snew;
  iter=iter+1;
  maxda=max(abs(da./a))
end


if maxda <= tol
  i=[1:length(a)];result=[i;a];
  for j=1:n
    f(j)=nucleation(x(j),a);
  end
  % Statistical calculations:
  % r^2 Coeef Det
  % Sum of squares due to error
  SSE=sum((y-f).^2);
  % Sum of squares about mean
  yavg=sum(y)/n;
  SSM=sum((y-yavg).^2);
  % Degree of freedom:
  DOF=n-m;
```

```
% Coefficient of determination
r2=1-SSE/SSM;
% DF Adj r2m degree of freedom adjusted r2
DOFr2=1-(SSE*(n-1))/(SSM*(DOF-1));
% Fit Standard Error
StdErr=(SSE/DOF)^0.5;
% F statistic value
F_stat=((SSM-SSE)/(m-1))/(SSE/DOF);
% Standard error
alpha=coeff('nucleation',x,f,a);
alpha1=alpha(1:m,1:m);
Coviance=inv(alpha1'*alpha1);
for i=1:m
  Cii(i)=Coviance(i,i);
end
% Based on DOF=14 , confidence level=0.05
tvalpha=2;
coefficientSE=tvalpha*(Cii.*SSE/DOF).^0.5
% Final standard error
% Calculation of variables for plotting
newn=100;
dxf=(x(length(x))-x(1))/50;
xfine=[x(1):dxf:x(length(x))];
for j=1:length(xfine)
  finalratem(j)=nucleation(xfine(j),a);
  if xfine(j)==1.1
    timefinal=time;
    finalresult=Cayfinal;
  else
    timefinal=[timefinal;time];
    finalresult=[finalresult;Cayfinal];
  end
end
Num=size(finalresult,2);
% Calculation of n1 at the tailing face corresponding the xfine
n1final=finalresult(:,Num-1);
% Calculation of nct at the tailing face corresponding the xfine
nctfinal=finalresult(:,Num);
% Carbon diffusion rate profile calculation
Rdjtailfinal=Ds.*(finalresult(:,Num-2)-finalresult(:,Num-1))./dx/dx;
for j=2:Num-1
  Rdjfinal(:,j)=Ds.*(finalresult(:,j-1)-finalresult(:,j))./dx./dx;
end
Rdjfinal(:,1)=0;
% Growth and nucleation rate
dgrowth=kgrowth*n1final.^stablesigmax.*nctfinal;
dnucleation=knucleation.*n1final.^criticalsigmai;
dnct=dnucleation;
```

```
dn1=Rdjfinal(:,Num-1)-criticalsigmai.*dnucleation-stablesigmax.*dgrowth;
Caprime(:,Num)=dn1;

figure(1)
surf(xdirection,timefinal(1:500:20000),finalresult(1:500:20000,1:Num-1))
colormap('cool')
xlabel('x direction, cm')
ylabel('Time, min')
zlabel('Site density, 1/cm^2')

figure(2)
plot(x,y,'ko')
xlabel('Time, min')
ylabel('Methane decomposition rate, mmol/min/g cat')
Legend('Experimental data','Fitted data')
hold on
plot(xfine,finalratem,'k-')
hold off

      figure(3)
subplot(2,2,1),plot(timefinal,n1final,'k-')
xlabel('Time, min')
ylabel('n_1, 1/cm^2')
subplot(2,2,2),plot(timefinal,nctfinal,'k-')
xlabel('Time, min')
ylabel('n_c_t, 1/cm^2')
Surface=6*6/10/10/weight;                                    % cm^2/g catalyst
subplot(2,2,3), plot(xfine,finalratem./1e3./Surface.*6.02e23,'k-')
xlabel('Time, min')
ylabel('R_d_j at leading face, 1/cm^2/s')
      subplot(2,2,4), plot(timefinal,Rdjtailfinal,'k-')
xlabel('Time, min')
ylabel('R_d_j at tailing face, 1/cm^2/s')

figure(4)
surf(xdirection,timefinal(1:500:20000),finalresult(1:500:20000,1:Num-1))
colormap('cool')
xlabel('x direction, cm')
ylabel('Time, min')
zlabel('Site density, 1/cm^2')
else
error('Marquardts method did not converge')
end
fprintf('\n literature with boltzman method\n')
% Print and plot results:
fprintf('\n Sucessful solution in %2.0f iterations!\n',iter)
fprintf('\n Parameter:\n')
fprintf('    a(%1.0f) = %8.6e\n',result)
```

```
fprintf('\n\n Numeric summary:\n')
fprintf(' SSE=%8.6f          SSM=%8.6f\n',SSE,SSM)
fprintf(' r^2 Coef Det=%8.6f    DF Ajsr2=%8.6f\n',r2,DOFr2)
fprintf(' fit Std Err=%8.6f     F-value=%8.6f\n',StdErr,F_stat)


fprintf('\n\n\n Result of constants :\n')
fprintf('    ns = %8.3e          Std= %8.3e\n\n',ns,coefficientSE(1)*ns/a(1))
fprintf('    Ds = %8.3e cm^2/s    Std= %8.3e\n',Ds/60,coefficientSE(2)*Ds/a(2)/60)
fprintf('          knucleation = %8.3e cm^2/s          Std= %8.3e\n',knucleation/60/exp(-
      35743*4.18/900/8.314),coefficientSE(3)*knucleation/60/a(3)/exp(-
      35743*4.18/900/8.314))
fprintf('          kgrowth = %8.3e cm^2/s          Std= %8.3e\n',kgrowth/60/exp(-
      30785*4.18/8.314/900),coefficientSE(3)*kgrowth/60/a(3)/exp(-30785*4.18/8.314/900))
```

```
function rate=nucleation(tset,a)
% m file for caculation of methane decomposition rate using parameter a at given time tset
global Ds ns Di
global dx weight
global time tsetfinal Cayfinal dx xdirection ac weight
global criticalsigmai stablesigmax D1 nx ni criticalI ns Ds dp Rdj ac tsetold Cayold knucleation
       kgrowth
% Calculation of surface diffusion coefficient
ns=a(1)*1e17;
Ds=a(2)*1e-14*1e4*60*1e4;
knucleation=a(3)*1e-175*60*exp(-35743*4.18/900/8.314);
kgrowth=a(4)*1e10*60*exp(-30785*4.18/8.314/900);
Surface=6*6/10/10/weight;   % cm^2/g catalyst
% Divide depth of Fe foil into 50 section
m=50+1;
xmax=dp;                    % Assuming 6m is the maximum distance i.e. infinite
mm=m-1;                     % n is the number of t points
dx=xmax/mm;xdirection=0:dx:xmax;
% Calculate a vector of Caj at time 0
% Initial condition at t=0 with all x>0, Ca=Ca0
if tset==1.1
  y0=[0];                   % nct
  Ca0=0;                    % Site density of carbon at the tailing face
  Ca1=ns;                   % Site density of carbon at the leading face
  % Initial condition of carbon site density
  for j=2:length(xdirection)
    Caj(j)=Ca0;
  end
  Caj(1)=Ca1;               % Boundary condition at surface at t=0, Ca=Ca1
  Cay=[Caj y0];
  [time,Ca]=ode23('molfun',[0 tset],Cay);
  Cayold=Ca(size(Ca,1),:);
  tsetold=tset;
  else
  [time,Ca]=ode23('molfun',[tsetold tset],Cayold);
end
if tset~=tsetold
  Cayold=Ca(size(Ca,1),:);
  tsetold=tset;
end
Cayfinal=Ca;
rate=Rdj/6.02e23*1e3*Surface; % mmol/min/cm^2  into mmol/min/g catalyst
rate=rate;
[tset rate]
```

```
function Caprime=molfun(t,Cay)
global criticalsigmai stablesigmax D1 nx ni criticalI ns Ds dp Rdj ac knucleation kgrowth
global dx weight
% molfun.m is a function file which can calculate rhs of pde, at any time t,
% the pde can be discretized at position i by using a central difference in space

% Input arguments:
%       t- time,vector
%       Cay- a vector of concentration at different x space direction at
%            same time direction t,and with xstable/Di/criticalsigmai,nx at the tailing face
% Output arguments:
%       Caprime- a vector of first directive of Ca at different x space direction
%                at the same time direction t

m=length(Cay);mm=m-2;
Ca=Cay(1:mm+1);
% n=[n1,n(ct)] the site density at the tailing face
n=Cay(m-1:m);
% Calculation of rhs of unsteady state diffusion equation
Caprime(1)=0;
for i=2:mm
  Caprime(i)=Ds*(Ca(i-1)-2*Ca(i)+Ca(i+1))/dx^2;
end
% Carbon diffusion rate at the tailing face
Rdjtail=Ds*(Ca(mm)-Ca(mm+1))/dx/dx;
n1=n(1);
nct=n(2);
% Calculation of impinging rate, diffusion rate
dgrowth=kgrowth*n1^stablesigmax*nct;
dnucleation=knucleation*n1^criticalsigmai;
dnct=dnucleation;
% Carbon site density change rate
dn1=Rdjtail-criticalsigmai*dnucleation-stablesigmax*dgrowth;
Caprime(mm+1)=dn1;
Caprime=[Caprime';dnct];
% Carbon diffusion rate at the leading face
Rdj=Ds*(Ca(1)-Ca(2))/dx/dx;
Surface=6*6/10/10/weight;                    % cm^2/g catalyst
rate=Rdj/6.02e23*1e3*Surface;
```

F.3 Model I with Surface Reaction

```
clear all
global PCH4 PH2 x y Ds criticalsigmai stablesigmax criticalI ns D1
global time dp tsetfinal nyfinaln Cayfinal dx xdirection
global k1 k2 PCH4 PH2 Sv0 ratej kp Surface

% "empirical.m" is matlab routine that uses Marquardt method
% to estimate parameters in the non-linear regression.
% Finite differences are used to estimate the differential needed;
% ODE is solved by matlab builtin function ODE45;

% Dependent variable is a set of methane decomposition rate, mmol/min/g
% Independent variables is a set of time, min

% It includes 4 subroutines as follows:
% 'sumf.m' evaluate the sum of squares for specified a;
% 'nucleation' evaluate the rate of methane decomposition using given parameeter a
% 'coeff.m' evaluate augmented matrix;
% 'molfun.m' gives the r.h.s. functions of ODEs;
% 'gaussj.m' is a function m-file that uses Gauss elimination with
%  scaled partial selection to solve linear equation.

criticalI=10;
criticalsigmai=4;stablesigmax=5;
dp1=18.1                    % Diameter of particle size, nm
site=0.105                  % CO adsorption data mmol/g cat
Surface=site*1e-3*6.02e23*6.79e-20*1e4;
dp=2/3*dp1*1e-7;            % Length of diffusion path, cm

% Given independent and dependent variable values for the regression (Y64):
x=[0.5:3.3:56.6];
y=[0.326 0.368 0.356 0.343 0.332 0.321 0.309 0.309 0.309 0.306 0.312 0.300 0.306 0.299 0.291
    0.293 0.272 0.279]
PCH4=0.23*101325; PH2=0.12*101325;

n=length(x);
%a=[Ds, Di, kf, kg, kp]
a0=[6 6.0 9.0 2 3.1]

tol=1e-3;maxit=100;
relax=1.0;
iter=0; maxda=1e10;

a=a0;m=length(a);
I=eye(m,m);relax=1.0;
% Step 2 and 3:Set initial lamda==1e-3 and calculate the sum of squares
lamda=1e-3;
```

```
S=feval('sumf',a);

while iter<maxit & maxda>tol
  % Step 4th : evaluate the augmented coeffient matrix
  alpha=coeff('nucleation',x,y,a);
  da=gaussj(alpha);
  acoeffold=alpha(1:m,1:m);
  b=alpha(:,m+1);
  % Step 5th: evaluate the new augmented coeffient matrix
  acoeff=acoeffold+I*lamda;
  alpha=[acoeff b];
  % Step 6th: calculate new da
  da=gaussj(alpha);
  % Step 7 th and 8th: calculate new a and Snew
  anew=a+relax*da;
  Snew=feval('sumf',anew);

  % Set suitable lambda to satisfy Snew > S
  while Snew > S
    lamda=10*lamda;
    acoeff=acoeffold+I*lamda;
    alpha=[acoeff b];
    da=gaussj(alpha);
    % Step 6th:calculate new da
    anew=a+relax*da;
    % Step 7 th and 8th: calculate new a and Snew
    Snew=feval('sumf',anew);
  end
  % Set and begin next newton's regression
  a=anew;lamda=0.1*lamda;S=Snew;
  iter=iter+1;
  maxda=max(abs(da./a))
  da
end

if maxda <= tol
  for j=1:n
    f(j)=nucleation(x(j),a);
  end
  % Statistical calculations:
  % r^2 Coeef Det
  % Sum of squares due to error
  SSE=sum((y-f).^2);
  % Sum of squares about mean
  yavg=sum(y)/n;
  SSM=sum((y-yavg).^2);
  % Degree of freedom:
  DOF=n-m;
```

```
% Coefficient of determination
r2=1-SSE/SSM;
% DF Adj r2m degree of freedom adjusted r2
DOFr2=1-(SSE*(n-1))/(SSM*(DOF-1));
% Fit Standard Error
StdErr=(SSE/DOF)^0.5;
% F statistic value
F_stat=((SSM-SSE)/(m-1))/(SSE/DOF);
% Standard error
alpha=coeff('nucleation',x,f,a);
alpha1=alpha(1:m,1:m)
Coviance=inv(alpha1'*alpha1);
for i=1:m
  Cii(i)=Coviance(i,i)
end
% Based on DOF=14, confidence level=0.05
tvalpha=2.0;
coefficientSE=tvalpha*(Cii.*SSE/DOF).^0.5;

% Calculation of plooting results
newn=100;
dxf=(x(length(x))-0.5)/100;
xfine=[0.5:dxf:x(length(x))];

for j=1:length(xfine)
  finalratem(j)=nucleation(xfine(j),a);
  if xfine(j)==0.5
    timefinal=time;
    finalresult=Cayfinal;
  else
    timefinal=[timefinal;time];
    finalresult=[finalresult;Cayfinal];
  end
end

Num=size(finalresult,2);
n1final=finalresult(:,Num-4); % Calculation of n1 at the tainlign face corresponding to xfine;
xfinal=criticalsigmai*Di.*finalresult(:,Num-3);% Calculation of xstable corresponding to xfine
nxfinal=finalresult(:,Num-2);        % Calcualtion of nx corresponding to xfine;
Svfinal=finalresult(:,Num-1); % Calculation of Sv on the leading face corresponding to xfine;
Spfinal=finalresult(:,Num); % Calculation of Sv on the leading face corresponding to xfine;
nsfinal=finalresult(:,1); % Calculation of Sv on the leading face corresponding to xfine;
% Calculation of diffusion at the tailing face
Rdjtailfinal=Ds/dx/dx.*(finalresult(:,Num-5)-finalresult(:,Num-4));
Ratej=k1*PCH4.*Svfinal.^2-k2*PH2^2.*(Sv0-Svfinal-Spfinal).*Svfinal; % Rate of reaction
% Rate of ns is equal to reaction rate minus diffusion rate minus the changing rate to
    encapsulating rate
% Rate of site encapsulated by the encapsulated carbon
```

```
dSp=kp.*nsfinal.^6;
Rdjfinal=zeros(size(finalresult,1),Num-4);
Rdjfinal(:,1)=Ratej-dSp;
      % Calculation of diffusion profile
for j=2:Num-4
  Rdjfinal(:,j)=-Ds/dx/dx.*(finalresult(:,j)-finalresult(:,j-1));
end
dn4=ratej-Rdjfinal(:,2)-dSp;                    % Rate of ns
dn5=-dn4-dSp;                                   % Rate of Sv
% Calculation of ni corresponding to xfine
for j=1:length(timefinal)
  if xfinal(j) > criticalI
    ni(j)=0.5*n1final(j)*(xfinal(j)-criticalI);
  else
    ni(j)=0;
  end
end
% Calculation of growth rate and changing rate of n1
dn3=Di.*n1final.*ni';
dn2=Rdjtailfinal-stablesigmax*Di.*n1final.*nxfinal-(criticalI+1)*criticalsigmai*dn3;% rate of
      n1

% Plot results
figure(1)
surf(xdirection,timefinal(50:50:1000),finalresult(50:50:1000,1:Num-4),-
      finalresult(50:50:1000,1:Num-4))
colormap('default')
xlabel('x direction, cm')
ylabel('Time, min')
zlabel('Site density, 1/cm^2')

figure(6)
surf(xdirection,timefinal(50:50:1000),finalresult(50:50:1000,1:Num-4))
colormap('cool')
xlabel('x direction, cm')
ylabel('Time, min')
zlabel('Site density, 1/cm^2')

figure(2)
plot(x,y,'ko')
xlabel('Time, min')
ylabel('Methane decomposition rate, mmol/min/g cat')
Legend('Experimental data','Fitted data')
hold on
plot(xfine,finalratem,'k-')
hold off

figure(3)
```

```
subplot(2,2,1),plot(timefinal,nsfinal,'k-')
xlabel('Time, min')
ylabel('n_s, 1/cm^2')
subplot(2,2,2),plot(timefinal,n1final,'k-')
xlabel('Time, min')
ylabel('n_1, 1/cm^2')
subplot(2,2,3),plot(timefinal,ni','k-')
xlabel('Time, min')
ylabel('n_i, 1/cm^2')
subplot(2,2,4),plot(timefinal,nxfinal,'k-')
xlabel('Time, min')
ylabel('n_x, 1/cm^2')

figure(4)
subplot(2,2,3),plot(timefinal,Rdjfinal(:,1),'k-')
xlabel('Time, min')
ylabel('Leading face R_d_j, 1/cm^2/s')
subplot(2,2,4),plot(timefinal,Rdjfinal(:,Num-4),'k-')
xlabel('Time, min')
ylabel('Tailing face R_d_j, 1/cm^2/s')
subplot(2,2,1),plot(timefinal,Svfinal,'k-')
xlabel('Time, min')
ylabel('S_v, 1/cm^2')
subplot(2,2,2),plot(timefinal,Spfinal,'k-')
xlabel('Time, min')
ylabel('S_p, 1/cm^2')

figure(5)
subplot(2,2,1),plot(timefinal,xfinal,'k-')
xlabel('Time, min')
ylabel('xstable, 1/cm^2')
subplot(2,2,2),plot(timefinal,dn2,'k-')
xlabel('Time, min')
ylabel('dn2, 1/cm^2/s')
subplot(2,2,3),plot(timefinal,dSp,'k-')
xlabel('Time, min')
ylabel('rate, 1/cm^2/s')
hold on
subplot(2,2,3),plot(timefinal,Ratej,'k-')
xlabel('Time, min')
ylabel('rate, 1/cm^2/s')
hold on
subplot(2,2,3),plot(timefinal,Rdjfinal(:,1),'k-')
xlabel('Time, min')
ylabel('rate, 1/cm^2/s')
hold off
subplot(2,2,4),plot(timefinal,dSp./Rdjfinal(:,1),'k-')
xlabel('Time, min')
```

```
  ylabel('ratio')
else
  error('Marquardts method did not converge')
end
% Print and plot results:
fprintf('\n Sucessful solution in %2.0f iterations!\n',iter)
i=[1:length(a)];result=[i;a];
fprintf('\n 10wtCo/SiO2\n')
fprintf('\n Parameter:\n')
fprintf('     a(%1.0f) = %8.3e\n',result)

fprintf('\n\n  Numeric summary:\n')
fprintf('  SSE=%8.6f              SSM=%8.6f\n',SSE,SSM)
fprintf('  r^2 Coef Det=%8.6f      DF Ajsr2=%8.6f\n',r2,DOFr2)
fprintf('  fit Std Err=%8.6f       F-value=%8.6f\n',StdErr,F_stat)

fprintf('\n\n\n Result of constants :\n')
fprintf('     Ds = %8.3e cm^2/s  Std= %8.3e\n',Ds/60,coefficientSE(1)*Ds/a(1)/60)
fprintf('     D1 = %8.3e cm^2/s  Std= %8.3e\n',Di/60,coefficientSE(2)*Di/a(2)/60)
fprintf('     k1 = %8.3e         Std= %8.3e\n',k1,coefficientSE(3)*k1/a(3))
fprintf('     k2 = %8.3e         Std= %8.3e\n',k2,coefficientSE(4)*k2/a(4))
fprintf('     kp = %8.3e         Std= %8.3e\n',kp,coefficientSE(5)*kp/a(5))

fprintf('\n\n\n Result of constants :\n')
fprintf('     Ds = %8.3e cm^2/s  Std= %8.3e\n',Ds/60,coefficientSE(1))
fprintf('     D1 = %8.3e cm^2/s  Std= %8.3e\n',Di/60,coefficientSE(2))
fprintf('     k1 = %8.3e         Std= %8.3e\n',k1,coefficientSE(3))
fprintf('     k2 = %8.3e         Std= %8.3e\n',k2,coefficientSE(4))
fprintf('     kp = %8.3e         Std= %8.3e\n',kp,coefficientSE(5))
```

```
function rate=nucleation(tset,a)
% function file for calculation of rate
global Ds ns D1 dx
global time dp tsetfinal nyfinaln Cayfinal dx xdirection ac
global k1 k2 PCH4 PH2 Sv0 ratej kp Surface
global criticalsigmai stablesigmax D1 Nr nx ni criticalI ns Ds dp Rdj ac
global criticalsigmai stablesigmax D1 Nr nx ni criticalI ns Ds dp Rdj ac tsetold Cayold

% Initial condition of Nr, nx,ni
Nr=0;nx=0;ni=0;
% Calculation of surface diffusion coefficient
% Base on iron case
Sv0=1/6.79e-20/1e4;          % 1/cm^2
Ds=a(1)*1e-14*60;
Di=a(2)*1e-19*60*1e3;        %cm^2/s
k1=a(3)*1e-19;
k2=a(4)*1e-22;
kp=a(5)*1e-74;
% y is a vector, y(1) is the x/sigmai/D;y(2)is n1;
% y(3)is active site on the leading face;encapsulating carbon site density;
% Divide the diffusion direction into finte grid
m=5+1;
xmax=dp;                     % Assuming 6m is the maximum distance i.e. infinite
mm=m-1;                      % n is the number of t points
dx=xmax/mm;xdirection=0:dx:xmax;
% Calculate a vector of Caj at time 0
% Initial condition at t=0 with all x>0, Ca=Ca0
if tset==0.5
  y0=[0 0 Sv0 0];   % Integral of n1 and nx ,active site,encapsulating carbon site density;
  Ca0=0;            % Concentration of oxygen at the leading face;
  Ca1=0;            % Concentation of carbon at the tailing face;
  for j=2:length(xdirection)
    Caj(j)=Ca0;
  end
  Caj(1)=Ca1;          % Boundary condition at surface at t=0, Ca=Ca1
  Cay=[Caj y0];
  [time,Ca]=ode23('molfun',[0 tset],Cay);
  % Set initial condition for the next time frame
  Cayold=Ca(size(Ca,1),:);
  tsetold=tset;
else
  [time,Ca]=ode23('molfun',[tsetold tset],Cayold);
end
if tset~=tsetold
  Cayold=Ca(size(Ca,1),:);
 tsetold=tset;
end
Cayfinal=Ca;
```

```
% Call ode45 to solve a series of ODEs: D
rate=ratej/6.02e23*1e3*Surface; % mmol/min/cm^2  into mmol/min/g catalyst
rate=rate;
[tset rate]

function Caprime=molfun(t,Cay)
global criticalsigmai stablesigmax D1 Nr nx ni criticalI ns Ds dp Rdj ac
global Ds ns Rdj Surface dx
global k1 k2 PCH4 PH2 Sv0 ratej kp

% molfun.m is a function file which can calculate rhs of pde, at any time t,
% the pde can be discretized at position i by using a central difference in space

% Input arguments:
%       t- time,vector
%       Cay- a vector of concentration at different x space direction at
%            same time direction t,and with xstable/Di/criticalsigmai,nx at the tailing face
% Output arguments:
%       Caprime- a vector of first directive of Ca at different x space direction
%            at the same time direction t

% Length of vector Cay
m=length(Cay);mm=m-3-2;
Ca=Cay(1:mm+1);
% n=[n1, n1 integral, n3, n(1), ns, sv, sp];
n=[Cay(m-2-2:m-2);Cay(1);Cay(m-1:m)];
ns=n(4);        % Carbon site density on the leading face;
Sp=n(6);        % Site density of encapsulating carbon on the leading face;
Sv=n(5);        % Surface active site on the leading face;
ratej=k1*PCH4*Sv^2-k2*PH2^2*(Sv0-Sv-Sp)*Sv; % Rate of reaction on the leading face;
% Rate of ns is equal to reaction rate minus diffusion rate minus the changing rate to
      encapsulating rate;
% Rate of site encapsulated by the encapsulated carbon;
dSp=kp*ns^6;                % Changing rate of encapsulating carbon site density;
Rdj=Ds*(Ca(1)-Ca(2))/dx/dx;% Carbon diffusion rate at the leading face;
dn4=ratej-Rdj-dSp;          % Rate of ns single atom on the surface
dn5=-ratej+Rdj;             % Rate of sv
% [t ns xstable n(2) n(3) Rdj dn4]
% Calulation of rhs of unsteady state diffusion equation
Caprime(1)=dn4;
for i=2:mm
  Caprime(i)=Ds*(Ca(i-1)-2*Ca(i)+Ca(i+1))/dx^2;
end
% Carbon diffusion rate at the tailing face
Rdjtail=Ds*(Ca(mm)-Ca(mm+1))/dx/dx;
% Changing rate of xstable/Di/criticalsigmai=dn1;
dn1=n(1);
xstable=criticalsigmai*Di*n(2);      % Calculation of xstable
```

```
% Calculation of ni
if xstable > criticalI
  ni=0.5*n(1)*(xstable-criticalI);
else
  ni=0;
end
% Calculation of growth rate
dn3=Di*n(1)*ni;
dn2=Rdjtail-stablesigmax*Di*n(1)*n(3)-(criticalI+1)*criticalsigmai*dn3;   % Rate of n1
Caprime(mm+1)=dn2;
Caprime=[Caprime';dn1;dn3;dn5;dSp];
% Calculation of methane decomposition rate, mmol/min/g
rate=ratej/6.02e23*1e3*Surface;
% [t xstable n(1) n(3) rate dn2 Sv Sv0-Sv-Sp dn5 ns Sp]
```

F.4 Common Matlab Function Files

```
%gaussj.m
function x=gaussj(A)
% gaussj.m is a function m-file that uses Gauss elimination with
% scaled partial selection to solve linear equation of the form:
%          [A]*{X}={C}
% Input argument:
%       A=argumented coefficient matrix with the column vector of the rhs
%       constants, c, included as its n+1st column
% Output argument:
%       X=vector of solution values

n=size(A,1); nm=n-1; np=n+1;

% Carry out elimination process n-1 times
for k=1:nm
  kp=k+1;

% Search for largest coefficient of x(k) for rows k through
% n. pivot is the row index of the largest scaled coefficient.
  for i=k:n
    maxAij(i)=abs(A(i,k));
    for j=k:n
      if abs(A(i,j))>maxAij(i);
        maxAij(i)=abs(A(i,j));
      end
    end
    S(i)=A(i,k)/maxAij(i);
  end
  absSpivot=abs(A(k,k))/maxAij(i); pivot=k;
  for i=kp:n
    if abs(S(i))>absSpivot
      absSpivot=abs(S(i)); pivot=i;
    end
  end

% Exchange rows k and pivot if pivot~=k
  if pivot~=k
    for j=k:np
      temp=A(pivot,j);
      A(pivot,j)=A(k,j);
      A(k,j)=temp;
    end
  end


% Eliminate coefficient of x(k) from rows k+1 through n
```

```
  for i=kp:n
    quot=A(i,k)/A(k,k); A(i,k)=0;
    for j=kp:np
      A(i,j)=A(i,j)-quot*A(k,j);
    end
  end
end

% Carry additional elimination process n-1 times to get the final matrix
% has non-zero elements only on the main diagonal.
for k=1:nm
  kn=np-k;
  if A(k,k)==0
    error('Zero pivot coefficient encountered!')
  end
% Eliminate coefficient of x(k) from rows n-k through 1
  for i=(n-k):-1:1
    quot=A(i,kn)/A(kn,kn);
    A(i,np)=A(i,np)-quot*A(kn,np);
  end
end
% Result
for i=1:n
  x(i)=A(i,np)/A(i,i);
end
```

```
function alpha=coeff(f,x,y,a)
% 'coeff.m' is a function m-file that calculates the
%  augmented Jacobian matrix required by Marquardt's
%  method for nonlinear curve fitting.
%
% Input arguments:
%     f = dummy name of curve fitting function
%    df = dummy name of partial derivative function
%     x = vector of x values
%     y = vector of y values
%     a = vector of parameter estimates
% Output argument:
%     alpha = augmented Jacobian matrix

% Evaluate lengths of x and a vectors
n=length(x);m=length(a);mp=m+1;
% Determine vector of differences and matrix of partial differentials
for k=1:n
  ftemp(k)=feval(f,x(k),a);
  diff(k)=y(k)-ftemp(k);
end
for i=1:m
  dela=1e-4*a(i);a(i)=a(i)+dela;
  for k=1:n
    ftempnew(k)=feval(f,x(k),a);
    dfda(i,k)=(-ftemp(k)+ftempnew(k))/dela;
  end
end
% Calculate elements of the augmented Jacobian matrix
alpha=zeros(m,mp);
for i=1:m
  for j=i:m
    for k=1:n
      alpha(i,j)=alpha(i,j)+dfda(i,k)*dfda(j,k);
    end
    if j~=i
      alpha(j,i)=alpha(i,j);
    end
  end
  for k=1:n
    alpha(i,mp)=alpha(i,mp)+diff(k)*dfda(i,k);
  end
end
```

```
function f=sumf(a)
global PCH4 PH2 x y tsetold
% Input argument:
%       a=given parameters
%       Output argument:
%       f=sum of difference square

n=length(y);
f=0;
for i=1:n
    fxik=nucleation(x(i),a);
    f=f+(y(i)-fxik)^2;
end
```

Appendix G Effect of t^* on the Estimate of r^* and $100k_d$

As described in the Section 3.4.2, the activity profile was described by the modified first order decay model Equation (3.2). Equation (3.2) required t^*, the reaction time corresponding to the maximum reaction rate to be determined. In order to estimate the error in r^* and $100k_d$, caused by the value of t^* determined from experimental data, value of t^* was shifted to one time interval before and after the chosen t^*. Then, r^* and $100k_d$ with standard errors were estimated corresponding to these different t^* values, as listed in Table G.1 and Figure G.1 to Figure G.4. Data of Table G.1 and Figure G.1 to Figure G.4 include the parameters with standard errors, estimated at different t^* values for two different activity profiles with different gas phase composition K_M.

Data of Table G.1 and Figure G.1 to Figure G.4 show that for both cases, the estimated errors in r^* and $100k_d$ resulting from possible errors in identifying t^*, are small since the estimations corresponding to the shifted t^* are located within the standard errors of the optimal r^* and $100k_d$ estimates.

Table G.1 Effect of t^* on the Estimation of r^* and $100k_d$.

	Identified t^*, min	r^*, mmol/min/g cat	$100\,k_d$, 1/min
K_M=0.02	10.4	1.42±0.09	3.30±0.31
	13.7 (Optimal)	1.42±0.07	3.82±0.31
	17.0	1.41±0.06	3.71±0.30
K_M=0.05	7.1	0.39±0.01	0.69±0.06
	10.4 (Optimal)	0.39±0.01	0.75±0.06
	13.7	0.39±0.01	0.78±0.07

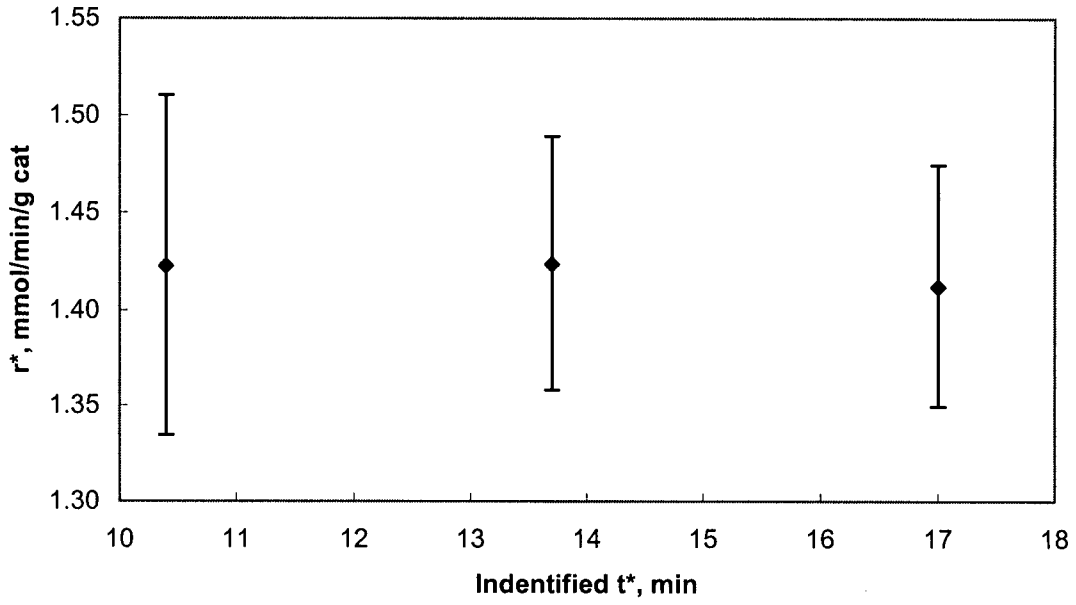

Figure G.1 Effect of t^* on the estimation of r^* (Activity profile with $K_M = 0.02atm$ of Figure 3.2).

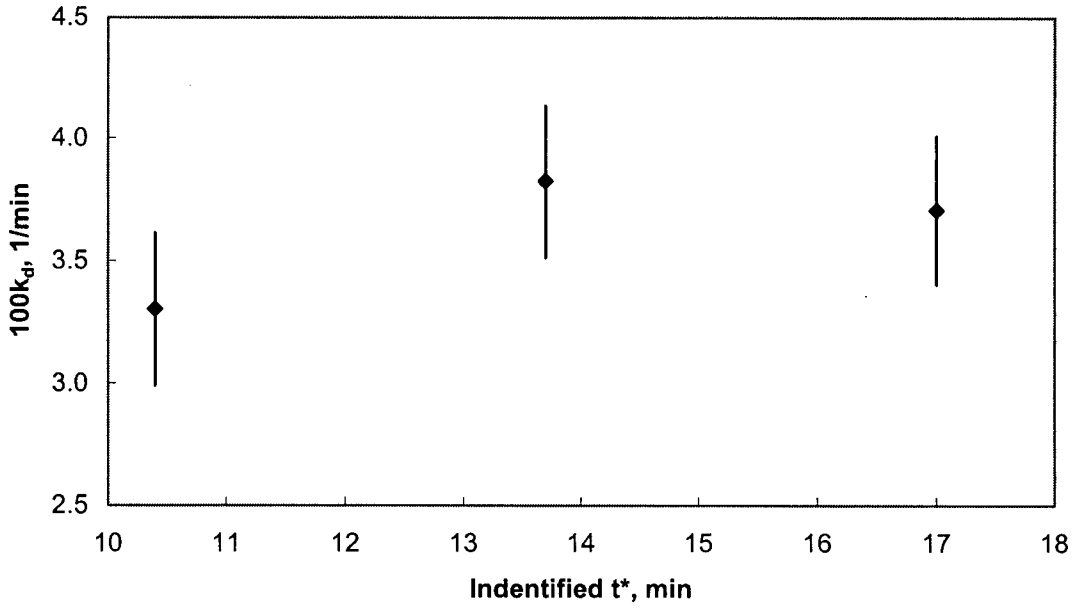

Figure G.2 Effect of t^* on the estimation of $100k_d$ (Activity profile with $K_M = 0.02atm$ of Figure 3.2).

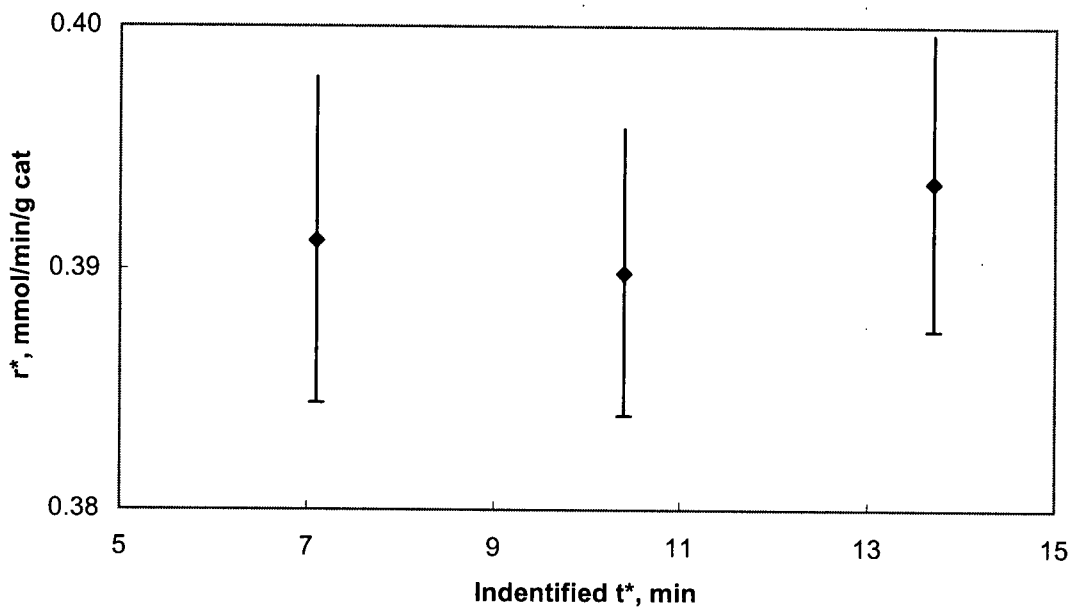

Figure G.3 Effect of t^* on the estimation of r^* (Activity profile with $K_M = 0.05atm$ of Figure 3.2).

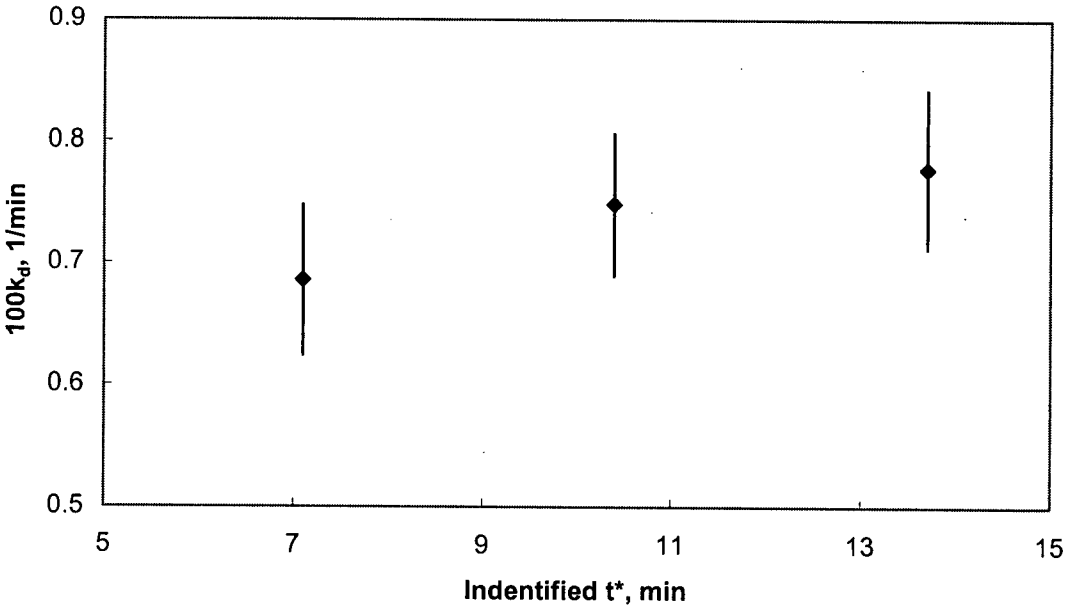

Figure G.4 Effect of t^* on the estimation of $100k_d$ (Activity profile with $K_M = 0.05atm$ of Figure 3.2).

Appendix H Conversion of K_M to Carbon Activity

In the present study, $K_M = P_{H_2}^2 / P_{CH_4}$ was used to describe the gas phase composition. The gas phase composition can also be expressed as carbon activity $a_c = K_e P_{CH_4} / P_{H_2}^2$. The conversion of $K_M = P_{H_2}^2 / P_{CH_4}$ to $a_c = K_e P_{CH_4} / P_{H_2}^2$ can be expressed as $a_c = K_e / K_M$. Herein, the equilibrium constant $K_e = 0.462 atm$ (Rostrup-Nielson, 1972).

Table H.1 Conversion table of $K_M = P_{H_2}^2 / P_{CH_4}$ to $a_c = K_e P_{CH_4} / P_{H_2}^2$.

$K_M = P_{H_2}^2 / P_{CH_4}$	$a_c = K_e P_{CH_4} / P_{H_2}^2$
0.01	46.2
0.02	23.1
0.03	15.4
0.04	11.6
0.05	9.2
0.06	7.7
0.07	6.6
0.08	5.8
0.09	5.1
0.1	4.6
0.11	4.2